

**ANALYSIS OF DATA FROM A CALIBRATION
NEUTRON MONITOR AT DOI INTHANON AND A
SHIP-BORNE NEUTRON MONITOR**

WARAPORN NUNTIYAKUL

**A THESIS SUBMITTED IN PARTIAL FULFILLMENT
OF THE REQUIREMENTS FOR
THE DEGREE OF DOCTOR OF PHILOSOPHY
(PHYSICS)
FACULTY OF GRADUATE STUDIES
MAHIDOL UNIVERSITY
2014**

COPYRIGHT OF MAHIDOL UNIVERSITY

Thesis
entitled
**ANALYSIS OF DATA FROM A CALIBRATION
NEUTRON MONITOR AT DOI INTHANON AND A
SHIP-BORNE NEUTRON MONITOR**

.....
Ms. Waraporn Nuntiyakul
Candidate

.....
Prof. David Ruffolo,
Ph.D. (Physics)
Major advisor

.....
Lect. Alejandro Sáiz,
Ph.D. (Physics)
Co-advisor

.....
Asst. Prof. Kittiwit Matan,
Ph.D. (Physics)
Co-advisor

.....
Prof. Banchong Mahaisavariya,
M.D., Dip Thai Board of Orthopedics
Dean
Faculty of Graduate Studies
Mahidol University

.....
Assoc. Prof. Weerachai Siripunvaraporn,
Ph.D. (Geophysics)
Program Director
Doctor of Philosophy Program
in Physics
Faculty of Science
Mahidol University

Thesis
entitled
**ANALYSIS OF DATA FROM A CALIBRATION
NEUTRON MONITOR AT DOI INTHANON AND A
SHIP-BORNE NEUTRON MONITOR**

was submitted to the Faculty of Graduate Studies, Mahidol University
for the degree of Doctor of Philosophy (Physics)

on
September 12, 2014

.....
Ms. Waraporn Nuntiyakul
Candidate

.....
Asst. Prof. Thiranee Khumlumlert,
Ph.D. (Physics)
Chair

.....
Prof. David Ruffolo,
Ph.D. (Physics)
Member

.....
Asst. Prof. Kittiwit Matan,
Ph.D. (Physics)
Member

.....
Lect. Alejandro Sáiz,
Ph.D. (Physics)
Member

.....
Prof. Banchong Mahaisavariya,
M.D., Dip Thai Board of Orthopedics
Dean
Faculty of Graduate Studies
Mahidol University

.....
Prof. Skorn Mongkolsuk,
Ph.D. (Biological Science)
Dean
Faculty of Science
Mahidol University

ACKNOWLEDGEMENTS

First of all, I would like to express my sincere appreciation and gratitude to my advisor Professor Dr. David Ruffolo. You have been a tremendous mentor for me. I would like to thank you for encouraging my research and for allowing me to grow as a research physicist. During my graduate study, you were always there to provide necessary assistance and academic resources. Your advice on both research as well as on my career have been priceless. I profusely thank Professor Dr. Paul Evenson who was my international co-advisor, and a father-like figure to me. You were always eager to help, be it a research issue or taking care of me when I visited the University of Delaware, USA for eight months. I would also like to thank my committee members, Dr. Alejandro Sáiz and Dr. Kittiwit Matan for taking the time serve as my committee members. I also want to thank you for letting my progress reports and defense be invaluable moments, and for your brilliant comments and suggestions, thanks to you.

I would like to especially thank Dr. Achara Seripienlert who is the best friend I have ever come across. I admire your positive attitude. The best feature of your unique character is being a great listener. You were always there to listen and to give me sincere advice about anything I hoped for. Much help during the work was provided by many people. I would like to thank Mr. Wirin Sonsretee, Dr. Kittipat Malakit, Dr. Pierre-Simon Mangeard and Dr. Warit Mitthumsiri in the Space Physics and Energetic Particles Lab for discussions about physics knowledge. All of you encouraged holding group workshops to promote and encourage learning for me.

I would like to thank my wonderful friends, Miss Wanna Wirojdanthai, Miss Porntip Terdbaramee and Miss Kanitta Onsiri from Chandrakasem Rajabhat University. You are always at my side when I feel tired, discouraged and despondent, so thanks to all of you. I would also like to thank Asst. Prof. Rawin Chaisittiporn who supported and suggested me in programming, and spurred me to strive towards my goal.

Finally, I would like to thank my family. Words cannot express how grateful I am to my mother, my father and two younger brothers for all of the sacrifices that you have made on my behalf. Your prayer for me was what sustained me thus far.

Waraporn Nuntiyakul

ANALYSIS OF DATA FROM A CALIBRATION NEUTRON MONITOR AT DOI
INTHANON AND A SHIP-BORNE NEUTRON MONITOR.

WARAPORN NUNTIYAKUL 5238713 SCPY/D

Ph.D. (PHYSICS)

THESIS ADVISORY COMMITTEE: DAVID RUFFOLO, Ph.D. (PHYSICS),
ALEJANDRO SÁIZ, Ph.D. (PHYSICS), KITTIWIT MATAN, Ph.D. (PHYSICS)

ABSTRACT

Neutron monitors are large ground-based detectors that provide accurate measurements of variations in the cosmic ray flux from space. At any given location, the magnetic field of the Earth blocks particles below a well-defined rigidity (momentum per unit charge) known as the cutoff rigidity. By carrying a neutron monitor to different locations, the Earth served as a magnet spectrometer. This work explores two topics concerning portable neutron monitors. The first topic is to filter bad data from a calibration neutron monitor (“calmon”) at Doi Inthanon. It was used to calibrate the Princess Sirindhorn Neutron Monitor (PSNM), which is particularly important because this has the world’s highest cutoff rigidity for a fixed station. From the raw data, we have extracted the calmon/PSNM count rate ratio as a function of the calmon location and environment. Another topic is to analyze data from a ship-borne neutron monitor. The Galactic cosmic ray spectrum exhibits subtle variations over the 22-year solar magnetic cycle in addition to the more dramatic variations over the 11-year sunspot cycle. By repeating ship-borne latitude surveys with identical equipment, a sensitive measurement of changes in the spectrum can be made. Here we analyze data from the 1994 through 2007 series of latitude surveys conducted by the Bartol Research Institute, the University of Tasmania, and the Australian Antarctic Division. We show that the curious “crossover” in spectra measured near sunspot minima during epochs of opposite solar magnetic polarity is related directly to a sudden change in the behavior of solar modulation at the time of the polarity reversal. We suggest that the crossover itself results from the interaction of effects due to gradient/curvature drifts with a systematic change in the interplanetary diffusion coefficient caused by turbulent magnetic helicity.

KEY WORDS: NEUTRON MONITORS / CROSSOVER / MODULATION /
GALACTIC COSMIC RAY SPECTRUM / LATITUDE SURVEY

178 pages

การวิเคราะห์ข้อมูลจากเครื่องตรวจวัดนิวตรอนสอบเทียบ ณ คอยอินทนนท์และเครื่องตรวจวัดนิวตรอนบนเรือ

ANALYSIS OF DATA FROM A CALIBRATION NEUTRON MONITOR AT DOI INTHANON AND A SHIP-BORNE NEUTRON MONITOR

วารกรณ์ นันทิกุล 5238713 SCPY/D

ปร.ด. (ฟิสิกส์)

คณะกรรมการที่ปรึกษาวิทยานิพนธ์: เดวิด รูฟโฟโล, Ph.D. (PHYSICS), อเลฮานโดร ซาอีสริเวรา, Ph.D. (PHYSICS), กิตติวิทย์ มาแทน, Ph.D. (PHYSICS)

บทคัดย่อ

เครื่องตรวจวัดนิวตรอนเป็นเครื่องวัดภาคพื้นดินขนาดใหญ่ที่ให้ค่าการวัดที่แม่นยำของการเปลี่ยนแปลงในฟลักซ์ของรังสีคอสมิกจากอวกาศ สนามแม่เหล็กของโลก ณ ตำแหน่งใดๆ จะกั้นไม่ให้อนุภาคผ่านถ้ามีค่าสภาพแข็งแรง (โมเมนต์ต่อหน่วยประจุ) ต่ำกว่าสภาพแข็งแรงตัด เมื่อเราขนเครื่องตรวจวัดนิวตรอนไปยังตำแหน่งต่างๆ โลกทำหน้าที่เป็นสเปกโตรมิเตอร์แม่เหล็ก งานนี้มีสองหัวข้อที่เกี่ยวข้องกับเครื่องตรวจวัดนิวตรอนแบบพกพา หัวข้อแรกเป็นการจัดข้อมูลจากเครื่องตรวจวัดนิวตรอนสอบเทียบ (“แคลมอน”) ที่คอยอินทนนท์ ซึ่งถูกใช้เพื่อสอบเทียบเครื่องตรวจวัดนิวตรอนสิรินธร (PSNM) ซึ่งสำคัญเป็นพิเศษเพราะที่นี่มีสภาพแข็งแรงตัดที่สูงที่สุดของโลกสำหรับสถานที่ที่ตั้งอยู่กับที่ จากข้อมูลดิบเราได้หาอัตราส่วนนับรังสีของแคลมอนต่อ PSNM ที่เป็นฟังก์ชันของตำแหน่งของแคลมอนและสิ่งแวดล้อมอีกหัวข้อหนึ่งเป็นการวิเคราะห์ข้อมูลจากเครื่องตรวจวัดนิวตรอนบนเรือ สเปกตรัมของรังสีคอสมิกจากกาแล็กซี่แสดงการเปลี่ยนแปลงที่ละเอียดอ่อนในวัฏจักร 22 ปีของสนามแม่เหล็กดวงอาทิตย์ นอกเหนือจากการเปลี่ยนแปลงอย่างมากในวัฏจักร 11 ปีของจุดมืดบนดวงอาทิตย์ การสำรวจละเอียดดูซ้ำบนเรือกับอุปกรณ์ที่เหมือนกัน ให้ข้อมูลละเอียดเกี่ยวกับการเปลี่ยนแปลงในสเปกตรัม ในที่นี้เราวิเคราะห์ข้อมูลจาก 1994 จนกระทั่งถึง 2007 ของการสำรวจละเอียดดูที่ดำเนินการโดยสถาบันวิจัยบาร์ทอล, มหาวิทยาลัยของแทสมเนีย และกองแอนตาร์กติกของออสเตรเลีย เราแสดงให้เห็นว่า “การตัดข้าม” ที่แปลกประหลาดในสเปกตรัมที่วัดได้ในช่วงที่มีจุดมืดบนดวงอาทิตย์น้อย เมื่อเทียบระหว่างยุคของขั้วแม่เหล็กของดวงอาทิตย์ที่ตรงกันข้ามนั้น ซึ่งเกี่ยวข้องโดยตรงกับการเปลี่ยนแปลงอย่างฉับพลันในผลกระทบของดวงอาทิตย์ต่อรังสีคอสมิกในเวลาของการกลับขั้ว เราเสนอว่าการตัดข้ามเองเป็นผลมาจากปฏิสัมพันธ์ระหว่างผลกระทบที่เกิดจากการลอยเลื่อนเกรเดียนต์/ความโค้งกับการเปลี่ยนแปลงเชิงระบบในสัมประสิทธิ์การฟุ้งระหว่างดาวเคราะห์ที่เกิดจากการเกลียวรอบของสนามแม่เหล็กปั่นป่วน

CONTENTS

| | Page |
|--|-------------|
| ACKNOWLEDGEMENTS | iii |
| ABSTRACT (ENGLISH) | iv |
| ABSTRACT (THAI) | v |
| LIST OF TABLES | viii |
| LIST OF FIGURES | x |
| CHAPTER I INTRODUCTION | 1 |
| 1.1 Background and Motivation | 1 |
| 1.1.1 Scientific Background of the Calibration Neutron Monitor | 2 |
| 1.1.2 Scientific Background of the Latitude Survey | 3 |
| 1.1.3 A Solar Modulation Mystery | 8 |
| 1.2 Objectives | 20 |
| 1.3 Expected Benefits | 20 |
| 1.4 Outline of Thesis | 20 |
| CHAPTER II LITERATURE REVIEW AND THEORETICAL BACKGROUND | 22 |
| 2.1 Neutron Monitors | 22 |
| 2.2 Calibration Neutron Monitor | 32 |
| 2.3 Intercalibration of the World's Neutron Monitors | 35 |
| 2.4 Ship-Borne Neutron Monitor | 38 |
| 2.5 Latitude Surveys | 43 |
| 2.6 Forbush Decreases | 48 |
| CHAPTER III EFFECTS OF THE ENVIRONMENT ON THE COUNT RATE OF A CALIBRATION NEUTRON MONITOR AT DOI INTHANON | 51 |
| 3.1 Detection Equipment and Observations | 54 |
| 3.2 Data Analysis | 56 |

CONTENTS (cont.)

| | Page |
|--|-------------|
| 3.2.1 Calmon Data | 56 |
| 3.2.2 Calibration Procedure and Results | 86 |
| 3.2.3 Effect of the Building | 88 |
| CHAPTER IV LATITUDE SURVEY INVESTIGATION OF GALACTIC COSMIC RAY SOLAR MODULATION DURING 1994-2007 | 89 |
| 4.1 Introduction | 89 |
| 4.2 Observations | 92 |
| 4.3 Data Preparation | 101 |
| 4.4 Data Reduction | 103 |
| 4.5 Response Functions | 123 |
| 4.6 Modeling | 132 |
| 4.7 Discussion | 135 |
| CHAPTER V DISCUSSION AND CONCLUSIONS | 138 |
| REFERENCES | 141 |
| APPENDICES | 148 |
| Appendix A Lists of Problematic Times | 149 |
| Appendix B Pressure Coefficient Determination | 152 |
| Appendix C Regression Coefficient for Short-Term Variations in Modulation Level | 159 |
| Appendix D The Nagashima Approach Applied to the Latitude Survey Data | 169 |
| BIOGRAPHY | 178 |

LIST OF TABLES

| Table | Page |
|---|-------------|
| 2.1 Specifications of the Princess Sirindhorn Neutron Monitor at Doi Inthanon, Chiang Mai, Thailand | 30 |
| 3.1 List of all configurations of the calmon at Doi Inthanon, Thailand | 58 |
| 3.2 Hourly count rates during the calibrations | 88 |
| 4.1 Route of the 1994-1995 voyage | 97 |
| 4.2 Route of the 1995-1996 voyage | 97 |
| 4.3 Route of the 1996-1997 voyage | 97 |
| 4.4 Route of the 1997-1998 voyage | 98 |
| 4.5 Route of the 1998-1999 voyage | 98 |
| 4.6 Route of the 1999-2000 voyage | 98 |
| 4.7 Route of the 2000-2001 voyage | 99 |
| 4.8 Route of the 2001-2002 voyage | 99 |
| 4.9 Route of the 2002-2003 voyage | 99 |
| 4.10 Route of the 2003-2004 voyage | 100 |
| 4.11 Route of the 2004-2005 voyage | 100 |
| 4.12 Route of the 2005-2006 voyage | 100 |
| 4.13 Route of the 2006-2007 voyage | 100 |
| 4.14 Days of each year when the ship was near McMurdo as described in the text | 105 |
| 4.15 The segment divisions that we used in the Dorman analysis | 122 |
| 4.16 Derived Dorman parameters | 124 |

LIST OF TABLES (cont.)

| Table | Page |
|---|-------------|
| 4.17 Coefficients of a linear regression analysis and force field model between mobile monitor data in multiple cutoff rigidity intervals and McMurdo neutron monitor data. The standard error (SE) refers to the standard error of the coefficient (in this case the slope) deduced from the scatter of the points from the fit line. In the case of the model, this is completely systematic deviation, since the model produces a slightly curved line, not a perfect straight line. | 131 |
| A.1 An example of a list of problematic times for the FIRST correction for half-hourly data in the 1998 survey year | 150 |
| A.2 An example of a list of problematic times for the SECOND correction for daily average data in the 1998 survey year | 151 |
| B.1 The data of cutoff rigidity bin (GV), center of rigidity bin (GV), β (all estimates), and β (usable estimates) | 157 |
| C.1 Cutoff rigidity and regression coefficient between the normalized mobile neutron monitor count rate corrected for tube ratios and pressure and the McMurdo count rate corrected for pressure for each apparent cutoff rigidity bin. | 167 |

LIST OF FIGURES

| Figure | Page |
|---|------|
| 1.1 Left panel shows a “cloud” of neutrons when there is no water in the swimming pool and right panel shows a reduced “cloud” of neutrons when adding some water in the swimming pool. | 3 |
| 1.2 Skymap of cutoff rigidity vs. direction for a specific location (43.92S, 76.64W) where the vertical cutoff is 8.23 GV and apparent cutoff is 8.65 GV. Nine solid dots indicate directions used in the efficient method to calculate the apparent cutoff. [Image credit: Clem et al. (1997)] | 6 |
| 1.3 The difference between the apparent cutoff and the vertical cutoff in GV for a latitude survey [Image credit: Bieber et al. (1997)] | 7 |
| 1.4 (a) Count rate recorded during the portion of the 1994-1995 Bartol/Tasmania latitude survey. The large dots indicate locations for which a cutoff sky map is calculated. (b) Observed neutron monitor count rate vs. apparent cutoff. Large dots indicate actual calculations and small dots indicate interpolated values. [Image credit: Clem et al. (1997)] | 8 |
| 1.5 Sample fit of a response function from a segment of the 1997-1998 voyage [Image credit: Bieber et al. (2003)] | 9 |
| 1.6 Data (boxes) and model fit (solid line) for the ship-borne detector’s 1997 latitude survey. Fit parameters are discussed in the text. | 10 |
| 1.7 Solar modulation: As solar activity rises (top panel), the count rate recorded by a neutron monitor in Thule, Greenland decreases (bottom panel). Effects of solar magnetic polarity are manifest as differences in modulation during alternate count rate maxima. [Image credit: http://neutronm.bartol.udel.edu/modplot.html] | 11 |

LIST OF FIGURES (cont.)

| Figure | Page |
|--|-------------|
| 1.8 Predicted dependence of the proton and antiproton intensity (top panel) and the antiproton/proton ratio at 1 AU upon the tilt angle of the heliospheric current sheet for 1 GeV kinetic energy (bottom panel) covering the two solar cycles of opposite magnetic polarity from the 2000 solar maximum to the 2010 solar maximum. [Image credit: Bieber et al. (1999)] | 12 |
| 1.9 Sketches of types of spectral crossovers | 13 |
| 1.10 Illustration of “spectral crossover” effect of response functions at 11 and 22 year intervals. The curves are labeled by the year of the latitude survey. [Image credit: Moraal et al. (1989)] | 14 |
| 1.11 Rigidity of the DRF peak is plotted versus the relative flux at the maximum for each of the 26 segments of the 1994-2002 survey years. Segments with positive solar dipole polarity (shown in green in the plot), while the solar activity increased from 1994 to 2000, lie along a single trend line. When modulation increased, the flux at spectrum peak became lower, but it appeared at a higher rigidity. Segments with negative solar dipole polarity (shown in red in the plot), while the solar activity decreased from 2000 to 2002, moved off the trend line of the positive magnetic polarity results. [Image credit: Bieber et al. (2003)] | 15 |
| 1.12 Comparison of the McMurdo neutron monitor count rate and 1.2 GV helium flux from Interplanetary Monitoring Platform 8 (IMP-8) vs. time. [Image credit: Bieber et al. (2007)] | 16 |
| 1.13 Balloon and spacecraft measurements of primary cosmic ray spectra. Protons (upper spectra) and helium (lower spectra) compiled by Clem et al. (2004). [Image credit: Clem et al. (2004)] | 17 |
| 1.14 Sequence of proton spectra from BESS spanning a polarity reversal [Image credit: Mitchell et al. (2008)] | 18 |

LIST OF FIGURES (cont.)

| Figure | Page |
|--|------|
| 1.15 Normalized magnetic helicity fluctuates in sign for frequencies above 10^{-5} Hz, but displays a definite dominant sign at lower frequencies. [Image credit: Smith & Bieber (1993)] | 19 |
| 2.1 The flux of cosmic rays as a function of their energy. The flux for the lowest energies could also have an additional contribution from solar energetic particles (not shown here) after the occasional occurrence of a major solar storm. The non-solar cosmic ray spectrum is curved in this region because access of cosmic rays coming from outside the solar system to the inner solar system is reduced by the solar wind and magnetic field of the Sun. The cosmic rays up to $\sim 10^{18.5}$ eV are galactic cosmic rays. There are breaks in the power law, for instance energy near $\sim 10^{15}$ eV called the “knee” of the cosmic ray spectrum. The cosmic rays with the highest energies are extragalactic cosmic rays. We can see an “ankle” of the cosmic ray spectrum at an energy near $\sim 10^{18.5}$ eV. [Image credit: http://astroparticle.uchicago.edu/] | 24 |
| 2.2 Primary cosmic ray particle colliding with a nucleus in the atmosphere and producing a shower [Image credit: http://scifun.ed.ac.uk/card/images/left/cosmic-rays.jpg] | 25 |
| 2.3 Structure of NM64-type neutron monitor. See text for details. | 26 |
| 2.4 The IGY (International Geophysical Year, 1957) neutron monitor design | 26 |
| 2.5 The Princess Sirindhorn Neutron Monitor building at Doi Inthanon, Chiang Mai, Thailand | 28 |
| 2.6 The placement of the Princess Sirindhorn Neutron Monitor (an 18NM64 monitor) at Doi Inthanon, Chiang Mai, Thailand | 29 |
| 2.7 A pulse height distribution from the PSNM at Doi Inthanon, Chiang Mai, Thailand | 29 |

LIST OF FIGURES (cont.)

| Figure | Page |
|--|------|
| 2.8 Illustration of a nuclear reaction between secondary neutrons and ^{10}B in a BP-28 proportional counter to produce ^7Li and ^4He [from Fowler (1963), as modified by P. Evenson.] | 31 |
| 2.9 Schematic diagram of a calibration neutron monitor with (a) an LND25382 neutron counter filled with ^3He gas. It is surrounded with (b) polyethylene (PE) moderator with inner and outer diameters of 60.5 and 99.5 mm, (c) lead producer with inner and outer diameters of 101 and 193 mm, and (d) polyethylene (PE) reflector with inner and outer diameters of 194 and 350 mm. | 32 |
| 2.10 Calibration neutron monitor with electronics head (cover removed) from Northwest University, Potchefstroom, South Africa | 33 |
| 2.11 Calibration neutron monitor with electronics head from Bartol Research Institute, U. Delaware, USA | 34 |
| 2.12 The ratio of the count rates of the IGY of Northwest University, Potchefstroom, South Africa and calibration neutron monitor as a function of the height of the calibration neutron monitor above a concrete floor, with different heights of water and brick underneath the calibrator. [Image credit: Krüger & Moraal (2010)] | 35 |
| 2.13 Operating neutron monitors in 2010 showing only stations (red solid points) that actively report data, including Doi Inthanon. [Modified from an image by Roger Pyle.] | 36 |
| 2.14 Hypothetical differential response function for 11 intercalibrated neutron monitors [Image credit: Krüger et al. (2011)] | 37 |
| 2.15 Ship-borne neutron monitor (3NM64) | 38 |
| 2.16 The TasVan | 39 |
| 2.17 Electronics racks. Most of the electronics are located in the rack adjacent to the onboard computer. | 40 |
| 2.18 BP-28 (Chalk River) Neutron Detectors | 41 |

LIST OF FIGURES (cont.)

| Figure | Page |
|--|------|
| 2.19 Clinometer Assembly | 42 |
| 2.20 Differential rigidity spectrum of galactic cosmic rays, primary proton flux and modulation function in 1965. Observed points are those compiled by Webber & Lezniak (1974). These data were originally presented by Ormes & Webber (1965), Fan et al. (1966), Anand et al. (1968), von Rosenvinge et al. (1969), Ryan et al. (1972) and Smith et al. (1973). [Image credit: Nagashima et al. (1989)] | 45 |
| 2.21 <i>a)</i> Comparison of $Y(U, x)$ with theory. Solid lines express the simulated experimental data of $Y(U, x)$ with $h_2(U, \eta_5)$ in eq. 2.15 and dashed lines are theoretical curves estimated by Murakami (1989) in private communication. Theoretical and experimental curves are normalized at $h = 1033 \text{ g/cm}^2$ and $U = 10 \text{ GeV}$. <i>b)</i> The same as in <i>a)</i> except that dashed lines are theoretical curves obtained by Dorman & Yanke (1981). [Image credit: Nagashima et al. (1989)] | 46 |
| 2.22 Rigidity dependence of the modulation function $M(p, t)$ near the maximum (dashed line, $J_{MtW}=1990$) and minimum solar activity (solid line, $J_{MtW}=2465$) [Image credit: Nagashima et al. (1989)] | 47 |
| 2.23 Differential response function $R(P_c, h, t)$ of a neutron monitor for several atmospheric depths in the periods of maximum and minimum solar activity. Figures attached to each curve express the atmospheric depth h in g/cm^2 . Solid lines are for minimum solar activity ($J_{MtW}=2465$), dashed lines are for maximum solar activity ($J_{MtW}=1990$). [Image credit: Nagashima et al. (1989)] | 49 |
| 2.24 A photograph of a CME taken by the SOHO spacecraft [Taken from http://www.nasa.gov] | 50 |
| 2.25 Graph of modulation level as a function of time to demonstrate explicitly both first step and second step of Forbush decreases during DOY 340 to 359 of 2006-2007 voyage of latitude survey data | 50 |

LIST OF FIGURES (cont.)

| Figure | Page |
|--|------|
| 3.1 Photograph of the calmon during testing inside the PSNM building at Doi Inthanon, Thailand | 52 |
| 3.2 Simple floor plan sketch with wiring connections of 18NM64 and calmon at PSNM, Doi Inthanon, Thailand during November, 2009 – June, 2010 | 53 |
| 3.3 Photographs of (a) the PSNM building, with two metal roof panels inclined at 45° , and inner vertical walls and a ceiling of concrete that define a smaller rectangular enclosure, and (b) the interior of the PSNM building. | 55 |
| 3.4 Calmon outside the PSNM building | 59 |
| 3.5 The results as a function of time of C1: (a) uncorrected Cal/NM ratio, (b) corrected ratio, (c) calmon counter temperature. | 60 |
| 3.6 The Cal/NM ratios with straight line fit as a function of temperature of C1: (a) uncorrected ratio and (b) corrected ratio. | 61 |
| 3.7 The results as a function of time of C2: (a) uncorrected Cal/NM ratio, (b) corrected ratio, (c) calmon counter temperature. | 62 |
| 3.8 The Cal/NM ratios with straight line fit as a function of temperature of C2: (a) uncorrected ratio and (b) corrected ratio. | 63 |
| 3.9 The results as a function of time of C3: (a) uncorrected Cal/NM ratio, (b) corrected ratio, (c) calmon counter temperature. | 64 |
| 3.10 The Cal/NM ratios with straight line fit as a function of temperature of C3: (a) uncorrected ratio and (b) corrected ratio. | 65 |
| 3.11 The results as a function of time of C4: (a) uncorrected Cal/NM ratio, (b) corrected ratio, (c) calmon counter temperature. | 66 |
| 3.12 The Cal/NM ratios with straight line fit as a function of temperature of C4: (a) uncorrected ratio and (b) corrected ratio. | 67 |

LIST OF FIGURES (cont.)

| Figure | Page |
|--|------|
| 3.13 The results as a function of time of C5: (a) uncorrected Cal/NM ratio, (b) corrected ratio, (c) calmon counter temperature. There appears to be a strong association of Cal/NM with counter temperature, but it is not consistent and may instead reflect increased noise at some times of high temperature. | 68 |
| 3.14 The Cal/NM ratios with straight line fit as a function of temperature of C5: (a) uncorrected ratio and (b) corrected ratio. | 69 |
| 3.15 The results as a function of time of C6: (a) uncorrected Cal/NM ratio, (b) corrected ratio, (c) calmon counter temperature. | 70 |
| 3.16 The Cal/NM ratios with straight line fit as a function of temperature of C6: (a) uncorrected ratio and (b) corrected ratio. | 71 |
| 3.17 The results as a function of time of C8 (BRI electronics). (a) The green line shows the corrected Cal/NM ratio and solid black boxes with a solid line show the daily average corrected ratio. (b) The blue line shows the PSNM pressure reading by Digiquartz in mm Hg and solid black boxes with a solid line show the daily average Digiquartz pressure. (c) The red line shows the temperature of the calmon and solid black boxes with the solid line show the daily average calmon temperature. | 72 |
| 3.18 The Cal/NM ratios with straight line fit as a function of temperature of C8 | 73 |
| 3.19 The results as a function of time of C9: (a) uncorrected Cal/NM ratio, (b) corrected ratio, (c) calmon counter temperature. | 74 |
| 3.20 The Cal/NM ratios with straight line fit as a function of temperature of C9: (a) uncorrected ratio and (b) corrected ratio. | 75 |
| 3.21 The results as a function of time of C10: (a) uncorrected Cal/NM ratio, (b) corrected ratio, (c) calmon counter temperature. | 76 |
| 3.22 The Cal/NM ratios with straight line fit as a function of temperature of C10: (a) uncorrected ratio and (b) corrected ratio. | 77 |

LIST OF FIGURES (cont.)

| Figure | Page |
|---|-------------|
| 3.23 The results as a function of time of C11: (a) uncorrected Cal/NM ratio, (b) corrected ratio, (c) calmon counter temperature. | 78 |
| 3.24 The Cal/NM ratios with straight line fit as a function of temperature of C11: (a) uncorrected ratio and (b) corrected ratio. | 79 |
| 3.25 The results as a function of time of C12: (a) uncorrected Cal/NM ratio, (b) corrected ratio, (c) calmon counter temperature. | 80 |
| 3.26 The Cal/NM ratios with straight line fit as a function of temperature of C12: (a) uncorrected ratio and (b) corrected ratio. | 81 |
| 3.27 The results as a function of time of C13: (a) uncorrected Cal/NM ratio, (b) corrected ratio, (c) calmon counter temperature. | 82 |
| 3.28 The Cal/NM ratios with straight line fit as a function of temperature of C13: (a) uncorrected ratio and (b) corrected ratio. | 83 |
| 3.29 The results as a function of time of C15 (BRI electronics). (a) The green line shows the corrected Cal/NM ratio and solid black boxes with a solid line show the daily average corrected ratio. (b) The blue line shows the PSNM pressure reading by Digiquartz in mm Hg and solid black boxes with a solid line show the daily average Digiquartz pressure. (c) The red line shows the temperature of the calmon and solid black boxes with the solid line show the daily average calmon temperature. | 84 |
| 3.30 The Cal/NM ratios with straight line fit as a function of temperature of C15 | 85 |
| 3.31 The corrected Cal/NM ratios for all usable configurations. The calmon height is indicated by color, i.e., blue indicates 140 cm (outside), green indicates 70 cm (outside), and red indicates 55 cm (inside). The error bars represent the standard error. | 86 |
| 3.32 The Cal/NM ratio for the Potchefstroom NM (open circles) and the PSNM at Doi Inthanon as function of varying height of water beneath the calibrator [Image credit: Krüger et al. (2011)] | 87 |

LIST OF FIGURES (cont.)

| Figure | Page |
|---|------|
| <p>4.1 Smoothed monthly international sunspot number (using 5-month boxcar smoothing) and McMurdo neutron monitor count rate as a function of time. The long-term drift at McMurdo has been corrected following Oh et al. (2013). A neutron monitor count rate indicates the Galactic cosmic ray flux, which undergoes “solar modulation” in association with solar activity. Solar modulation includes dramatic 11-year variations with the sunspot cycle, and a 22-year variation with the solar magnetic cycle, seen here in changes in the solar modulation pattern between positive ($A > 0$) and negative ($A < 0$) magnetic polarity. In this work we present observations of spectral changes in Galactic cosmic rays in association with solar modulation and changing solar magnetic polarity for the time period 1994-2007, indicated by a horizontal bar.</p> | 90 |
| <p>4.2 (a) Insulated container (“TasVan”) used for 3NM64 neutron monitor latitude surveys on the <i>Polar Star</i> and <i>Polar Sea</i>. (b) 3NM64 installed inside the container. For this and several other voyages a small calibration neutron monitor (Krüger et al. 2008a) was installed near the door.</p> | 93 |
| <p>4.3 The track of the ship-borne neutron monitor latitude surveys for 1994–2007, superimposed on contours of the vertical cutoff rigidity indicated by black solid lines. Italic numbers at each contour indicate the vertical cutoff rigidity in GV.</p> | 96 |
| <p>4.4 Diagram of the steps of preparation of the LatSur files for all survey years. In each step, we use different appropriate programs to produce the files needed. The LatSur files are the key files for scientific analysis of the survey data.</p> | 102 |
| <p>4.5 An example of the count rates for each tube vs. time in survey year 2000, including some bad count rates for individual tubes.</p> | 103 |
| <p>4.6 The count rates as a function of time for all survey years after applying the second step of correction in the analysis</p> | 104 |

LIST OF FIGURES (cont.)

| Figure | Page |
|--|-------------|
| 4.7 The mobile/McMurdo count rate ratio as a function of time after normalized by the factors explained in the text. | 106 |
| 4.8 The data for the 1994 survey year. (a) Geomagnetic cutoff rigidity as a function of time. The black line traces the apparent geomagnetic cutoff rigidity while the red line shows the vertical effective cutoff rigidity. (b) Mobile (ship-borne) neutron monitor count rate after all corrections as discussed in the text. (c) Corrected count rate as a function of apparent geomagnetic cutoff rigidity for all four segments (i.e., the four transitions between low and high cutoff rigidity). | 109 |
| 4.9 Like Figure 4.8, for the 1995 survey year. | 110 |
| 4.10 Like Figure 4.8, for the 1996 survey year. | 111 |
| 4.11 Like Figure 4.8, for the 1997 survey year. | 112 |
| 4.12 Like Figure 4.8, for the 1998 survey year. | 113 |
| 4.13 Like Figure 4.8, for the 1999 survey year. | 114 |
| 4.14 Like Figure 4.8, for the 2000 survey year. | 115 |
| 4.15 Like Figure 4.8, for the 2001 survey year. | 116 |
| 4.16 Like Figure 4.8, for the 2002 survey year. | 117 |
| 4.17 Like Figure 4.8, for the 2003 survey year. | 118 |
| 4.18 Like Figure 4.8, for the 2004 survey year. | 119 |
| 4.19 Like Figure 4.8, for the 2005 survey year. | 120 |
| 4.20 Like Figure 4.8, for the 2006 survey year. | 121 |

LIST OF FIGURES (cont.)

| Figure | Page |
|--|------|
| 4.21 (a)–(d) Corrected mobile neutron monitor count rate for survey years 1994 to 1997 (solar minimum conditions) as a function of apparent geomagnetic cutoff (averaged over 0.5 GV rigidity bins). A solid symbol indicates that data were available for multiple voyage segments (as defined in the text). Vertical error bar represents the standard error between multiple segments; in many cases the error bar is smaller than the plot symbol. An open symbol with no error bar indicates that data were available for only one segment. Solid lines indicate Dorman function fits. (e)–(h) Inferred differential response functions, obtained as the derivatives of the Dorman function fits. | 125 |
| 4.22 Like Figure 4.21, for the 1998-2002 survey years, showing the transition from solar minimum to solar maximum conditions. | 126 |
| 4.23 Like Figure 4.21, for the 2003-2006 survey years, showing the transition from solar maximum to solar minimum conditions. | 127 |
| 4.24 Differential response functions for two survey years, near solar minimum, of opposite polarity and similar modulation level. A crossover is apparent near 5 GV. | 128 |
| 4.25 Regression of count rates for the mobile monitor in different cutoff rigidity bins against the count rate of the McMurdo neutron monitor during (a) $A > 0$ solar magnetic polarity (before 2000) and (b) $A < 0$ solar magnetic polarity (after 2000). Symbols indicate average values over each survey year. | 129 |

LIST OF FIGURES (cont.)

| Figure | Page |
|---|------|
| <p>4.26 Alternative presentation of the data in Figure 4.25 using every third rigidity bin for clarity and superimposing the data for different solar magnetic polarities. Filled triangles are used to indicate positive ($A > 0$) solar magnetic polarity with solid lines showing the linear fits. Open triangles indicate data for negative ($A < 0$) solar magnetic polarity while the dotted lines are linear fits to these data. There are clear differences in cosmic ray modulation before and after the solar magnetic polarity reversal.</p> | 130 |
| <p>4.27 Like Figure 4.25, for calculations using a force field model as described in the text. Each line corresponds to a 1-GV bin in apparent cutoff rigidity, ranging from the 0-1 GV bin at the top to the 15-16 GV bin at the bottom.</p> | 133 |
| <p>4.28 Regression coefficients for the lines in Figures 4.25 and 4.27 as a function of apparent cutoff rigidity. Red squares are from fits to data before 2000, blue triangles are from fits to data after 2000, and black circles are from fits to the force field calculation. Vertical error bar represents the standard error of the regression coefficient deduced from the scatter of the points from the fit line. There are clear differences in modulation before and after the solar magnetic polarity reversal.</p> | 134 |
| <p>B.1 Linear fitting of residuals from 24-hour averages of the logarithmic count rate and the barometric pressure (mm Hg), using latitude survey data from all survey years to find the slopes for each rigidity bin from $P_c : 0 - 1$ GV to $P_c : 5 - 6$ GV. The symbol \checkmark or \times shows whether we obtained a usable estimate of the slope (pressure coefficient).</p> | 154 |
| <p>B.2 Like Figure B.1, from $P_c : 6 - 7$ GV to $P_c : 12 - 13$ GV.</p> | 155 |
| <p>B.3 Like Figure B.1, from $P_c : 13 - 14$ GV to $P_c : 18 - 19$ GV.</p> | 156 |
| <p>B.4 The pressure coefficient (β) as a function of apparent cutoff P_c</p> | 158 |
| <p>C.1 Three dimensional plot among mobile monitor count rate corrected for tube ratios and pressure (s^{-1}), McMurdo count rate corrected for pressure (s^{-1}), and apparent cutoff rigidity (GV) for survey years 1994-1997.</p> | 161 |

LIST OF FIGURES (cont.)

| Figure | Page |
|--|------|
| C.2 Like Figure C.1, for survey years 1998-2001. | 162 |
| C.3 Like Figure C.1, for survey years 2002-2006. | 163 |
| C.4 Linear fitting of mobile monitor count rate (s^{-1}) against McMurdo count rate (s^{-1}) for the 1994-2006 survey years to find the slopes for rigidity bins from 0-1 GV to 5-6 GV. | 164 |
| C.5 Like Figure C.4, for rigidity bins from 6-7 GV to 11-12 GV. | 165 |
| C.6 Like Figure C.4, for rigidity bins from 12-13 to 17-19 GV. | 166 |
| C.7 The regression coefficient S as a function of apparent cutoff rigidity P_c | 168 |
| D.1 (a)-(d) Mobile neutron monitor count rate (black squares) and Nagashima model fit (red line) for survey years 1994 to 1997 as a function of apparent geomagnetic cutoff. (e)-(h) Inferred differential response functions (at sea level). | 172 |
| D.2 Like Figure D.1 of Nagashima technique, for 1998-2002 survey years, showing the transition from solar minimum to solar maximum conditions. | 173 |
| D.3 Like Figure D.1 of Nagashima technique, for 2003-2006 survey years, showing the transition from solar maximum to solar minimum conditions. | 174 |
| D.4 Residuals (s^{-1}) from the fits between mobile neutron monitor count rate and Nagashima model fit for all survey years as a function of cutoff rigidity. | 175 |
| D.5 Differential response functions (at sea level) for all the voyages together as a function of rigidity (GV). Red upward triangles are from data before 2000, green downward triangles are from data after 2000 and black squares are from data of 2000. There is clear no crossover in the spectrum described by the Nagashima technique. | 176 |
| D.6 Comparisons of the barometer correction from equation (2) of Clem et al. (1997) (red lines), from this work following equation 4.2 (blue lines), and from the Nagashima analysis (black lines), which is at a different level for each survey year. | 177 |

CHAPTER I

INTRODUCTION

1.1 Background and Motivation

The overall topic of research is the analysis of data from portable neutron monitors. A neutron monitor (NM) is a ground- (or sea-) based detector of the flux of cosmic ray particles in space. High-energy cosmic rays interact in the upper atmosphere, leading to a shower of subatomic particles, some of which reach Earth's surface. This is a key source of natural radiation. A neutron monitor is mostly sensitive to the neutron component of the shower. The neutron monitor is a large detector containing lead that fragments when hit by a high-energy neutron. Some of the fragments are neutrons, which are moderated and trapped by polyethylene. These neutrons can be detected by induced nuclear fission of ^{10}B in a $^{10}\text{BF}_3$ gas proportional counter. In Thailand, we have the Princess Sirindhorn Neutron Monitor (PSNM) at Doi Inthanon (high altitude greatly improves the count rate). This has 29 tons of lead and 18 $^{10}\text{BF}_3$ counter tubes to provide one of the world's top count rates, as well as the world's highest energy threshold due to its location near the geomagnetic equator. Neutron monitors typically make use of Earth's magnetic field as a magnetic spectrometer. Strictly speaking, passage through Earth's magnetic field depends on the "rigidity" (P) or momentum per charge, in units of GV, which for protons of $P \gg 1$ GV is roughly equivalent to their energy in GeV. Thus we say that the monitor at Doi Inthanon has the highest vertical cutoff rigidity, 16.8 GV, of any fixed monitor in the world.

In this research, the data analysis is divided into two sections since the sources of data are different. The first data series came from the experiment of a calibration neutron monitor that was located beside our station at Doi Inthanon for almost a year. The experiment was performed from November 2009 to June 2010. The second data series came from a latitude survey. The latitude survey was conducted on an icebreaker ship carrying three neutron monitors (3NM64) that traversed a wide range of latitudes covering a wide range of cutoff rigidity. We will give details about

the scientific background for both experiments in this section.

1.1.1 Scientific Background of the Calibration Neutron Monitor

Two calibration neutron monitors were constructed by Prof. Harm Moraal's group at Northwest U. (NWU; formerly Potchefstroom U.), South Africa. They proposed a concept that calibration monitors should have a small size and low mass (only 201 kg, not including the cart). The calibration monitor consists of one ^3He counter tube (type LND25373 with 97% ^3He and 3% CO_2) surrounded by an inner polyethylene moderator, lead producer, and outer polyethylene reflector (Krüger et al. 2003). The purpose is to calibrate some of the ~ 40 stationary neutron monitors around the world. For this reason, the calibration neutron monitor ("calmon") was sent to Doi Inthanon. At Doi Inthanon, the calmon was used to calibrate PSNM, which has 18 $^{10}\text{BF}_3$ counter tubes. The count rate measured by the calmon is low compared with the PSNM count rate because the calmon has only one counter tube. To achieve sufficient statistical accuracy, it must be operated long enough to accumulate $\sim 10^6$ counts, which requires about 4 days at the summit of Doi Inthanon.

An appropriate place for calmon collocation should have no obstructions overhead, down to within 20° of the horizon in all directions. In order to shield against environment dependent reflection of neutrons, we should put the calmon above a swimming pool with a known water height, to moderate the effect of the surface below (Krüger et al. 2008b). The calibration data can be very useful if the calmon count rate truly depends only on altitude, latitude, and longitude; at the same time, a similar calmon was operated at Potchefstroom, South Africa, for comparison purposes.

In this experiment, we operated the calmon in several configurations with varying height above the bottom of the pool (or height above the cement roof of the bunker) and varying water height. We also moved the calmon inside the station. It rests on a cart with steerable wheels. We need to determine the count rate for various calmon configurations located both outside and inside the station in order to compare these data, determine environmental effects, and also obtain precise calibration data. During the experiment we contacted Prof. Paul Evenson from the Bartol Research Institute to bring the electronics head called "Bartol electronics" to use in addition to the electronics head from Potchefstroom U. called "Potch electronics"

In our scientific interpretation, we consider the cloud of neutrons that result

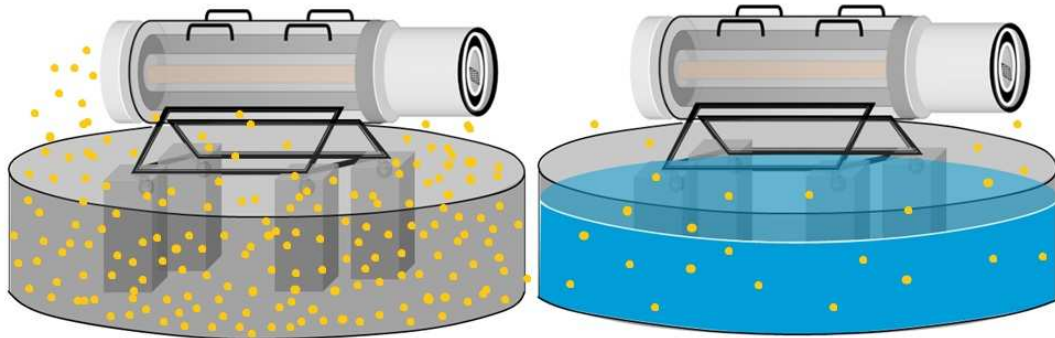


Figure 1.1: Left panel shows a “cloud” of neutrons when there is no water in the swimming pool and right panel shows a reduced “cloud” of neutrons when adding some water in the swimming pool.

from interactions of atmospheric neutrons in the concrete and wood under the calmon. In order to reduce the cloud of neutrons, which depends on the materials around the calmon, we should raise the calmon and add more water to the pool (Krüger & Moraal 2010) (see Figure 1.1). The water added will help to absorb the neutrons. Two things that we did not know exactly when the experiment began were how much the heights of calmon and water should be and how we can obtain the scientifically useful data. That is why this research was interesting and challenging.

This research will be even more useful if Prof. Harm Moraal’s group can derive a differential response function from the count rate of stationary neutron monitors including PSNM, and then we can directly compare the results from experiments with the results of Monte Carlo simulation, e.g., using software called FLUktuierende KAskade or FLUKA.

1.1.2 Scientific Background of the Latitude Survey

From our previous explanation, we know that the count rate of a latitude survey can be measured by a 3NM64 collocated on a ship. In this research we worked toward deriving the Galactic cosmic ray spectrum, which is sensitive to the large-scale structure of the heliosphere and cannot be measured directly. In this step, we need to know the equation of the count rate, which is related to the Galactic cosmic ray spectrum.

The count rate $N(\Theta, \Phi, h, t)$ of a NM resulting from the impact of cosmic

rays at the top of the atmosphere can be described formally by:

$$N(\Theta, \Phi, h, t) = \int_0^\infty \left[\sum_i G_i(P) M_i(P, t) Y_i(P, h) \right] T(P, \Theta, \Phi, t) dP \quad (1.1)$$

where the function G_i (as a function only of rigidity (P), momentum per unit charge in units of GV) is the local interstellar Galactic cosmic ray spectrum for primaries of particle type i , assumed to be time invariant. The cosmic rays are mostly composed of protons, whereas approximately 40% of the cosmic ray nucleons are bound in helium nuclei. The function M_i (as a function of rigidity (P) and time (t)) describes the time evolution, which exhibits variations with the 22-year solar magnetic cycle, called solar modulation for primaries of particle type i , due to interaction with the solar wind and magnetic fields in interplanetary space. The function T (as a function of rigidity (P), latitude (Θ), longitude (Φ) and time (t)) describes transmission through the magnetosphere of the Earth. Seasonal and diurnal time dependences arise from the changing relationship of the offset and tilted dipole axis of the Earth to the flow direction of the solar wind. There is also explicit time dependence due to changes in the magnetosphere in response to fluctuations in the solar wind velocity and embedded magnetic field. Then Y_i (as a function of rigidity (P) and atmospheric depth (h) represented by barometric pressure) is the yield function for primaries of particle type i , related with the inherent description of the atmosphere and the observed count rate from the neutron monitor.

We follow the usual approach of representing the geomagnetic transmission T as a step function at a ‘‘cutoff’’ rigidity (P_c), which depends on latitude, longitude, and time. Actually, at a given latitude and longitude, the effective cutoff rigidity for transmission through Earth’s magnetic field depends on the arrival direction of each primary cosmic ray indicated by the local zenith and azimuthal angle. However, it is more convenient to use a single value, P_c , that ideally averages over all arrival directions; we call such an average the ‘‘apparent cutoff rigidity.’’ The count rate relation becomes:

$$N(P_c, h, t) = \int_{P_c}^{P_L} \sum_i G_i(P) M_i(P, t) Y_i(P, h) dP. \quad (1.2)$$

We introduce a limiting rigidity (P_L) as a numerical convenience because Y_i (as a function of P) increases without bound and G_i falls steeply at high rigidity. In our work, taking T to be independent of arrival direction implicitly assumes that

the incoming flux at the top of the atmosphere is isotropic, which it is not. We deal with this by using the “apparent cutoff” (Clem et al. 1997). The apparent cutoff is calculated individually at one hour intervals at the actual position of the ship with a time dependent model of the magnetic field according to an “efficient” method (Bieber et al. 1997). Briefly, the apparent cutoff considers momentum per charge of both vertically incident particles and obliquely incident particles. We used a particle propagation code from the Bartol Research Institute (Lin et al. 1995) together with an accurate model of the terrestrial magnetic field and K_p index to calculate vertical and apparent cutoffs at each location where the ship moved through the entire trip. The K_p index indicates variation of the horizontal magnetic field of the Earth with an integer in the range 0-9. This indicates geomagnetic storm conditions, i.e., a lower number indicates no storm and a higher number indicates a stronger geomagnetic storm. The program calculated the apparent cutoff by an efficient method of averaging the vertical cutoff with the average of cutoffs at 8 points at a zenith angle of 30 degrees and equally spaced azimuthal angles, for a total of 9 points of calculation. In Figure 1.2, solid dots show the angular directions for which cutoffs are calculated.

Figure 1.3 illustrates the difference between the apparent cutoff and the vertical cutoff as calculated by Bieber et al. (1997). Figure 1.4 increases confidence that we should use the apparent cutoffs to interpret latitude survey data because the apparent cutoff supports more realistic physics (Clem et al. 1997).

In our analysis, we aim to determine the response function of the detector. For this reason, we need to know that the count rate as a function of apparent cutoff rigidity represents the integral response function of a 3NM64 neutron monitor and the integrand of Equation (1.2) is referred to as the *differential response function* (DRF), which can be measured from a latitude survey by transporting a detector through a wide range of geomagnetic cutoff rigidity values. The response function of the detector can be obtained from subtracting the observed count rate of a ship-borne neutron monitor at two different cutoffs and dividing by the (assumed small) difference in apparent cutoff.

Figure 1.5 illustrates the most common type of determination of integral and differential response functions from pressure-corrected data during part of the latitude survey data in the 1997-1998 voyage of the latitude survey using the “Tasvan” (Bieber et al. 2003). To deal with the scatter in the data, they fit with a “Dorman function” (Dorman et al. 1970) which in turn has an analytic derivative, also shown in the figure.

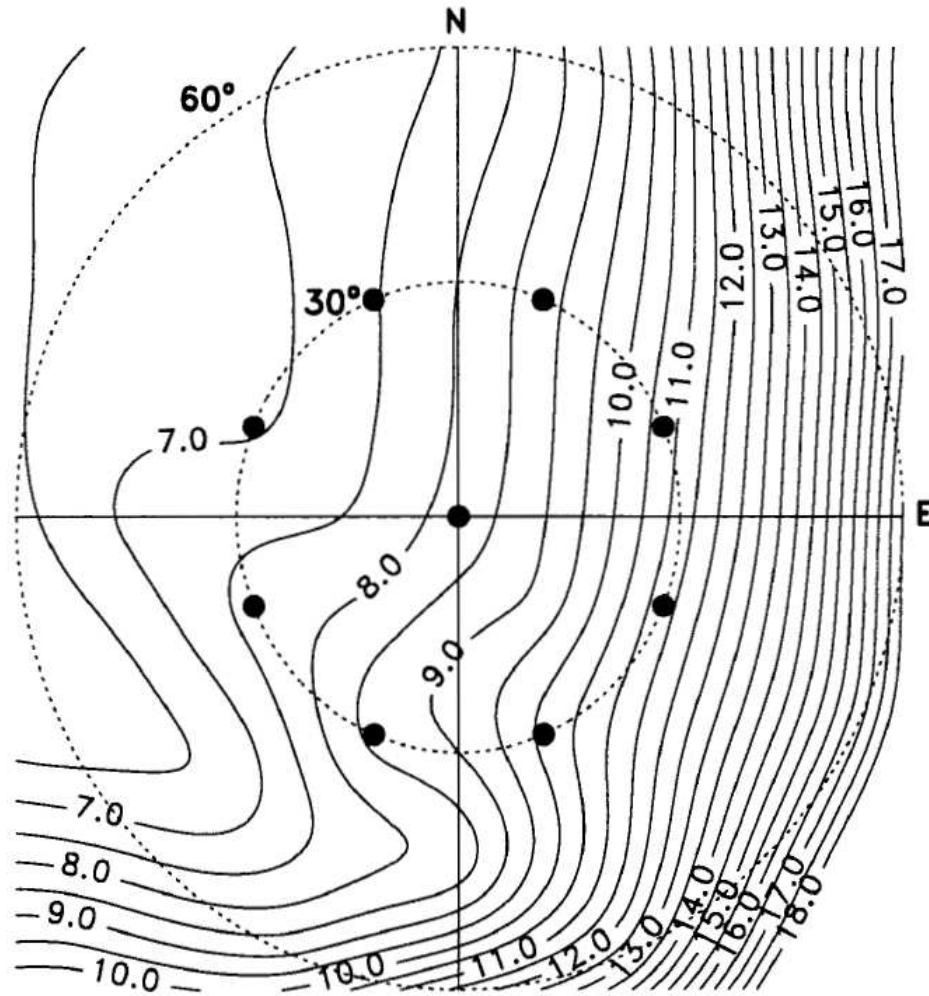


Figure 1.2: Skymap of cutoff rigidity vs. direction for a specific location (43.92S, 76.64W) where the vertical cutoff is 8.23 GV and apparent cutoff is 8.65 GV. Nine solid dots indicate directions used in the efficient method to calculate the apparent cutoff. [Image credit: Clem et al. (1997)]

This derivative is exactly the DRF for the NM.

In our analysis, we have two methods for determination of response functions from a series of latitude surveys. At first, we used a function developed by Nagashima et al. (1989) in which the functions in the integrand of Equation (1.2) are parameterized separately to create a model of the survey. Corrections for barometric pressure and changing cosmic ray level are now implicit in the model. This should be aesthetically a great improvement, since the corrections themselves are functions of cutoff rigidity. Nagashima et al. (1989) also tried to make their parameterization have some physical

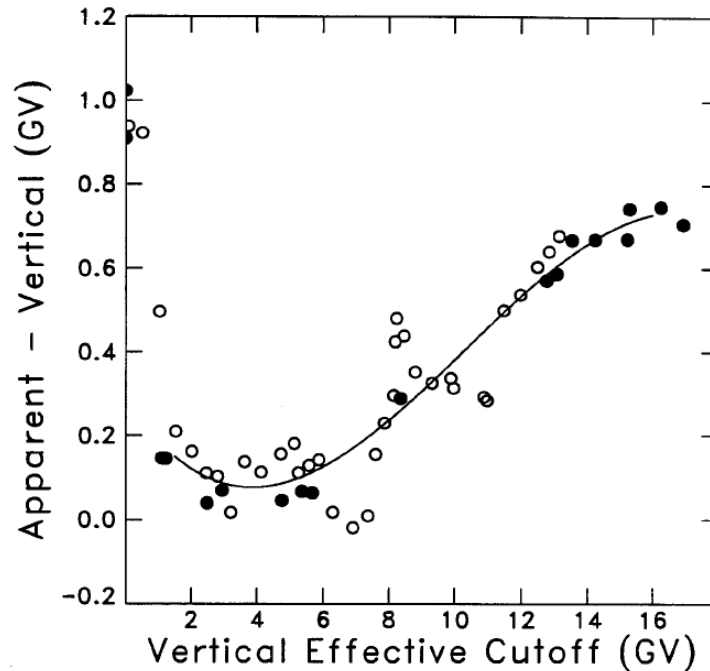


Figure 1.3: The difference between the apparent cutoff and the vertical cutoff in GV for a latitude survey [Image credit: Bieber et al. (1997)]

content, but there were some problems that were not solved. The model, with its many parameters, can then be fitted to the data. The drawback of the approach is the amount of computation required and some concern whether the fit obtained is an absolute or a local minimum. This is a reason why this technique is interesting to perform. If we can solve the problems for this technique, it can be deemed a success, and if we do it well but are ultimately unable to resolve the problems, at least we have the experience and learning. In the second method, we cleaned the data, e.g., using tube ratios, calibrated using data from the McMurdo neutron monitor, and fitted to a Dorman function, which we know has parameters with non-physical content. Eventually if we have to use Dorman technique, the analysis should be advanced more than before. That means we are going to develop optimal methods for extracting cosmic ray spectra from the latitude survey.

In order to show the broader viewpoint of Nagashima fitting, Figure 1.6 illustrates an example of the Nagashima approach applied to the latitude survey data from the 3NM64. The boxes show 30 minute averages of the count rate (counts/second) plotted against the apparent cutoff calculated at the center point of the averaging interval. The solid line shows the model achieved after 61 iterations of our fitting routine.

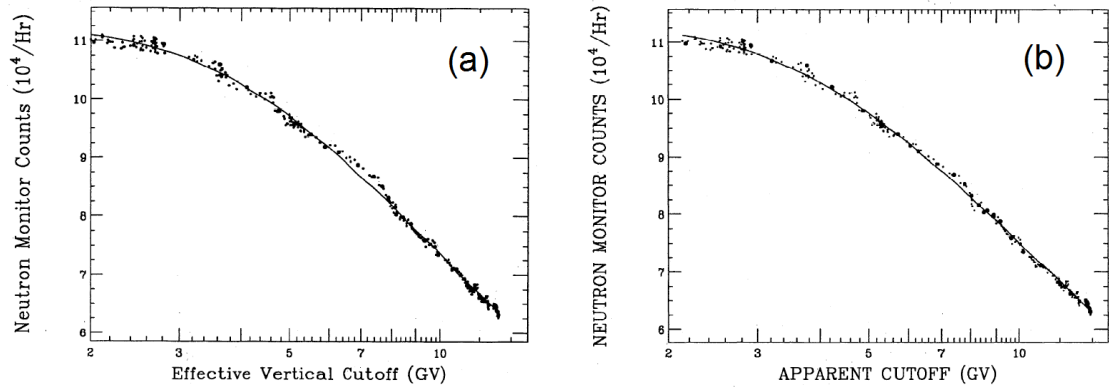


Figure 1.4: (a) Count rate recorded during the portion of the 1994-1995 Bartol/Tasmania latitude survey. The large dots indicate locations for which a cutoff sky map is calculated. (b) Observed neutron monitor count rate vs. apparent cutoff. Large dots indicate actual calculations and small dots indicate interpolated values. [Image credit: Clem et al. (1997)]

The quality indicates the square of the accumulated count rate difference. The values obtained for the Nagashima et al. (1989) parameters are indicated in the figure. Briefly, γ_1 functions as an overall normalization while the other parameters describe the yield function explained in Chapter 2. These are the only parameters we varied because our objective is to characterize the response functions.

1.1.3 A Solar Modulation Mystery

Generally when we talk about the word “modulation” we will imagine to the process of decreasing from one or more properties in a periodic waveform. But in cosmic ray astrophysics, when we refer to this word it means “solar modulation”.

The solar modulation is the influence the Sun exerts upon the intensity of galactic cosmic rays, e.g., as detected using a neutron monitor. When the Sun is active, we get fewer cosmic rays. From Figure 1.7, we see that the count rate recorded by a neutron monitor in Thule, Greenland decreases (bottom panel) when solar activity rises. The period of most solar activity and highest sunspot number in the 11-year solar cycle of the Sun is called “solar maximum,” which is contrasted with “solar minimum.” Many people may wonder why it has to be every 11 years. There is no clear scientific answer yet, but we knew that the cycle also involves the solar magnetic polarity, which reverses every 11 years, and has a strong influence on heliospheric (solar) modulation,

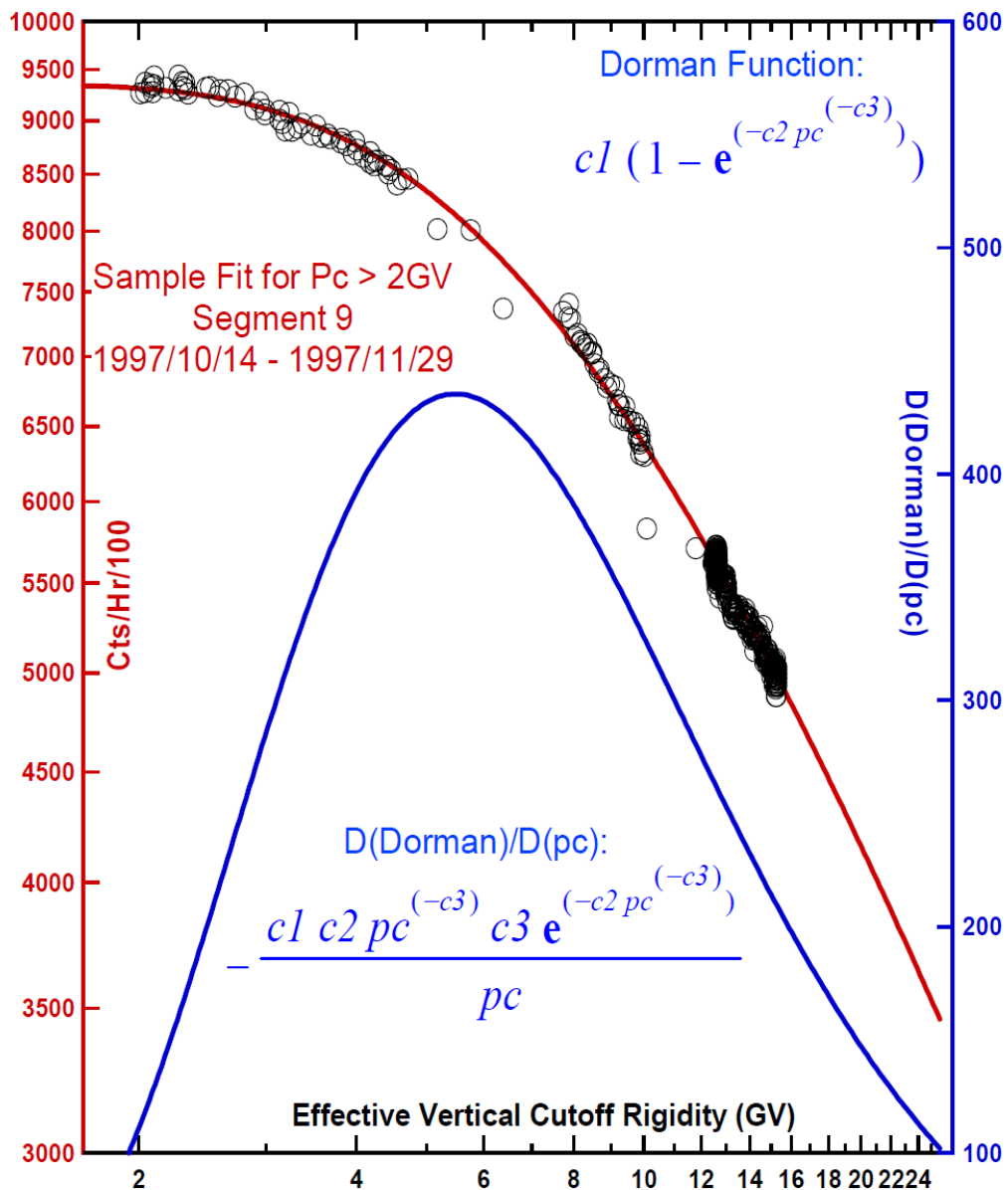


Figure 1.5: Sample fit of a response function from a segment of the 1997-1998 voyage [Image credit: Bieber et al. (2003)]

since the magnetic polarity of the Sun becomes embedded in the large scale structure of the solar wind.

The influence of solar magnetic polarity is seen in one way by comparing the intensity of particles of the same charge to mass ratio but opposite charge sign. For example, Bieber et al. (1999) compared the intensities of protons and antiprotons (see Figure 1.8).

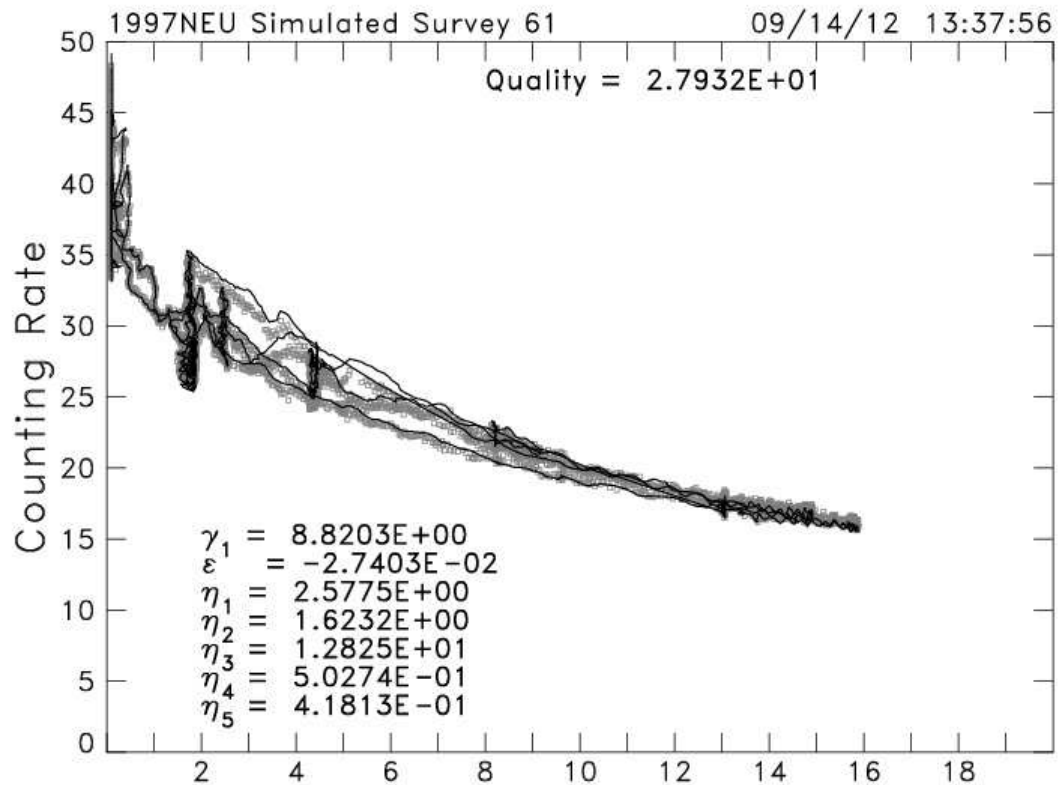


Figure 1.6: Data (boxes) and model fit (solid line) for the ship-borne detector’s 1997 latitude survey. Fit parameters are discussed in the text.

Nowadays we can explain many things about modulation but one of the most puzzling aspects of modulation phenomenology is the “crossover” in spectral form during opposite magnetic polarity epochs, and its origin still is not clear.

We start with a basic definition of a “crossover.” Suppose we have two functions, A and B, describing spectra (or DRFs), shown as blue and red curves in Figure 1.9. They are said to have a crossover if function A is greater than function B for some values of the independent variable and function A is less than function B for other values of the independent variable. The “crossover” is simply the point at which the graphs of the functions coincide. Thus in the sketches of Figure 1.9, the top drawing (labeled 0) does not have a crossover, whereas the two middle drawings (labeled 1) each have a crossover, and the bottom drawing (labeled 2) has two crossovers. We think it may also be useful to distinguish between a crossover of type 1H, where the crossover occurs at an energy above the maximum of (at least) one of the curves, and type 1L, where the crossover occurs below the maximum of both curves.

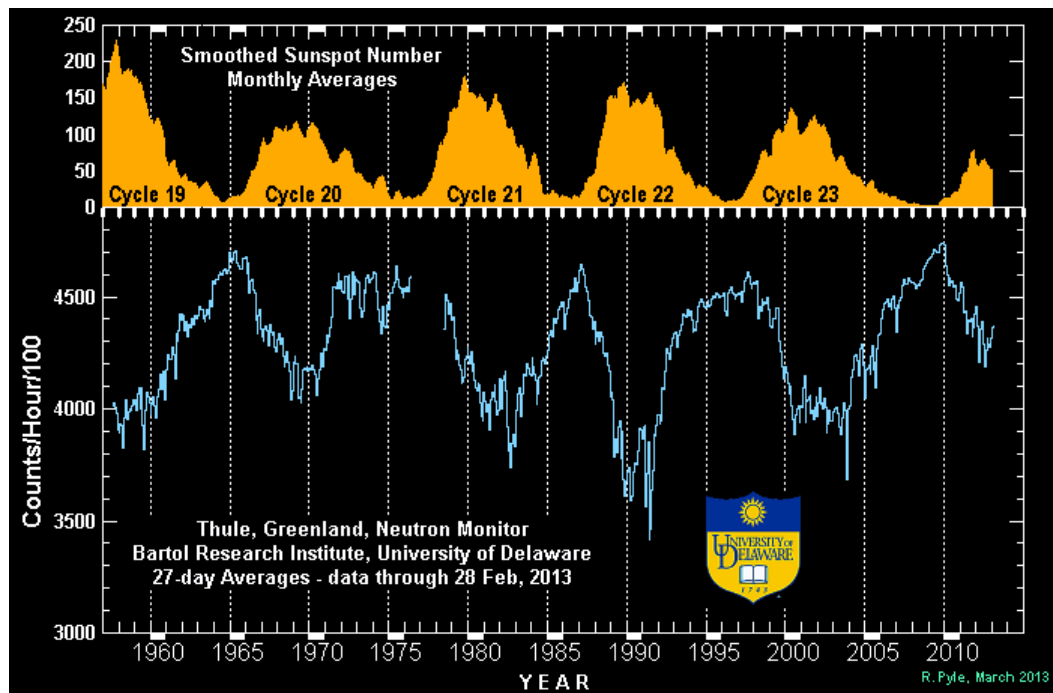


Figure 1.7: Solar modulation: As solar activity rises (top panel), the count rate recorded by a neutron monitor in Thule, Greenland decreases (bottom panel). Effects of solar magnetic polarity are manifest as differences in modulation during alternate count rate maxima. [Image credit: <http://neutronm.bartol.udel.edu/modplot.html>]

From Figure 1.10, Moraal et al. (1989) illustrates the pairs of differential response functions (DRFs) selected at 11-year intervals (two solar cycles of opposite magnetic polarity) and 22-year intervals (two solar cycles of same magnetic polarity). We clearly see the crossover effect at approximately 6 GV in DRFs taken during opposite polarity epochs.

In this terminology, we think that what Moraal reports is a type 1H crossover in “opposite polarity” solar minima, and no crossover in “same polarity” solar minima. In some of the literature, mainly papers by Lockwood & Webber (1996), they talked about a type 2L crossover. To reconcile Lockwood & Webber (1996) and Moraal et al. (1989) might involve postulating two or even three crossovers. However for this work we think we can just say we are considering energies above 1 GeV and not worry about linking to the Lockwood & Webber (1996) results.

Such a crossover was confirmed by Lockwood & Webber (1996) and Bieber et al. (2004) albeit with some questions as to the primary proton energy at the crossover.

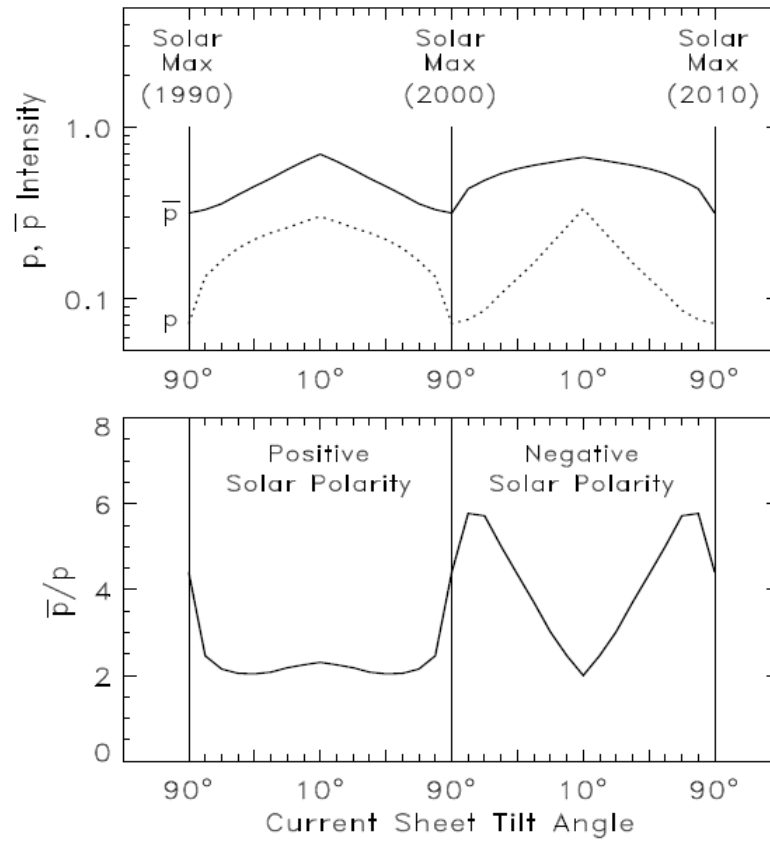


Figure 1.8: Predicted dependence of the proton and antiproton intensity (top panel) and the antiproton/proton ratio at 1 AU upon the tilt angle of the heliospheric current sheet for 1 GeV kinetic energy (bottom panel) covering the two solar cycles of opposite magnetic polarity from the 2000 solar maximum to the 2010 solar maximum. [Image credit: Bieber et al. (1999)]

The problem of the existence of the crossover effect, and that there could be two crossovers, at least at some times, was addressed by Reinecke et al. (1997).

The analysis of Bieber et al. (2004) used a similar data set of a series of latitude surveys to indicate clearly a change in character of the spectrum with changing magnetic polarity. As shown in Figure 1.11, they performed Dorman function fits to 26 segments of latitude survey series. A segment is a transition from low cutoff (about zero GV) to the geomagnetic equator or the reverse. These surveys were conducted between Seattle and McMurdo. Each round trip could produce four segments. This condition for dividing the segments was also used in our research. Figure 1.11 plots the rigidity at which the response function peaks vs. the relative value of the response

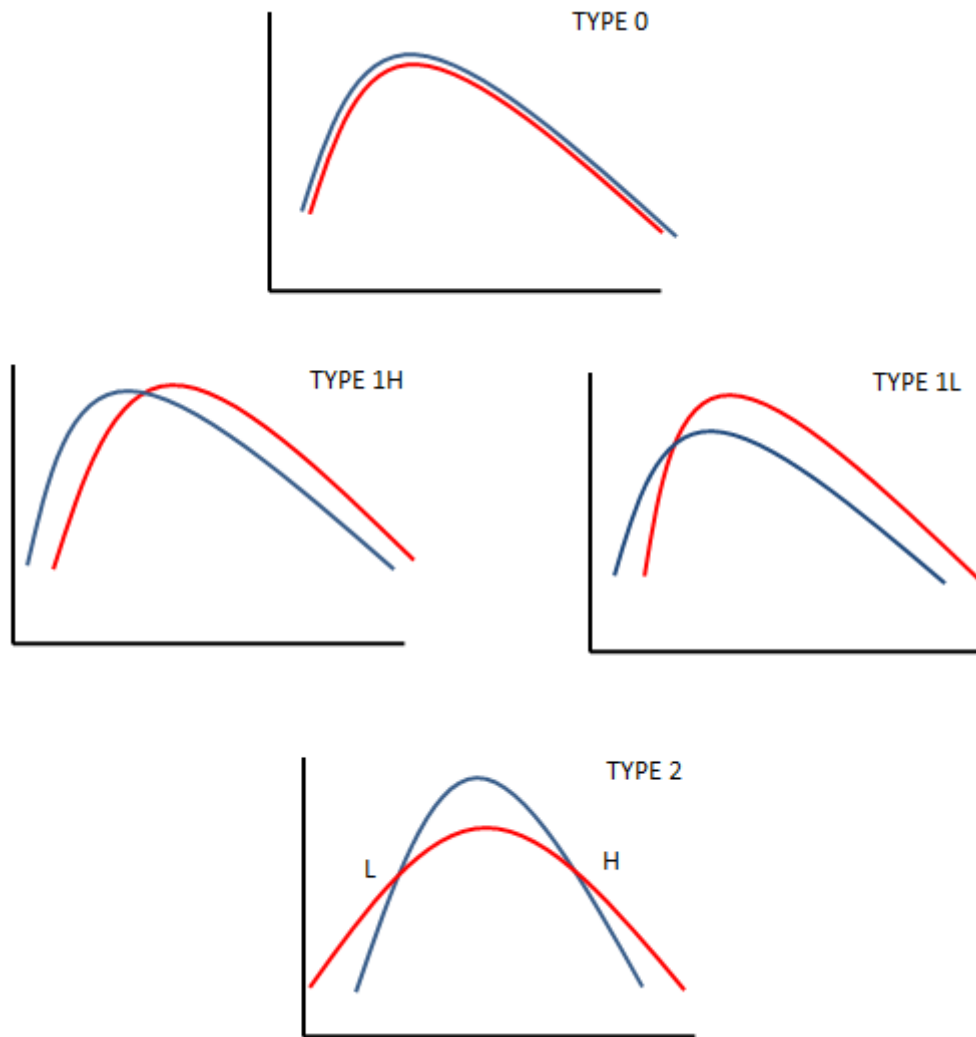


Figure 1.9: Sketches of types of spectral crossovers

function at the peak, using the segment number as the symbol and connecting the points by lines to make the time sequence clear. There are two clearly distinct clusters of points divided by color, which indicates the solar dipole polarity during the segment. Green color indicates the positive polarity and red color indicates the negative polarity. However, there are some points, such as 18-20, that stray off the original correlation line just before the polarity change. The authors hypothesized that these results could arise from drift and/or magnetic helicity effects in solar modulation. We view this as an indication that the relation between the interplanetary field and the solar dipole polarity is not a simple one. There is obviously a change in the character of the spectrum, but whether it is a crossover or not did not appear in this analysis.

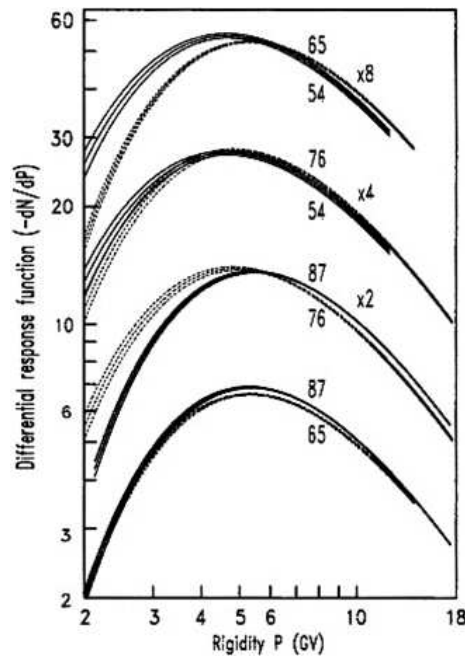


Figure 1.10: Illustration of “spectral crossover” effect of response functions at 11 and 22 year intervals. The curves are labeled by the year of the latitude survey. [Image credit: Moraal et al. (1989)]

The conclusion is that there is a typical expectation that there is a 22-year cycle of modulation whereby the polarity of the solar magnetic field switches every 11 years (more or less). It is expected that periods of one polarity have the same spectral sequence with modulation, which is different from changes of spectrum as a function of modulation of the other polarity. A “crossover” is one type of difference that authors have claimed.

Another way to visualize the crossover is shown in Figure 1.12. Bieber et al. (2007) compares modulation of helium nuclei at approximately 1.2 GV, indicated by “flat-topped” and “pointy”, with that of the McMurdo neutron monitor. Both show the classic observational support for the influence of gradient and curvature drifts (Jokipii et al. (1977), Potgieter & Moraal (1985)) in heliospheric modulation. The helium observations are presented on a simple linear scale with no offset while McMurdo data have been adjusted in scale and offset to (approximately) coincide during the “pointy” cycle of the 1980s. With this normalization it is easy to see that, while the helium fluxes are lower at their peak in the 1980’s than they were in the decades on either side, the neutron monitor was higher. This again is the “spectral crossover”.

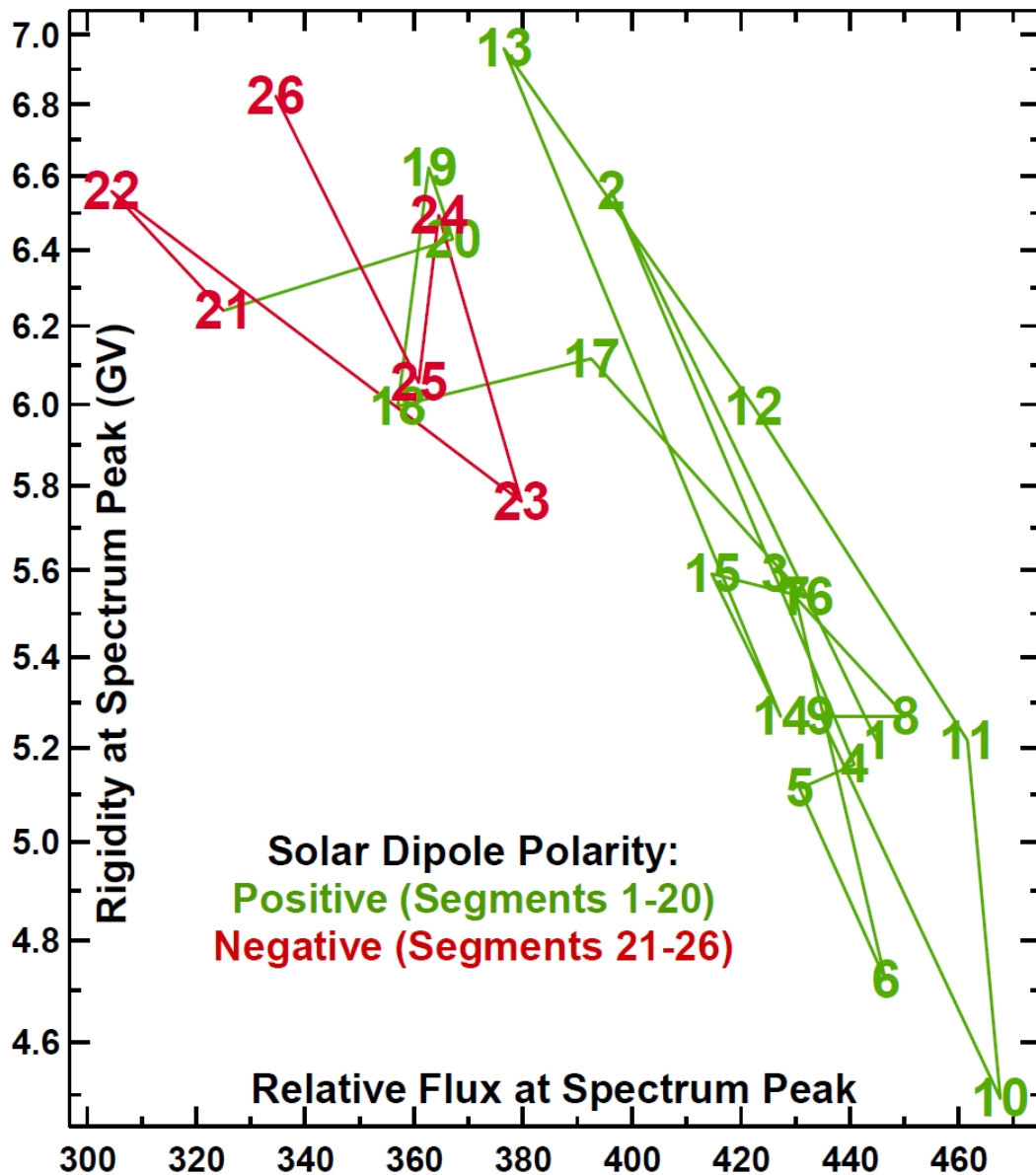


Figure 1.11: Rigidity of the DRF peak is plotted versus the relative flux at the maximum for each of the 26 segments of the 1994-2002 survey years. Segments with positive solar dipole polarity (shown in green in the plot), while the solar activity increased from 1994 to 2000, lie along a single trend line. When modulation increased, the flux at spectrum peak became lower, but it appeared at a higher rigidity. Segments with negative solar dipole polarity (shown in red in the plot), while the solar activity decreased from 2000 to 2002, moved off the trend line of the positive magnetic polarity results. [Image credit: Bieber et al. (2003)]

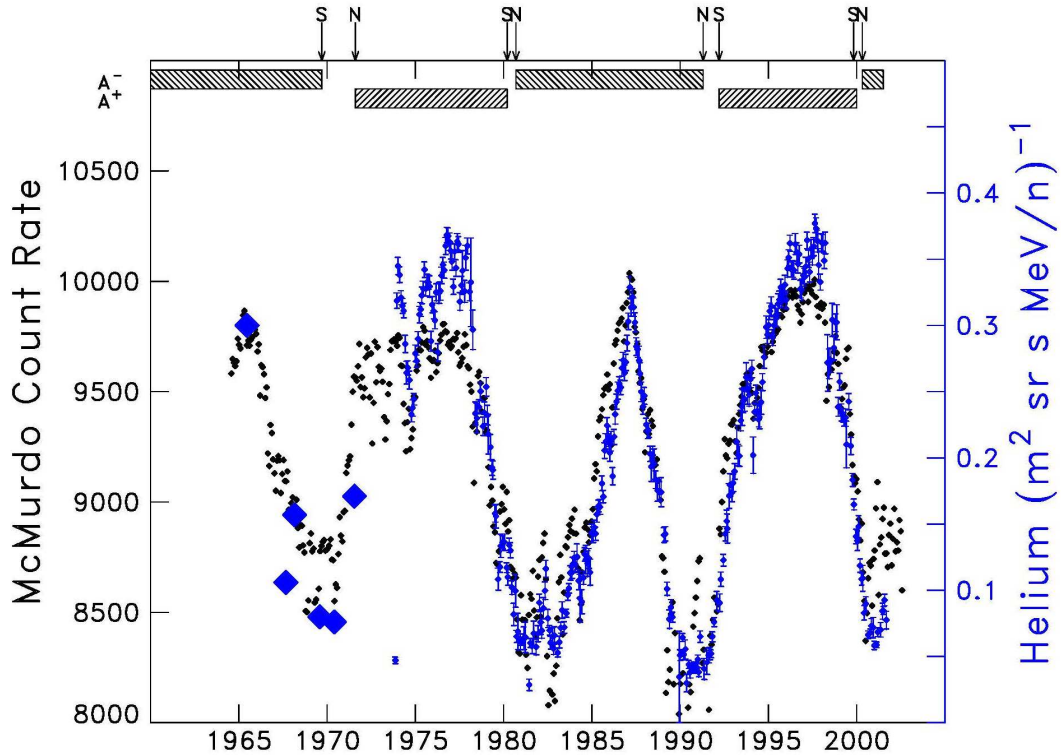


Figure 1.12: Comparison of the McMurdo neutron monitor count rate and 1.2 GV helium flux from Interplanetary Monitoring Platform 8 (IMP-8) vs. time. [Image credit: Bieber et al. (2007)]

Owing to the large detector mass required to detect high-energy cosmic rays, ground-based instruments have remained the state-of-the-art method for studying time variations of these elusive particles (Simpson et al. 1953; McDonald 2000). There have been several direct observations of the full spectrum from balloon-borne and space-based instruments for specific epochs. Typically measurements have not been available for the same instrument and the same level of modulation in opposite polarities, so they have not confirmed a crossover per se. Clem et al. (2003) presented a compilation of proton and alpha particle spectra from several sources. The most direct comparison to the present work is provided by the series of proton spectra from the BESS payload (Mitchell et al. 2008) that span the year 2000 solar polarity reversal with observations from the same instrument. Mitchell et al. (2008) also fit their data to a force field model which, apart from normalization, has only one adjustable parameter. The fits to the BESS data may be good, but they are not perfect. Close examination reveals that the

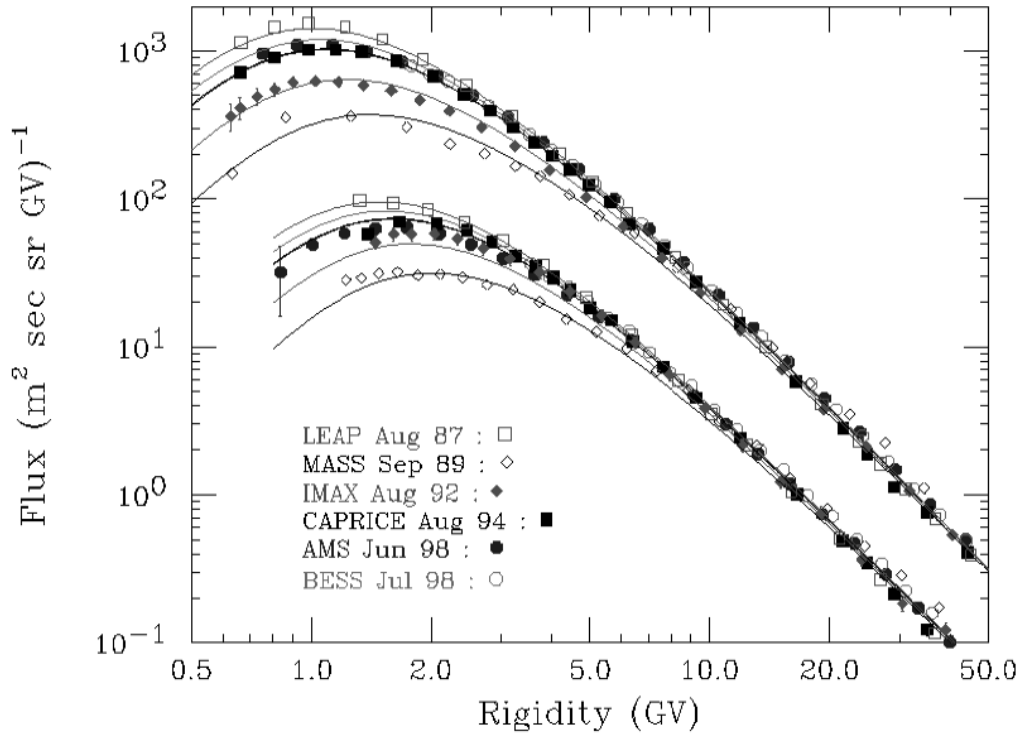


Figure 1.13: Balloon and spacecraft measurements of primary cosmic ray spectra. Protons (upper spectra) and helium (lower spectra) compiled by Clem et al. (2004). [Image credit: Clem et al. (2004)]

fits to spectra after the polarity reversal (BESS-2002 and BESS-Polar, in 2004) are not as good as those to spectra before the reversal. The fits in fact fail by overpredicting the data at low energy, just as we find in our results. We therefore consider that the BESS data are consistent with our results.

A crossover would be significant because drift effects are clearly established as an important factor in solar polarity dependence of modulation but they have not been shown to be the only factor. In and of itself the drift picture does not predict a crossover. However charge sign dependence is not the only modulation effect sensitive to the interplanetary magnetic field polarity. There is also the “twenty-year wave” observed in the phase angle of the cosmic ray diurnal anisotropy (Bieber & Chen (1991)). Although this has also been attributed to particle drifts, Chen & Bieber (1993) showed that it is related to their finding that the cosmic ray scattering mean free path is systematically larger during epochs of negative solar polarity than during epochs of positive polarity.

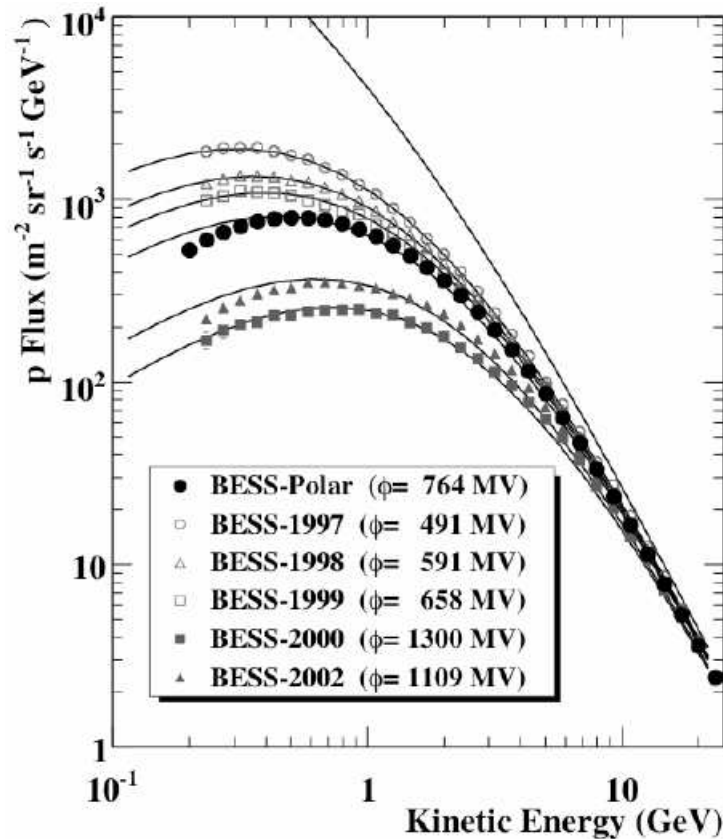


Figure 1.14: Sequence of proton spectra from BESS spanning a polarity reversal [Image credit: Mitchell et al. (2008)]

Diffusion coefficients can change radically with solar polarity because of helicity in the solar wind magnetic field and systematically organized magnetic helicity is actually observed in direct measurements of the interplanetary magnetic field. Bieber et al. (1987a) reported that the net (that is, integrated over wave number) helicity of the field has a definite dominant sign, negative north of the heliospheric current sheet and positive south of it. The helicity dependence of the mean free path is a function of the product of the sign of the helicity and the polarity of the large-scale field (Bieber et al. (1987b); Bieber & Burger (1990)). This means that at any given time the effect upon the mean free path is the same in both hemispheres (because the helicity and polarity BOTH reverse sign across the sheet), however when the solar polarity reverses the magnetic polarity reverses sign, but helicity does not. This will produce a larger mean free path during negative solar polarity, consistent with the Chen & Bieber (1993) result.

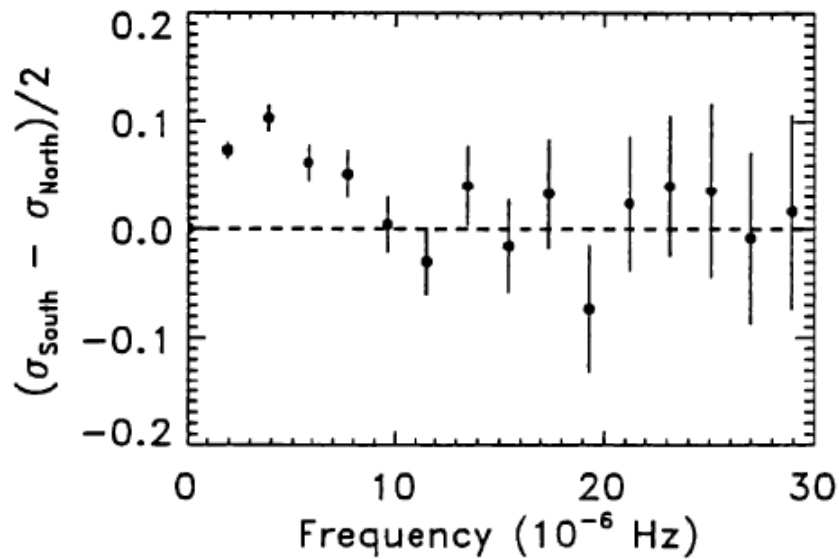


Figure 1.15: Normalized magnetic helicity fluctuates in sign for frequencies above 10^{-5} Hz, but displays a definite dominant sign at lower frequencies. [Image credit: Smith & Bieber (1993)]

An indication that magnetic helicity may become more important at neutron monitor energies was provided by Smith & Bieber (1993), who measured the magnetic helicity spectrum extended to very low frequency. As shown in Figure, they found that for frequencies above 10^{-5} Hz, the helicity fluctuates in sign and is statistically consistent with zero (Matthaeus & Goldstein (1982)). At lower frequencies, however, the helicity assumes a definite dominant sign. It is this low-frequency turbulence that corresponds to wave numbers resonant with cosmic rays in the neutron monitor regime.

This produces a natural explanation for the crossover since the enhanced diffusion coefficients would work in the opposite direction of drifts. During the negative polarity state, when drifts operate to limit fluxes, a larger diffusion coefficient, particularly at the higher energies, permits enhanced access. With such competing effects, each having a different energy dependence, a crossover would be just an observational result that one effect dominates at low energy and the other dominates at high energy. In fact it is also likely that the relative importance would change as a function of solar activity.

1.2 Objectives

This research has two specific objectives in addition to providing a significant enhancement to Ph.D research at the Mahidol University. These objectives are:

1. To compare count rates of the calibration monitor under various conditions.
2. To determine the best method to characterize the evolution of the cosmic ray spectrum using data from the series of latitude surveys conducted from 1994 through 2007.

1.3 Expected Benefits

This research has four expected benefits. These are:

1. The ability to compare the cosmic ray intensity at any two sites with different cutoff rigidity and atmospheric depth.
2. Deriving useful differential response functions from the neutron monitor network.
3. Developing optimal methods for extracting cosmic ray spectra from latitude surveys.
4. Providing correct information on how the sunspot cycle and solar magnetic cycle affect cosmic rays.

1.4 Outline of Thesis

This thesis is organized as follows: Chapter 1 introduces the importance and scientific background related to the calibration by the calmon and latitude surveys. Explaining the concepts also clarifies the author's motivation to do this research. This allows the readers to understand the researchers point of view and see the novelty of this research. The objectives and expected benefits are also given in this chapter. Chapter 2 provides the theoretical background and literature review about the calibration neutron monitor, intercalibration of the world's neutron monitors, ship-borne neutron monitor, latitude surveys and Forbush decreases. Chapter 3 proposes the experimental procedure and analysis procedure in order to describe the effects of the environment on the count

rate of a calmon at Doi Inthanon. Chapter 4 presents the methods to clean the data and to calibrate the count rate of the ship-borne neutron monitor. This chapter introduces two techniques to characterize the evolution of the cosmic ray spectrum using latitude survey data. The first technique is “fitting with a Nagashima function,” for which the ultimate goal is to go beyond the Dorman functions to more physical response functions. The second technique is “direct determination.” Chapter 5 (the final chapter) provides the discussion and conclusions, including ideas for further work.

CHAPTER II

LITERATURE REVIEW AND THEORETICAL BACKGROUND

We briefly described the calibration neutron monitor, ship-borne neutron monitor and latitude surveys in Chapter 1. In this chapter we will discuss their features in more detail, starting with a review about the propagation of cosmic rays and their secondary collision products through the Earth's atmosphere until hitting the neutron monitor.

2.1 Neutron Monitors

Outer space is filled with particles that have been accelerated to very high energy, mainly originating outside the Solar System. We call such particles “cosmic rays.” There are three main types of cosmic rays classified by the source and the energy range (see Figure 2.1).

1. **Solar Energetic Particles (SEPs)** are produced by solar storms, which are explosions in the atmosphere of the Sun. They range from suprathermal energy to about 10^7 eV. Most SEPs are protons or other ions with a composition similar to the atmosphere of the Sun.

2. **Galactic Cosmic Rays (GCRs)** are the cosmic rays that come from outside the solar system, having been accelerated by other processes in the Milky Way Galaxy. They are mainly protons having an energy range of about 10^7 - 10^{19} eV. GCRs continually arrive at Earth, but when there is a violent explosion in the atmosphere of the Sun, i.e., a solar storm, a resulting shock wave could lead to a decreased flux of GCRs for a few days. This event is called a “Forbush decrease”. The flux of high-energy charged particles that strike the Earth's atmosphere from outer space can be measured using a ground-based detector called a “**Neutron Monitor**.” Forbush decreases were discovered by Scott Ellsworth Forbush in 1937 (Forbush 1937). We will explained the

Forbush decrease in more detail in the last section of this chapter.

3. **Extragalactic Cosmic Rays (EGCRs)** are cosmic rays that come from outside the galaxy and sometimes move into our solar system. They are accelerated from several physical processes such as supernova explosions and so on. EGCRs have very high energies, up to 10^{20} eV, and could be accelerated in conjunction with gamma ray bursts or active galactic nuclei.

All of the cosmic rays described above, which are known to have originated outside of Earth's atmosphere, are called "primary cosmic rays." About 99% are nuclei (stripped of their electron shells) of well-known atoms, and about 1% are solitary electrons (similar to beta particles). Most of the nuclei, about 90%, are protons, i.e., hydrogen nuclei, 9% are alpha particles, and 1% are ions of heavier elements and electrons. When a primary cosmic ray enters Earth's atmosphere, it interacts with molecules, mainly nitrogen and oxygen. They can produce mostly neutrons and other sub-atomic particles called "secondary cosmic rays" or "secondary particles," which can reach the ground of the Earth. The cascade of lighter particles is called a "shower" and is schematically shown in Figure 2.2. Figure 2.2 is a modified version of an original image produced by the European Organization for Nuclear Research, known as CERN.

Most secondary particles in Earth's atmosphere are neutrons so we are interested to measure this particle species by a neutron monitor. Other particles that are not high-energy secondary neutrons will be screened out by the polyethylene reflector that surrounds the monitor. An incoming neutron interacts with a nucleus of lead and produces several low energy neutrons. These neutrons thermalize in polyethylene or other material containing a lot of hydrogen. There is also a polyethylene moderator surrounding each tube, which serves to reduce (moderate) the neutron energy, which increases the probability of neutron interactions in the $^{10}\text{BF}_3$ gas.

There are two standard types of detectors which are well known: the International Geophysical Year (year 1957; IGY) and NM64 designs. The first neutron monitors were used in the US and Peru to study geomagnetic effects. The first worldwide network of neutron monitors used the IGY design (see Figure 2.4), similar to the design used by John Simpson for the first neutron monitor in 1948. The components of the IGY monitor are neutron sensitive proportional tubes, surrounded by a paraffin moderator material and a lead target. In 1957-1958, 50 IGY monitor stations were installed at different locations around the world. After that, in 1964, a new generation

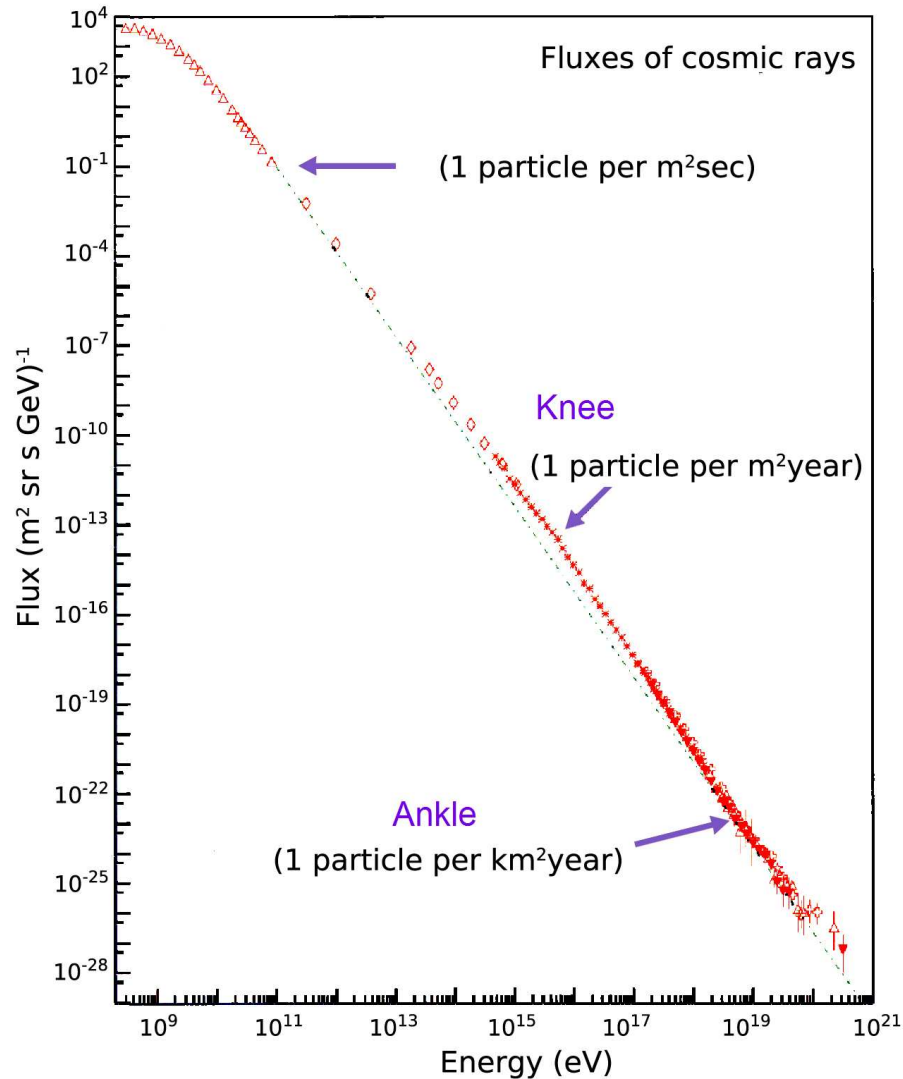


Figure 2.1: The flux of cosmic rays as a function of their energy. The flux for the lowest energies could also have an additional contribution from solar energetic particles (not shown here) after the occasional occurrence of a major solar storm. The non-solar cosmic ray spectrum is curved in this region because access of cosmic rays coming from outside the solar system to the inner solar system is reduced by the solar wind and magnetic field of the Sun. The cosmic rays up to $\sim 10^{18.5}$ eV are galactic cosmic rays. There are breaks in the power law, for instance energy near $\sim 10^{15}$ eV called the “knee” of the cosmic ray spectrum. The cosmic rays with the highest energies are extragalactic cosmic rays. We can see an “ankle” of the cosmic ray spectrum at an energy near $\sim 10^{18.5}$ eV. [Image credit: <http://astroparticle.uchicago.edu/>]

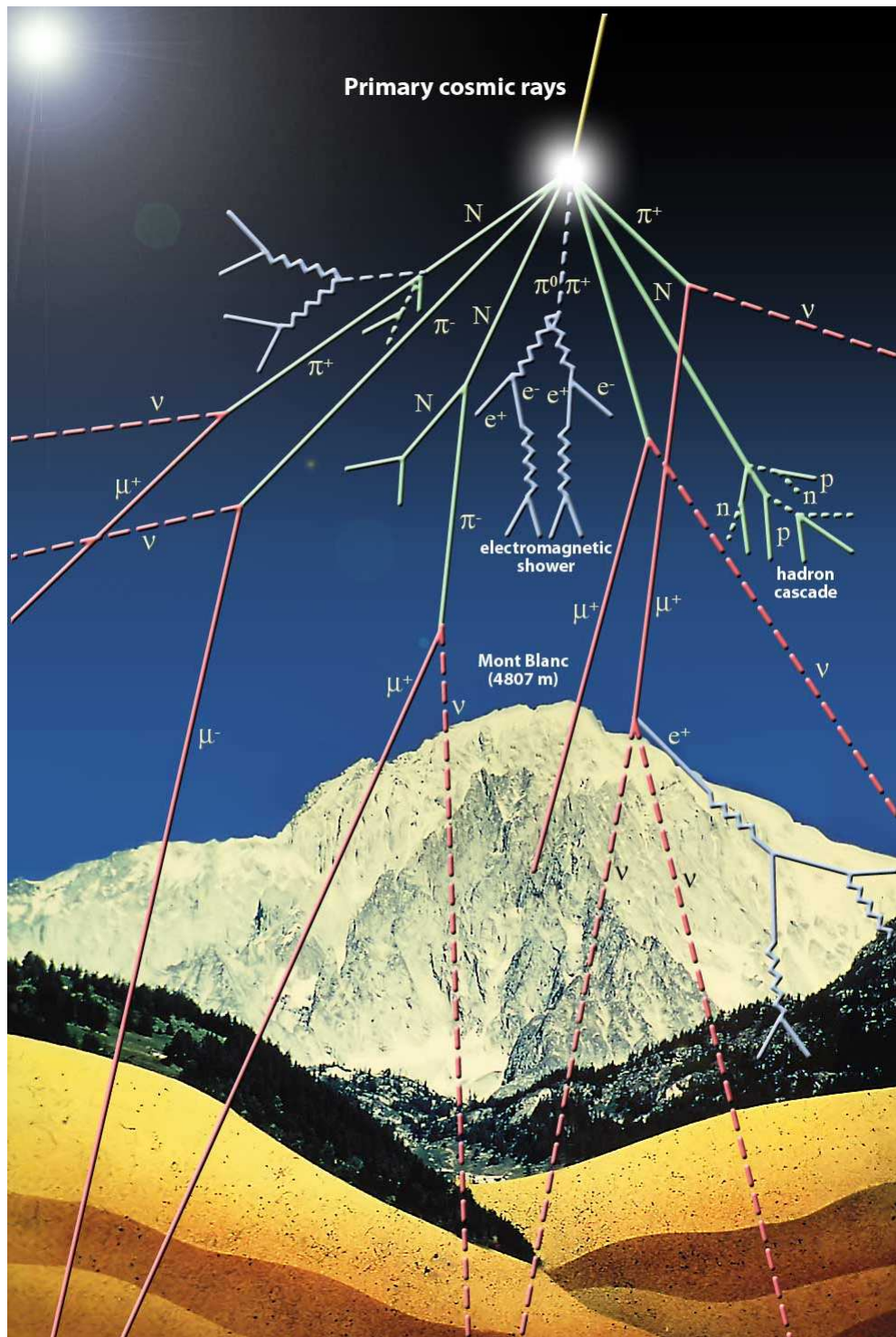


Figure 2.2: Primary cosmic ray particle colliding with a nucleus in the atmosphere and producing a shower [Image credit: <http://scifun.ed.ac.uk/card/images/left/cosmic-rays.jpg>]

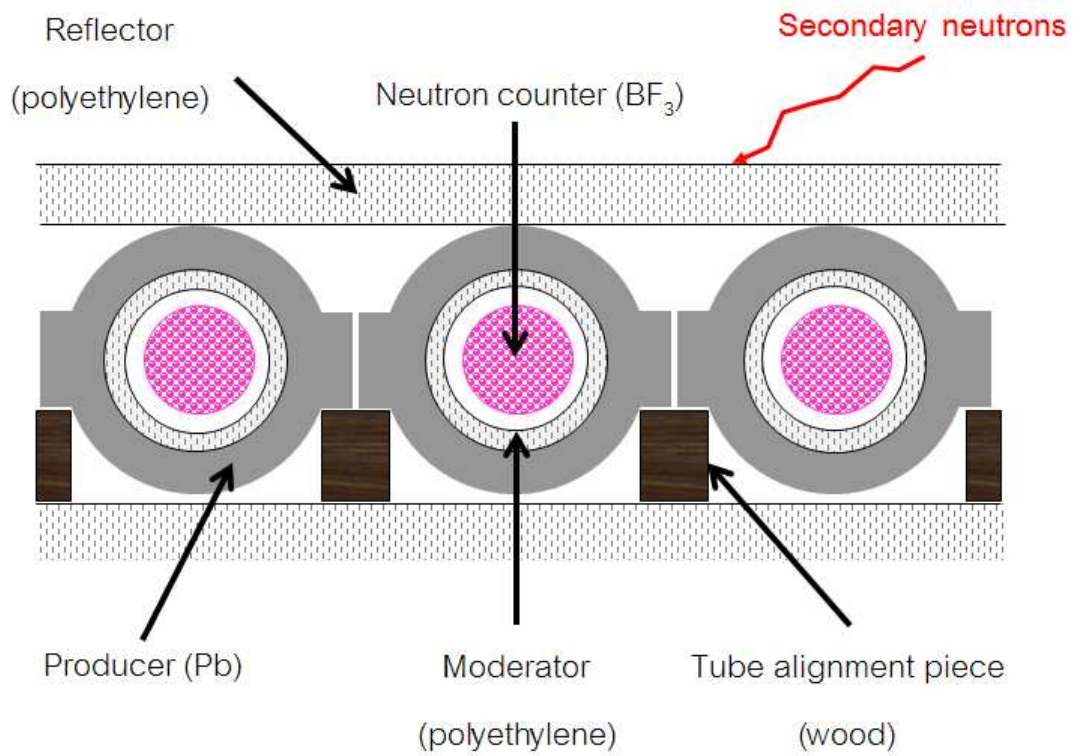


Figure 2.3: Structure of NM64-type neutron monitor. See text for details.

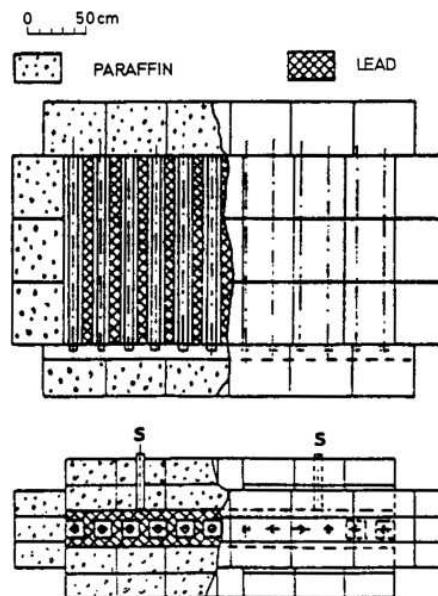


Figure 2.4: The IGY (International Geophysical Year, 1957) neutron monitor design

of neutron monitors was developed, with the NM64 design (see Figures 2.3 and 2.6). Hatton & Carmichael (1964) described that the IGY type of NM records evaporation neutrons produced in the lead of the NM with an efficiency of 1.9% and the NM64 records them with an efficiency of 5.7%, which increases by 3.3 times the count rate per unit area of lead producer. Hatton (1971) and Clem (1999) pointed out that the IGY has a different response in both magnitude and shape as a function of primary rigidity (GV) than the NM64. The thicker reflector of the IGY is much more effective in preventing response to environmental thermal neutrons than the NM64. Hatton & Carmichael (1964) also provided various specifications for the NM64:

“Counters. The effective diameter of the IGY counters specified by Simpson (1957) is 0.225 of the mean free path of thermal neutrons in ^{10}B , whereas for the NM-64 counters it is 0.375. If we assume that the difference of effective diameters can be represented as a change of the pressure in an NM-64 counter (normally filled to 20 cm Hg at 22°C) the equivalent IGY pressure is $20 \times 0.225 / 0.375 = 12$ cm Hg. ... We find the NM-64 counter to be *1.37* more efficient than the IGY counter.”

“Moderator thickness. The IGY monitor has about 3.7-cm thickness of paraffin wax around each counter instead of 2.0 cm used in the NM64.... The NM64 at 2.0 cm (0.75 in.) appears to be *1.13* times more efficient than at 3.7 cm (1.46 in.).”

“Producer thickness. The average thickness of lead producer in the NM-64 monitor is 5.7 in. compared with 5.33 in. for the IGY monitor. Hence 4.7% more nucleons will interact in the lead if it is assumed that the interaction mean free path of the nucleonic component is 215 g cm^{-1} . This gives a factor of *1.05*.”

“Reflector thickness. The thickness of paraffin wax above the IGY monitor is 12 in. and of polyethylene above the NM-64 3 in. ... This difference gives a factor of *1.23* in favor of the NM-64”

“Solid angle. The product of the above four factors is 1.94, whereas the observed efficiency ratio per unit area of lead is 3.3. ... We believed that the needed additional factor is supplied by the fact that the diameters of the counters and, more important, of the inner moderators in the NM-64 are so much larger than in the IGY monitor. These diameters have been increased without increasing the thickness (2 in.) of the surrounding lead producer. Hence the moderating material presents on the average a larger solid angle to the producer in the NM-64 than in the IGY monitor. Estimates of the relative sizes of the two solid angles gave a ratio of *1.6*, which is in satisfactory



Figure 2.5: The Princess Sirindhorn Neutron Monitor building at Doi Inthanon, Chiang Mai, Thailand

agreement with the factor of 1.7 needed.”

Let us emphasize only the NM64 design because the neutron monitors in our research are related with this type of neutron monitor only. There are basically two types of gas that are filled in the counters for the NM64 design. They are $^{10}\text{BF}_3$ (boron-10 trifluoride) and ^3He (helium-3). Hatton (1971) described that a neutron monitor with a $^{10}\text{BF}_3$ (boron-10 trifluoride) proportional counter records thermal neutrons produced by interacting incident neutrons, protons, pions, and muons, which have relative contributions to the counting rate as 85%, 7%, 1%, and 6%, respectively.

Our research group, in cooperation with Mahidol University, Chulalongkorn University and Ubon Ratchathani University installed the first neutron monitor station in Thailand in 2007, named the “Princess Sirindhorn Neutron Monitor (PSNM),” shown in Figure 2.5. It was set up at the highest mountain in Thailand (2,565 meters), Doi Inthanon in Chiang Mai province, in order to measure the count rate of secondary neutrons, which is related to the flux of cosmic rays in space. The specifications of



Figure 2.6: The placement of the Princess Sirindhorn Neutron Monitor (an 18NM64 monitor) at Doi Inthanon, Chiang Mai, Thailand

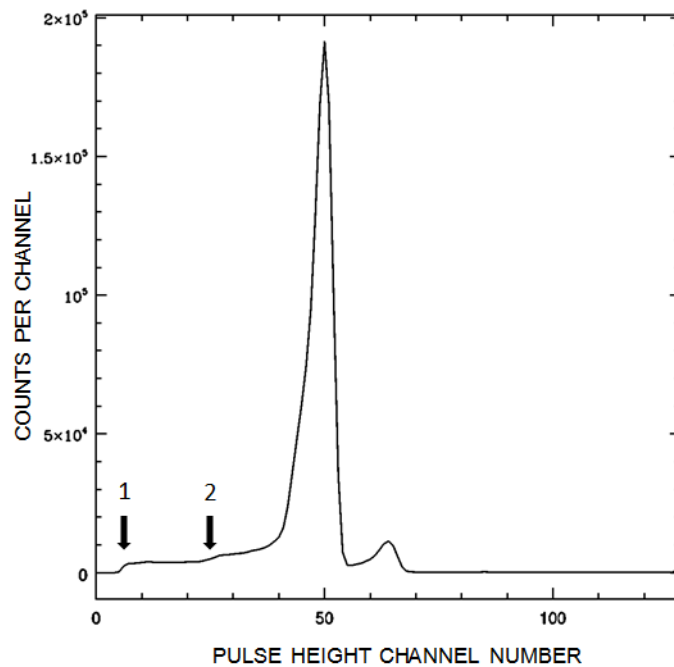


Figure 2.7: A pulse height distribution from the PSNM at Doi Inthanon, Chiang Mai, Thailand

Table 2.1: Specifications of the Princess Sirindhorn Neutron Monitor at Doi Inthanon, Chiang Mai, Thailand

| | |
|------------------------------------|---|
| Location | |
| Latitude | 18°35'11" N |
| Longitude | 98°29'17" E |
| Altitude | 2560 m |
| Estimated vertical cutoff rigidity | 16.8 GV |
| Counter[†] | |
| Type | 18-tube NM64, BP28 from Chalk River Lab. (Canada) |
| Filling | Boron trifluoride (BF ₃), enriched to 96% ¹⁰ B |
| Pressure | 200 mm Hg at 22°C |
| Pressure coefficient | 0.854%/mm Hg, reference pressure 563 mm Hg |
| Diameter | 5.785 to 6.03 inches (corrugated) |
| Overall Length | 2.25 m (including electronics devices) |
| Active Length | 1.90 m |
| Resolution | 12% average FWHM for 2.3 MeV Peak |
| Background Counts | ~4/minute |
| Operating Voltage | -2800 V |
| Inner Moderator | |
| Material | Polyethylene |
| Diameter | 7.9 inches (20 cm) |
| Thickness | 0.8 inches (2 cm) |
| Producer | |
| Material | Lead |
| Thickness of one ring | 3 inches |
| Inner Diameter | 10 inches |
| Outer Diameter | 14 inches |
| Wings Height | 6 inches |
| Total Width Including Wings | 19 inches |
| Reflector | |
| Material | Polyethylene |
| Thickness | 3 inches |

[†] Source: BP28 Chalk River Neutron Counter Operating Data.

the Princess Sirindhorn Neutron Monitor (18NM64) are shown in Table 2.1. The “18” refers to the fact that there are eighteen counter tubes installed in the station. Figure 2.6 shows the placement of the 18NM64 inside the station. It includes components such as the proportional counters (¹⁰BF₃ tubes), the “remote” electronics boards (with high voltage generator sub-boards) attached to the tubes, the “master” electronics boards connected to the counter electronics and PC running data acquisition software. The proportional counters are filled with a BF₃ gas enriched in ¹⁰B. They produce a signal when a ¹⁰B nucleus reacts with a neutron, and the cross-section of the reaction is highest

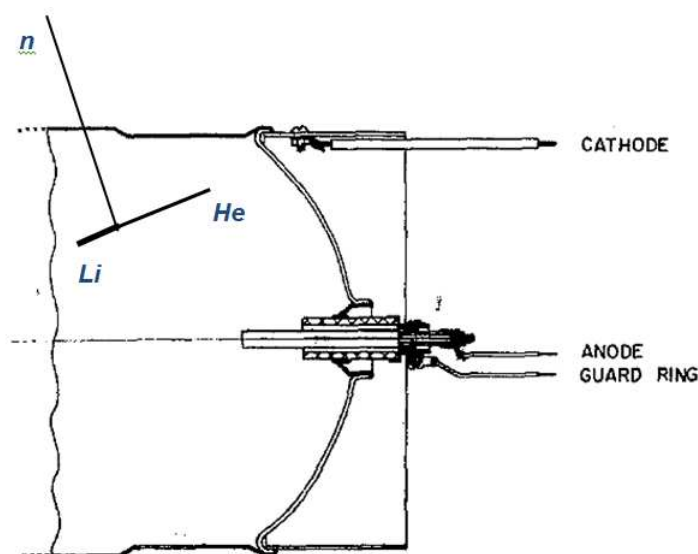


Figure 2.8: Illustration of a nuclear reaction between secondary neutrons and ^{10}B in a BP-28 proportional counter to produce ^7Li and ^4He [from Fowler (1963), as modified by P. Evenson.]

for low-energy (thermal) neutrons. The reaction products (^7Li and ^4He) ionize the gas and high voltage between the outer cylinder and central wire (-2800 V) accelerates free electrons to produce an electron cascade measured as a pulse of charge, a process called the “electron avalanche.” The pulse height is roughly proportional to energy deposited in the $^{10}\text{BF}_3$ gas. Figure 2.7 shows a histogram in pulse height channel number, which is proportional to energy deposited in the $^{10}\text{BF}_3$ gas, from one day of data for one counter tube. Stoker et al. (2000) presented that the proportional counters filled with ^3He respond to neutrons by the reaction $^3\text{He}(n, p)^3\text{H}$, whereas the BP28 ($^{10}\text{BF}_3$) tube responds to neutrons by $^{10}\text{B}(n, \alpha)^7\text{Li}$. The Q -value of the ^3He -neutron reaction is 765 keV and that of the ^{10}B neutron reaction is 2.791 MeV. In 94% of the $^{10}\text{B}(n, \alpha)^7\text{Li}$ reactions the ^7Li is left in an excited state (see the highest peak in Figure 2.7), whereas 6% lead to the ground state (see the second peak in Figure 2.7).

The numbers 1 and 2 in Figure 2.7 indicate “wall effect onset energies.” These effects occur when secondary neutrons react with ^{10}B in a proportional counter and then splits into ^7Li and ^4He (see Figure 2.8), one of which collides, with the wall of the counter and fewer secondary electrons are produced, resulting in lower charge collection. Number 1 indicates the minimum charge collection when ^4He hits the wall

and number 2 indicates that when ${}^7\text{Li}$ hits the wall. Their ratio provides an estimate of the energy ratio $E({}^4\text{He})/E({}^7\text{Li})$, which by using the conservation of momentum and energy should equal the mass ratio $m({}^7\text{Li})/m({}^4\text{He}) = 6.941/4.003 \approx 1.73$.

2.2 Calibration Neutron Monitor

Physicists at Northwest U., South Africa have built two calibration neutron monitors, completed in September 2002, with the purpose to intercalibrate the worldwide network of ~ 40 fixed neutron monitor stations and derive a differential response function. A calibration monitor is a miniature version of the neutron monitor. It is being carried to various locations to test and calibrate against standard monitors. The counter is a ${}^3\text{He}$ gas-filled tube of the type LND25382 with a pressure of four atmospheres, instead of the 0.26 atmospheres of the standard ${}^{10}\text{BF}_3$ counters, in order to obtain a similar energy response, as described by Clem & Dorman (2000).

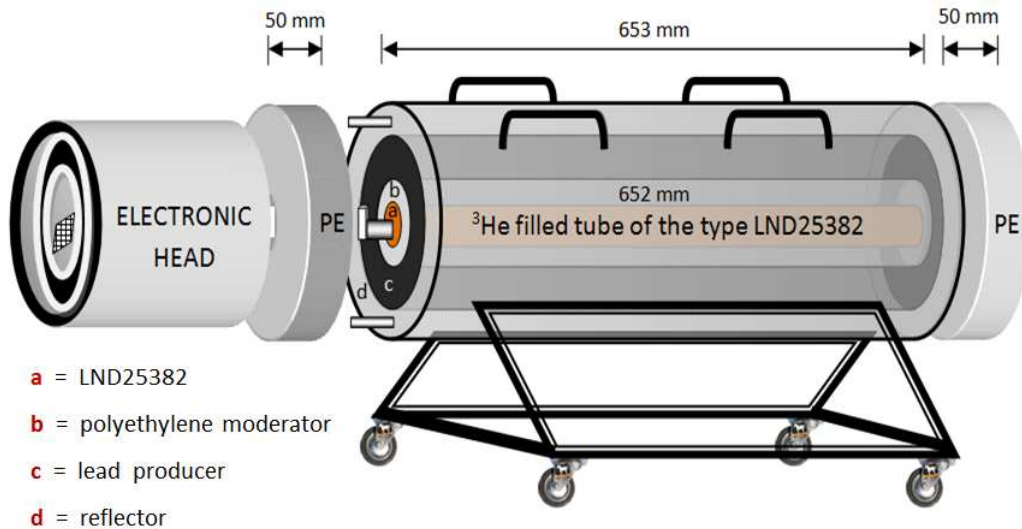


Figure 2.9: Schematic diagram of a calibration neutron monitor with (a) an LND25382 neutron counter filled with ${}^3\text{He}$ gas. It is surrounded with (b) polyethylene (PE) moderator with inner and outer diameters of 60.5 and 99.5 mm, (c) lead producer with inner and outer diameters of 101 and 193 mm, and (d) polyethylene (PE) reflector with inner and outer diameters of 194 and 350 mm.

Krüger et al. (2003) described the calmon dimensions by the following final design (see schematic diagram in Figure 2.9 and photograph of calibrator with electron-

ics head from Northwest U. (South Africa) in Figure 2.10 and that with the electronics head from Bartol Research Institute (DE, USA) in Figure 2.11): "... its counter, 51 mm diameter and 652 mm long. It is surrounded by a polyethylene moderator with inner and outer diameters of 60.5 and 99.5 mm, a lead producer with diameters 101 and 193 mm, and finally an outer reflector with diameters 194 and 350 mm. All these cylinders are 653 mm long. The front and back of the counter are covered with 50 mm polyethylene ends with a diameter of 350 mm. The total ... length of the monitor therefore is $653 + 100 = 753$ mm. Its mass is 201 kg, of which 145 kg is lead. It rests on a cradle with steerable wheels, and the total mass with cradle is 223 kg. The system records the number of counts, barometric pressure, high voltage, temperature, GPS co-ordinates and GPS altitude once per second."



Figure 2.10: Calibration neutron monitor with electronics head (cover removed) from Northwest University, Potchefstroom, South Africa

Krüger et al. (2008a) described that the accuracy of NM calibration needs to be less than 0.2% to produce useful spectra. They found that the energy response of a calibrator over the cutoff rigidity interval from the poles to the equator differs from



Figure 2.11: Calibration neutron monitor with electronics head from Bartol Research Institute, U. Delaware, USA

that of a standard 3NM64 neutron monitor by almost 4%. It was also determined that not only the calibrator, but also the NM64 and IGY that have fairly large temperature sensitivity (when using ^3He tubes), which should be taken into account in calibration procedures. The calibrator shows a large sensitivity to environmental effects including the surface beneath. Krüger & Moraal (2010) studied the sensitivity to its environment. Their experiments found that the calibrator count rate increases (noticed from the decreasing ratio in Figure 2.12) with increasing elevation above the surface. This implies that there is more of a neutron “cloud” from cosmic ray interactions further above ground level. This counter-intuitive result may have arisen because their experiment was carried out in a building. Figure 2.12 also shows that the calibration neutron monitor count rate decreases with increasing water height. This may be because the calibration neutron monitor has a large sensitivity to the materials and surface underneath it.

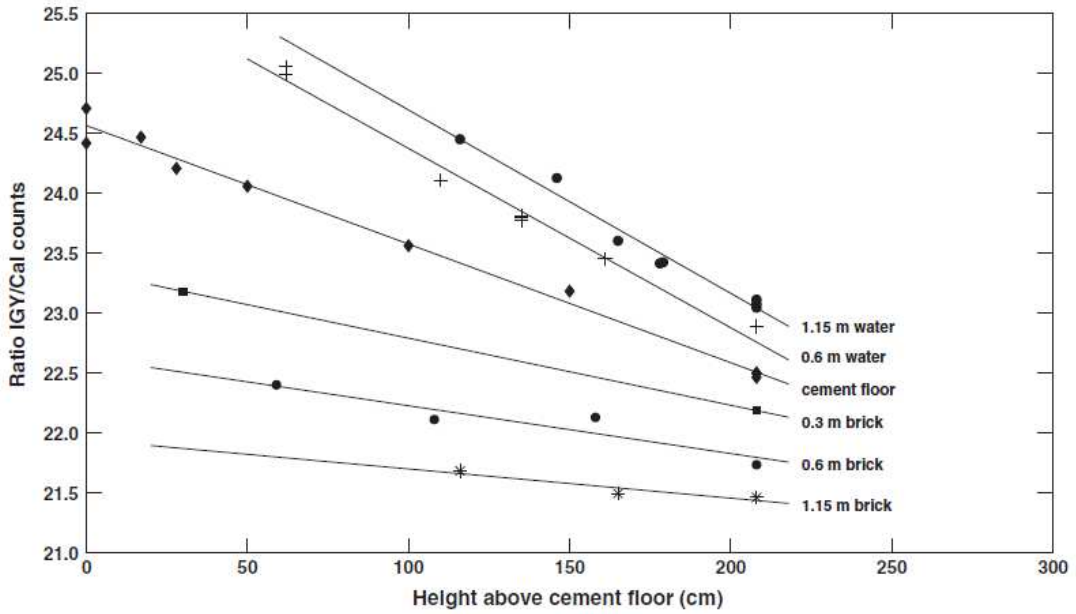


Figure 2.12: The ratio of the count rates of the IGY of Northwest University, Potchefstroom, South Africa and calibration neutron monitor as a function of the height of the calibration neutron monitor above a concrete floor, with different heights of water and brick underneath the calibrator. [Image credit: Krüger & Moraal (2010)]

2.3 Intercalibration of the World’s Neutron Monitors

Each neutron monitor (from the total of approximately 40 stations) in the worldwide network (see Figure 2.13) has its own detection efficiency and different design, in a different environment, at different cutoff rigidities and altitudes.

Bieber et al. (2003), Hatton & Carmichael (1964), Hatton (1971), Clem & Dorman (2000), Moraal et al. (2000), Stoker et al. (2000), and Krüger (2006) referred to the observed count rate, N , from neutron monitors as a function of geomagnetic cutoff rigidity, P_c :

$$N(P > P_c) = \int_{P_c}^{\infty} \left| \frac{dN}{dP} \right| dP, \tag{2.1}$$

$$-\frac{dN}{dP} = S(P, x)j(P, t), \tag{2.2}$$

where dN/dP is the differential response function, $S(P, x)$ is the yield function for secondary cosmic rays at atmospheric depth x and $j(P, t)$ is the galactic cosmic ray spectrum expressed as a function of rigidity P above the atmosphere.

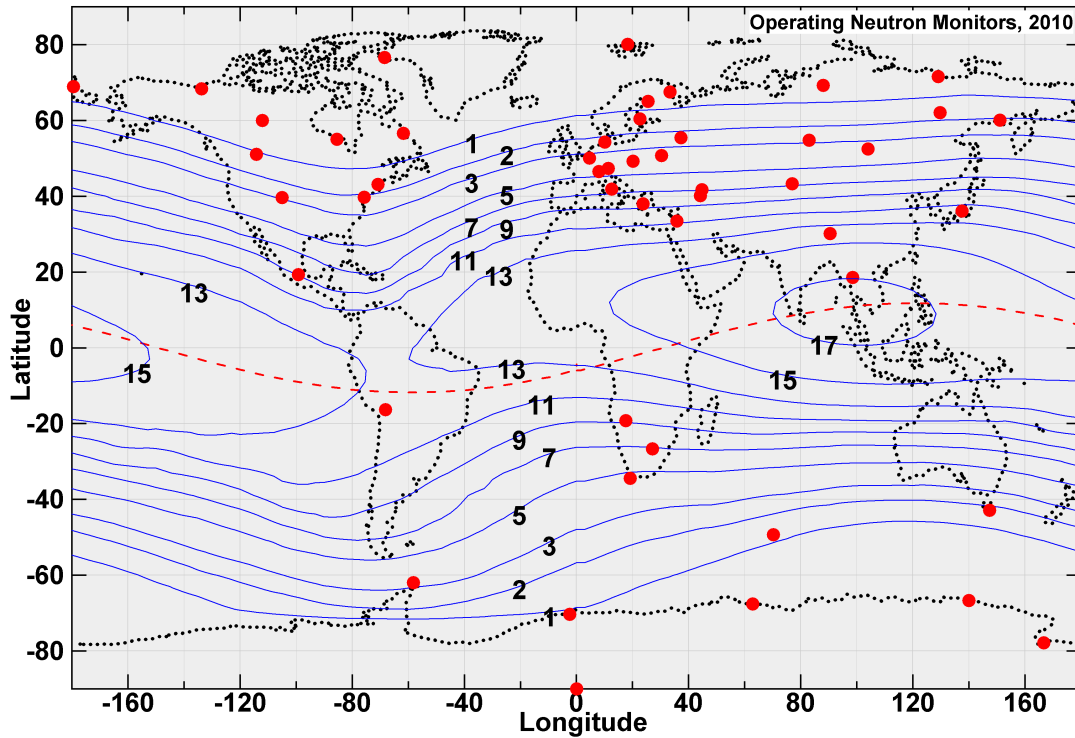


Figure 2.13: Operating neutron monitors in 2010 showing only stations (red solid points) that actively report data, including Doi Inthanon. [Modified from an image by Roger Pyle.]

In order to derive such a differential response function from the count rates of the world's stationary neutron monitors, they need to be intercalibrated accurately by some means. Krüger et al. (2008a) suggested that the differential response functions for deriving energy spectra from the worldwide stationary neutron monitor network can be calculated from the difference in count rates divided by the difference in cutoff rigidities:

$$\frac{dN}{dP} \approx \frac{N(P_{c2}) - N(P_{c1})}{P_{c2} - P_{c1}}, \quad (2.3)$$

where P_{c1} and P_{c2} are the cutoff rigidities at different stationary neutron monitors, and $N(P_{c1})$ and $N(P_{c2})$ are their observed counting rates.

For this purpose, two identical calibrators were designed to normalize the count rates. Figure 2.14 shows a hypothetical example of a differential response function obtained from 11 intercalibrated neutron monitors. The cutoff rigidity intervals increase in steps of 30%. The vertical error bars result from an assumed 0.2% uncertainty in the count rate of each individual neutron monitor.

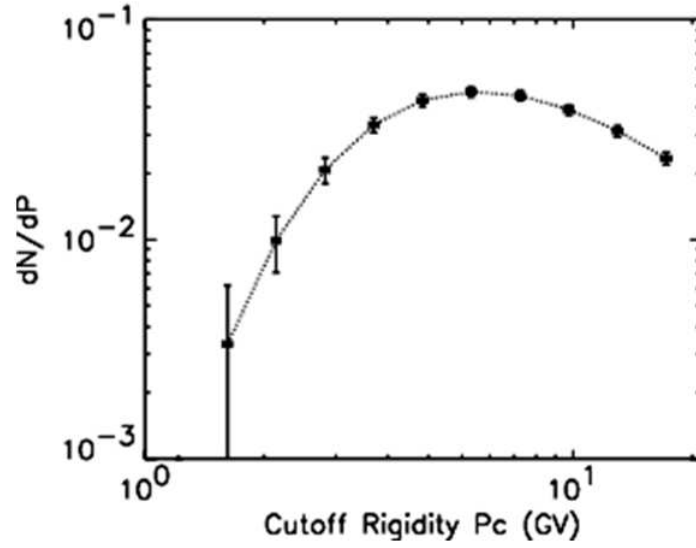


Figure 2.14: Hypothetical differential response function for 11 intercalibrated neutron monitors [Image credit: Krüger et al. (2011)]

Moraal et al. (2000) proposed that the residual uncertainties in this intercalibration are mainly due to (i) different designs of neutron monitors providing different responses to primary intensity variations, (ii) different responses of the monitors to atmospheric factors such as temperature and pressure, and (iii) different environments due to the inability to set the calibrator at the identical environment of the stationary neutron monitor.

Actually, there are several methods to derive a differential response function from the count rates. Apart from the intercalibration method mentioned above, there were airborne altitude and latitude surveys. Raubenheimer & Stoker (1974) analyzed the values of parameters to fit the count rate of a 3NM64 monitor during airborne trips throughout the atmosphere from the formula

$$N(P > P_0) = N_0[1 - \exp(-\alpha P_c^{-k})] \exp[\beta(p_s - p)], \quad (2.4)$$

where $N_0 = 125,000$ counts per hour, $\alpha = 10$, $k = 1.4 - 0.0006p$, p is pressure measured in mm Hg, $\beta = 1\% \text{ mm}^{-1}\text{Hg}$ and $p_s = 760$ mm Hg. The differential response function is

$$-\frac{dN}{dP} = N_0 \alpha k P^{-k-1} \exp(-\alpha P^{-k}) \exp[\beta(p_s - p)]. \quad (2.5)$$

The maximum value of this spectrum is at $P = [\alpha k / (k + 1)]^{1/k}$.

Furthermore, physicists also widely use ship-borne latitude surveys to derive such a differential response function. We will elaborate on this topic in Sections 2.4 and 2.5.

2.4 Ship-Borne Neutron Monitor

The University of Delaware Bartol Research Institute, the University of Tasmania, and the Australian Antarctic Division collaborated on annual latitude surveys from 1994 to 2007, including a solar minimum, a solar maximum and magnetic polarity reversal (2000), and a near return to solar minimum. The Australian contribution was primarily for equipment, while Bartol managed the operation and logistics. Both groups participated in initial scientific evaluation of the data. In this section, we aim to identify and describe not only the ship-borne neutron monitor but also the other main equipment to record necessary data to use in the analysis for the latitude survey, such as the TasVan, electronics of ship's log, data logger, climate control, BP-28 neutron detectors, Bartol electronics, digiquartz barometer(s), AIR barometer, clinometer assembly and GPS receivers.



Figure 2.15: Ship-borne neutron monitor (3NM64)

The ship-borne neutron monitor. The scientific instrument is a neutron monitor, technically known as a 3NM64 as shown in Figure 2.15 which we previously described in the “Neutron Monitor” topic of this chapter. The “3” refers to three neutron counters installed in the “TasVan” as shown in Figure 2.16. The ship-borne neutron monitor is also constructed from lead and polyethylene, with the neutron detectors inserted through the holes in the lead rings. The detectors are cylinders filled with BF_3 gas (enriched in the isotope ^{10}B). The ^{10}B nuclei react with neutrons and undergo nuclear fission. The resulting bursts of energy ionize the gas and eventually produce electrical pulses on a wire maintained at a potential of (typically) -2800 volts. These electrical pulses are counted by the electronics inside the TasVan.



Figure 2.16: The TasVan

TasVan. This is the insulated shipping container in which all equipment is housed. It conforms to all applicable standards and may be handled in any standard way. When moving with a fork lift, note that the load is unbalanced. For operation, the TasVan requires both 110 and 220 volt electric power and a supply of seawater for internal cooling.

Electronics of ship’s log. Racks inside the TasVan (see Figure 2.17)



Figure 2.17: Electronics racks. Most of the electronics are located in the rack adjacent to the onboard computer.

record all data automatically, along with the ship's position (derived from GPS receivers) and barometric pressure. Accurate position and pressure information is vital to the success of the experiment. The ship's log serves as a backup data source in case of failure of the automatic units.

University of Tasmania Data Logger. Located in the electronics rack (see Figure 2.17), the data logger records data from the detectors and one barometer in a solid-state memory. The logger has its own DC power supply. Data summaries from the logger appear on the computer display for diagnostic purposes. The one-second light should flash once per second in normal operation, with occasional longer flashes. If this light is not flashing, or if there is no recent transmission displayed on the screen of the computer, the "Reset" button should be pushed. If no lights flash when the reset button is pushed, check that power is reaching the unit from the power supply. No other field service is possible.

Climate Control. Automatic heating and cooling systems are installed

in the TasVan to maintain proper operating conditions for the equipment. Different systems are used during different parts of the voyage. The transfer of systems is typically made during port calls in Australia or New Zealand, both when entering and leaving Antarctic waters.

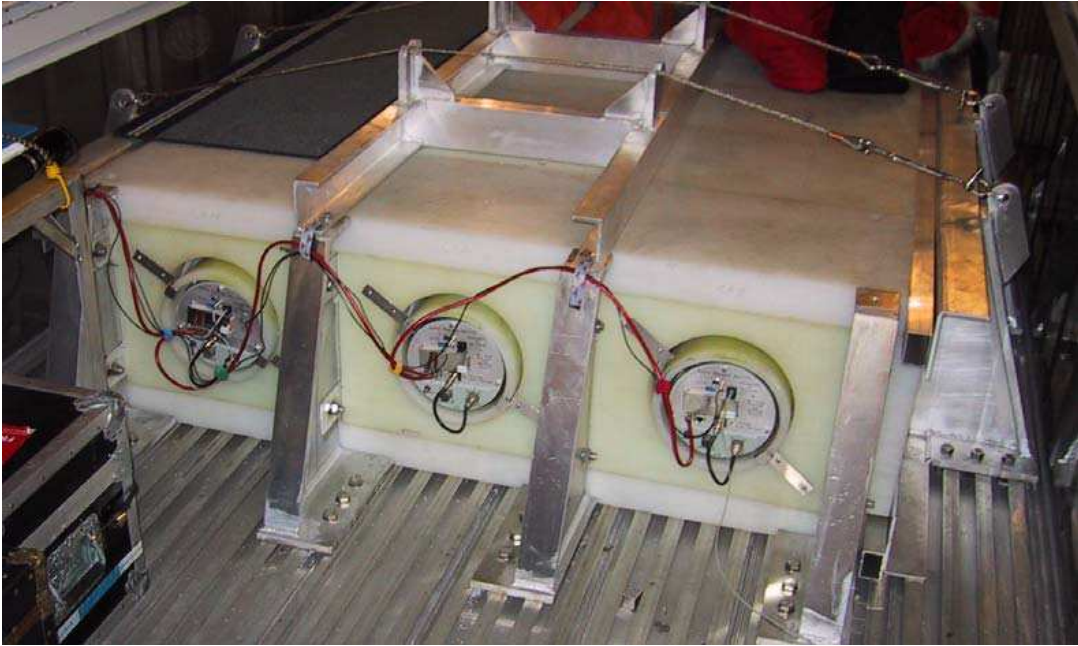


Figure 2.18: BP-28 (Chalk River) Neutron Detectors

BP-28 Neutron Detectors. BP-28 (Chalk River) neutron detectors (see Figure 2.18) are mounted in the NM64. Input is low voltage power to the electronics, with an internal supply generating -2800 volts (nominal) to the detector. Outputs are logic pulses, each of which corresponds to the detection of a single neutron. The units operate independently, so it is possible to disconnect an individual unit if a failure causes interference. Since the units are daisy-chained, such removal may require reconfiguration of the wiring. The logic pulses are counted by independent and redundant data acquisition systems (the logger and the Bartol electronics.)

Bartol Electronics. Card cage located in the electronics rack. Several printed circuit boards perform different functions, to produce a consolidated data stream for analysis by the computer. They are powered from the low voltage supply. To reset, cycle the power.

Digiquartz Barometer(s). Mounted on boards in the Bartol electronics. One or two units may be installed. The output consists of two square-wave signals, with

frequencies related to the barometric pressure and operating temperature by a complex formula. The outputs are sent redundantly to the logger and the Bartol electronics.

AIR Barometer. Located in the electronics rack. Output is a digitally coded signal giving barometric pressure. Powered and read by the Bartol electronics.

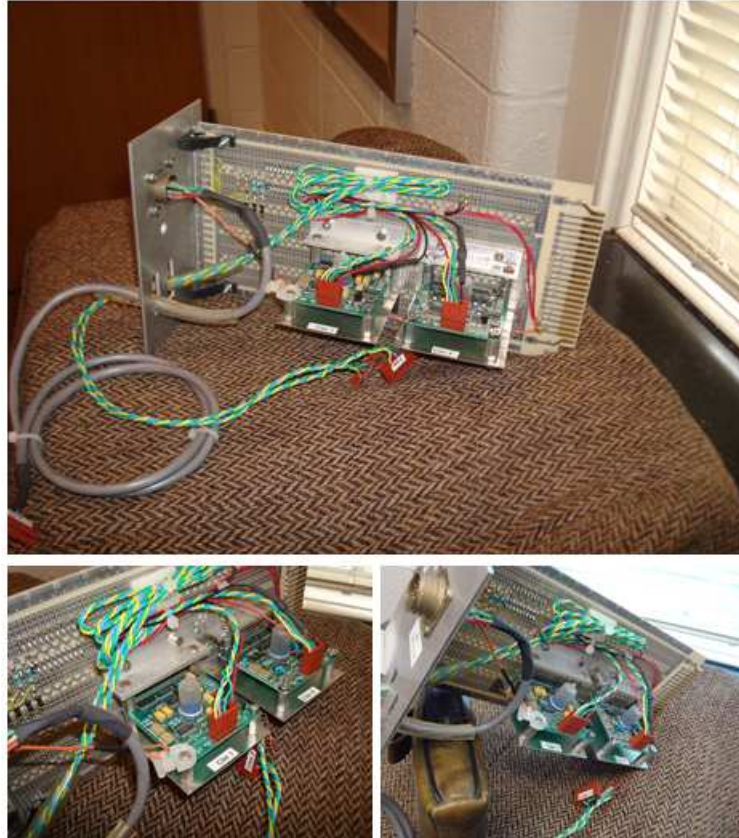


Figure 2.19: Clinometer Assembly

Clinometer Assembly. Redundant sensors are located on a board in the Bartol electronics. Output of each sensor is three analog signals giving inclination on two axes and unit temperature. The values shown on the display are uncalibrated engineering units. Figure 2.19 (upper panel) provides an overview. Figure 2.19 (lower left and lower right) aims to show how the liquid surface in the little volumes stays horizontal when the clinometer assembly is tilted.

GPS Receivers. Two are mounted in the rack to furnish data to the consolidated data stream. The most recent record read from each is always displayed on the PC screen. The last valid position from each is displayed in a separate location on the PC screen. Another GPS receiver is located in the calibration monitor. Antennae

are mounted on the forward bulkhead of the TasVan. The antennae are all identical, and may be interchanged if necessary for troubleshooting.

2.5 Latitude Surveys

Moraal et al. (1989), Dorman et al. (2000), and Bieber et al. (2003) defined that a neutron monitor latitude survey is transported with a transportable neutron monitor or mobile neutron monitor that records count rates through a range of cutoff rigidities as rapidly as possible. Clem (1999) note that the count rate of a neutron monitor relates to the primary cosmic ray particles which are not rejected by the geomagnetic field entering the atmosphere and undergoing multiple interactions resulting in showers of secondary particles that can reach ground level and can be detected by a neutron monitor. Stoker & Moraal (1995), Clem et al. (1997), and Bieber & Evenson (1995) suggested that oblique particles may be responsible for certain anomalies in neutron monitor latitude surveys because the geomagnetic cutoff varies with direction of incidence, so obliquely incident particles must be included to eliminate systematic errors in latitude surveys. The variation in count rate of the neutron monitor as a function of geomagnetic cutoff rigidity permits a measurement of the cosmic ray spectrum (integrated over particle type) at energies where direct spacecraft measurement is difficult or impossible due to the limit of detector size. Observed deviations from perfect ordering of the data by the calculated cutoff rigidity may be used to produce refined models of the magnetic field of the earth. Bieber et al. (2004) described that for precise determination of particle anisotropies and spectra, it is necessary to understand the neutron monitor energy response or yield function, the relationship between the observed count rate and the energy-dependent flux of cosmic rays at the top of the atmosphere, and the spectrum of galactic cosmic ray primaries in space. Moraal et al. (1989) and Bieber et al. (1997) indicated that the product of the yield function and the spectrum of galactic cosmic ray primaries is obtained from a latitude survey.

There are two techniques in this research to characterize the evolution of the galactic primary cosmic ray spectrum. These are the Dorman technique and Nagashima technique.

The Dorman technique uses a parameterized function of apparent geomag-

netic cutoff, the Dorman function,

$$N = N_0(1 - e^{-\alpha P_c^{-\kappa}}), \quad (2.6)$$

where N_0 , α , and κ are free parameters. Although this parameterization has no physical content, it provides an excellent representation of the integral response function N and can be differentiated to determine the DRF:

$$N = \int_{P_c}^{\infty} (DRF) dP \quad (2.7)$$

$$DRF = N_0 \alpha P^{-\kappa-1} \kappa (e^{-\alpha P^{-\kappa}}), \quad (2.8)$$

We can see an example result of Dorman fitting of latitude survey data from Figure 1.5.

The Nagashima technique was proposed to us by Prof. Paul Evenson, to make use of the approach of Nagashima et al. (1989) that the best fit to latitude survey data could be obtained by considering accurate parameterization of 3 functions. These are the heliospheric modulation (M), the local interstellar galactic cosmic ray spectrum (G), and yield function (Y). The response function is the product of these three terms as

$$R = - \left[\frac{dN}{dP_c} \right]_P = G(P)M(P, t)Y(P, h). \quad (2.9)$$

The Galactic cosmic ray spectrum (G -function)

The galactic cosmic ray spectrum $G(P)$ is the unmodulated energy spectrum of galactic cosmic rays, which is assumed to be time invariant and a function only of rigidity (momentum per unit charge). We use a functional form for the unmodulated differential rigidity spectrum of galactic cosmic rays expressed in terms of the total energy (U) of cosmic rays:

$$G(u, \gamma_n) = \frac{\gamma_1}{(\gamma_2 + u)^{\gamma_3}}, \quad (2.10)$$

or

$$G(u, \gamma_n) dU = \frac{\gamma_1}{(\gamma_2 + u)^{\gamma_3}} dU, \quad (2.11)$$

in which $u = U/U_0$, U_0 is the rest energy, and γ_1 to γ_3 are nonnegative parameters that do not depend on depth in the atmosphere, h .

In Figure 2.20, we can model G with the following equation:

$$G(u) du = \frac{\gamma_1(h)}{(0.0 + u)^{2.58 \pm 0.004}} du, \gamma_1(0) = (1.2 \pm 0.02) \times 10^4. \quad (2.12)$$

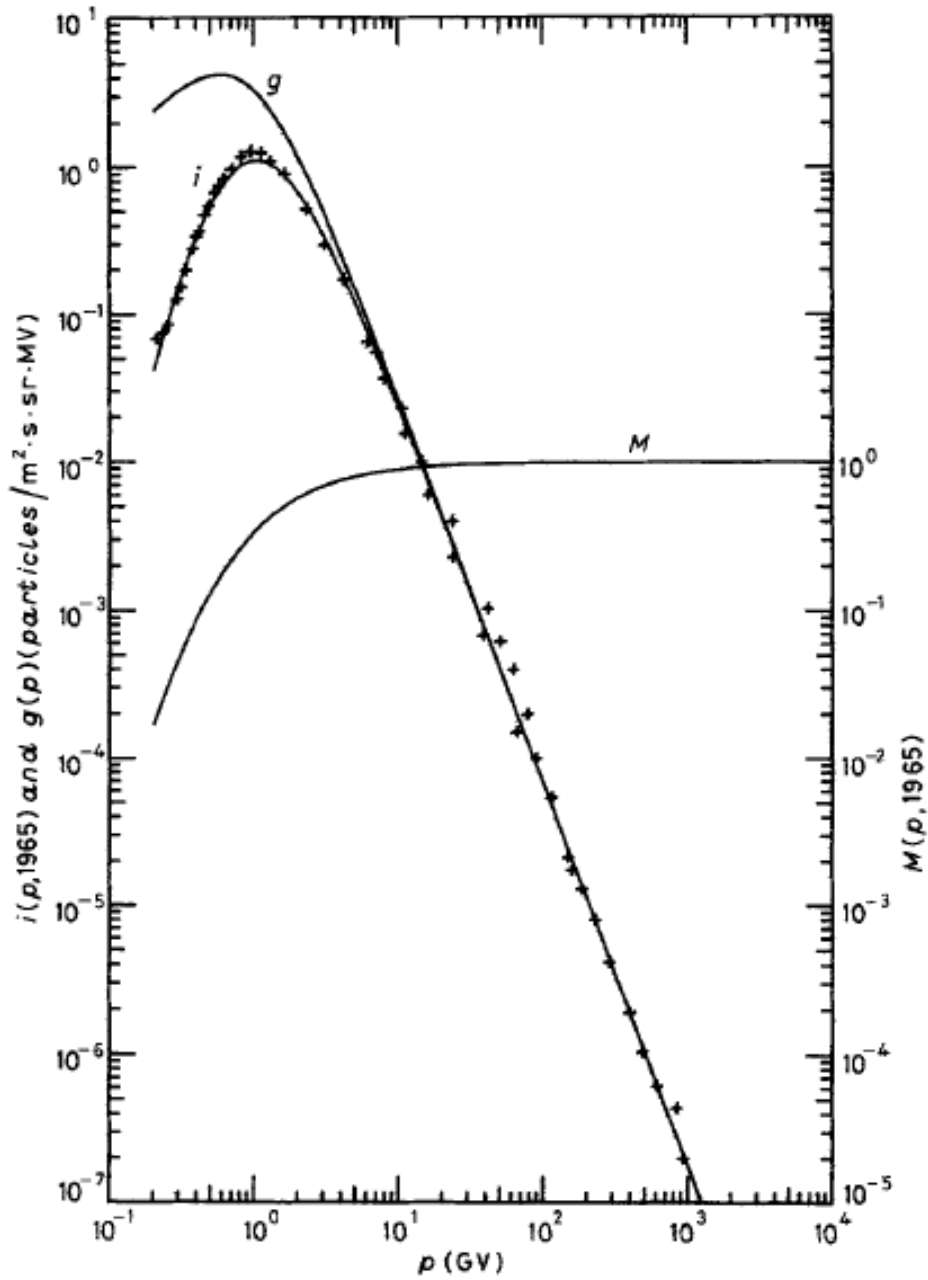


Figure 2.20: Differential rigidity spectrum of galactic cosmic rays, primary proton flux and modulation function in 1965. Observed points are those compiled by Webber & Lezniak (1974). These data were originally presented by Ormes & Webber (1965), Fan et al. (1966), Anand et al. (1968), von Rosenvinge et al. (1969), Ryan et al. (1972) and Smith et al. (1973). [Image credit: Nagashima et al. (1989)]

From Eq. (2.12), $G(u)$ has a power-law spectrum with the exponent of 2.585, which nearly coincides with the primary-proton results of other reports.

The yield function (Y -function)

The yield function Y is the relationship between the observed count rate and the energy-dependent flux of cosmic rays at the top of the atmosphere. It is a function of cutoff rigidity (P_c) and atmospheric depth (h). For the yield function, we assume an analytical formula expressed in terms of the total energy (U) and atmospheric depth (h), as

$$Y(U, h, \varepsilon, \eta_n) = Y_0 u^\varepsilon \exp \left[-\eta_1 \left(\frac{h}{1033} \right)^{\eta_2} - \eta_3 \left(\frac{h}{1033} \right)^{\eta_4} k_l(u, \eta_5) \right], \quad (2.13)$$

where

$$k_l(u, \eta_5) = k_1(u, \eta_5) = (u - 1)^{-\eta_5}, \quad (2.14)$$

$$k_l(u, \eta_5) = k_2(u, \eta_5) = (\ln u)^{-\eta_5}, \quad (2.15)$$

and Y_0, ε and η_n 's are nonnegative parameters. Y_0 is set to unity, as it is multiplied by the free parameter γ_1 in eq. (2.12). The value of the exponent ε in eq. (2.13) is expected to be less than 0.3.

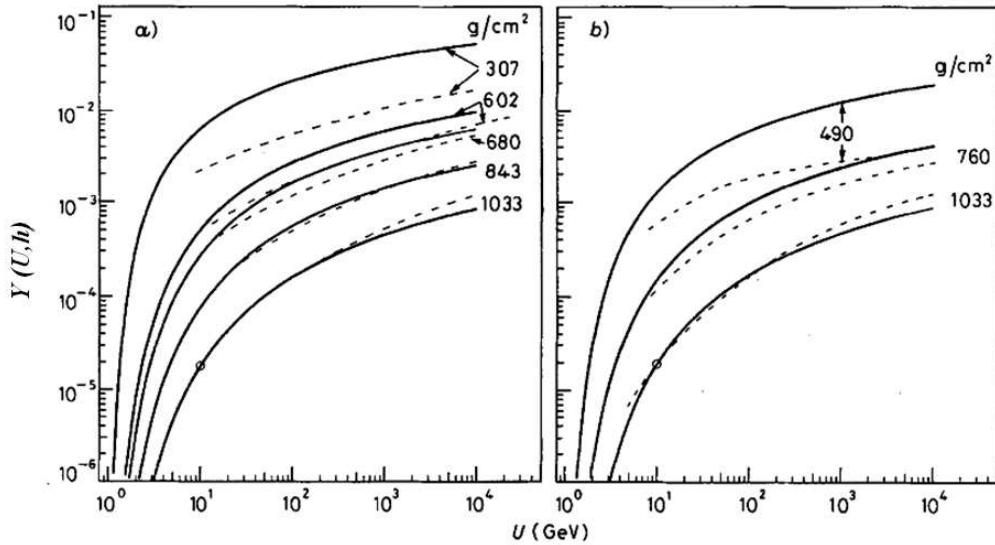


Figure 2.21: *a)* Comparison of $Y(U, x)$ with theory. Solid lines express the simulated experimental data of $Y(U, x)$ with $h_2(U, \eta_5)$ in eq. 2.15 and dashed lines are theoretical curves estimated by Murakami (1989) in private communication. Theoretical and experimental curves are normalized at $h = 1033 \text{ g/cm}^2$ and $U = 10 \text{ GeV}$. *b)* The same as in *a)* except that dashed lines are theoretical curves obtained by Dorman & Yanke (1981). [Image credit: Nagashima et al. (1989)]

Nagashima et al. (1989) determined Y as follows:

$$Y(U, h) = u^{0.0 \pm 0.1} \exp \left[- (2.2 \pm 2.5) \left(\frac{h}{1033} \right)^{1.62 \pm 0.96} - \frac{12.7 \pm 5.6}{(\ln u)^{0.42 \pm 0.21}} \left(\frac{h}{1033} \right)^{0.50 \pm 0.09} \right] \quad (2.16)$$

Modulation function (M -function)

The modulation function M as a function expresses the status of the diffusion and convection of cosmic rays in interplanetary magnetic fields. Consider a spherically symmetric model of the interplanetary medium in which the solar wind radially carries magnetic irregularities, which cause perfect elastic scattering of cosmic rays in a frame of reference moving with the solar wind.

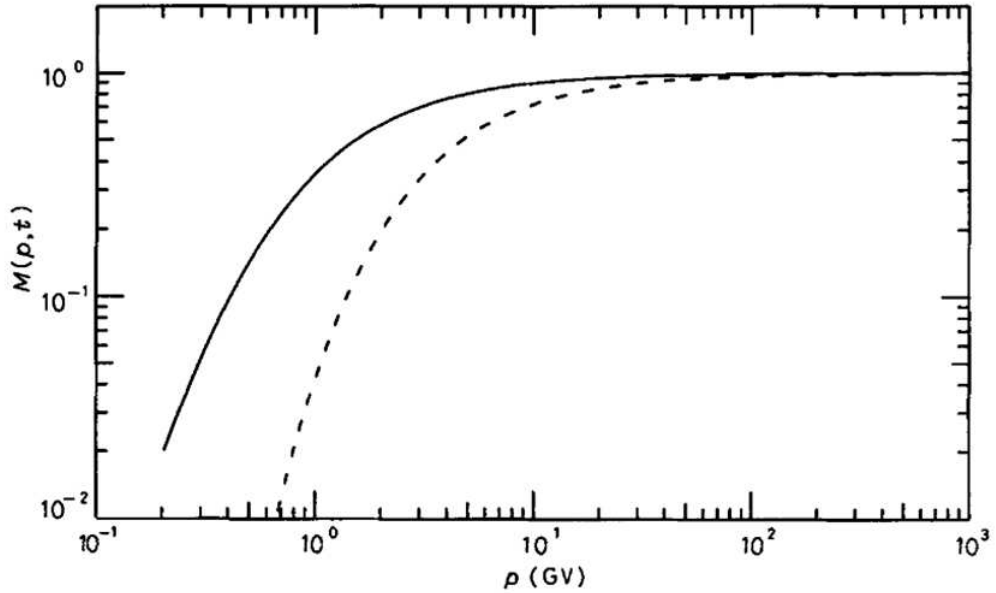


Figure 2.22: Rigidity dependence of the modulation function $M(p, t)$ near the maximum (dashed line, $J_{MtW}=1990$) and minimum solar activity (solid line, $J_{MtW}=2465$) [Image credit: Nagashima et al. (1989)]

From Figure 2.22 shows the rigidity dependence of the modulation function for periods of the maximum and minimum solar activity. The general expression of M is given by

$$M(P_c, t) = \exp \left[\frac{-\mu_1(t)}{\mu_2 + (P_c/1 \text{ GV})^{\mu_2}} \right], \quad (2.17)$$

An analytical expression of M is given by

$$M(P_c, t) = \exp \left[\frac{-\mu_1(t)}{(0.097 \pm 0.009) + (P_c/1 \text{ GV})^{1.02 \pm 0.02}} \right], \quad (2.18)$$

where $\mu_1(t)$ is a function of other parameters and variables and is recomputed according to

$$\mu_1(t) = \mu_4 + \mu_5 \left(1 - \frac{J_{MtW}(t)}{J_{MtW}(t_{max})} \right)^{\mu_6} \quad (2.19)$$

when $J_{MtW}(t)$ is neutron intensity at Mt. Washington at any time and $J_{MtW}(t_{max})$ is neutron intensity at Mt. Washington at solar maximum. Here we use $J_{MtW}(t_{max}) = 1990$ counts/hour and $t_{max} = 1965$ AD. Nagashima et al. (1989) determined optimal parameters as shown in the following equation:

$$\mu_1(t) = (1.15 \pm 0.02) + (14.9 \pm 0.8) \left(1 - \frac{J_{MtW}(t)}{J_{MtW}(t_{max})} \right)^{1.12 \pm 0.03} \quad (2.20)$$

On the basis of Nagashima analysis, it is considered that the response function $R(P_c, h, t)$ as a product of these three terms (G , Y , and M) defined in eq. 2.9 would be reasonable or at least more appropriate than the others, especially in the low atmosphere. Using eqs. (2.12), (2.16), and (2.18)-(2.20), we can estimate the response function $R(P_c, h, t)$ at any time and at any depth greater than 307 g/cm^2 .

2.6 Forbush Decreases

A ‘‘Forbush Decrease’’ means a transient and rapid decrease in the number of galactic cosmic rays reaching the Earth, which is usually observable by a neutron monitor within a few days after an explosion at the Sun (solar storm) that releases a large amount of mass with high velocity, known as a coronal mass ejection (CME). Figure 2.24 shows a photograph captured from a video of an actual CME that blasted off from the Sun on January 27, 2012. A Forbush decrease occurs because the magnetic field of the CME sweeps some of the galactic cosmic rays away from Earth. Forbush decreases were first described in 1937 by an American physicist named Scott Ellsworth Forbush (1904-1984). Barnden (1973) investigated models of Forbush decreases. Some of the models concentrated on enhanced drift while other models focused on diffusion of scattering models; however, both of them reinforce that the magnitude of the Forbush decrease is proportional to the magnetic intensity and magnetic irregularities caused by the associated interplanetary space disturbances. Cane (2000) explained that there can be two steps of Forbush decreases caused by shocks and by CMEs. The first step involves the turbulent structure behind the shock and the second step involves the enhanced magnetic field and loop-like field configuration of the CME.

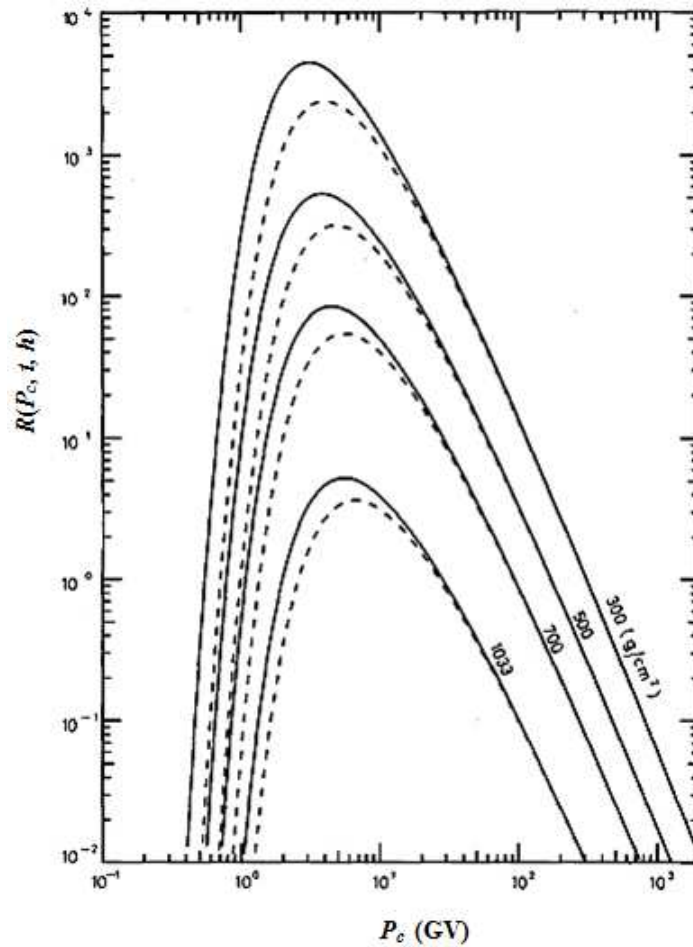


Figure 2.23: Differential response function $R(P_c, h, t)$ of a neutron monitor for several atmospheric depths in the periods of maximum and minimum solar activity. Figures attached to each curve express the atmospheric depth h in g/cm^2 . Solid lines are for minimum solar activity ($J_{MtW}=2465$), dashed lines are for maximum solar activity ($J_{MtW}=1990$). [Image credit: Nagashima et al. (1989)]

Figure 2.25 shows the “modulation level” (the McMurdo count rate scaled to resemble J_{MtW} , a Mt. Washington count rate) vs. time. For the survey the modulation range was so small that it seemed sufficient just to use a scaled McMurdo rate in place of Mt. Washington. This is a good example to demonstrate clearly that during DOY 340 to 359 of the 2006-2007 voyage in latitude survey data (the data set used in this research) there were a first step and second step of the Forbush decrease.



Figure 2.24: A photograph of a CME taken by the SOHO spacecraft [Taken from <http://www.nasa.gov>]

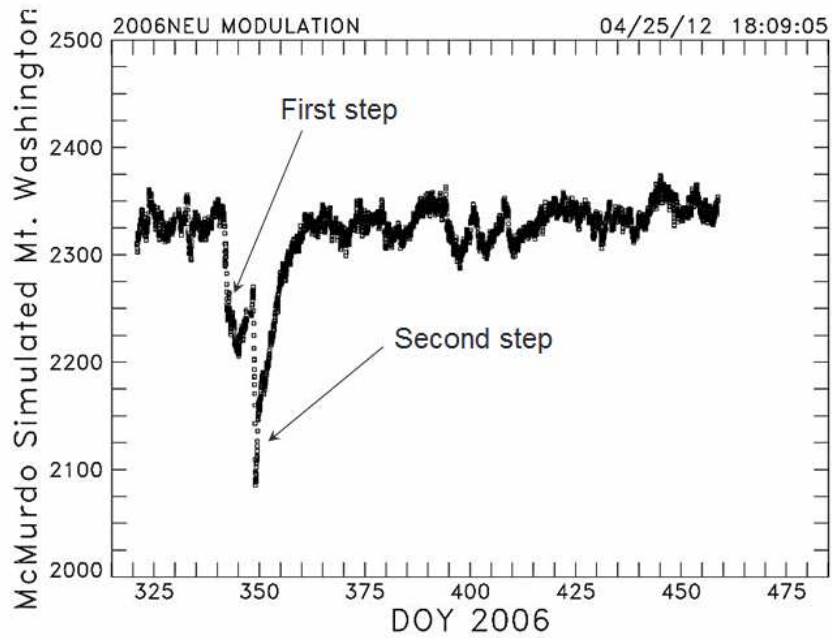


Figure 2.25: Graph of modulation level as a function of time to demonstrate explicitly both first step and second step of Forbush decreases during DOY 340 to 359 of 2006-2007 voyage of latitude survey data

CHAPTER III

EFFECTS OF THE ENVIRONMENT ON THE COUNT RATE OF A CALIBRATION NEUTRON MONITOR AT DOI INTHANON

A neutron monitor is a standard ground-based instrument for measuring time variations of Galactic cosmic rays (GCRs) by detecting secondary particles (mostly neutrons) from their atmospheric showers. Using the Earth as a magnetic spectrometer, to a good approximation cosmic rays can reach a given location on Earth only if their rigidity (related to momentum per charge) exceeds the local geomagnetic cutoff rigidity. Ideally, simultaneous measurements from different stations in the worldwide neutron monitor network with various cutoff rigidities could be combined to determine the GCR spectrum continuously as a function of time (Moraal et al. 2000; Krüger & Moraal 2010). However, such a comparison requires an accurate intercalibration between the stations, to $\sim 0.2\%$. The yield function (efficiency) of neutron monitors is not completely understood, and is expected to depend on the number of counter tubes, configuration, and building or structure within which the neutron monitor is housed. While much interesting science can be done without precise knowledge of the yield function, a neutron monitor will become a more powerful instrument when its yield function is fully understood, and then data from the worldwide network of neutron monitors could be combined to precisely track the GCR spectrum.

In this work, we report on an advance toward these goals by making use of a relatively portable calibration neutron monitor or “calmon” (Krüger et al. 2008b), shown in Figure 3.1, in conjunction with the *Princess Sirindhorn Neutron Monitor* (PSNM) at the summit of Doi Inthanon, Thailand’s highest mountain. PSNM, with an 18-tube NM64 neutron monitor (18NM64), has the world’s highest geomagnetic cutoff rigidity for a fixed station (16.8 GV vertical cutoff) and is therefore of particular importance to anchor the high end of the GCR spectrum as inferred from neutron monitor data. Figure 3.2 shows a simple floor plan sketch of the 18NM64 inside and calmon outside of



Figure 3.1: Photograph of the calmon during testing inside the PSNM building at Doi Inthanon, Thailand

the PSNM building. In the measurements reported here, we have calibrated the PSNM count rate relative to the calmon, thereby relating its station-specific count rate to other stations around the world that have been or will be similarly calibrated.

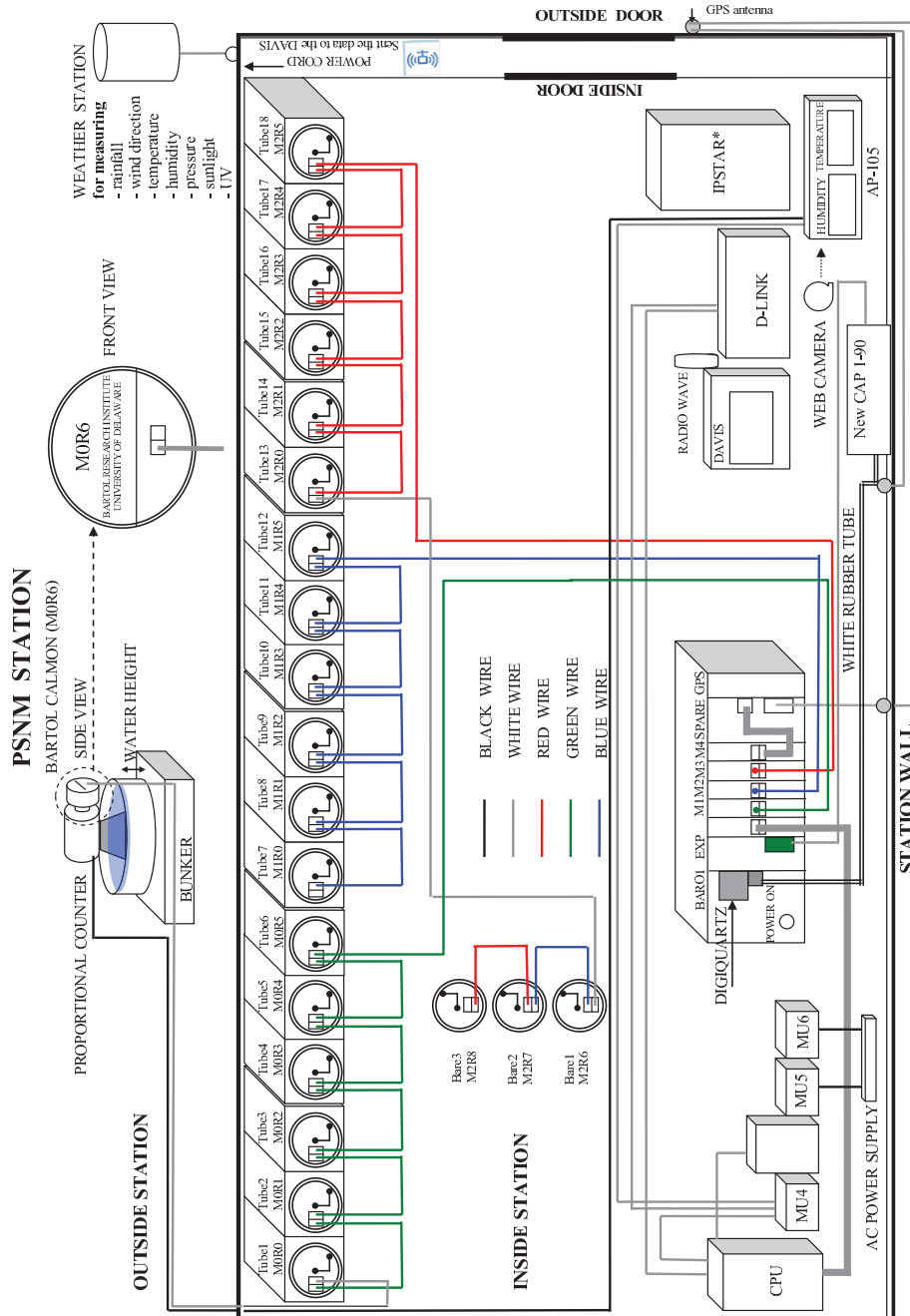


Figure 3.2: Simple floor plan sketch with wiring connections of 18NM64 and calmon at PSNM, Doi Inthanon, Thailand during November, 2009 – June, 2010

3.1 Detection Equipment and Observations

The calmon used in this work is relatively compact, with a length of 753 mm and a mass of 223 kg (including the cradle), allowing it to be transported to various locations around the world. Figure 3.1 shows a photo of the calmon during deployment inside the PSNM building at Doi Inthanon, Thailand. The innermost component is an LND25382 proportional counter tube (manufactured by LND, Inc.) of 51 mm diameter filled with 4 atm of ^3He (97%) and CO_2 quench gas (3%), in which neutrons can be detected by means of the reaction $^3\text{He}(n,p)^3\text{H}$. This is surrounded by a cylindrical polyethylene moderator of 39 mm thickness. The lead producer comprises 7 rings that together form a cylinder of 92 mm thickness. Atmospheric secondary cosmic rays of various species can interact in the lead to produce spallation neutrons that are then detected in the ^3He counter. (The detector response is predominantly due to sub-GeV atmospheric neutrons.) Finally the outermost cylinder is a polyethylene reflector of 156 mm that serves to block most neutrons in the MeV-range or lower produced in the calmon's surroundings, and also helps trap neutrons from the lead producer. At Doi Inthanon a typical count rate was ≈ 3.5 Hz.

The PSNM station, at the summit of Doi Inthanon, is located at geographic coordinates 18.59°N and 98.49°E, at an altitude of about 2,560 m. It is inside a Royal Thai Air Force base, in a wide fenced area with restricted access, so the configurations were quite stable with time. The building, indicated in Figure 3.3(a), has an area of $10 \times 10 \text{ m}^2$ and two metal roof panels inclined at 45°. There are also inner vertical walls and ceiling of concrete that define a smaller rectangular enclosure. The main neutron monitor contains 18 counter tubes in one continuous row, with the standard NM64 design (Hatton & Carmichael 1964) that includes lead producer (29 tons) and polyethylene moderator and reflector. A typical count rate is ≈ 34 Hz per tube. The building also houses 3 bare neutron counters, each with moderator but no producer or reflector, which are also visible in Figure 3.3(b) and count ≈ 6 Hz per tube. The count rates of tubes in the neutron monitors are higher than those of bare tubes, mainly because the lead producer can generate multiple neutrons from a single incident atmospheric secondary particle. Data from the three bares were not used for the present study.

Based on prior experience using the calmon in other locations, it was suggested that the calmon should be operated over a pool of water, to provide a standard

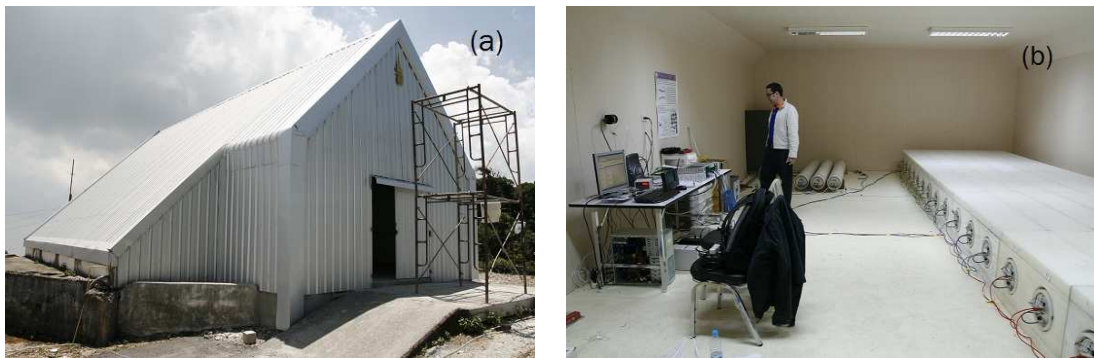


Figure 3.3: Photographs of (a) the PSNM building, with two metal roof panels inclined at 45° , and inner vertical walls and a ceiling of concrete that define a smaller rectangular enclosure, and (b) the interior of the PSNM building.

surface underneath, and in open atmosphere, far away from any structures that absorb or produce structures (Krüger & Moraal 2010). In practice, the latter requirement is expressed as a need to avoid any obstructions higher than 20° above the horizon. At Doi Inthanon, a site meeting these requirements was found on top of a bunker a few meters high, located a few meters south of the PSNM building and down a rocky incline. This allowed a power cable and data cable to be connected to the building and the data acquisition computer within. A portable swimming pool with a wire framework and vinyl lining, provided with the calmon, was set up and filled with water to the desired height. The calmon cradle was placed on 4 concrete pillars in the center of the swimming pool, keeping the calmon itself above the water level.

The calmon was operated inside or near the PSNM station during November, 2009 to June, 2010. This time period corresponded to solar minimum conditions, and indeed our observations started near the time of the highest cosmic ray rates ever recorded in the space age (Mewaldt et al. 2010). In the present work, we focus on the relative count rates of the calmon and PSNM, hereafter called the “Cal/NM” ratio, and we did not find evidence for a time dependence of this ratio over the 7-month duration of the observations.

The minimum requirement for the calibration is to acquire 10^6 counts, which required only about 4 days of data taking at our high altitude location. Therefore, we also took the opportunity to measure the difference in the count rate ratio for the calmon outside or inside the building, and for different environmental conditions outside, where we varied the height of the calmon (the underside of the reflector) above the bottom of

the pool, which we call “calmon height,” and also varied the water height. We operated for a total of 15 configurations, but there were technical difficulties with Configurations 7 and 14, so these are not included in Table 3.1 and those data were not analyzed.

An important component of the calmon is the electronics head (including a cylindrical metal cover) attached directly to the front. In these observations, we employed 3 different sets of electronics. We used two different pre-amplifiers (attached to the counter tube) with an electronics head made at North-West University, S. Africa specifically for the calmon. We refer to the two combinations of pre-amplifier and electronics head as the NWU1 and NWU2 electronics. We also used a remote electronics head made by the Bartol Research Institute, University of Delaware, USA, which we refer to as the BRI electronics. Table 3.1 specifies which electronics were used for each configuration.

3.2 Data Analysis

3.2.1 Calmon Data

Operating in the outdoor location with tropical heat and humidity posed technical challenges for the electronics. Fortunately, the NWU1 and NWU2 electronics recorded data with a cadence of 1 s, allowing individual seconds to be rejected as necessary. While the standard count rate was 3.5 Hz, the NWU1 electronics recorded 1 to 2 s of noise (>10 counts) with a period of about 10 s, especially during time periods with direct sunlight. Therefore, an individual 1-s record was rejected if there were >10 counts in that record and also in a record 9, 10, or 11 s earlier or later. A record was also rejected if the temperature or voltage value was abnormal. During some hours, typically during daytime, up to 20% of the records were rejected for these reasons. For the NWU2 electronics, the noise period was about 5 s, and the same rejection logic could be applied, resulting in rejection of up to 40% of the records. While the hourly Cal/NM ratio was extracted for both the NWU1 and NWU2 electronics, the NWU2 data are considered to be less reliable. The hourly ratio for these electronics was corrected for the temperature of the counter tube (not the temperature of the electronics), which varied over 10 to 30°C. The data were corrected to removed a positive correlation with temperature of

0.04% C⁻¹, correcting to a standard counter temperature 24°C as follows:

$$N_T = N_0 e^{-0.0004 \times (T-24)} \quad (3.1)$$

In this case, N_T is the count rate corrected for temperature, N_0 is the secondly average count rate in one hour and T is the temperature.

The BRI electronics were designed for indoor use but nevertheless we made use of them in the extreme outdoor heat. Because the standard count rate output did not function properly for an electronics temperature $T > 60^\circ\text{C}$ was measured in the electronics head, and the PH data were found to be unusable for an hour with electronics temperature $T > 51^\circ\text{C}$ and for 2 hours afterward. This problem did not arise for observations with the calmon inside the building. For the BRI electronics, we did not find a significant correlation of the Cal/NM ratio with counter temperature and did not perform a temperature correction.

Table 3.1: List of all configurations of the calmon at Doi Inthanon, Thailand

| Config-uration | Calmon Height (cm) | Water Height (cm) | Start DOY | Start hour (UT) | Stop DOY | Stop hour (UT) | Electronics | Cal/NM | S.E. | N |
|----------------|--------------------|-------------------|-----------|-----------------|----------|----------------|-------------|----------|----------|------------|
| C1 | 140 | 0 | 2009/327 | 11 | 2009/341 | 03 | NWU1 | 0.005710 | 5.51E-06 | 2,965,581 |
| C2 | 140 | 50 | 2009/342 | 01 | 2009/349 | 03 | NWU1 | 0.005635 | 6.07E-06 | 1,982,671 |
| C3 | 140 | 68 | 2009/349 | 08 | 2009/357 | 06 | NWU1 | 0.005622 | 5.59E-06 | 2,111,037 |
| C4 | 140 | 25 | 2009/357 | 07 | 2009/362 | 02 | NWU1 | 0.005659 | 6.88E-06 | 1,268,646 |
| C5 | 70 | 0 | 2009/362 | 08 | 2010/005 | 01 | NWU1 | 0.005744 | 7.18E-06 | 2,172,952 |
| C6 | 70 | 60 | 2010/008 | 11 | 2010/017 | 04 | NWU1 | 0.005505 | 5.48E-06 | 2,275,589 |
| C8 | 70 | 65 | 2010/042 | 07 | 2010/079 | 01 | BRI | 0.005546 | 2.10E-06 | 11,058,422 |
| C9 | 70 | 65 | 2010/098 | 08 | 2010/110 | 08 | NWU1 | 0.005506 | 4.35E-06 | 2,677,387 |
| C10 | 70 | 65 | 2010/112 | 05 | 2010/127 | 05 | NWU2 | 0.005637 | 5.67E-06 | 2,759,291 |
| C11 | 70 | 50 | 2010/127 | 06 | 2010/132 | 01 | NWU2 | 0.005771 | 1.15E-05 | 899,003 |
| C12 | 70 | 25 | 2010/132 | 01 | 2010/155 | 02 | NWU2 | 0.005695 | 5.57E-06 | 4,542,313 |
| C13 | 70 | 0 | 2010/155 | 04 | 2010/158 | 04 | NWU2 | 0.005756 | 1.47E-05 | 645,102 |
| C15 | 55 | 0 | 2010/162 | 07 | 2010/179 | 02 | BRI | 0.005722 | 2.80E-06 | 5,468,561 |



Figure 3.4: Calmon outside the PSNM building

For all configurations listed in Table 3.1, the Cal/NM ratio was determined for each hour of usable data, and these were used to determine the average value and uncertainty (standard error) of the ratio for each configuration. All usable configurations were outdoors (as in Figure 3.4), except for Configuration 15, for which the calmon was inside the PSNM building (as in Figure 3.1). Results for the 3 sets of electronics can be directly compared for configurations 8 to 10, for which data were taken in succession with no changes to the calmon height and water height. The three measurements of Cal/NM have a spread of 2.4%, compared with a maximum standard error of 0.1% for individual measurements. We found no significant effect of atmospheric pressure on the Cal/NM ratio, i.e., the calmon and PSNM seem to have the same barometric coefficient to within measurement uncertainty. Thus the Cal/NM ratio has not been corrected for atmospheric pressure. The results of the data for all configurations are shown in Figures 3.5-3.30, except for Configurations 7 and 14, and Figure 3.31 shows the corrected ratios for all configurations except Configurations 7 and 14, where the error bars represent standard errors.

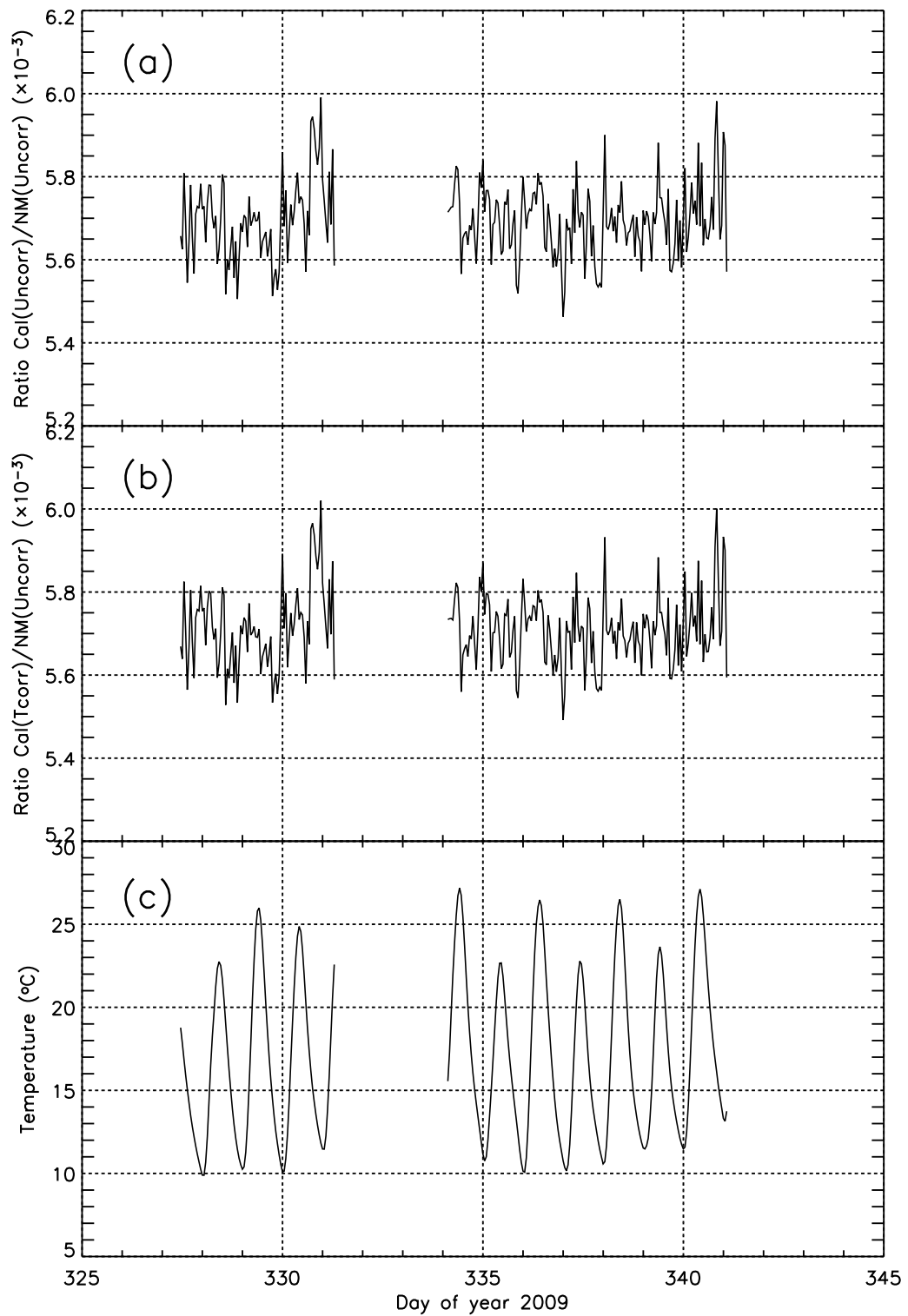


Figure 3.5: The results as a function of time of C1: (a) uncorrected Cal/NM ratio, (b) corrected ratio, (c) calmon counter temperature.

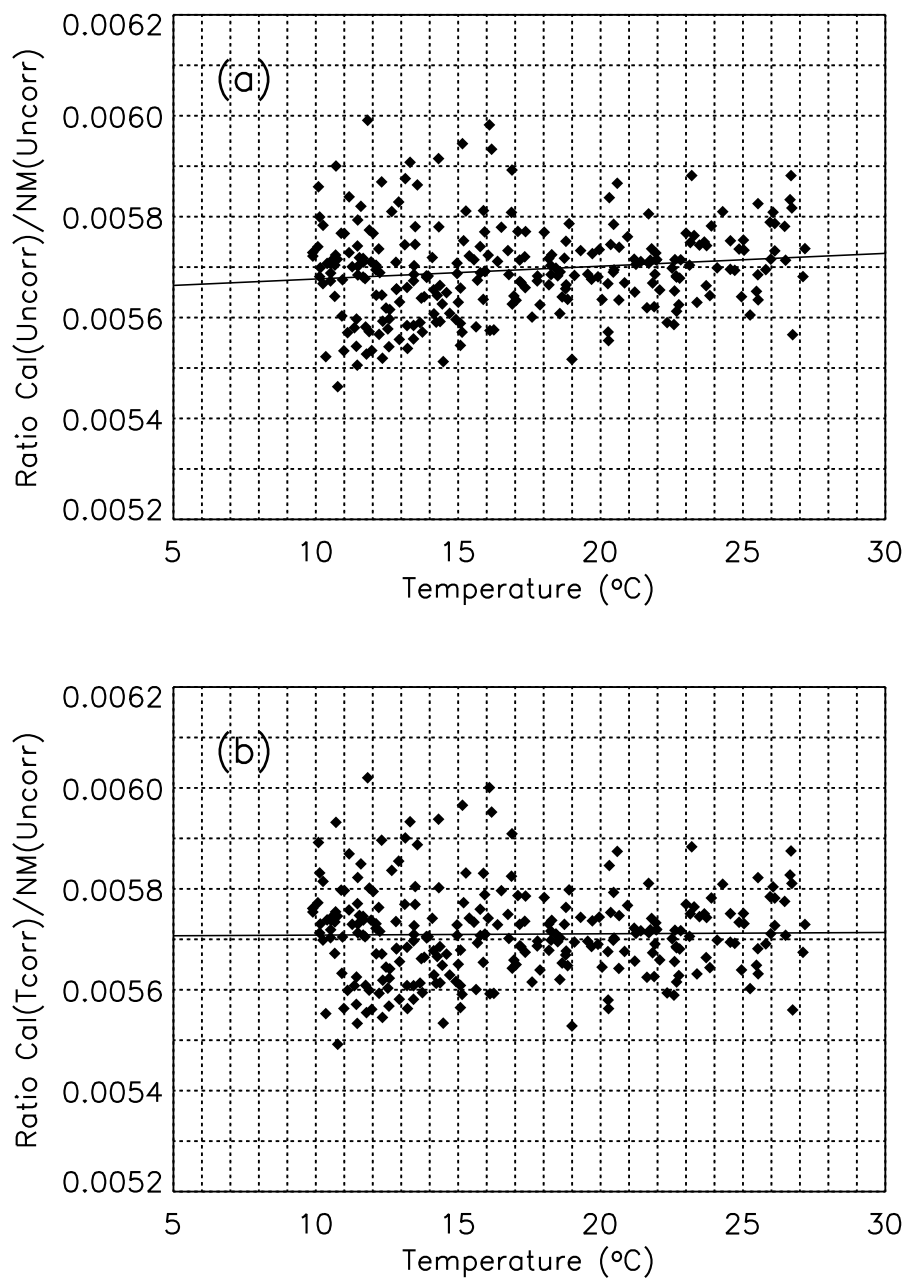


Figure 3.6: The Cal/NM ratios with straight line fit as a function of temperature of C1: (a) uncorrected ratio and (b) corrected ratio.

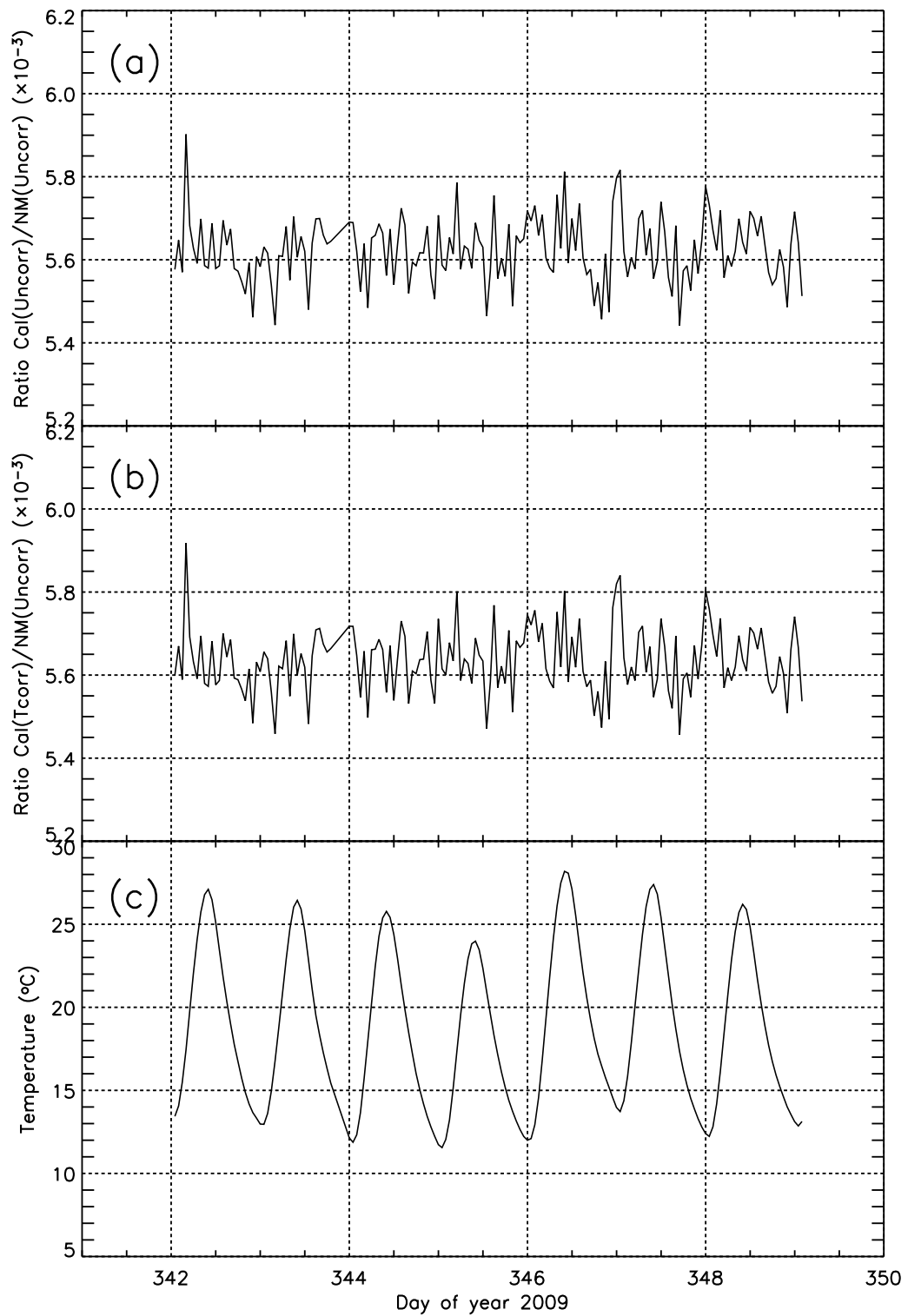


Figure 3.7: The results as a function of time of C2: (a) uncorrected Cal/NM ratio, (b) corrected ratio, (c) calmon counter temperature.

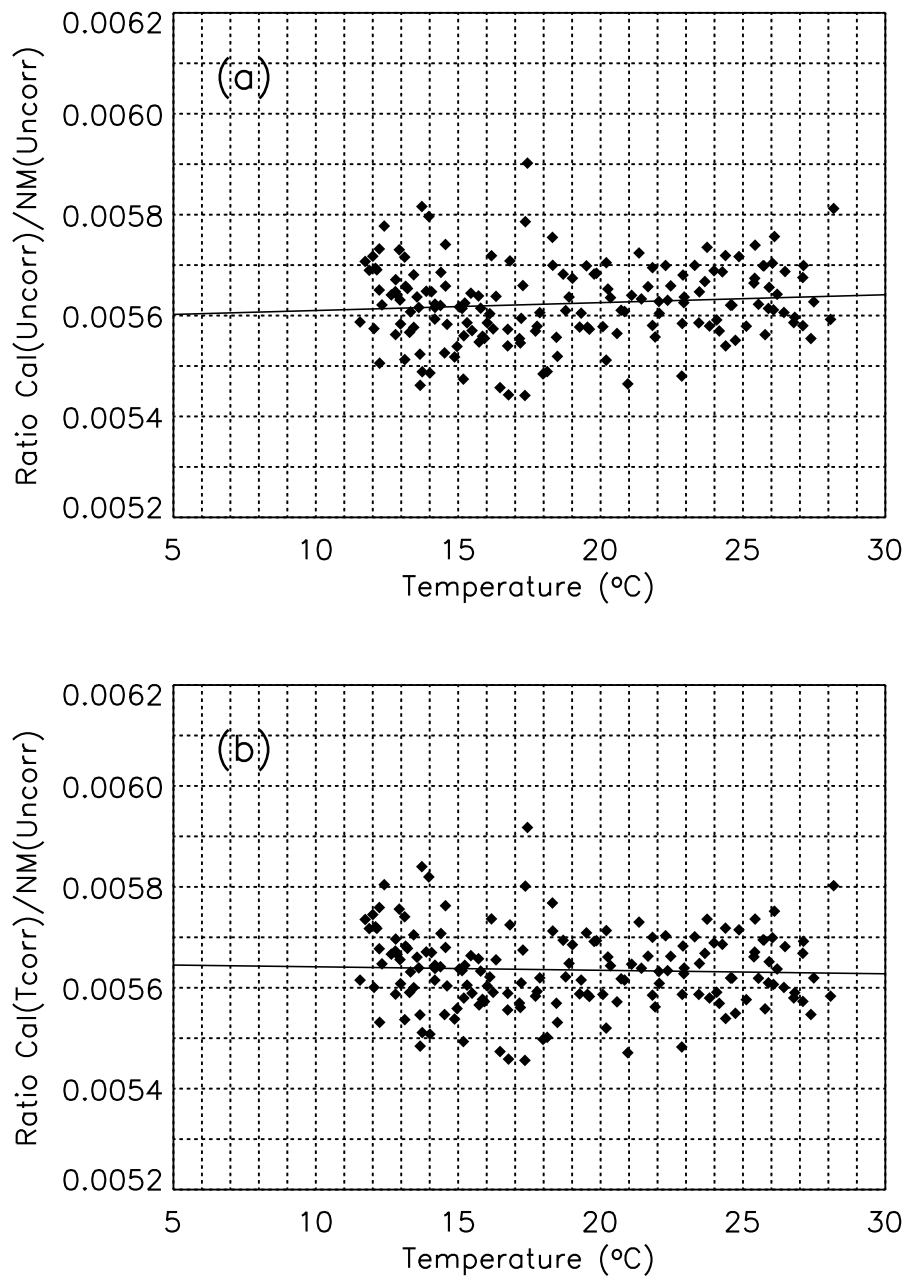


Figure 3.8: The Cal/NM ratios with straight line fit as a function of temperature of C2: (a) uncorrected ratio and (b) corrected ratio.

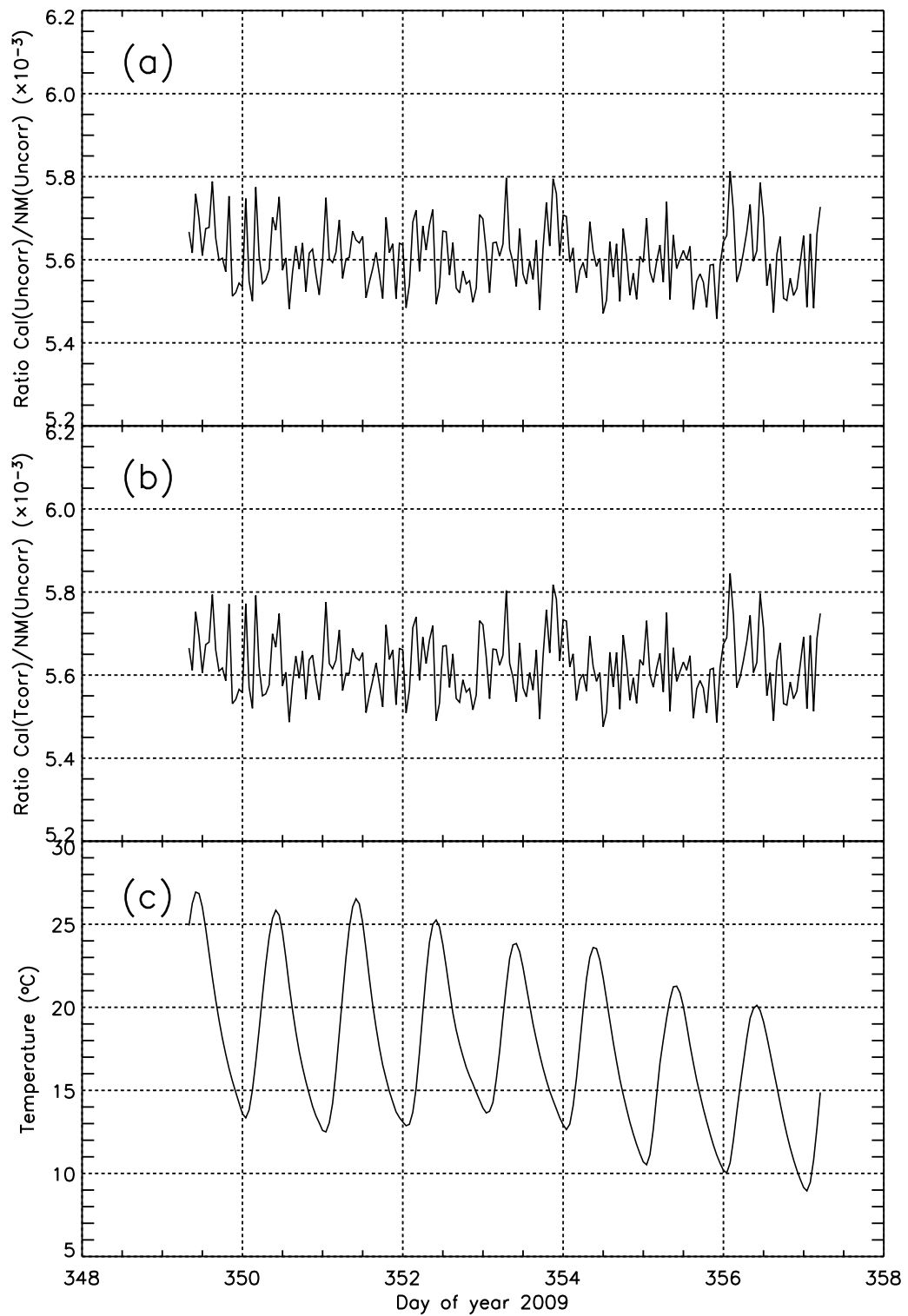


Figure 3.9: The results as a function of time of C3: (a) uncorrected Cal/NM ratio, (b) corrected ratio, (c) calmon counter temperature.

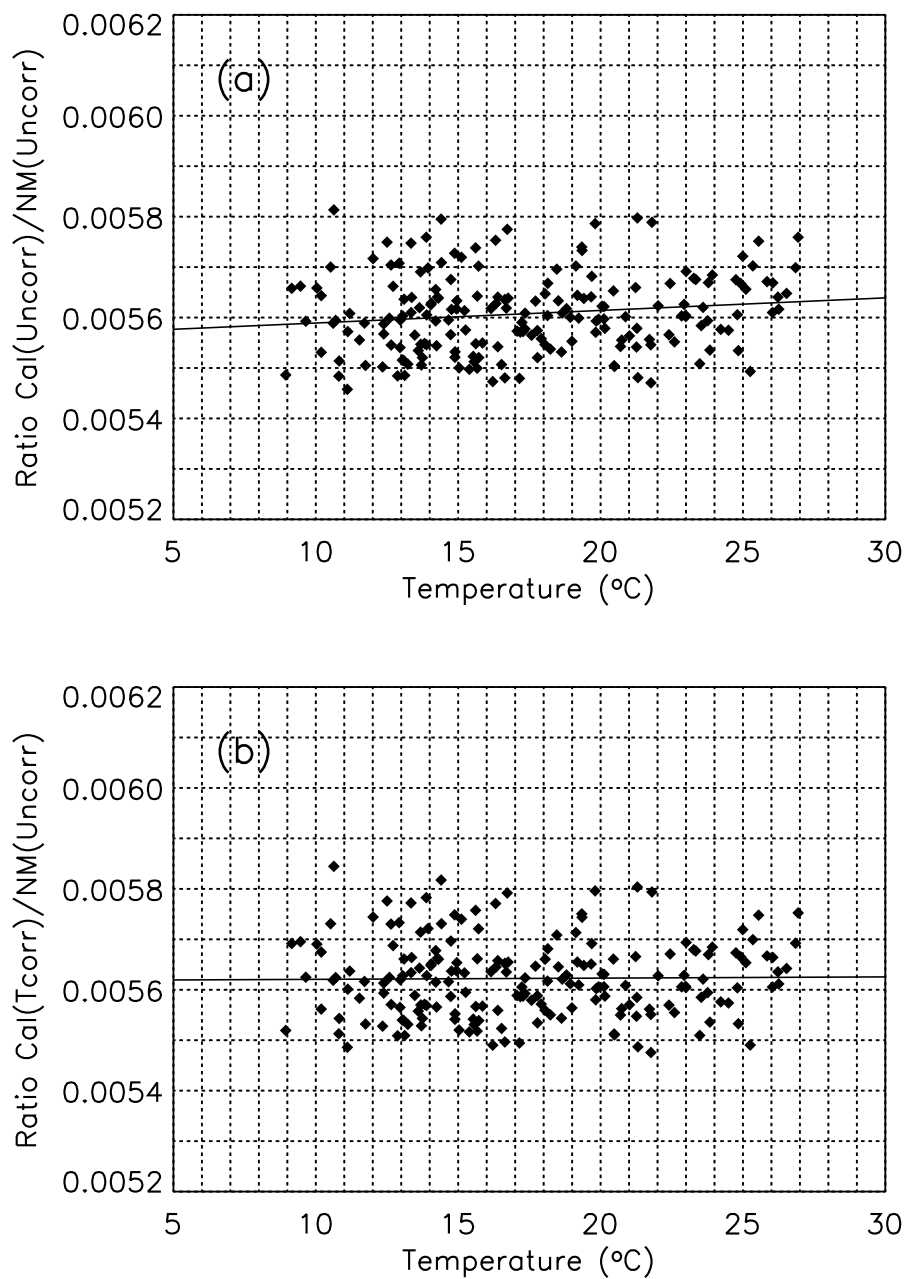


Figure 3.10: The Cal/NM ratios with straight line fit as a function of temperature of C3: (a) uncorrected ratio and (b) corrected ratio.

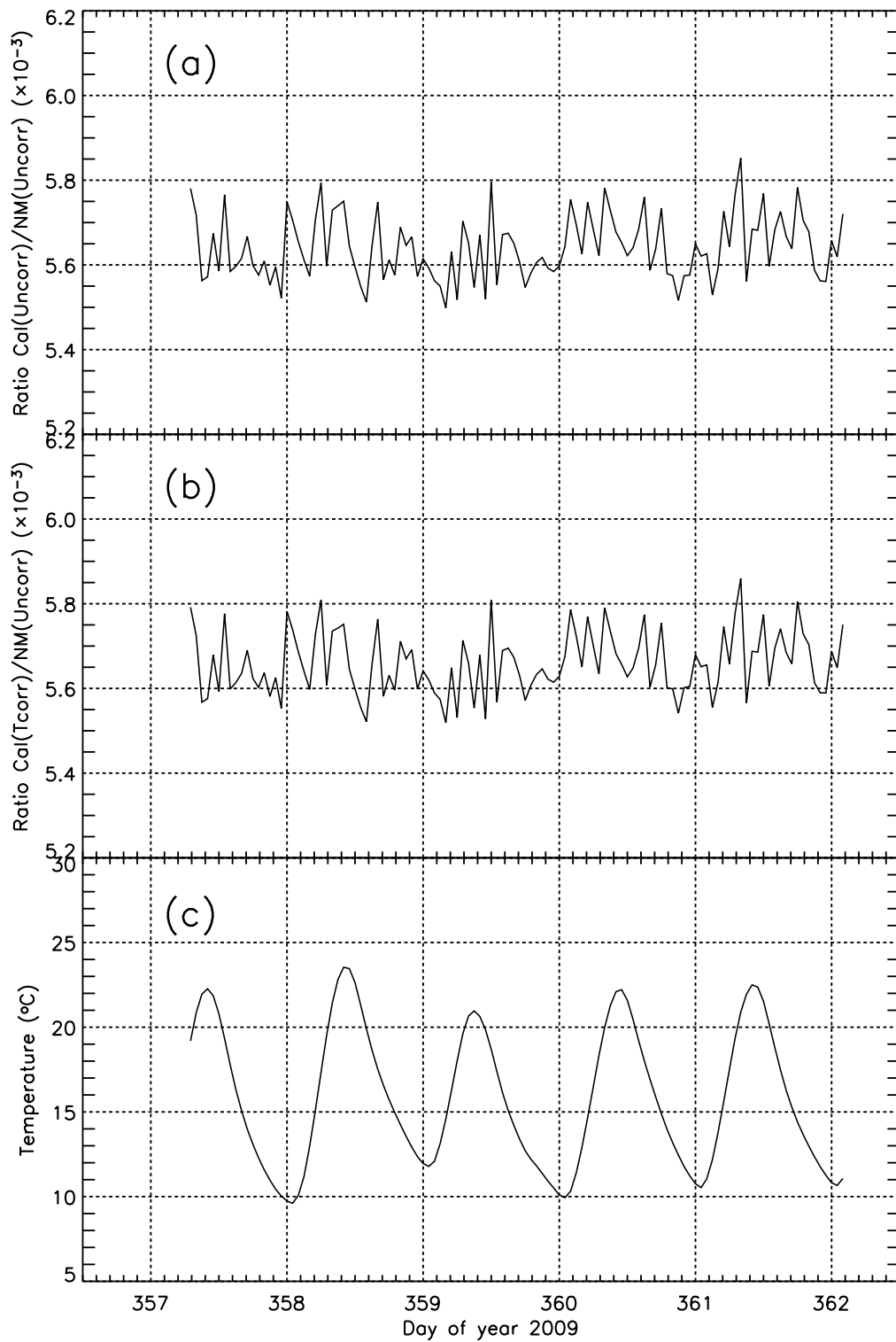


Figure 3.11: The results as a function of time of C4: (a) uncorrected Cal/NM ratio, (b) corrected ratio, (c) calmon counter temperature.

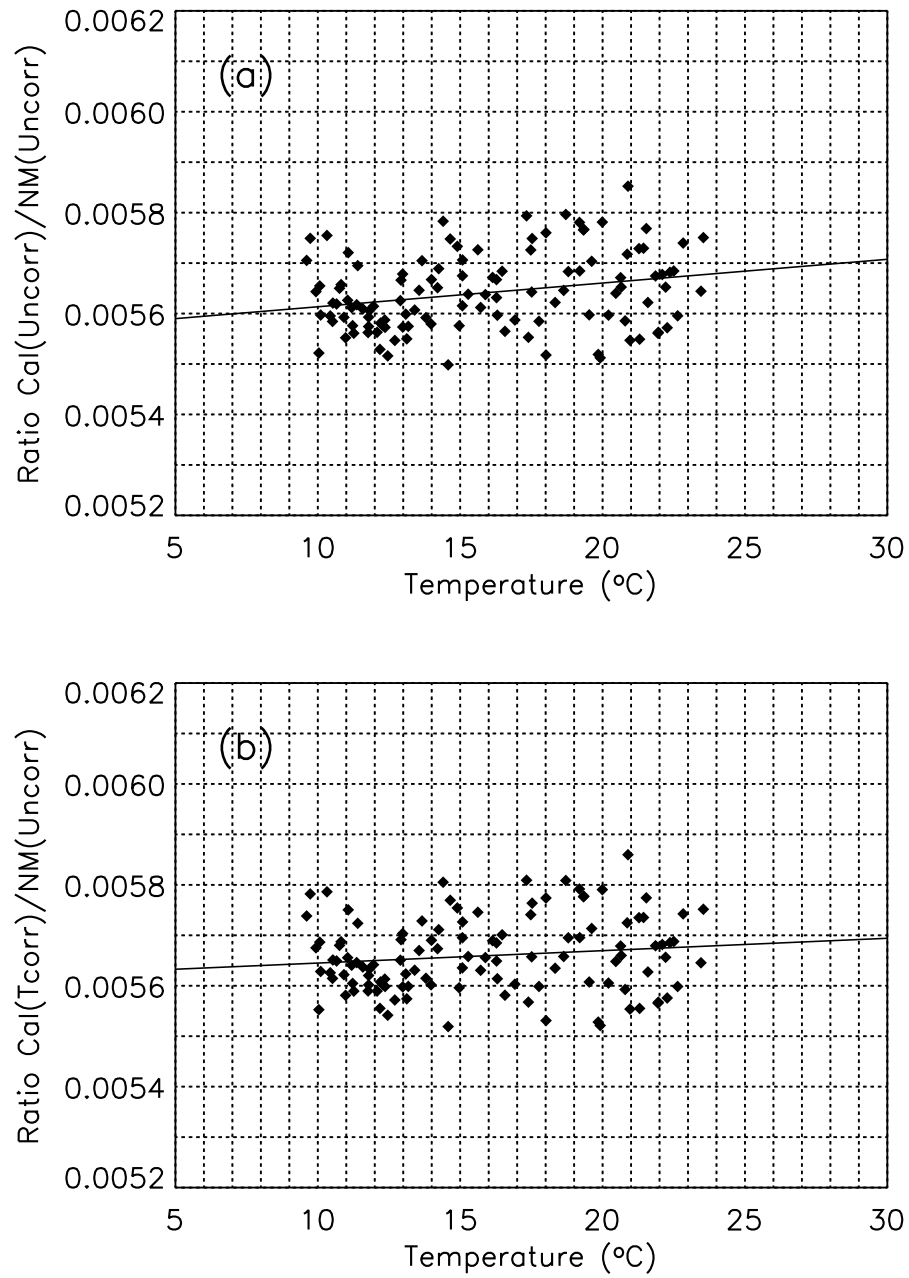


Figure 3.12: The Cal/NM ratios with straight line fit as a function of temperature of C4: (a) uncorrected ratio and (b) corrected ratio.

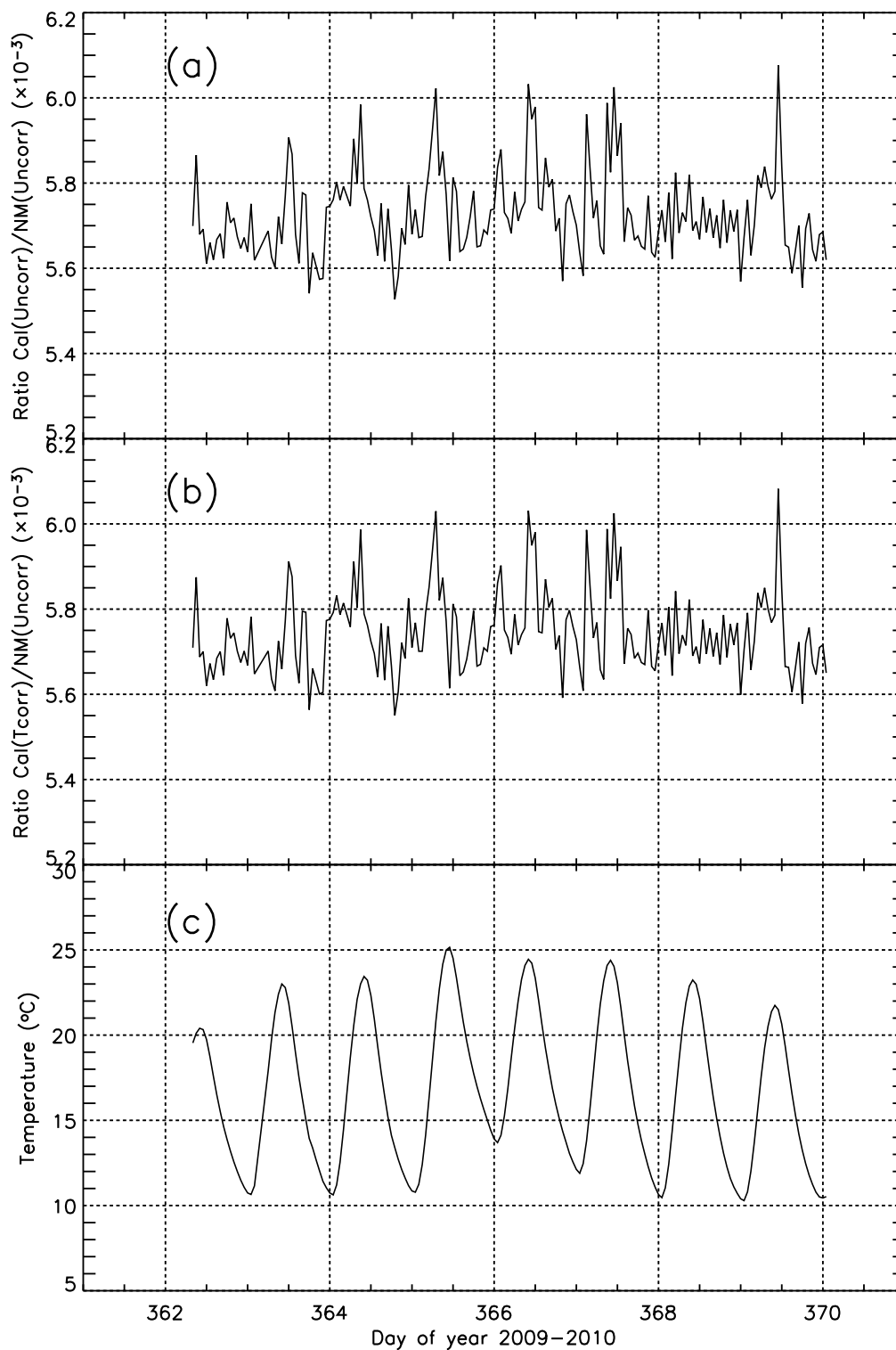


Figure 3.13: The results as a function of time of C5: (a) uncorrected Cal/NM ratio, (b) corrected ratio, (c) calmon counter temperature. There appears to be a strong association of Cal/NM with counter temperature, but it is not consistent and may instead reflect increased noise at some times of high temperature.

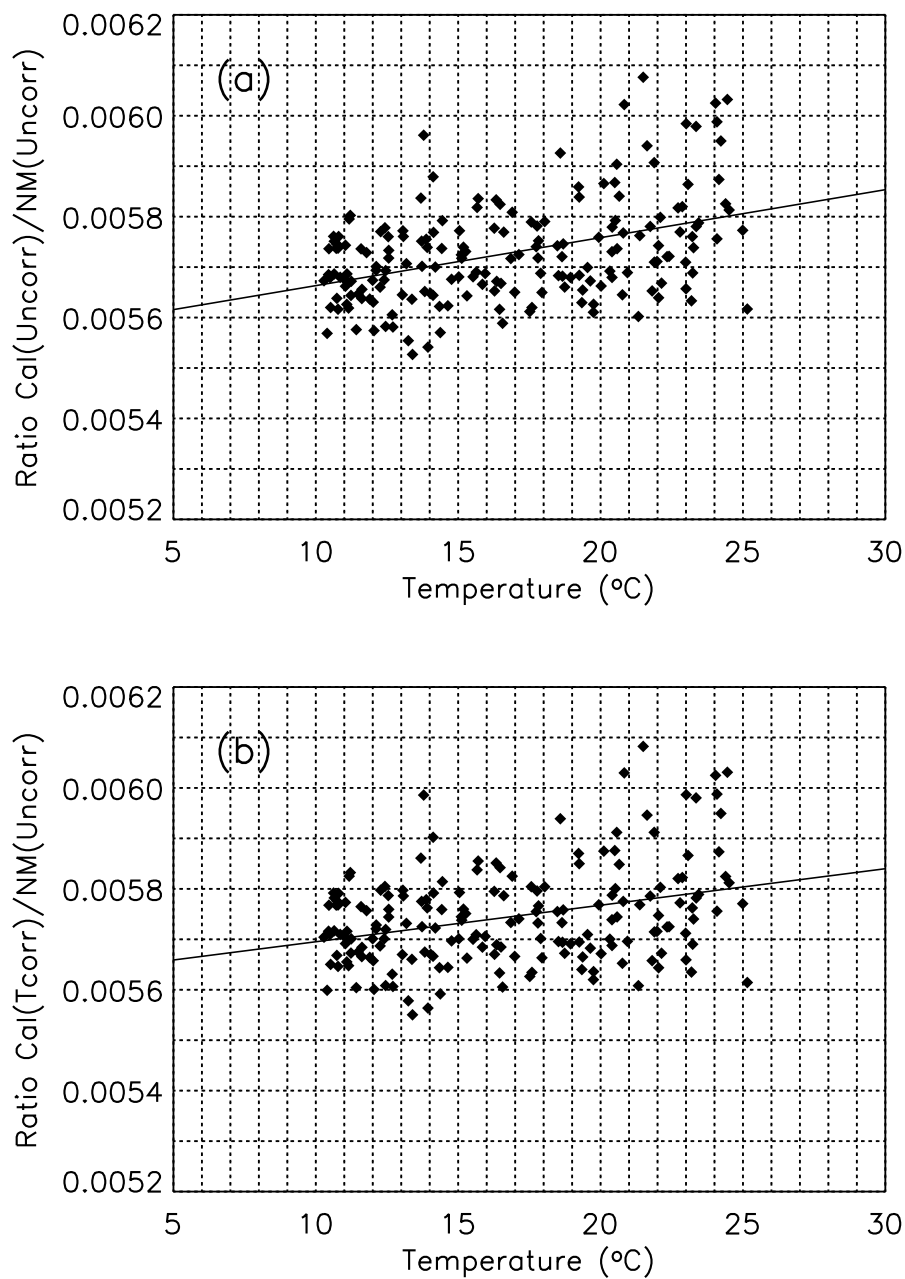


Figure 3.14: The Cal/NM ratios with straight line fit as a function of temperature of C5: (a) uncorrected ratio and (b) corrected ratio.

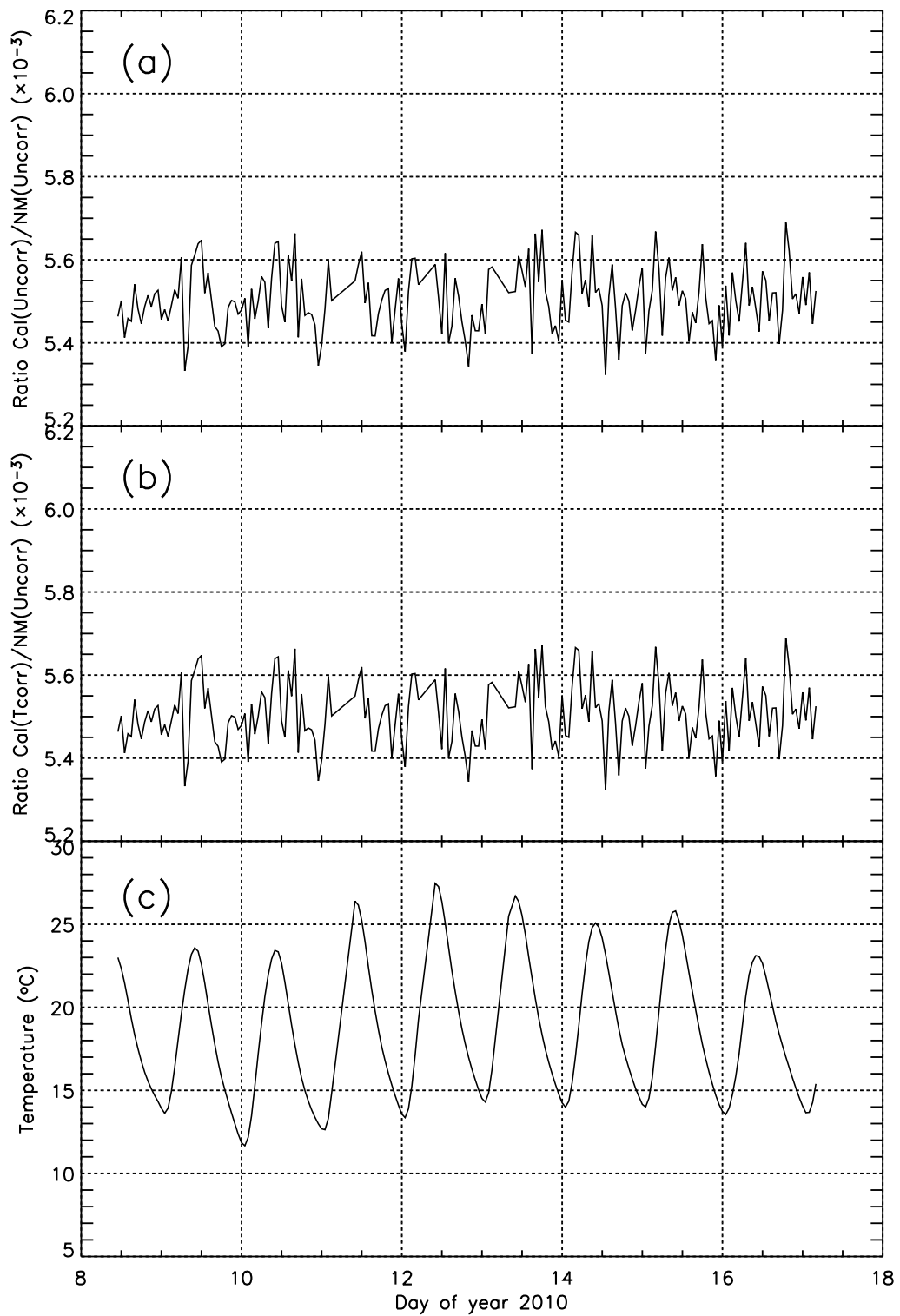


Figure 3.15: The results as a function of time of C6: (a) uncorrected Cal/NM ratio, (b) corrected ratio, (c) calmon counter temperature.

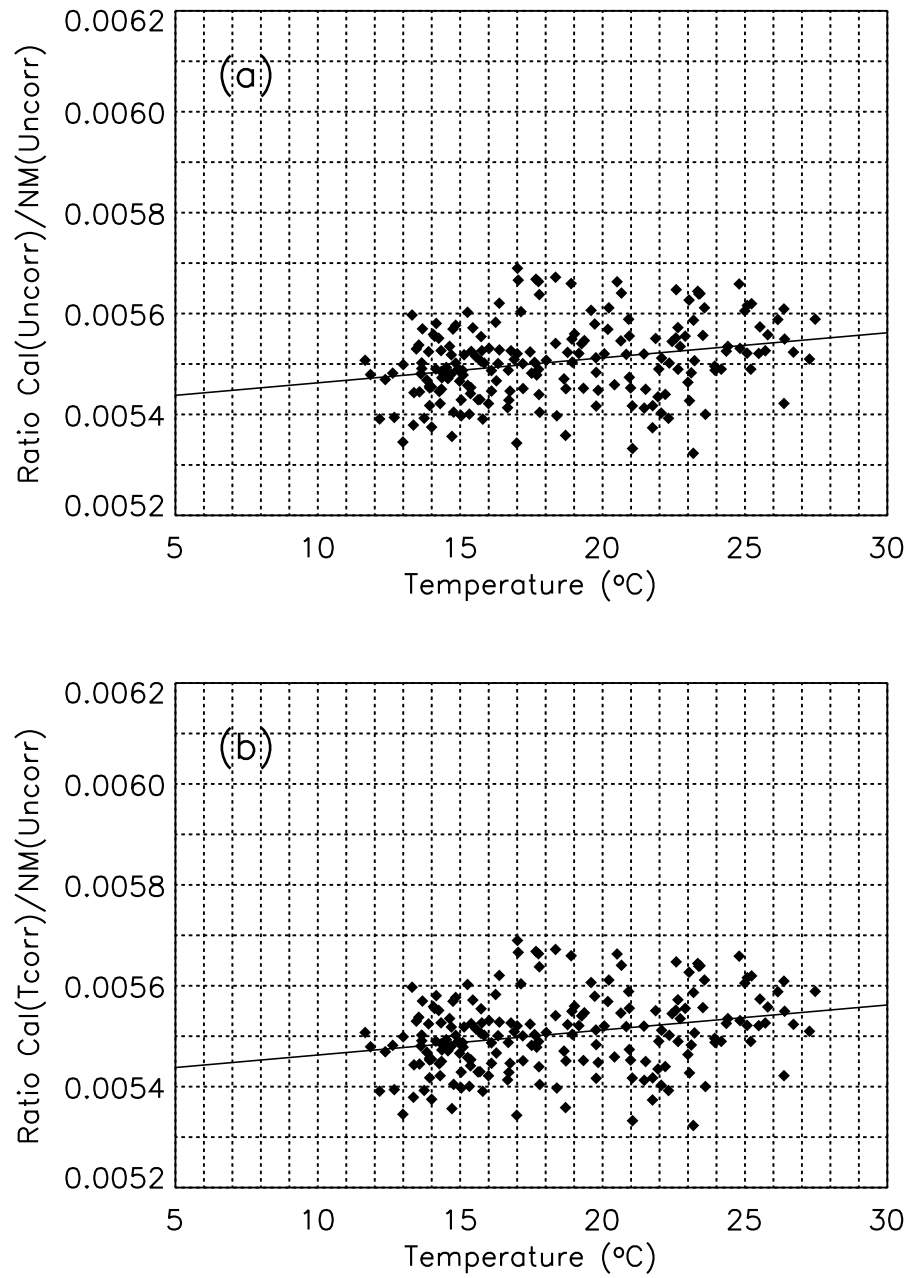


Figure 3.16: The Cal/NM ratios with straight line fit as a function of temperature of C6: (a) uncorrected ratio and (b) corrected ratio.

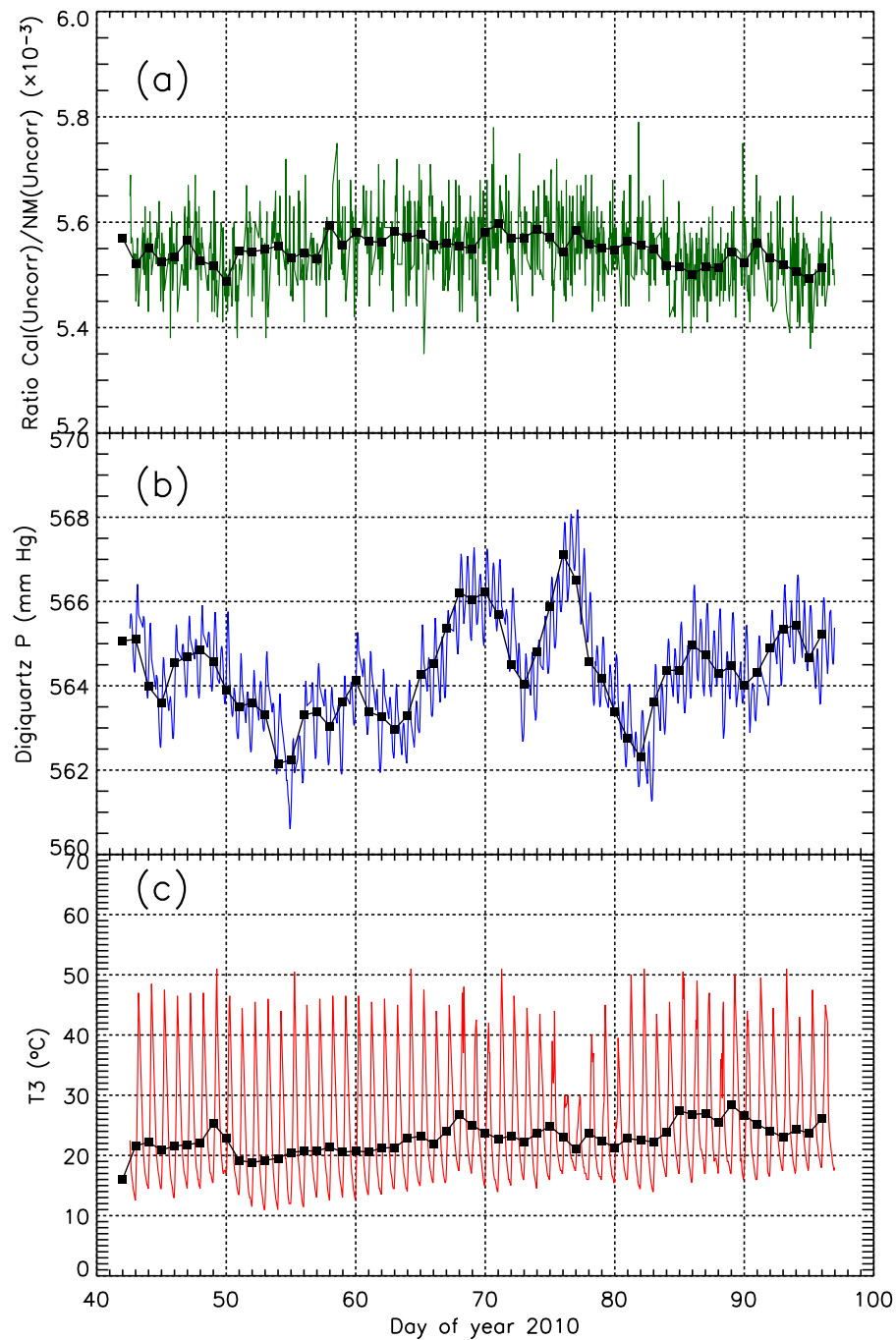


Figure 3.17: The results as a function of time of C8 (BRI electronics). (a) The green line shows the corrected Cal/NM ratio and solid black boxes with a solid line show the daily average corrected ratio. (b) The blue line shows the PSNM pressure reading by Digiquartz in mm Hg and solid black boxes with a solid line show the daily average Digiquartz pressure. (c) The red line shows the temperature of the calmon and solid black boxes with the solid line show the daily average calmon temperature.

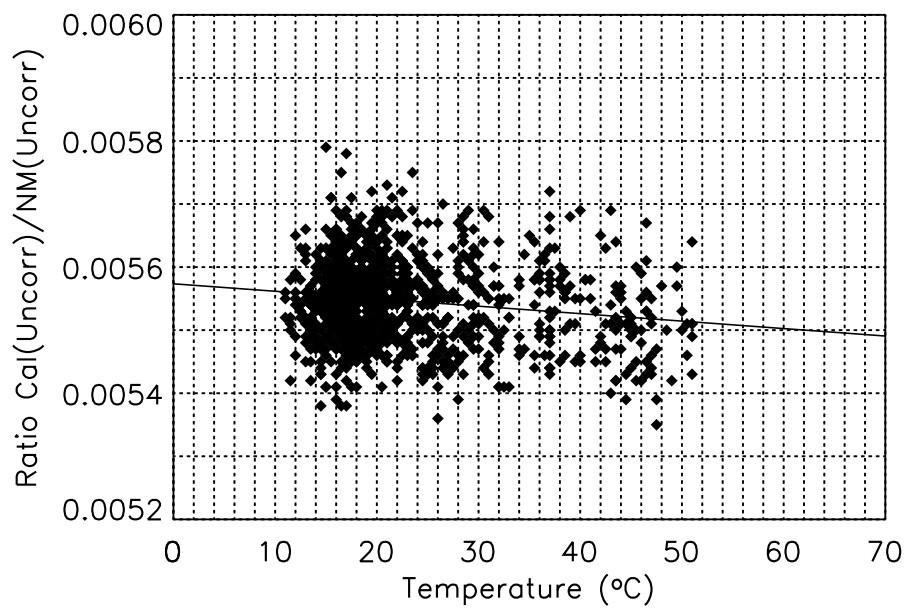


Figure 3.18: The Cal/NM ratios with straight line fit as a function of temperature of C8

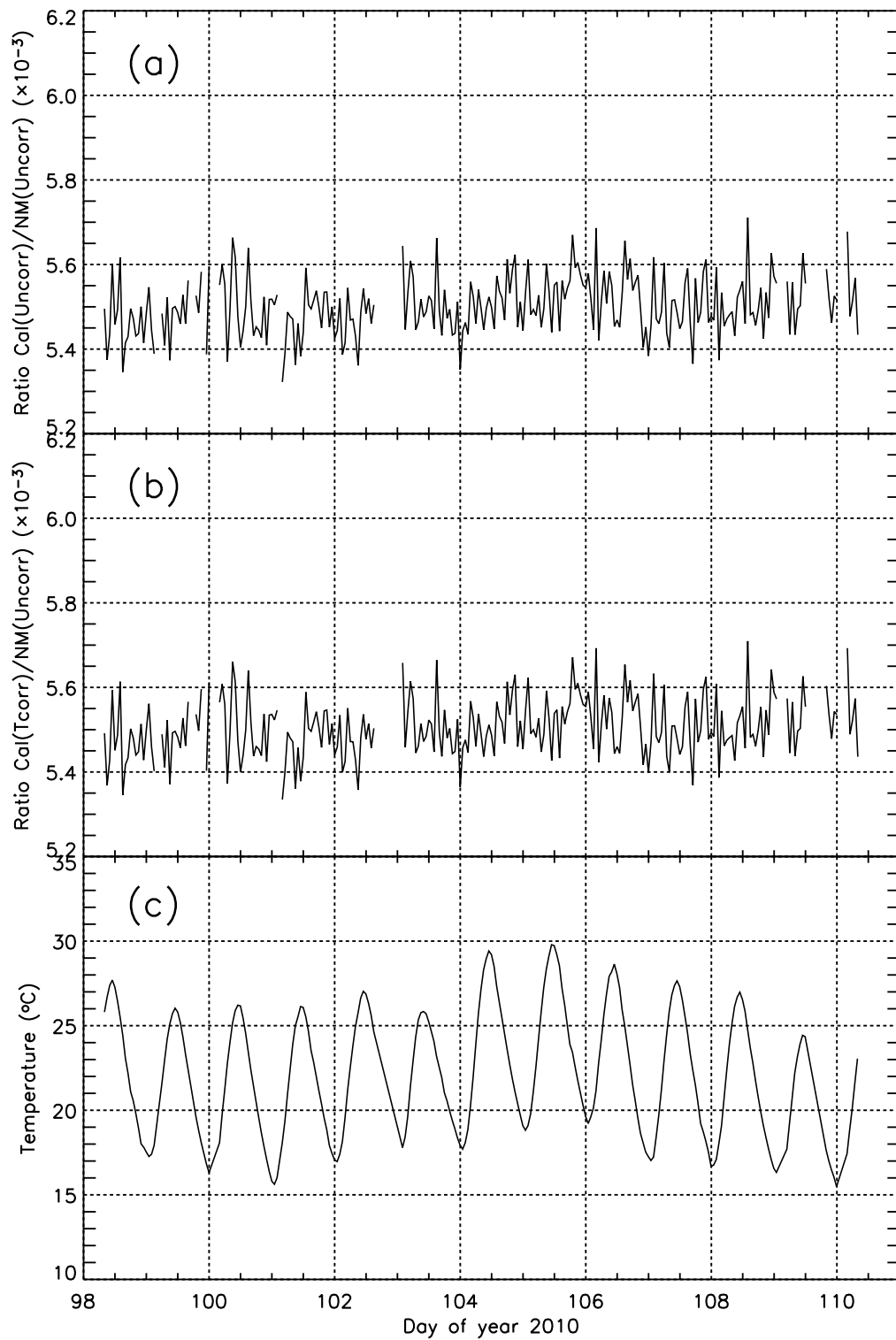


Figure 3.19: The results as a function of time of C9: (a) uncorrected Cal/NM ratio, (b) corrected ratio, (c) calmon counter temperature.

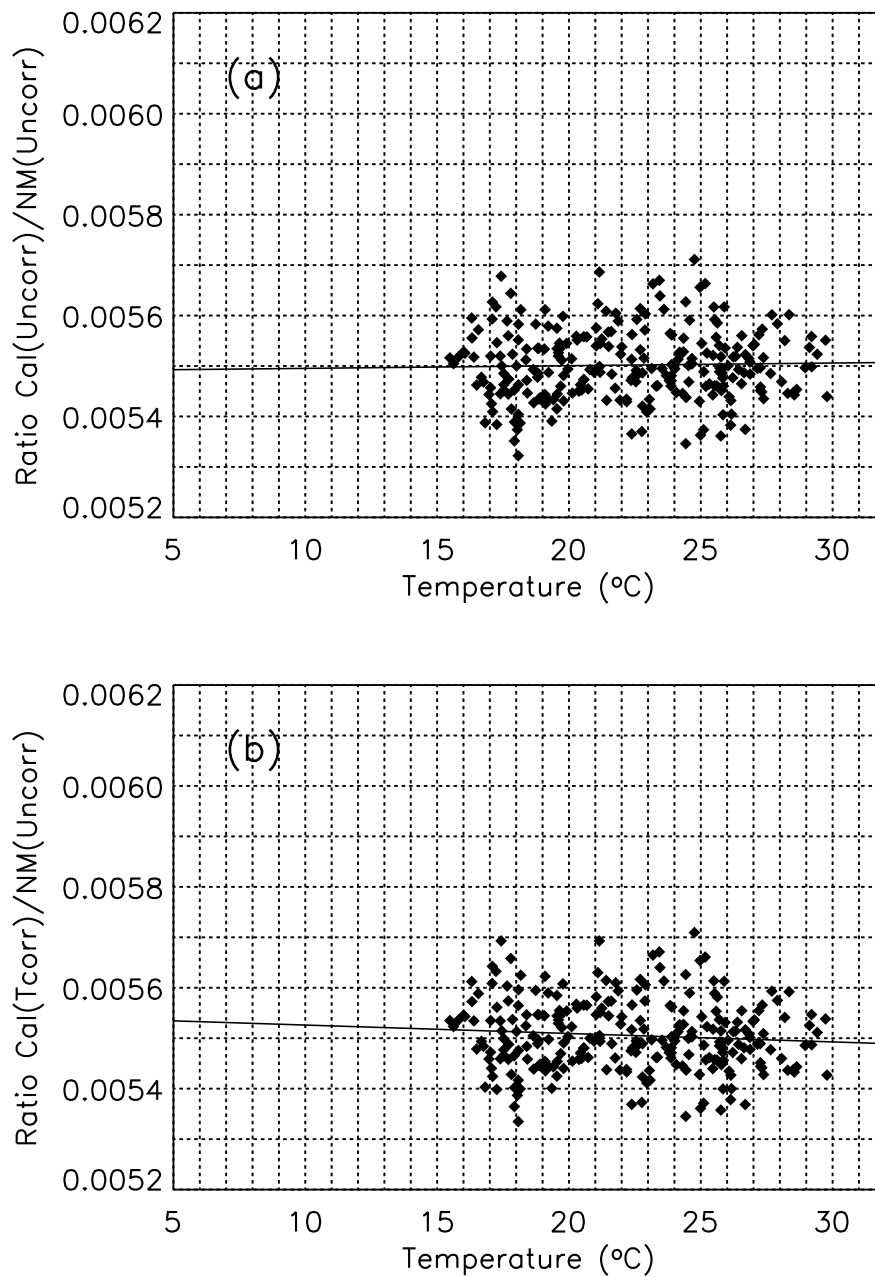


Figure 3.20: The Cal/NM ratios with straight line fit as a function of temperature of C9: (a) uncorrected ratio and (b) corrected ratio.

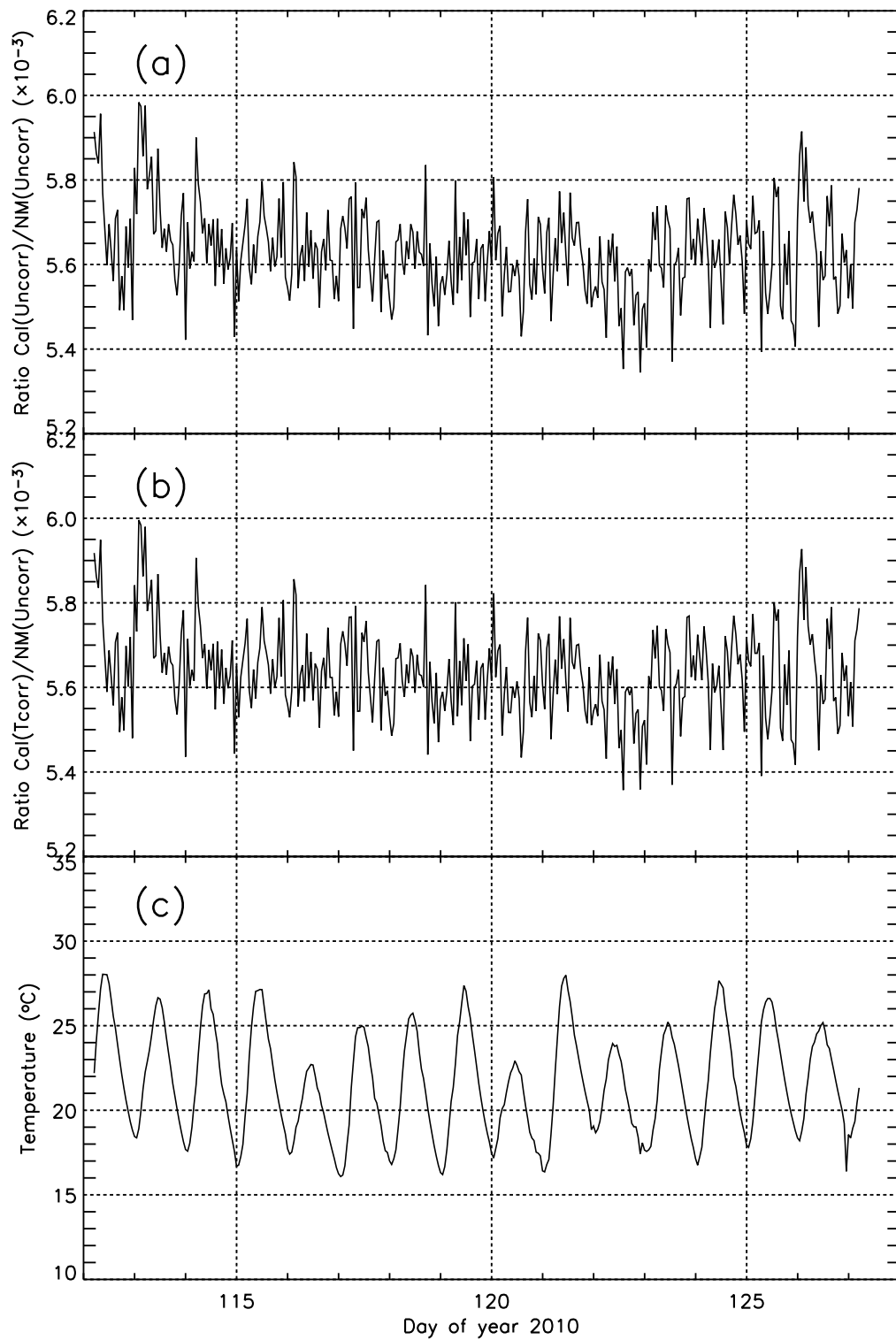


Figure 3.21: The results as a function of time of C10: (a) uncorrected Cal/NM ratio, (b) corrected ratio, (c) calmon counter temperature.

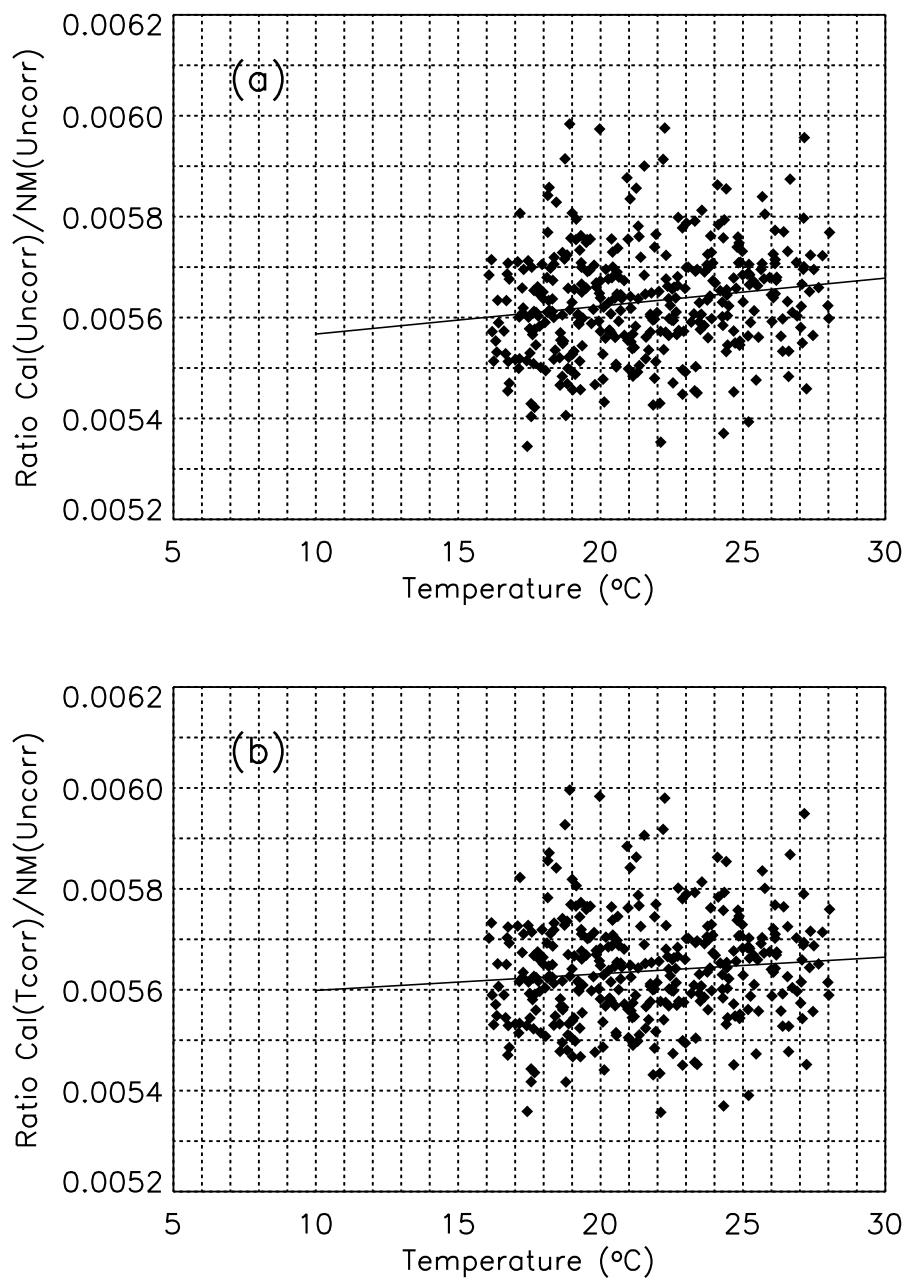


Figure 3.22: The Cal/NM ratios with straight line fit as a function of temperature of C10: (a) uncorrected ratio and (b) corrected ratio.

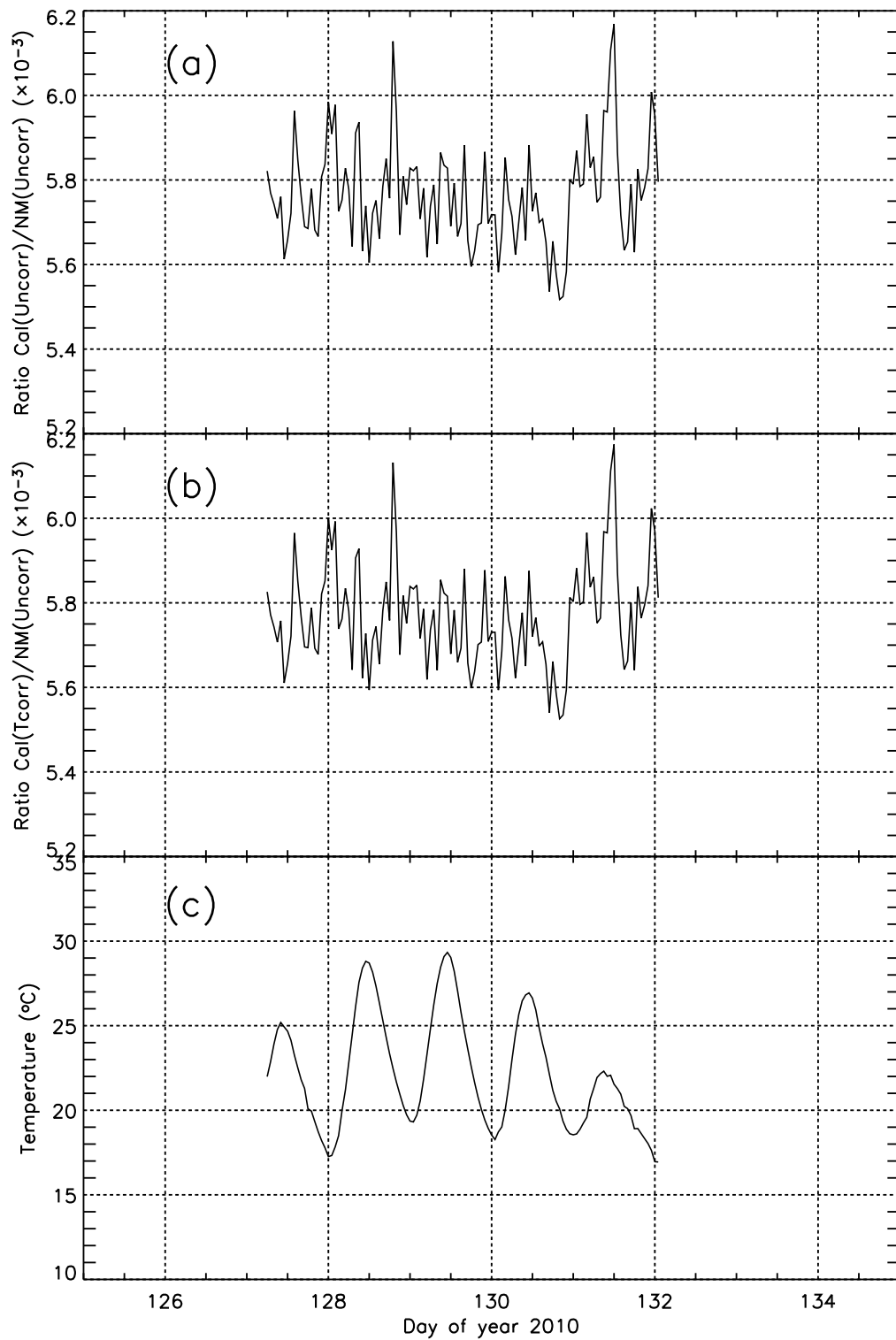


Figure 3.23: The results as a function of time of C11: (a) uncorrected Cal/NM ratio, (b) corrected ratio, (c) calmon counter temperature.

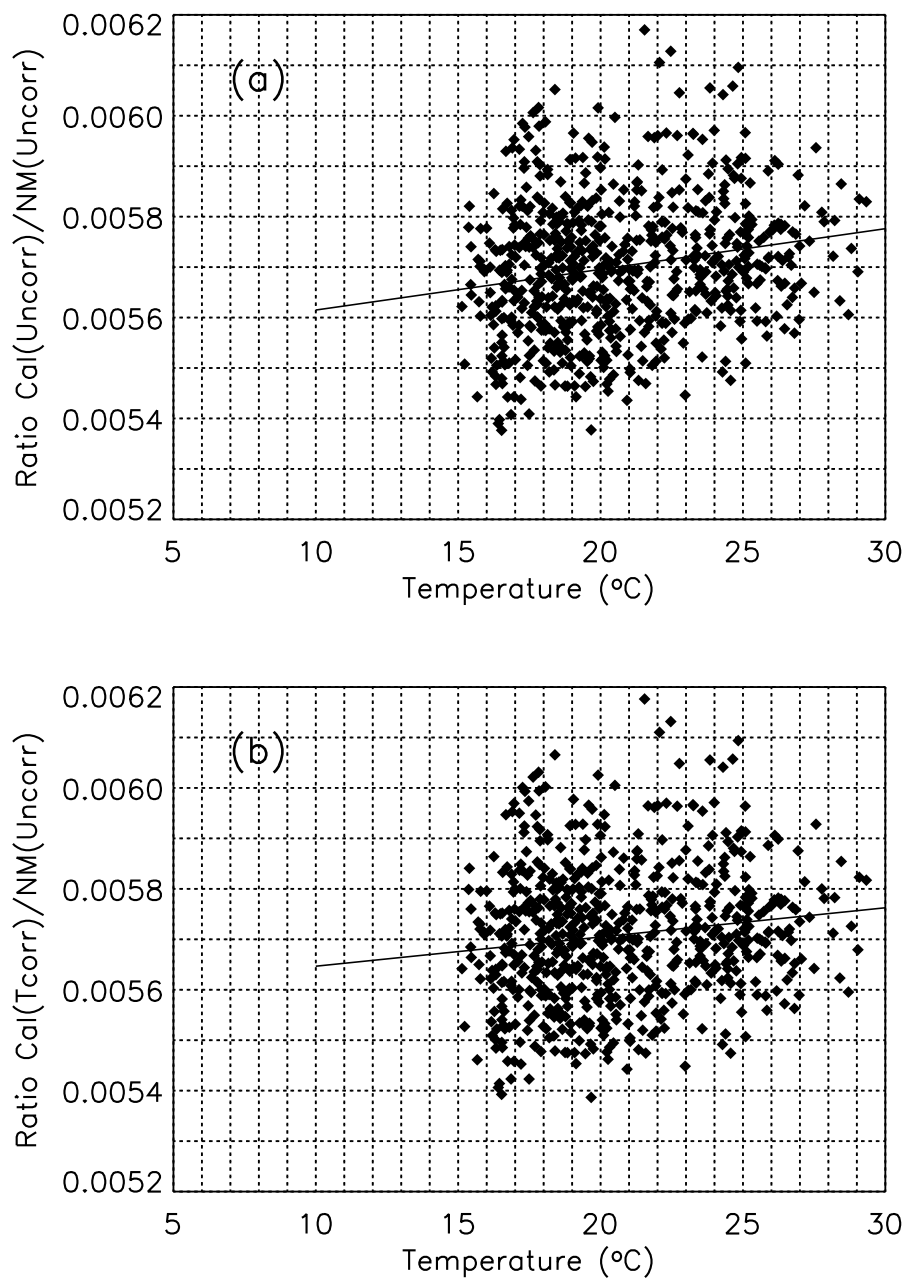


Figure 3.24: The Cal/NM ratios with straight line fit as a function of temperature of C11: (a) uncorrected ratio and (b) corrected ratio.

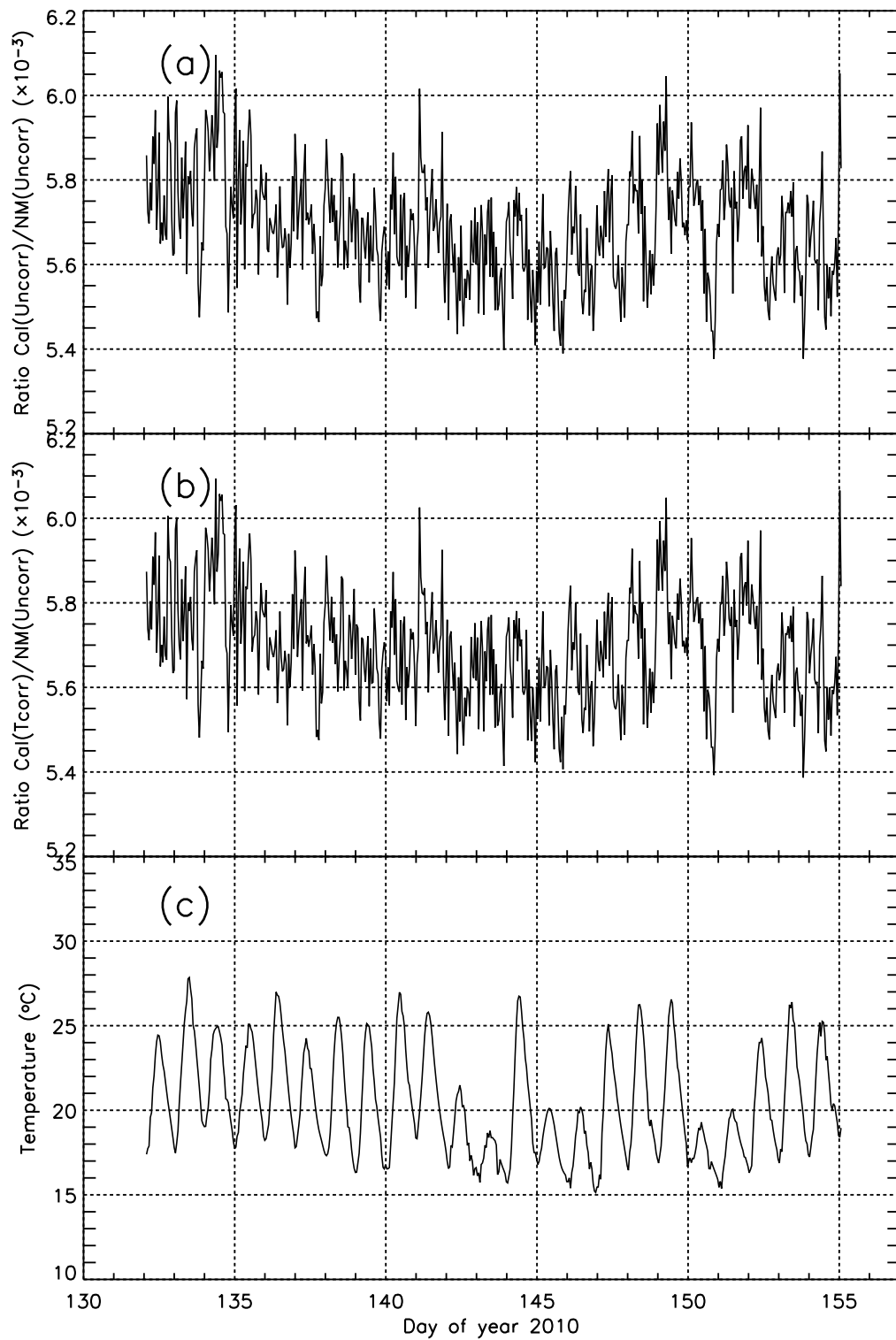


Figure 3.25: The results as a function of time of C12: (a) uncorrected Cal/NM ratio, (b) corrected ratio, (c) calmon counter temperature.

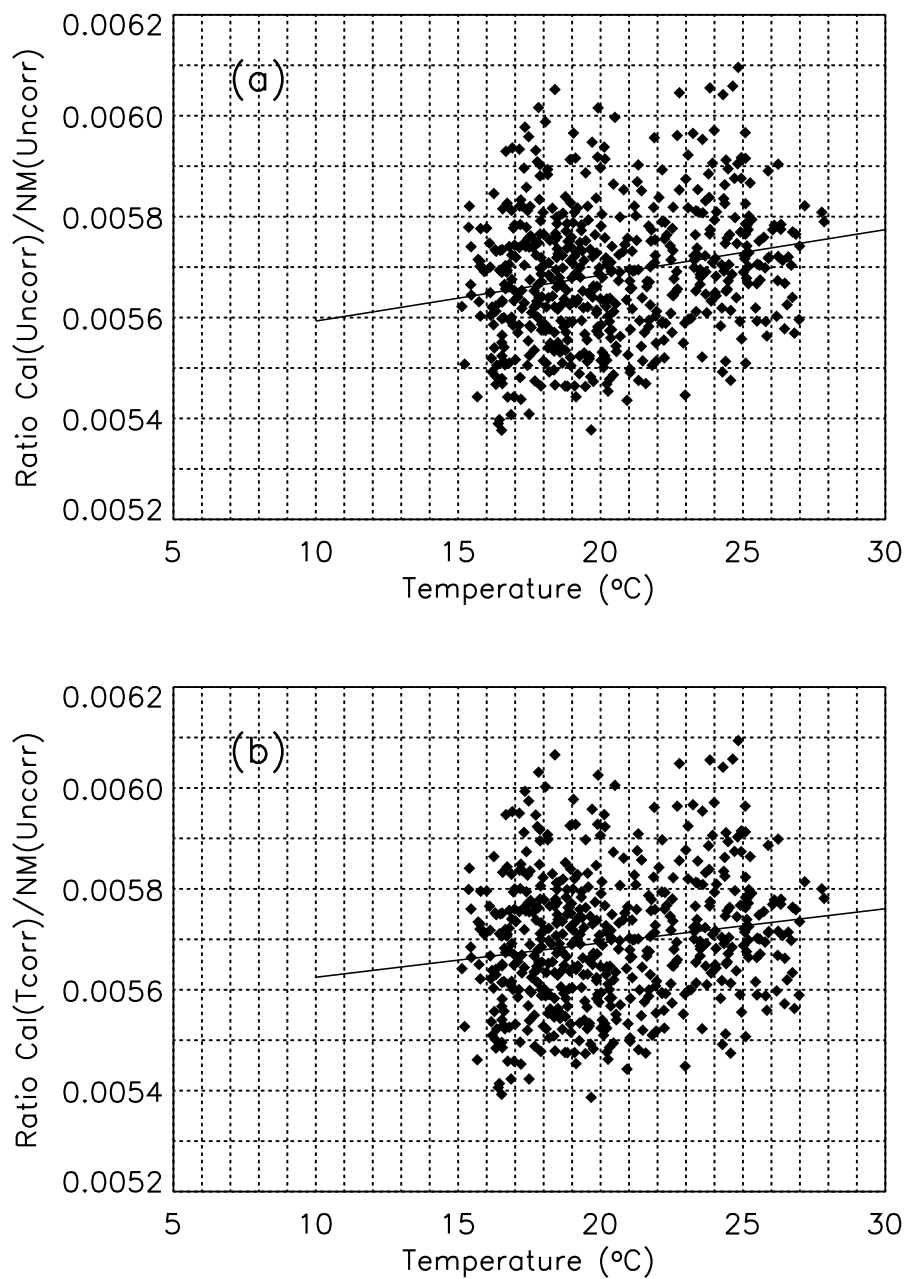


Figure 3.26: The Cal/NM ratios with straight line fit as a function of temperature of C12: (a) uncorrected ratio and (b) corrected ratio.

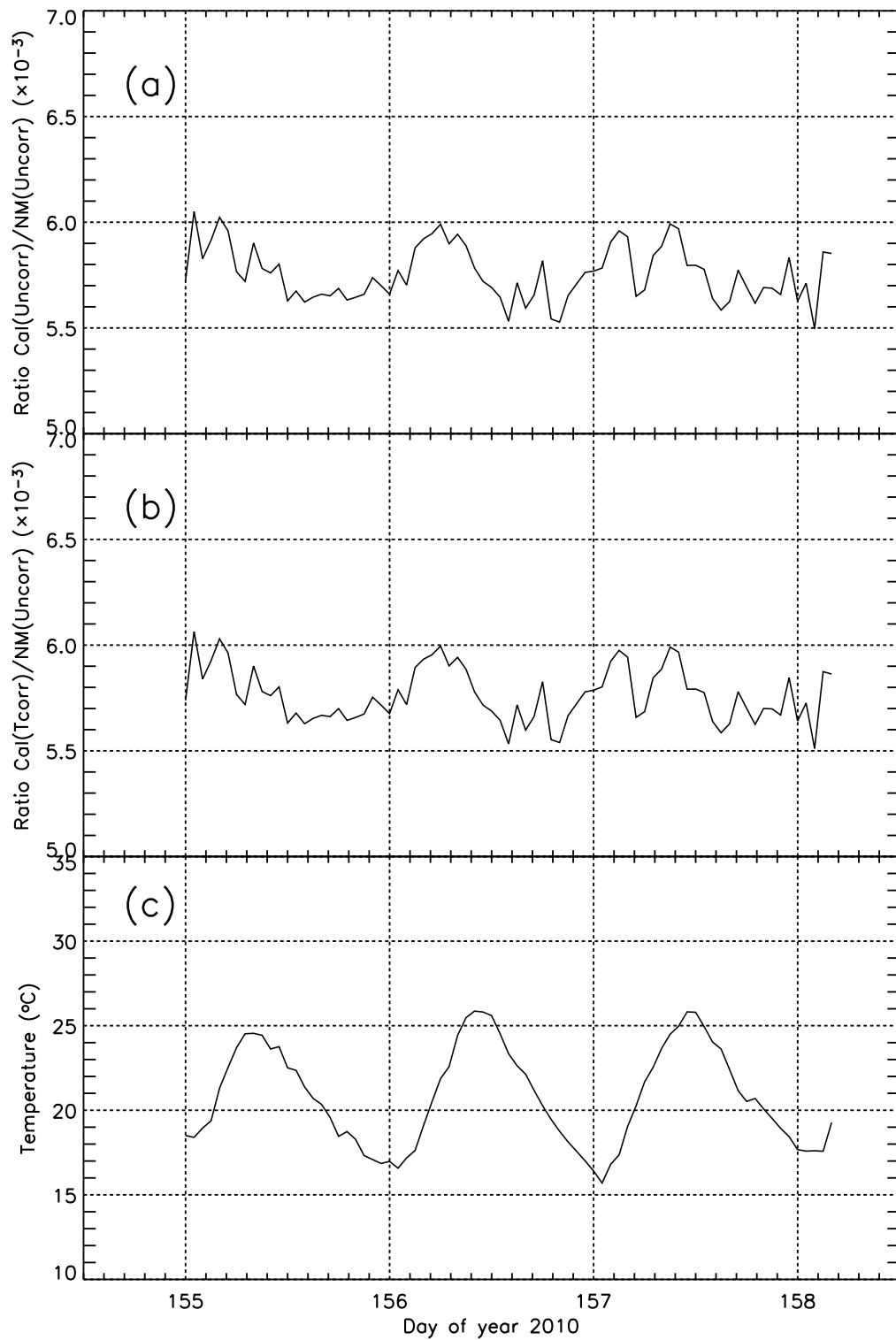


Figure 3.27: The results as a function of time of C13: (a) uncorrected Cal/NM ratio, (b) corrected ratio, (c) calmon counter temperature.

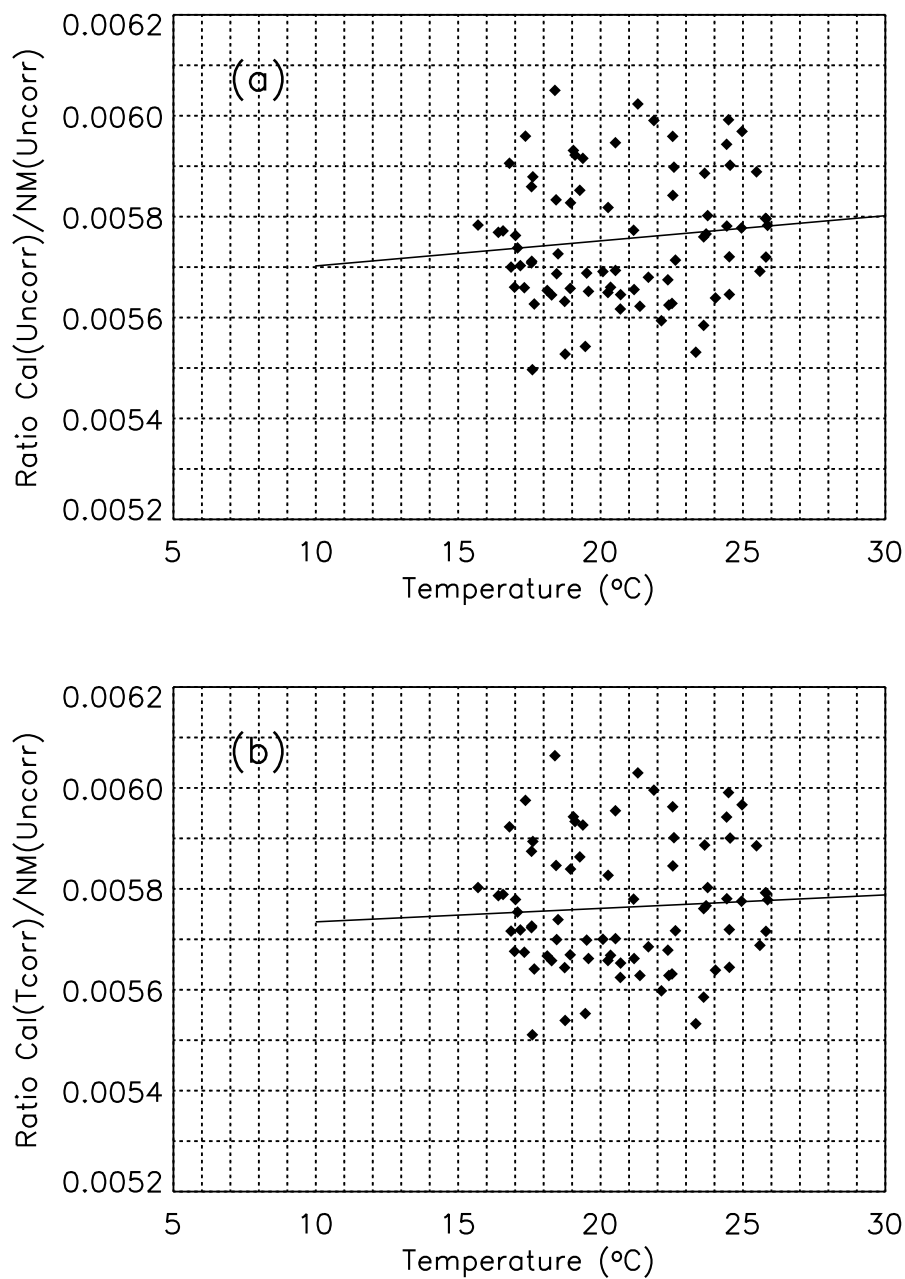


Figure 3.28: The Cal/NM ratios with straight line fit as a function of temperature of C13: (a) uncorrected ratio and (b) corrected ratio.

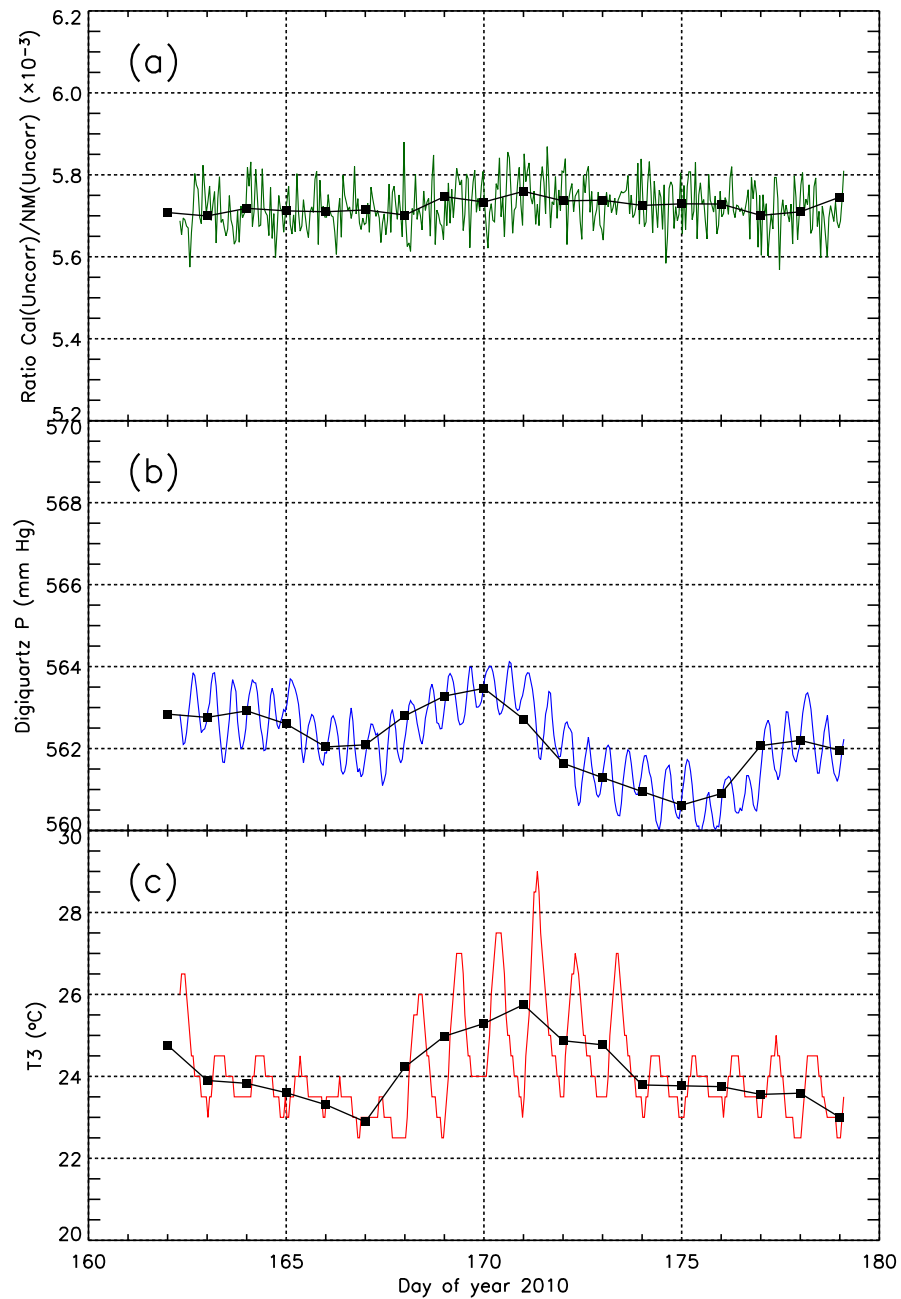


Figure 3.29: The results as a function of time of C15 (BRI electronics). (a) The green line shows the corrected Cal/NM ratio and solid black boxes with a solid line show the daily average corrected ratio. (b) The blue line shows the PSNM pressure reading by Digiquartz in mm Hg and solid black boxes with a solid line show the daily average Digiquartz pressure. (c) The red line shows the temperature of the calmon and solid black boxes with the solid line show the daily average calmon temperature.

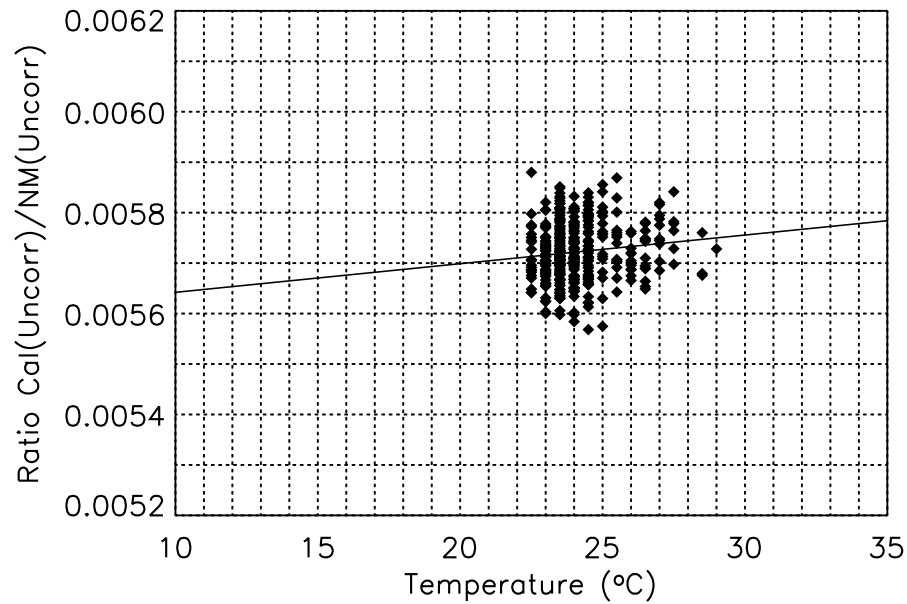


Figure 3.30: The Cal/NM ratios with straight line fit as a function of temperature of C15

In experiments we planned to set the calmon height at three different levels above the surface, 140 cm (outside), 70 cm (outside), and 55 cm (inside), as shown in Figure 3.31. In Figure 3.31 we show the Cal/NM ratio for all usable configurations in single graph. In the analysis of data with the calmon outside, we considered the results when calibrator was set at two heights above the surface, at 140 cm and 70 cm, as shown in 3.32, to compare with the results from previous work at Potchefstroom, S. Africa. When the calibrator was at 140 cm, it seems that the counting rate leveled off at a height of water ≈ 70 cm. The decrease in the count rate was only 1.56%. However, when the calibrator was at 70 cm above the surface, the decrease was $\approx 4.2\%$, confirming the previous results at Potchefstroom (Krüger et al. 2011).

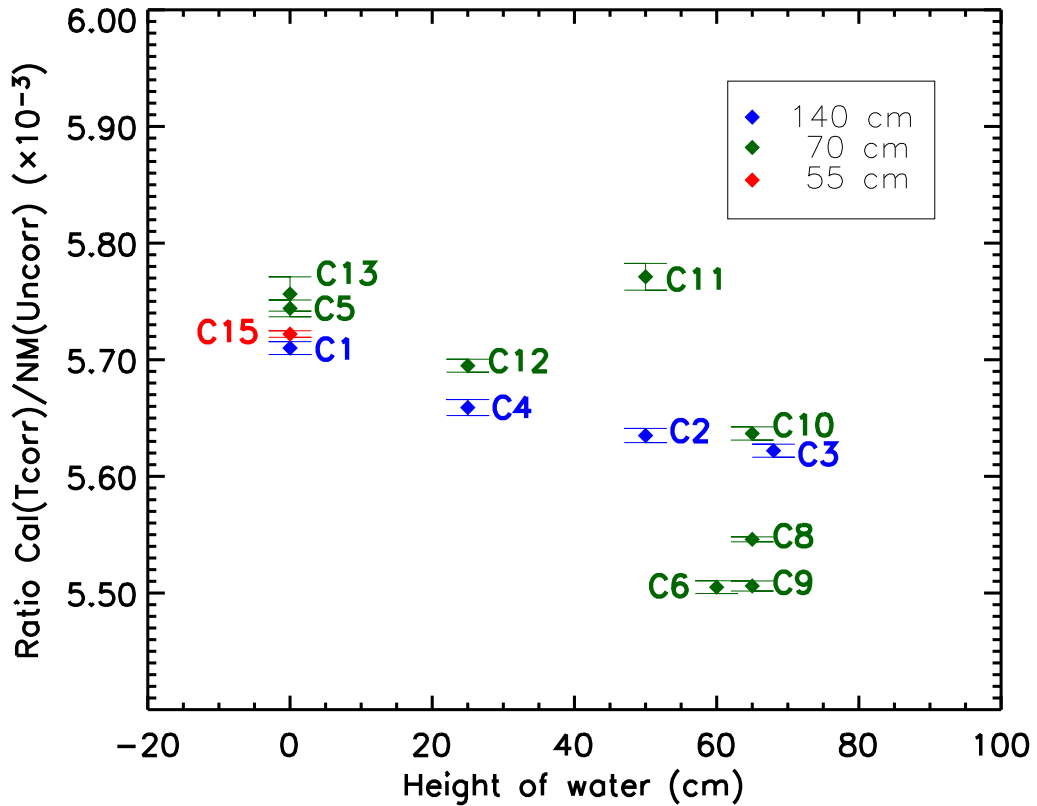


Figure 3.31: The corrected Cal/NM ratios for all usable configurations. The calmon height is indicated by color, i.e., blue indicates 140 cm (outside), green indicates 70 cm (outside), and red indicates 55 cm (inside). The error bars represent the standard error.

3.2.2 Calibration Procedure and Results

We used the above results to standardize the calibration procedure, namely that it must be done outside, removed from any buildings and structures, and that it must be done above 30 cm of water. If these conditions are met, the cosmic-ray intensity at any two sites can be compared, because then the difference is only due to different cutoff rigidity and atmospheric depth. The necessary temperature corrections involved in the calibration were calculated as in equation 3.1. To quantify the calibration process, consider two NMs at different cutoff rigidities and altitudes, with different efficiencies (due to difference in type of neutron monitor, number of counters, and different environment). Suppose NM1 is calibrated against the calibrator at time t_1 , and similarly NM2 is calibrated at time t_2 . Then we have the following five measurements:

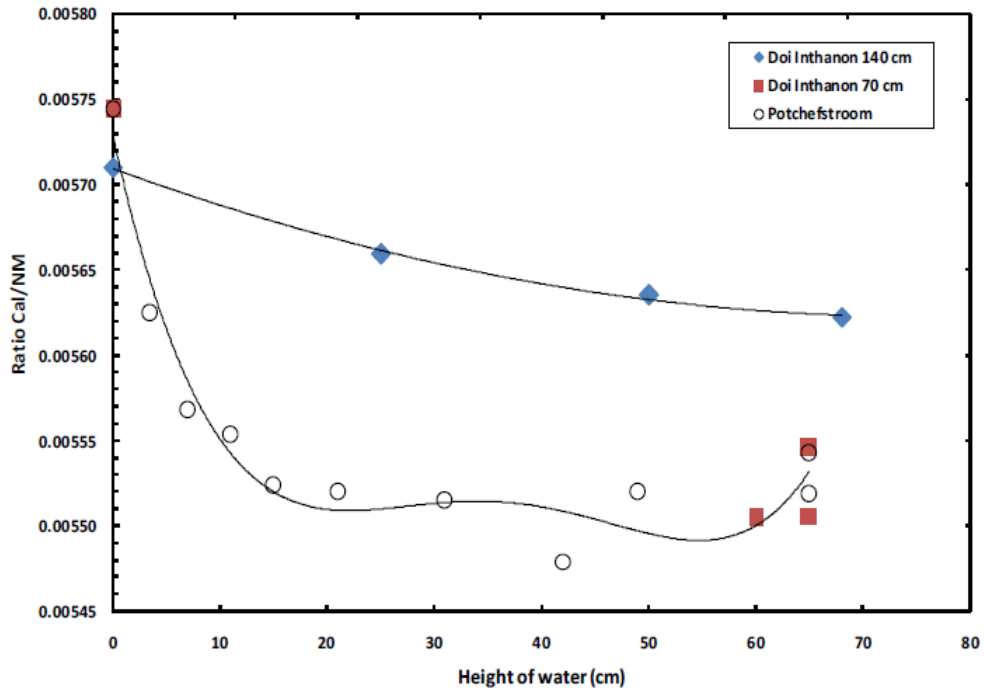


Figure 3.32: The Cal/NM ratio for the Potchefstroom NM (open circles) and the PSNM at Doi Inthanon as function of varying height of water beneath the calibrator [Image credit: Krüger et al. (2011)]

1. At time t_1 the count rate (CR) of NM1 is $N_{1,1}$
2. At time t_2 the CR of NM1 is $N_{1,2}$
3. At time t_2 the CR of NM2 is $N_{2,2}$
4. At time t_1 the CR of the calibrator at NM1 is $C_{1,1}$
5. At time t_2 the CR of the calibrator at NM2 is $C_{2,2}$

At time t_2 the count rate of the calibrator at NM1 can then be calculated as $C_{1,2} = (N_{1,2}/N_{1,1}) \times C_{1,1}$.

The ratio $R_m = N_{2,2}/N_{1,2}$ is the measured ratio of the two NMs at time t_2 . This ratio includes the differences in efficiency. The ratio $R_c = C_{2,2}/C_{1,2}$ is the “measured” ratio of the calibrator counts at the two positions. (We note that $C_{1,2}$ is not actually measured, but can be calculated as mentioned above.) The calibrator at the two different positions should have the same efficiency.

Hence the ratio of efficiency of the two NMs is

$$R_{eff} = \frac{R_m}{R_c} = \frac{N_{2,2} C_{1,2}}{N_{1,2} C_{2,2}} = \frac{N_{2,2} C_{1,2}}{C_{2,2} N_{1,2}} = \frac{N_{2,2} C_{1,1}}{C_{2,2} N_{1,1}} \quad (3.2)$$

Table 3.2: Hourly count rates during the calibrations

| | t_1 , Potchefstroom | t_2 , Doi Inthanon |
|--------------------------------|-----------------------|----------------------|
| PSNM | | 2,198,262 |
| Calibrator | 10,197 | 12,123 |
| IGY in Potchefstroom | 216,767 | 215,230 |
| Efficiency ratio (R_{eff}) | 1.000 | 8.530 |

This ratio reflects the difference in the count rates of the two NMs due to their different design and environmental conditions. Therefore, to compare the count rate of NM2 relative to NM1, the count rate of NM2 must be divided by this number.

The results for the Doi Inthanon relative to Potchefstroom (NM1) are reported. The Potchefstroom IGY is used as the standard (NM1), and therefore time interval t_1 is DOY 295 to 302 of 2008. Time t_2 is 98 to 110 of 2010 at Doi Inthanon (C9). After rejecting spurious counts, the 1-second count rates were integrated into hourly rates. Pressure uncorrected counts were used, because the monitors have the same atmosphere above them during each set of measurements. Table 3.2 shows the average count rate per hour and the ratio of efficiency of the monitors.

This procedure describes the essence of the calibration procedure. When about 10 neutron monitors are calibrated in this way, Prof. Moraal's group at Northwest U. will be ready to derive differential response functions from them.

3.2.3 Effect of the Building

To determine the effect of the building on the count rate ratio, we compared data for Configuration 8, with the calmon outdoors at a calmon height and water height as recommended for calibration purposes (Krüger & Moraal 2010), with those from Configuration 15, with the calmon inside the building. For these two configurations we collected 11.1×10^6 and 5.5×10^6 counts, respectively, and used the same (BRI) electronics, so we are able to precisely determine the small change in the Cal/NM ratio. This ratio was 0.005546(2) outdoors and 0.005722(3) indoors, for a change of $1.76(4) \times 10^{-4}$ and a percentage change of $(3.12 \pm 0.06)\%$.

CHAPTER IV

LATITUDE SURVEY INVESTIGATION OF GALACTIC COSMIC RAY SOLAR MODULATION DURING 1994-2007

4.1 Introduction

The Galactic cosmic ray (GCR) flux in the solar system is strongly influenced by solar variations (Forbush 1954), a process known as solar modulation. Solar modulation itself is dominated by the roughly 11-year sunspot cycle in which the Galactic cosmic ray flux decreases during sunspot maximum, the time period of maximum solar activity, and increases during sunspot minimum (Figure 4.1). This can be described by a spherically symmetric model with a single “modulation” parameter related to the solar wind speed and the GCR diffusion coefficient, such as the force-field model (Gleeson & Axford 1968).

However, as described in Section 1.1.3, there is also a roughly 22-year GCR variation corresponding to the solar magnetic cycle, wherein the dominant solar magnetic polarity reverses at each sunspot maximum (Thambyahpillai & Elliot 1953). In other words, 11-year periods with opposite magnetic polarity exhibit distinct GCR variations. These effects are associated with a variety of interesting phenomena, such as guiding center drifts, latitudinal GCR gradients, particle charge sign dependence, and changing diffusion coefficients (e.g., Jokipii & Levy 1977; Garcia-Munoz et al. 1986; Bieber & Chen 1991). These phenomena depend on the sign of qA , where q is the particle charge and A is the solar magnetic polarity.

Effects of solar magnetic polarity are clearly seen in the GCR flux as a function of time, which is more “pointy” or “flat-topped” in alternating sunspot cycles (Jokipii & Thomas 1981; Webber & Lockwood 1988, see Figure 1), and by comparing fluxes of particles of the same charge to mass ratio but opposite charge sign, such as electrons to positrons or protons to antiprotons (Bieber et al. 1999). There are many

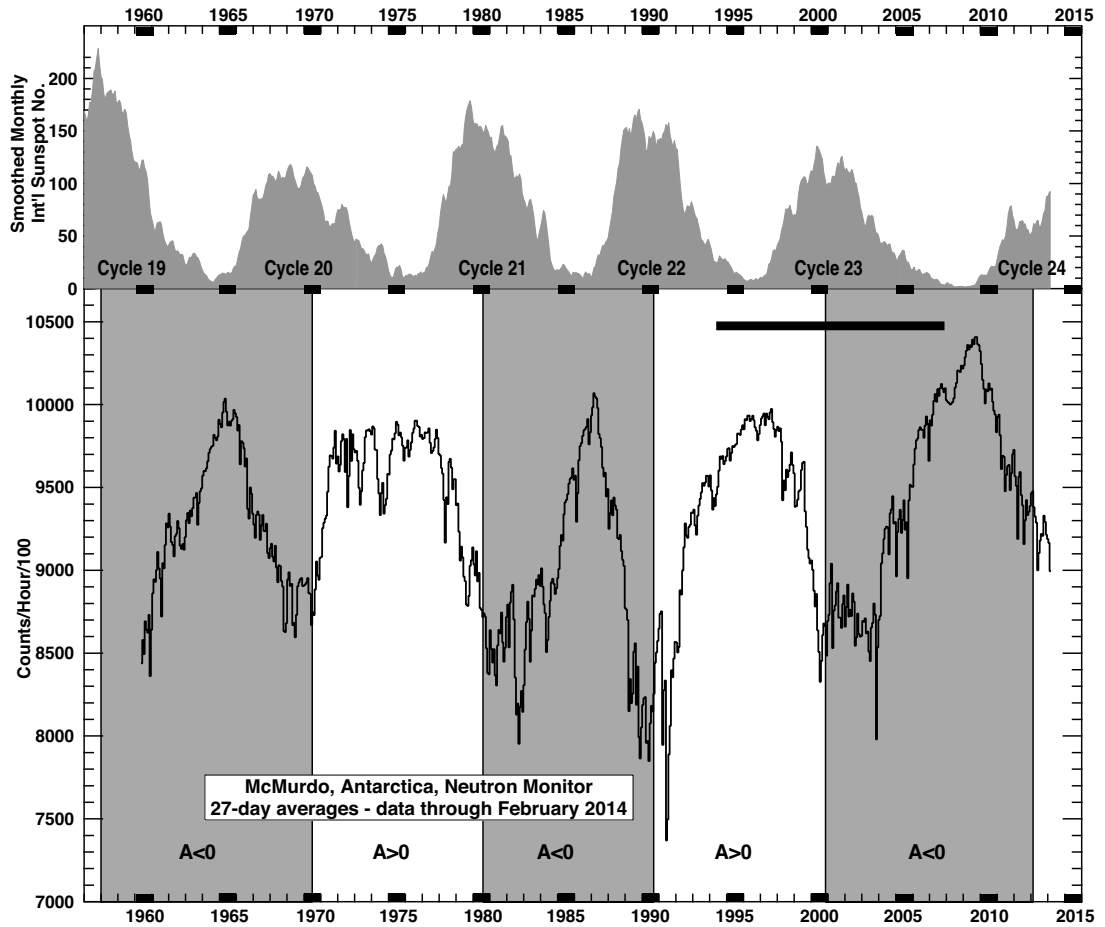


Figure 4.1: Smoothed monthly international sunspot number (using 5-month boxcar smoothing) and McMurdo neutron monitor count rate as a function of time. The long-term drift at McMurdo has been corrected following Oh et al. (2013). A neutron monitor count rate indicates the Galactic cosmic ray flux, which undergoes “solar modulation” in association with solar activity. Solar modulation includes dramatic 11-year variations with the sunspot cycle, and a 22-year variation with the solar magnetic cycle, seen here in changes in the solar modulation pattern between positive ($A > 0$) and negative ($A < 0$) magnetic polarity. In this work we present observations of spectral changes in Galactic cosmic rays in association with solar modulation and changing solar magnetic polarity for the time period 1994-2007, indicated by a horizontal bar.

more subtle manifestations as well. One of the most puzzling aspects of modulation phenomenology is the so-called “crossover” in spectral form during opposite magnetic polarity epochs. This has been observed by means of ship-borne neutron monitor surveys

that study the GCR spectrum by traveling across a wide range of geomagnetic cutoff rigidities. With significant reliance on the work of Webber & Lockwood (1988), Moraal et al. (1989) extensively discussed and characterized the effect by comparing neutron monitor response functions obtained at solar minima separated by 11-year intervals (opposite magnetic polarity) and 22-year intervals (same magnetic polarity). They reported a crossover at a rigidity (momentum per charge) of approximately 6 GV in spectra taken during opposite polarity epochs. Intensities at different energies are not uniformly higher or lower. In the negative polarity state the low energy fluxes are suppressed while the high energy fluxes are enhanced, with just the opposite being true in the positive polarity state.

Reports of crossovers in the literature have usually compared observations at two different time periods “near solar minimum,” but it has recently become clear that different solar minima can have different levels of solar modulation (Oh et al. 2013). The question of whether or at what rigidity the spectra intersect at successive solar minima depends on the relative level of modulation at the two time periods. Actually, the key physical issue is whether solar modulation of GCR spectra is independent of solar magnetic polarity for similar modulation conditions. Such a polarity dependence can be demonstrated by the existence of a spectral crossover at any similar modulation conditions for different magnetic polarities, or equivalently, if a model of solar modulation that matches the GCR spectral evolution during one solar magnetic polarity systematically deviates from that for the opposite polarity. Additional questions that immediately come to mind involve the transition in solar modulation from one polarity state to the other. Is this transition smooth or abrupt? Alternatively, the crossover might be a phenomenon that appears as a result of some special conditions that appear and disappear only very near solar minimum. To investigate the nature of this transition, a series of neutron monitor latitude surveys was conducted between 1994 and 2007 by the Bartol Research Institute of the University of Delaware, the University of Tasmania, and the Australian Antarctic Division. In this thesis we discuss the analysis of the data from these surveys and show that the data indicate that the crossover is most probably associated with a major transition in some aspect of modulation that occurs nearly simultaneously with the solar polarity reversal.

4.2 Observations

As described in Section 1.1.2, the count rate of a mobile neutron monitor can be expressed in terms of an effective “cutoff” rigidity P_c , which depends on latitude, longitude, zenith angle, azimuth, and time. In this case the relation becomes:

$$N(P_c, h, t) = \int_{P_c}^{P_L} \sum_i G_i(P) M_i(P, t) Y_i(P, h) dP. \quad (4.1)$$

In our analysis, data from the mobile (ship-borne) neutron monitor are pressure-corrected to standard sea level (760 mm Hg), so we remove the dependence on h . The mobile monitor rapidly moved in P_c , while the solar modulation, M_i , varied slowly over a scale of years. (Note that temporary Forbush decreases due to solar activity are excluded from our analysis.) Therefore, $N(P_c, t)$ can be measured as a function of P_c at nearly constant t , and in this sense is commonly referred to as the (integral) response function for a neutron monitor at epoch t .

The integrand of this simplified equation is referred to as the differential response function (DRF). Measuring the signal in the detector at two different geomagnetic cutoffs P_c and subtracting one measurement from the other determines the response of the detector to that little part of the spectrum lying between the two cutoffs. When divided by the small difference in cutoff this gives the DRF directly. For physical interpretation of the DRF, a common assumption is that G_i , M_i , and Y_i are independent of particle species i up to a constant, which is absorbed in the factors so that the sum in Equation (4.1) is replaced by the product $G(P)M(P, t)Y(P)$. (Note that measurement of the DRF does *not* require this assumption.) Then when an identical detector is used in successive surveys, a fractional change in the DRF is interpreted as a fractional change in the spectrum $G(P)$, which can be determined without knowledge of the yield function.

In our series of surveys, atmospheric neutrons were detected by a ship-borne mobile neutron monitor as described in Section 2.4. Figure 4.2(a) shows the other point of view of the TasVan (in contrast with Figure 2.16) and Figure 4.2(b) shows the ship-borne neutron monitor inside the container.

The 3NM64 mobile monitor was operated during 1994–2007 aboard one of two U.S. Coast Guard icebreakers, the *Polar Sea* or the *Polar Star* (see Figure 4.2), which traversed the Pacific Ocean from Seattle, USA to McMurdo, Antarctica and back during a ~6-month voyage. We refer to a “survey year” by the year in which the

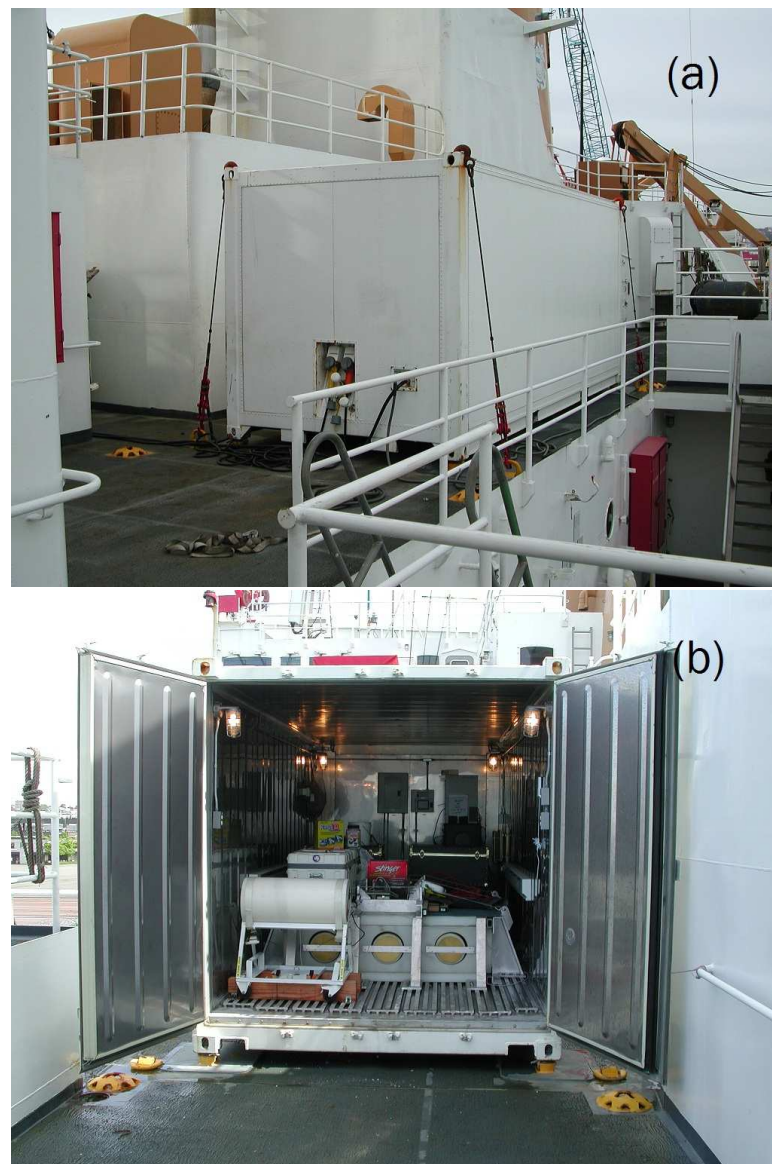


Figure 4.2: (a) Insulated container (“TasVan”) used for 3NM64 neutron monitor latitude surveys on the *Polar Star* and *Polar Sea*. (b) 3NM64 installed inside the container. For this and several other voyages a small calibration neutron monitor (Krüger et al. 2008a) was installed near the door.

voyage began; each voyage then extended throughout the Austral Summer into the next calendar year. For example, data for “survey year 1997” refer to data of the voyage from October, 1997 to April, 1998. We obtained data for 13 consecutive survey years (from 1994 to 2006). The geographic routes of all surveys are plotted in Figure 4.3; also shown for reference are contours of constant 1980 vertical effective geomagnetic cutoff rigidity.

During survey year 1994, the ship traveled from Hobart, Australia to McMurdo, maneuvered three quarters of the way around Antarctica, and then passed through the Straits of Magellan. Data taking ended near the Equator. In survey year 1995, the data were recorded starting in San Diego, USA, and from there to McMurdo, where the data taking stopped. In survey years 1996 and 1998, the ship started from Seattle and crossed the Pacific Ocean with stopovers in Honolulu, Hawaii and Hobart before going to McMurdo, then returning to Seattle with a stopover in Adelaide, Australia and passing near Thailand, the region of the world's highest cutoff rigidity. The routes of survey years 1997 and 1999 started from Seattle and crossed the Pacific Ocean with a stopover in Honolulu before going to McMurdo and back to Seattle passing through Mazatlán, Mexico. In survey years 2000, 2002–2004, and 2006, the ship traveled from Seattle via Honolulu to McMurdo and returned the same way, while in survey year 2001, the ship returned via Valparaíso, Chile. In survey year 2005, the data were recorded starting in McMurdo, and from there via Honolulu to Seattle. The details of the survey routes and latitude and longitude for all port calls are indicated in Tables 4.1 - 4.13, listing only times when data were taken.

In addition to the mobile neutron monitor and data acquisition systems, a variety of additional equipment was carried in the TasVan, as described in Section 2.4. A special feature of the electronics, started in the 1995 survey year, was the measurement of histograms of neutron time delay, i.e., the time interval from the detection of one neutron to the next (Bieber et al. 2004). The time delay spectrum is related to the energy distribution of cosmic rays impinging on the atmosphere. It depends strongly on the cutoff rigidity, and in principle could be analyzed to provide some additional information about the cosmic ray spectrum during the surveys (Mangeard et al., in preparation).

During survey year 1994, the ship's "sea state" was recorded as the measure of pitch and roll. In order to directly monitor orientation effects on the mobile monitor count rate we installed clinometers, i.e., sensors of inclination (see Section 2.4), for the remaining surveys (starting in survey year 1995) to measure the pitch and roll each second. The clinometers were composed of redundant sensors located on board in the card cage in the electronics rack. The output of each sensor provided three analog signals giving the inclination along two axes and the unit temperature. Counts from the 3NM64 were recorded once per second, together with data from the clinometers.

Once per minute, pressure data and the GPS-derived latitude, longitude and time were recorded. In our subsequent data analysis, the pitch and roll were found to have only a minor effect so the data in the present analysis were not corrected for the pitch and roll.

During certain survey years, additional neutron detection equipment was included. Bare neutron counters were mounted in the 1995-1996 survey year, which permitted a calibration of the bare counter to neutron monitor count ratio as a function of the cutoff rigidity. A compact calibration neutron monitor was mounted near the access door during several surveys to test its operation and calibrate it against the standard monitor (Krüger et al. 2008a).

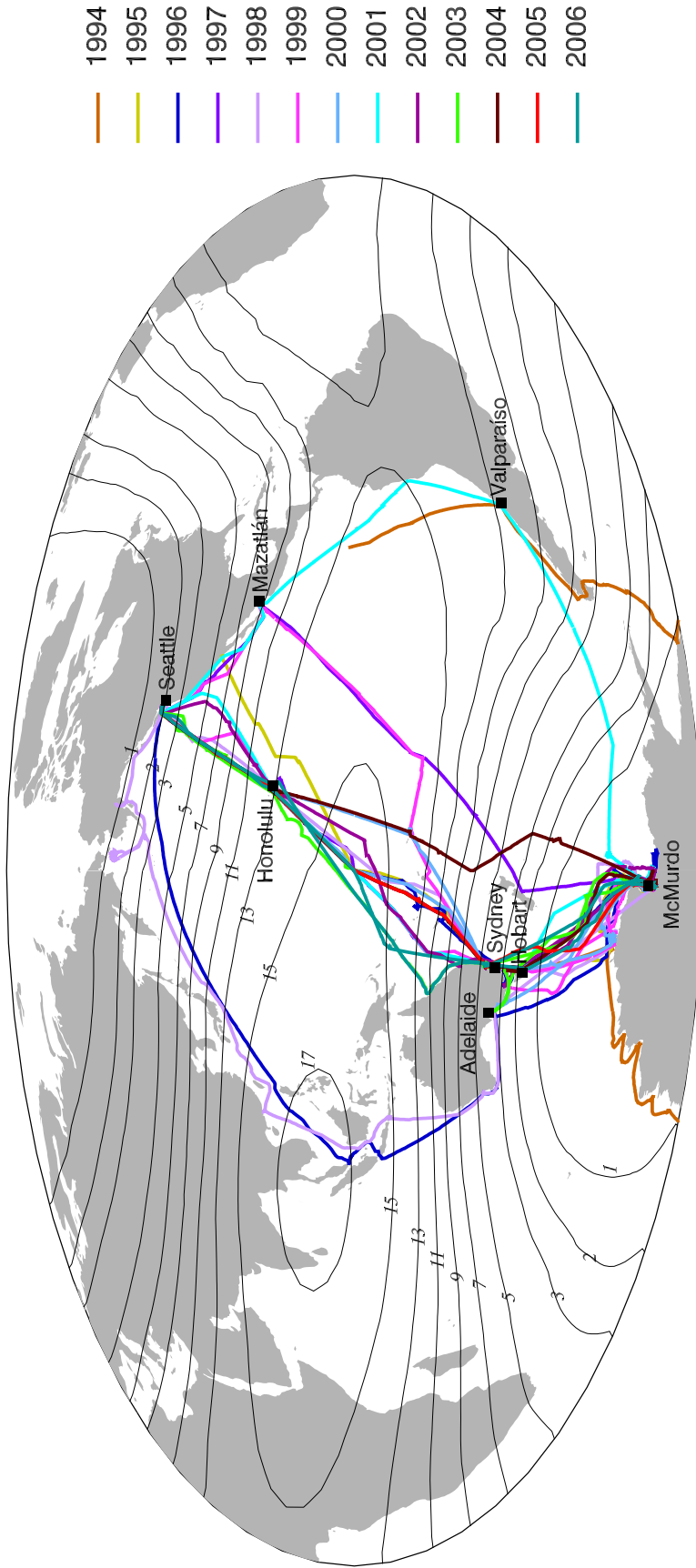


Figure 4.3: The track of the ship-borne neutron monitor latitude surveys for 1994–2007, superimposed on contours of the vertical cutoff rigidity indicated by black solid lines. Italic numbers at each contour indicate the vertical cutoff rigidity in GV.

Table 4.1: Route of the 1994-1995 voyage

| Location | Latitude (degrees N) | Longitude (degrees E) |
|------------------------------|-----------------------------|------------------------------|
| Hobart, Australia (START) | -43 | +147 |
| McMurdo, Antarctica | -77 | +166 |
| South of Capetown, S. Africa | -69 | +18 |
| Greenwich Meridian | -69 | 0 |
| Straits of Magellan | -53 | -70 |
| Valparaíso, Chile | -33 | -72 |
| Equator | 0 | -91 |
| (END) | +1 | -96 |

Table 4.2: Route of the 1995-1996 voyage

| Location | Latitude (degrees N) | Longitude (degrees E) |
|------------------------|-----------------------------|------------------------------|
| San Diego, USA (START) | +32 | -117 |
| Equator | 0 | -179 |
| Sydney, Australia | -33 | +151 |
| Hobart | -43 | +147 |
| McMurdo | -76 | +166 |
| (END) | -56 | +154 |

Table 4.3: Route of the 1996-1997 voyage

| Location | Latitude (degrees N) | Longitude (degrees E) |
|----------------------|-----------------------------|------------------------------|
| Seattle, USA (START) | +47 | -122 |
| Honolulu, Hawaii | +21 | -157 |
| Equator | 0 | -179 |
| New Caledonia | -22 | +166 |
| Melbourne, Australia | -37 | +144 |
| Hobart | -43 | +147 |
| McMurdo | -76 | +169 |
| Adelaide, Australia | -34 | +138 |
| Perth, Australia | -32 | +115 |
| Java, Indonesia | -6 | +106 |
| Vietnam | +9 | +110 |
| Equator | 0 | +106 |
| Seattle (END) | +47 | -122 |

Table 4.4: Route of the 1997-1998 voyage

| Location | Latitude (degrees N) | Longitude (degrees E) |
|-----------------------|-----------------------------|------------------------------|
| Seattle (START) | +47 | -122 |
| Honolulu | +21 | -157 |
| Equator | 0 | -179 |
| Sydney | -33 | +151 |
| Hobart | -43 | +147 |
| McMurdo | -76 | +168 |
| Wellington, Australia | -42 | +175 |
| Equator | 0 | -133 |
| Mazatlán, Mexico | +22 | -107 |
| San Francisco, USA | +37 | -122 |
| Seattle (END) | +47 | -122 |

Table 4.5: Route of the 1998-1999 voyage

| Location | Latitude (degrees N) | Longitude (degrees E) |
|-----------------|-----------------------------|------------------------------|
| Seattle (START) | +47 | -122 |
| Honolulu | +21 | -157 |
| Equator | 0 | -175 |
| Sydney | -33 | +151 |
| Hobart | -43 | +147 |
| McMurdo | -76 | +168 |
| Adelaide | -34 | +138 |
| Perth | -32 | +115 |
| Java | -8 | +115 |
| Vietnam | +12 | +112 |
| Hong Kong | +22 | +114 |
| Seattle (END) | +47 | -122 |

Table 4.6: Route of the 1999-2000 voyage

| Location | Latitude (degrees N) | Longitude (degrees E) |
|------------------|-----------------------------|------------------------------|
| Seattle (START) | +47 | -122 |
| Honolulu | +21 | -157 |
| Equator | 0 | -179 |
| Sydney | -33 | +151 |
| Hobart | -43 | +147 |
| McMurdo | -76 | +168 |
| Melbourne | -37 | +144 |
| French Polynesia | -17 | -151 |
| Equator | 0 | -133 |
| Mazatlán | +22 | -107 |
| San Francisco | +37 | -122 |
| Seattle (END) | +47 | -122 |

Table 4.7: Route of the 2000-2001 voyage

| Location | Latitude (degrees N) | Longitude (degrees E) |
|-----------------|-----------------------------|------------------------------|
| Seattle (START) | +47 | -122 |
| Honolulu | +21 | -157 |
| Equator | 0 | -179 |
| Sydney | -33 | +151 |
| Hobart | -43 | +147 |
| McMurdo | -76 | +168 |
| Adelaide | -34 | +138 |
| Sydney | -33 | +151 |
| American Samoa | -14 | -169 |
| Equator | 0 | -165 |
| Honolulu | +21 | -157 |
| Seattle (END) | +47 | -122 |

Table 4.8: Route of the 2001-2002 voyage

| Location | Latitude (degrees N) | Longitude (degrees E) |
|-------------------|-----------------------------|------------------------------|
| Seattle (START) | +47 | -122 |
| Honolulu | +21 | -157 |
| Equator | 0 | -179 |
| Sydney | -33 | +151 |
| Hobart | -43 | +147 |
| McMurdo | -76 | +168 |
| Valparaíso, Chile | -33 | -71 |
| Lima, Peru | -12 | -77 |
| Mazatlán | +22 | -107 |
| San Diego | +32 | -117 |
| Seattle (END) | +47 | -122 |

Table 4.9: Route of the 2002-2003 voyage

| Location | Latitude (degrees N) | Longitude (degrees E) |
|---------------------|-----------------------------|------------------------------|
| Seattle (START) | +47 | -122 |
| Honolulu | +21 | -157 |
| Equator | 0 | -179 |
| Sydney | -33 | +151 |
| Hobart | -43 | +147 |
| McMurdo | -76 | +168 |
| Melbourne | -37 | +144 |
| Brisbane, Australia | -27 | +153 |
| Equator | 0 | -170 |
| Seattle (END) | +47 | -122 |

Table 4.10: Route of the 2003-2004 voyage

| Location | Latitude (degrees N) | Longitude (degrees E) |
|-----------------------|-----------------------------|------------------------------|
| Seattle (START) | +47 | -122 |
| Honolulu | +21 | -157 |
| Equator | 0 | -179 |
| Sydney | -33 | +151 |
| McMurdo | -76 | +168 |
| Adelaide | -34 | +138 |
| Melbourne | -39 | +143 |
| Sydney | -33 | +151 |
| Townsville, Australia | -19 | +146 |
| Equator | 0 | +174 |
| Seattle (END) | +47 | -122 |

Table 4.11: Route of the 2004-2005 voyage

| Location | Latitude (degrees N) | Longitude (degrees E) |
|-----------------|-----------------------------|------------------------------|
| Seattle (START) | +47 | -122 |
| Honolulu | +21 | -157 |
| Equator | 0 | -179 |
| Sydney | -33 | +151 |
| Hobart | -43 | +147 |
| McMurdo | -76 | +168 |
| American Samoa | -14 | -169 |
| Equator | 0 | -164 |
| Honolulu | +21 | -157 |
| Seattle (END) | +47 | -122 |

Table 4.12: Route of the 2005-2006 voyage

| Location | Latitude (degrees N) | Longitude (degrees E) |
|-----------------|-----------------------------|------------------------------|
| McMurdo (START) | -78 | +164 |
| Sydney | -33 | +151 |
| Equator | 0 | -179 |
| Honolulu | +21 | -157 |
| Seattle (END) | +47 | -122 |

Table 4.13: Route of the 2006-2007 voyage

| Location | Latitude (degrees N) | Longitude (degrees E) |
|-----------------|-----------------------------|------------------------------|
| Seattle (START) | +47 | -122 |
| Honolulu | +21 | -157 |
| Equator | 0 | -179 |
| McMurdo | -76 | +168 |
| Townsville | -19 | +146 |
| Equator | 0 | +174 |
| Honolulu | +21 | -156 |
| Seattle (END) | +47 | -122 |

4.3 Data Preparation

We developed a program that allows the user to “read,” reformat, and/or process the DAT files. These have all of the data from the latitude surveys in them. We started with the latest group of the survey data and worked backwards to make it easier to see the small changes in format for each year. It is important to know the main pattern of existing data in order to write or edit the appropriate program. We use a Visual Basic (VB) program to produce “Minute” files that give the fraction of the day of year (DOY) and accumulated counts of 3NM64 and produce “Baro” files that give the pressure data from the Digiquartz and/or AIR barometer. Then, we produce a “course” file that gives the ship position and barometer reading for each hour of the voyage. We used a personal computer that runs Windows 7 at the Bartol Research Institute, University of Delaware.

The next step was to understand the trajectory code described by Lin et al. (1995) and then use it to determine the apparent cutoff for every hour of data during all the voyages. The trajectory code was used to trace particles back through Earth’s magnetic field. In practice, antiparticles were traced along the reverse direction from the atmosphere above the monitor. If antiparticles can escape out of Earth’s magnetosphere, then likewise the cosmic ray particles can enter the atmosphere from space. We have to trace in different ways for calculating the apparent cutoff rigidity. We used the trajectory code written as a Fortran program to apply to all latitude surveys to produce the “CUTOFFS” file. This can be done with two computer clusters. The first cluster is the Mills community cluster. It consists of 200 computer nodes (5160 cores, 14.5 TB memory) running at the University of Delaware. The second cluster is the Galaxy cluster. It consists of about 24 quad-core 64-bit machines, each with approximately 4 GB of RAM running in the Space Physics and Energetic Particles Lab, Mahidol University. If we run the program on a usual personal computer, we spend ~ 14 hours to process one day of data on average, but spend much less time if we separate jobs and run the program on clusters.

The next step after obtaining the CUTOFFS files for all survey years is to produce the “Binsum” files by using a VB program. The Binsum VB program includes the average values of the barometer, the modulation level, and the geomagnetic cutoff in the records. They are simply internally indexed by DOY, and the year is actually

implicit, so these files have to be constructed for each year. The Baro file can be made from “course” files, but the modulation level file has McMurdo neutron monitor data (and other stations) and the cutoff file is what we were working on calculating. The Binsum file gives the ship’s attitude (roll and pitch). We worked to determine the variation of the count rate with that ship attitude. We cannot see any evidence of the tilt fluctuations in the count rate, so we decided that no correction is needed.

Then finally, the most important file for our analysis is the “LatSur” file. This file format involves essential latitude survey data for further analysis. The steps above are presented in diagram form in Figure 4.4.

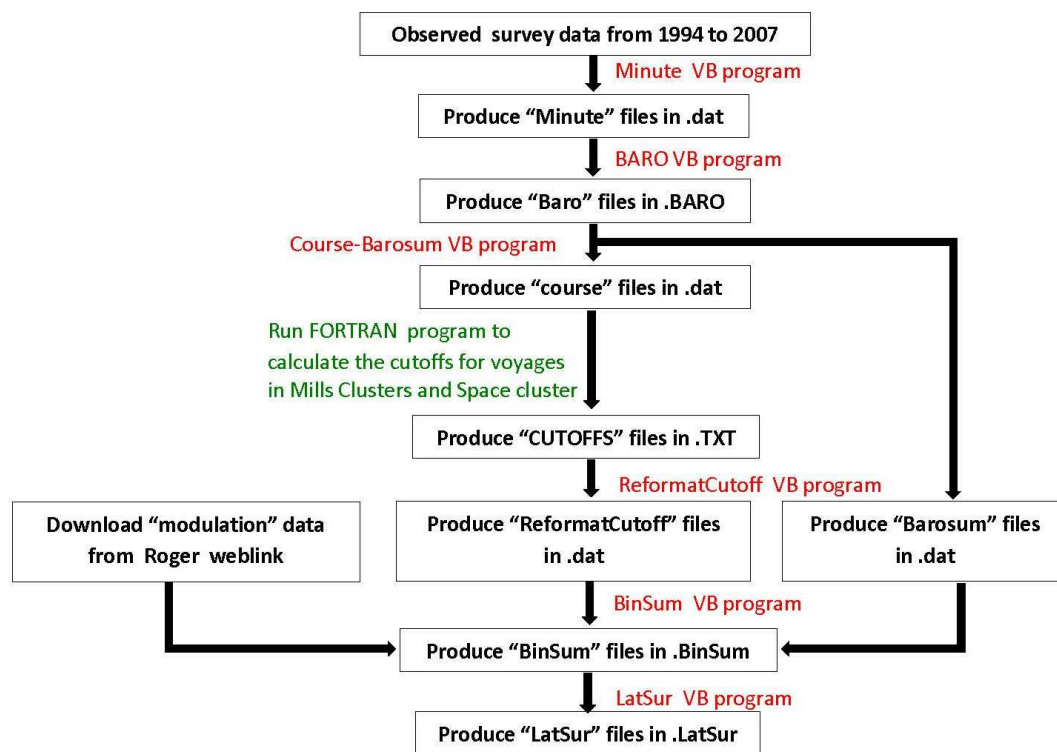


Figure 4.4: Diagram of the steps of preparation of the LatSur files for all survey years. In each step, we use different appropriate programs to produce the files needed. The LatSur files are the key files for scientific analysis of the survey data.

4.4 Data Reduction

The count rates of the three detector tubes (which we refer to as T1, T2 and T3), of which examples are shown in Figure 4.5, were corrected for errors in several steps. In the first step, we considered the three tube ratios T1/T2, T2/T3, and T3/T1 for each data interval. The data interval duration was 1 h for survey year 1994 and 30 min for subsequent survey years. The rough and changing conditions on board the ships caused the response of individual tubes to occasionally change, become noisy, or even stop completely. In order to correct for these effects during the surveys we used the inherent redundancy of the three detectors. We identified time intervals with anomalous tube ratios by comparing the tube ratios with the average tube ratios for the whole survey, which we call S1/S2, S2/S3 and S3/S1. Then we calculated a corrected count rate from the actual count rate of the properly operating detectors. If only one tube was ignored, e.g., if T1 was removed, we calculated the corrected count rate from $[(S1+S2+S3)/(S2+S3)] \times (T2+T3)$. If two tubes were removed we similarly used the remaining tube to determine the corrected count rate. If none of the tubes was operating properly the result was a data gap. We took records of all changes in the first correction for all surveys, an example of which is shown in Table A.1 of Appendix A.

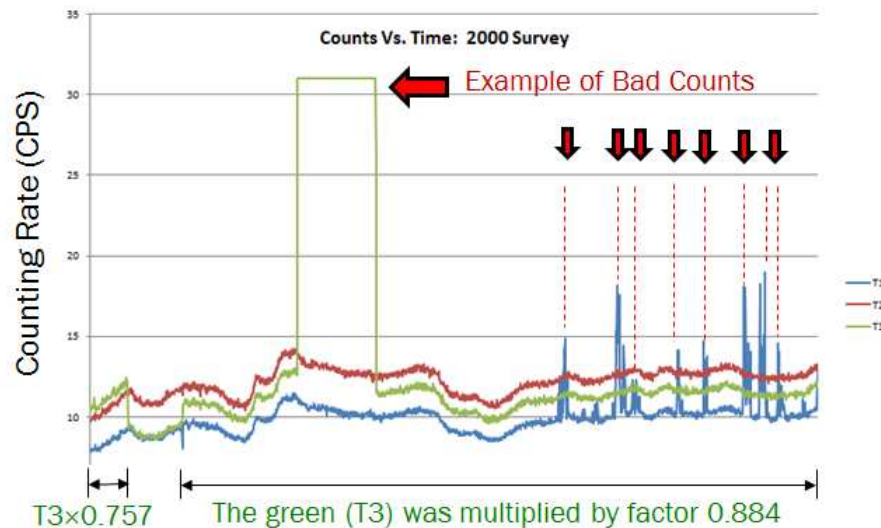


Figure 4.5: An example of the count rates for each tube vs. time in survey year 2000, including some bad count rates for individual tubes.

For the second step of correction, we calculated the daily average tube ratios for all surveys and plotted them on one long plot as a function of time. With

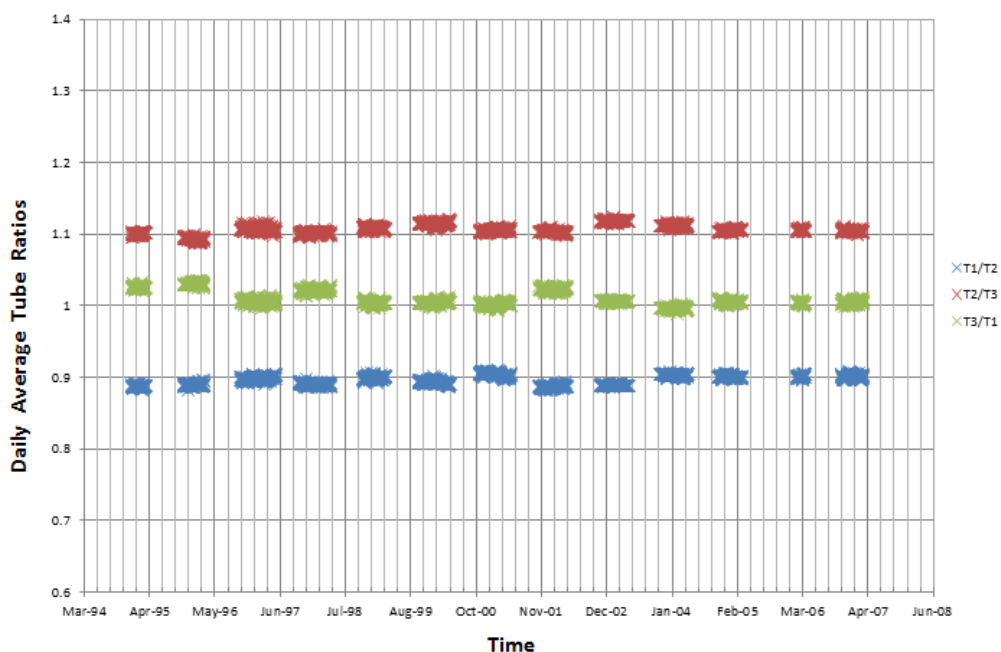


Figure 4.6: The count rates as a function of time for all survey years after applying the second step of correction in the analysis

their greater statistical accuracy, the daily average tube ratios provide a much more sensitive indication of tube drifts or noise. We identified anomalous time periods by eye and applied corrections when possible; otherwise, the data were excluded. We also took records of all changes in the second correction for all surveys, an example of which is shown in Table A.2 of Appendix A. The results for all survey years after applying the second step of correction in the analysis are expressed in Figure 4.6.

Although the basic monitor assembly was quite similar each year, the Tas-Van was not always mounted on the ship in the same location or orientation. Additionally, in December of 2001 we moved the detector tubes to a nominally identical lead/polyethylene assembly in a new shipping container. (The old one had become leaky and impossible to maintain properly.) To develop a correction for such systematic changes, the count rate (corrected for pressure) of the McMurdo neutron monitor was used in a regression analysis with the mobile monitor count rate (corrected independently for pressure) when the ship was near McMurdo, i.e., in a roughly square 220×220 km² area centered on the McMurdo neutron monitor station, defined as $(77.85 \pm 2)^\circ\text{S}$, $(166.67 \pm 9.5)^\circ\text{E}$. The days of each year when the ship was near McMurdo are noted in Table 4.14.

Table 4.14: Days of each year when the ship was near McMurdo as described in the text

| Survey year | Near McMurdo | |
|-------------|--------------|---------|
| | START | END |
| 1994-1995 | 370.000 | 407.375 |
| 1995-1996 | 369.242 | 385.490 |
| | 389.238 | 398.986 |
| 1996-1997 | 366.560 | 400.420 |
| 1997-1998 | 360.193 | 411.873 |
| 1998-1999 | 367.015 | 376.988 |
| 1999-2000 | 367.026 | 400.307 |
| | 405.931 | 412.899 |
| 2000-2001 | 363.290 | 385.779 |
| | 388.828 | 407.992 |
| | 410.252 | 411.798 |
| | 412.476 | 417.833 |
| 2001-2002 | 353.176 | 354.933 |
| | 356.754 | 399.341 |
| | 399.425 | 400.737 |
| | 403.913 | 404.231 |
| | 404.358 | 407.726 |
| 2002-2003 | 358.744 | 428.353 |
| 2003-2004 | 362.746 | 366.260 |
| | 368.419 | 402.077 |
| 2004-2005 | 354.374 | 356.893 |
| | 358.608 | 407.142 |
| 2005-2006 | 409.938 | 413.664 |
| 2006-2007 | 365.223 | 411.118 |

We used the mobile/McMurdo count rate ratio for the 2006 survey year, 0.194 ± 0.001 , as a reference. During most survey years, the ratio when the ship was near McMurdo was close to this value, but there were five survey years for which the data needed to be normalized. The normalization factors for survey years 1995, 1997, 1998, 1999, and 2000 were 1.015, 1.040, 1.039, 1.047, and 1.026, respectively. Figure 4.7 shows a single plot for all survey years of the mobile/McMurdo count rate ratio after normalized by these factors.

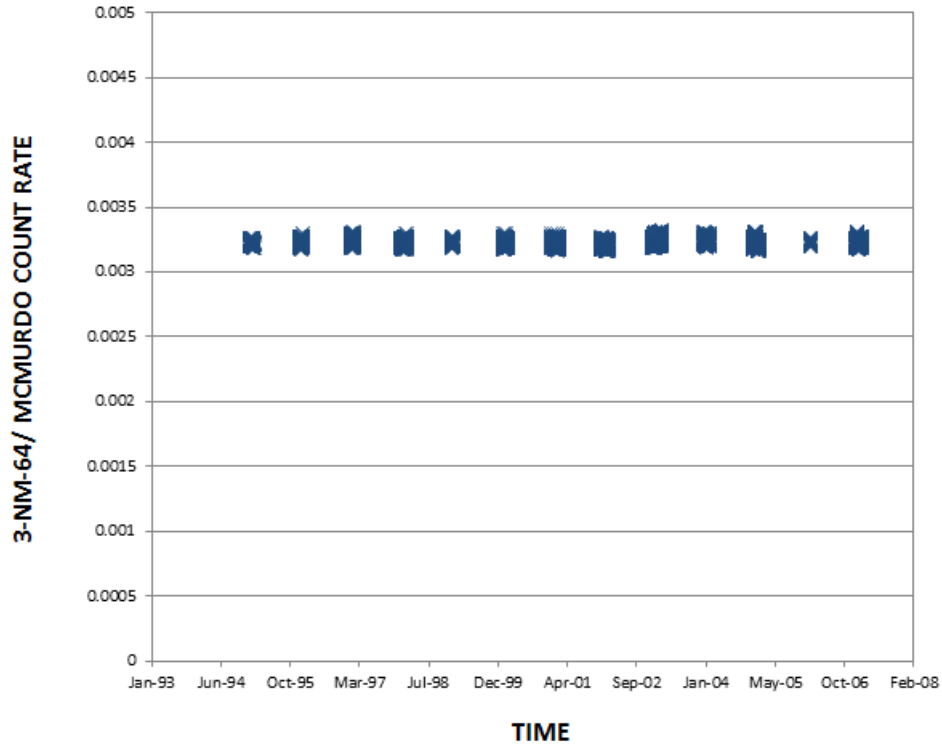


Figure 4.7: The mobile/McMurdo count rate ratio as a function of time after normalized by the factors explained in the text.

Proper correction for variations in barometric pressure is vital to the success of our project for two reasons. First, and most obvious, is the need to remove short term fluctuations from the data. Less obvious is the correlation of average barometric pressure with geographic latitude, causing a correlation with cutoff. We corrected to 760 mm Hg using an empirical pressure coefficient β in units of percent per mm Hg varying with cutoff rigidity as determined from our survey data (see more details in Appendix B):

$$\beta = 1.006 - 0.01534P_c, \quad (4.2)$$

$$C_{TP} = C_T e^{\beta(p-760)}, \quad (4.3)$$

where C_T is the mobile monitor count rate in units of s^{-1} corrected for tube anomalies and normalized to McMurdo, C_{TP} is the mobile monitor count rate in units of s^{-1} corrected for tube anomalies, normalized to McMurdo, and corrected for pressure, P_c is the apparent cutoff rigidity in units of GV, and p is the barometric pressure in units of mm Hg.

To generate a summary set of response functions we also applied a correction for short term variations in modulation level over the course of the survey based on variations in the McMurdo counting rate. First we determined regression coefficients between the normalized mobile neutron monitor count rate corrected for tube ratios and pressure and the McMurdo count rate corrected for pressure for each P_c bin, i.e., 0-1 GV, 1-2 GV, ..., 17-19 GV (where 17-18 GV and 18-19 GV were grouped together). We found that the regression coefficient S as a function of apparent cutoff rigidity P_c (see more details in Appendix C) was well fit by

$$S = 0.211e^{-0.141P_c}. \quad (4.4)$$

We then used this value of S to correct each survey year's mobile monitor data to the average McMurdo value for that survey year according to

$$C_{TPM} = C_{TP} - S(m - \bar{m}), \quad (4.5)$$

where C_{TPM} is the normalized mobile monitor count rate in units of s^{-1} corrected for tube anomalies, pressure, and short-term GCR variations m is the McMurdo count rate in units of s^{-1} , and \bar{m} is the average McMurdo count rate in units of s^{-1} for that survey year. Then C_{TPM} was used to determine the response functions. Figures 4.8-4.20(b) and 4.8-4.20(c) show the mobile monitor count rate for all survey years after applying all corrections.

Strong Forbush decreases (FDs) clearly did not follow the same regression relation as other short term rate fluctuations, so we excluded them from the dataset, treating the time intervals as data gaps. The criterion for rejection was a maximum percentage decrease (%D) > 10 in the McMurdo neutron monitor, which occurred three times during our mobile monitor surveys. The intervals that were excluded from our analysis due to the three FDs were: 1) from 2004 Nov 07 to 2004 Nov 18 (%D = 11.6), 2) from 2004 Jan 17 to 2004 Jan 26 (%D = 14.3), and 3) from 2006 Dec 06 to 2006 Dec 25 (% D = 10.8).

We also organized the data into survey "segments," where a segment is defined as a transition (in either direction) between high geomagnetic latitude (with low cutoff) and the cosmic ray (geomagnetic) equator (CRE, with high cutoff). We define "segment A" from the US West Coast to the CRE, "segment B" from the CRE to McMurdo, "segment C" from McMurdo to the CRE and "segment D" from the CRE

to Seattle. Each survey therefore could have up to four segments, which provide four distinct measurements of the response function. However, equipment failure or major Forbush decreases resulted in fewer than four available segments in the 1994, 1995, 2005, and 2006 survey years. In total, the 13 surveys provided 44 segments of data. The days of year (referring to the starting year of the survey) for each segment as used for the analysis are shown in Table 4.15.

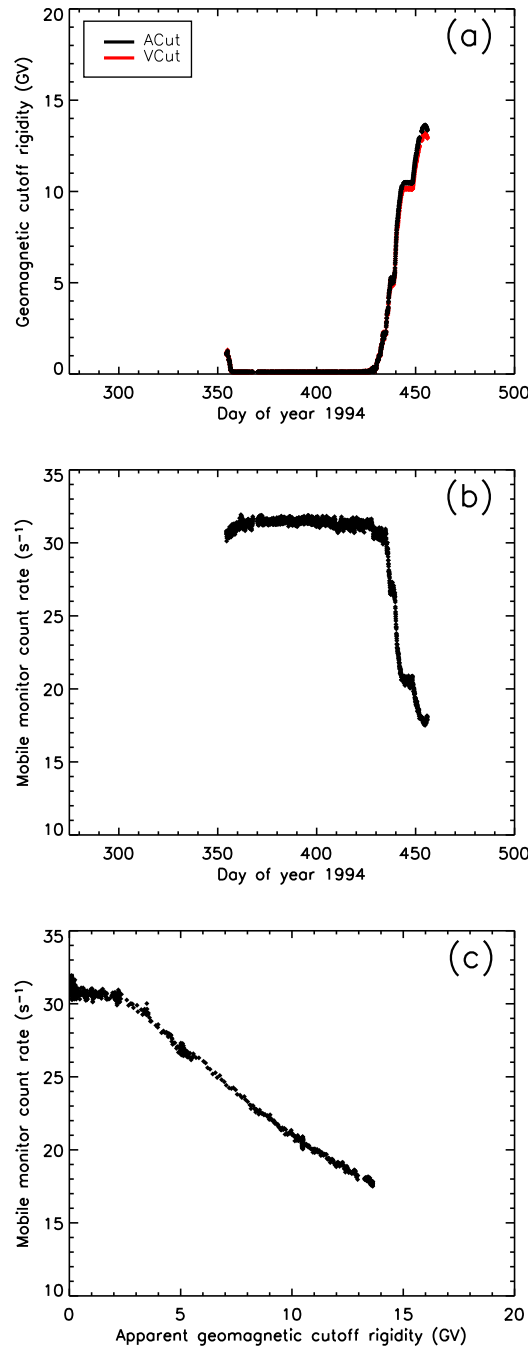


Figure 4.8: The data for the 1994 survey year. (a) Geomagnetic cutoff rigidity as a function of time. The black line traces the apparent geomagnetic cutoff rigidity while the red line shows the vertical effective cutoff rigidity. (b) Mobile (ship-borne) neutron monitor count rate after all corrections as discussed in the text. (c) Corrected count rate as a function of apparent geomagnetic cutoff rigidity for all four segments (i.e., the four transitions between low and high cutoff rigidity).

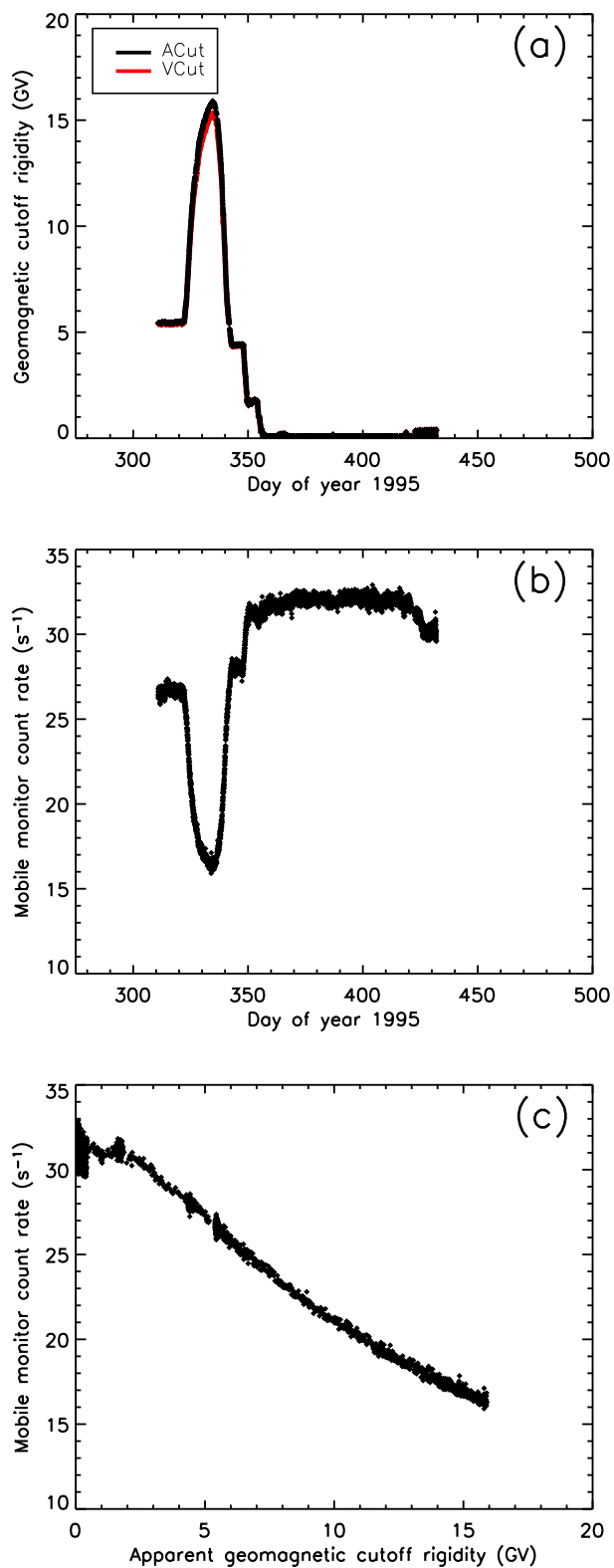


Figure 4.9: Like Figure 4.8, for the 1995 survey year.

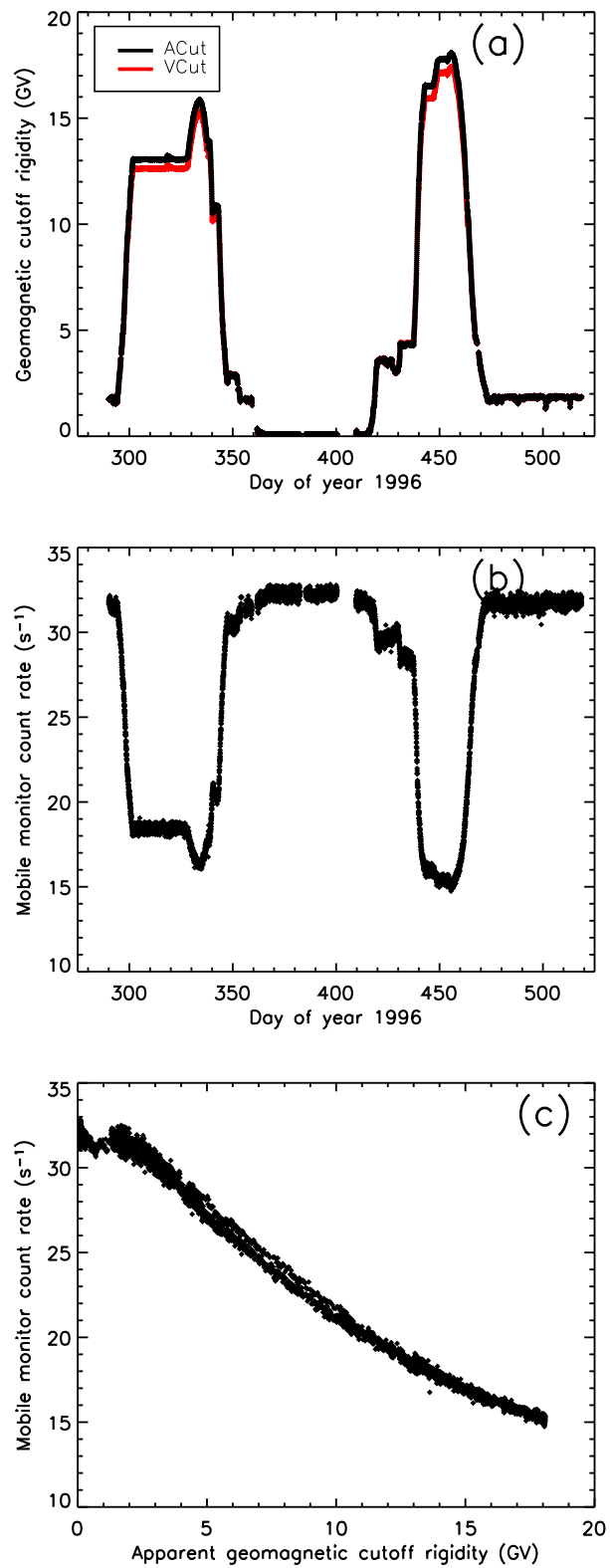


Figure 4.10: Like Figure 4.8, for the 1996 survey year.

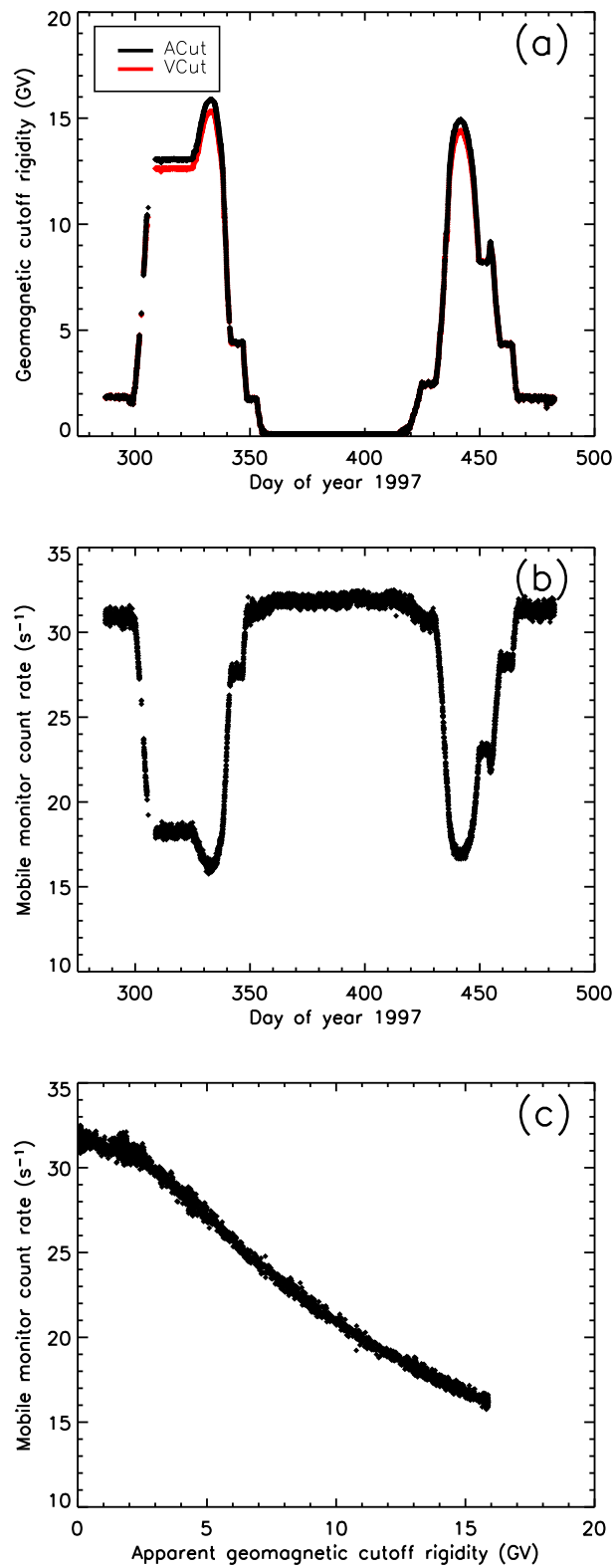


Figure 4.11: Like Figure 4.8, for the 1997 survey year.

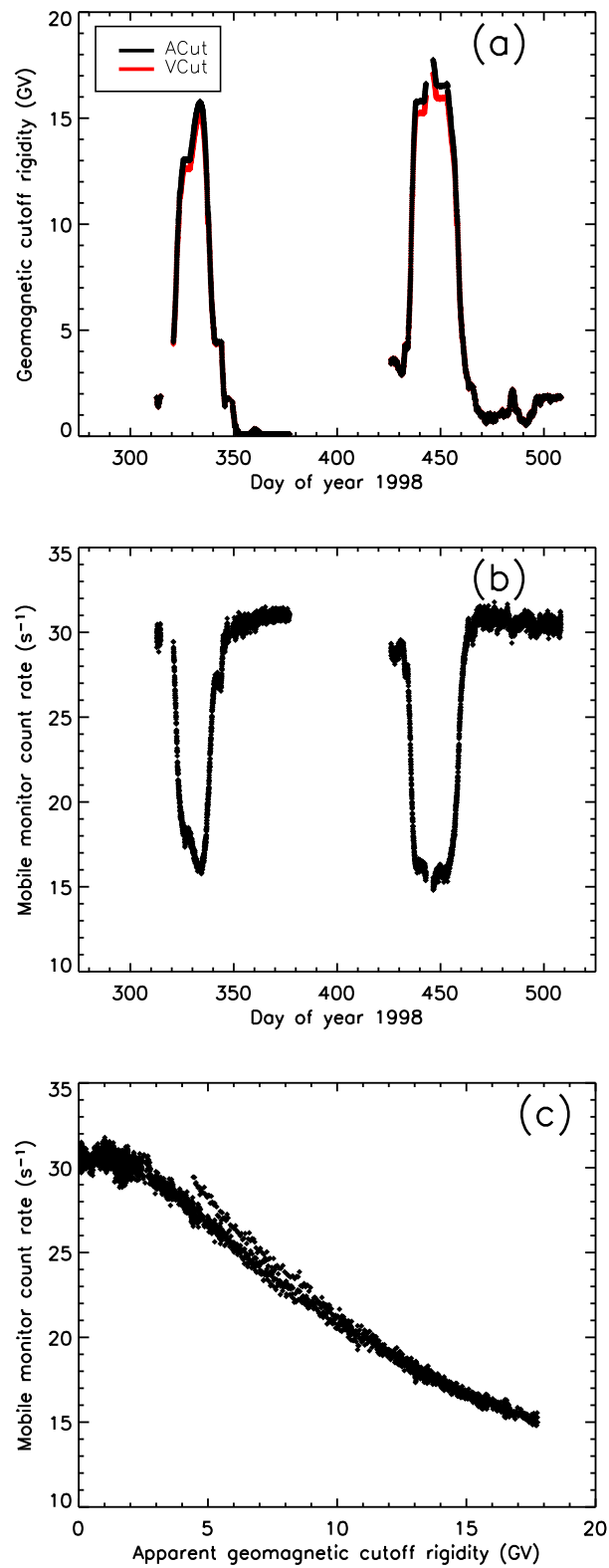


Figure 4.12: Like Figure 4.8, for the 1998 survey year.

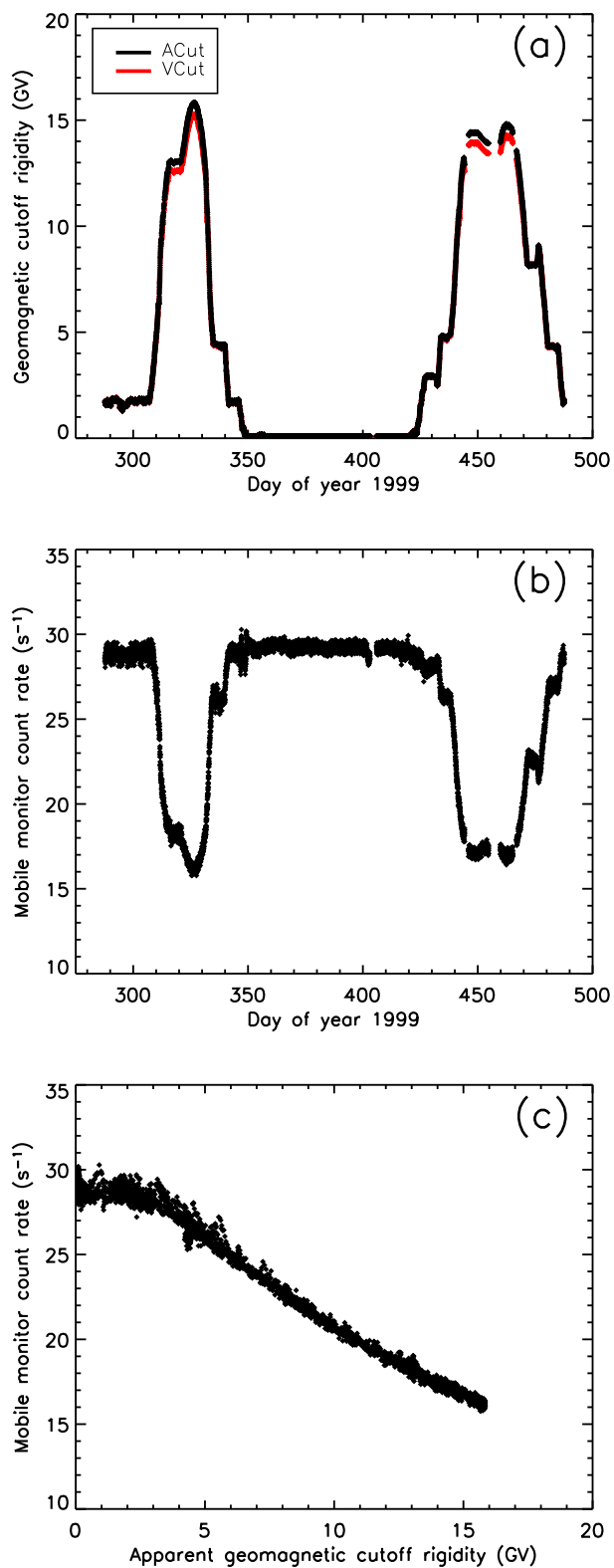


Figure 4.13: Like Figure 4.8, for the 1999 survey year.

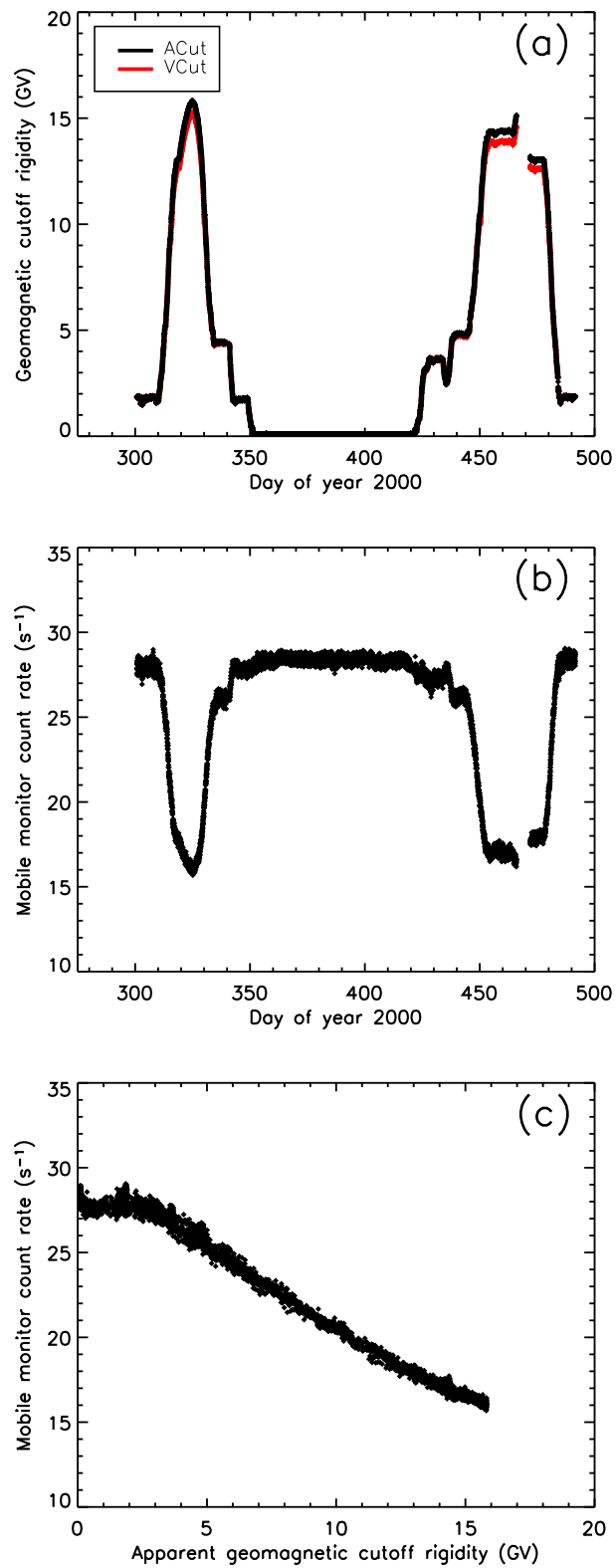


Figure 4.14: Like Figure 4.8, for the 2000 survey year.

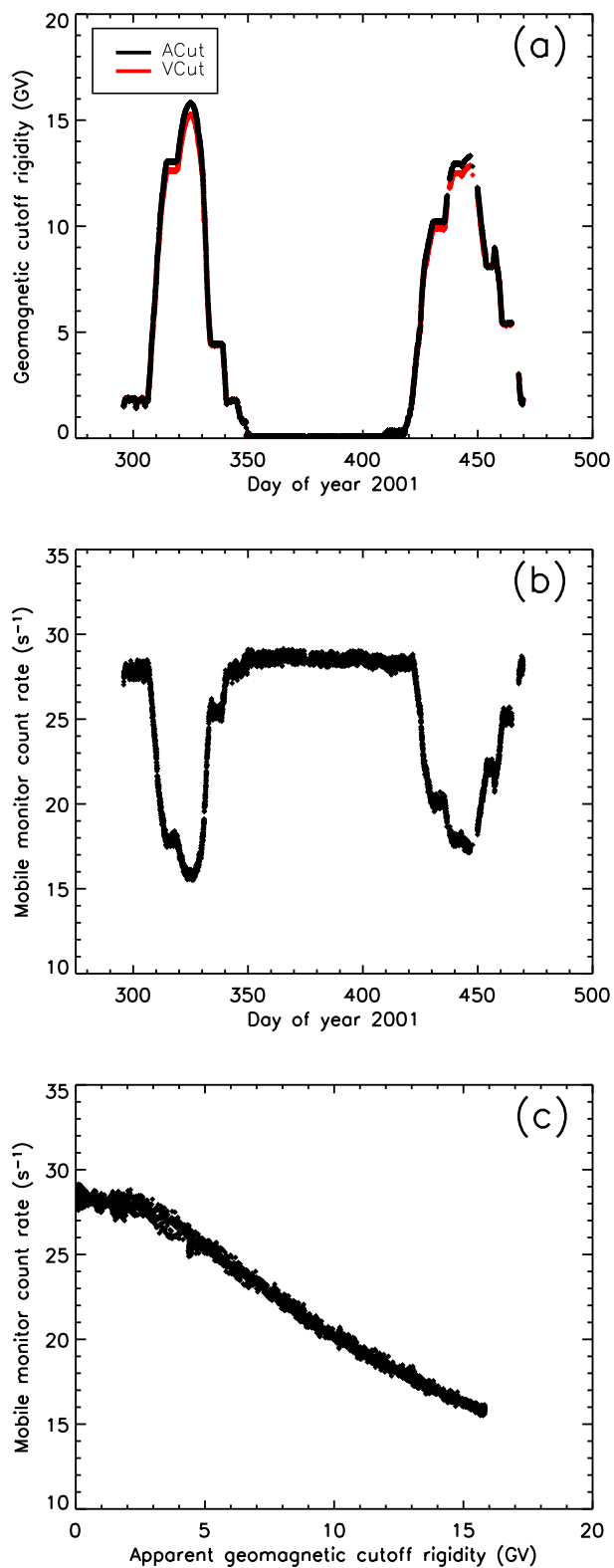


Figure 4.15: Like Figure 4.8, for the 2001 survey year.

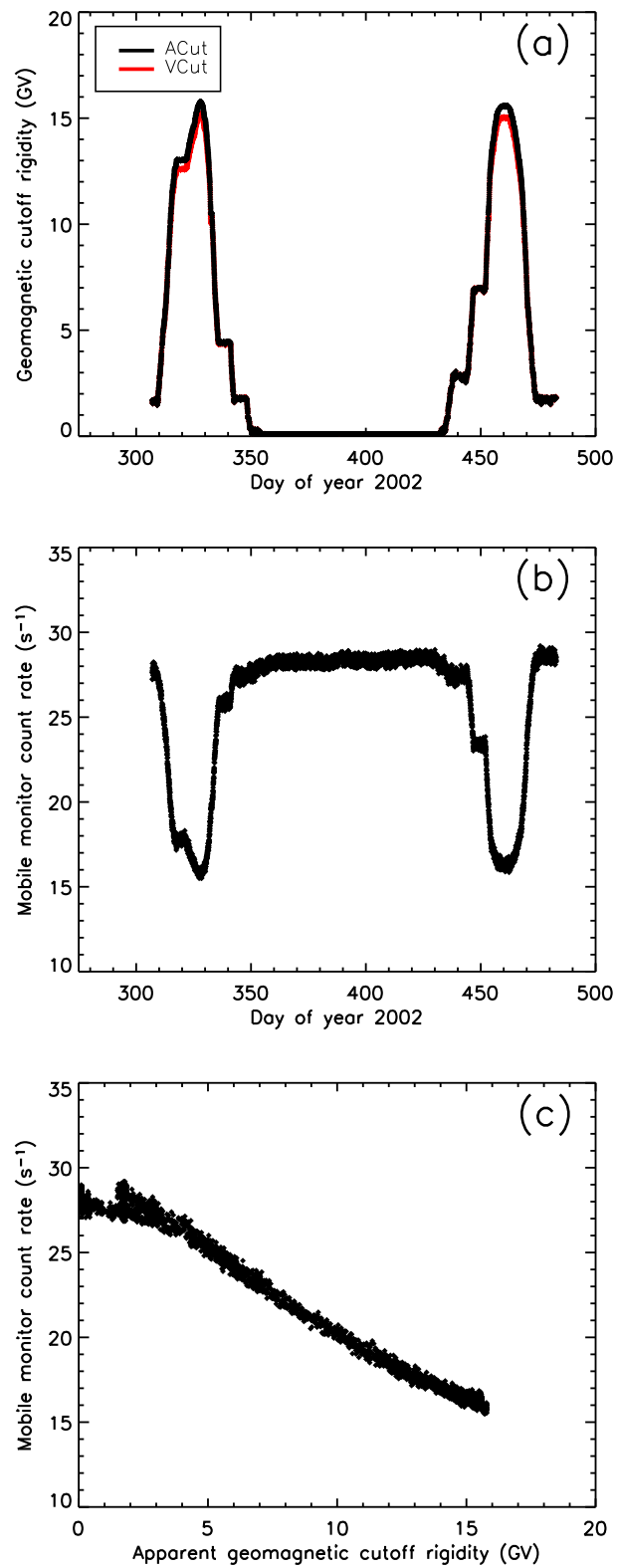


Figure 4.16: Like Figure 4.8, for the 2002 survey year.

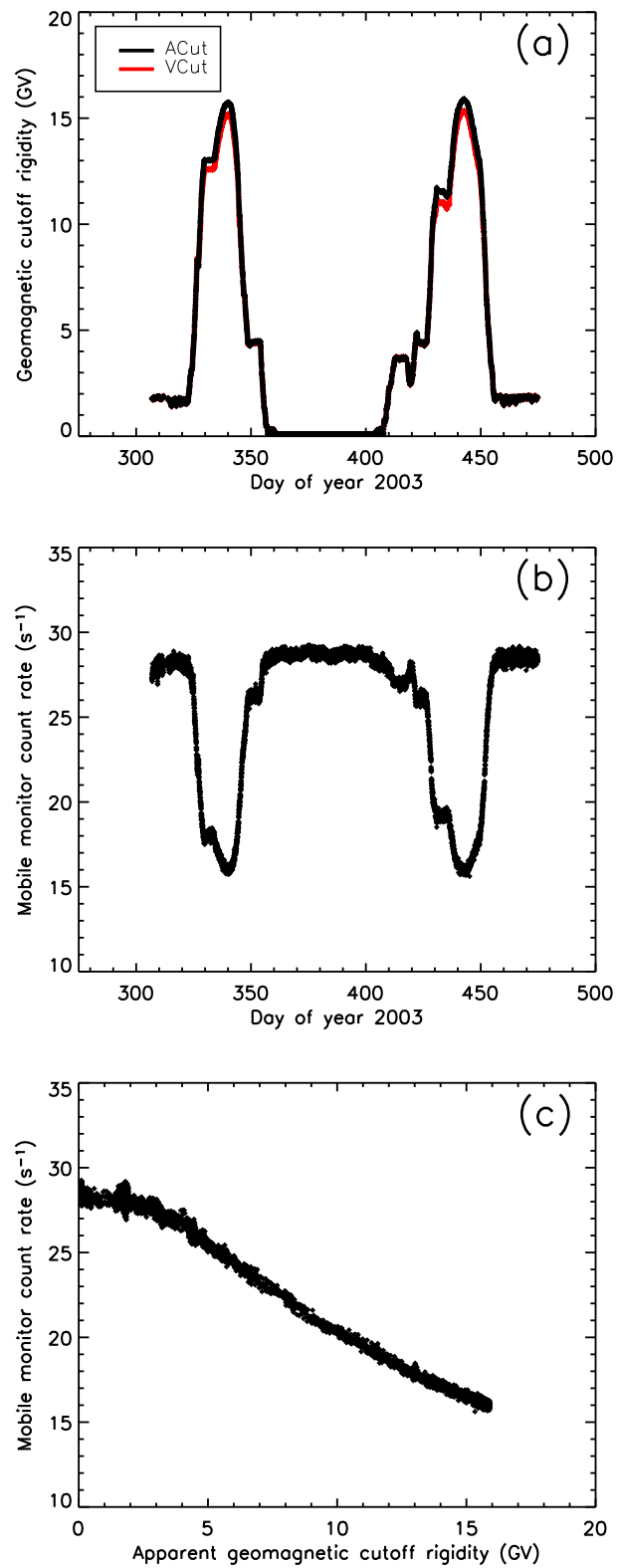


Figure 4.17: Like Figure 4.8, for the 2003 survey year.

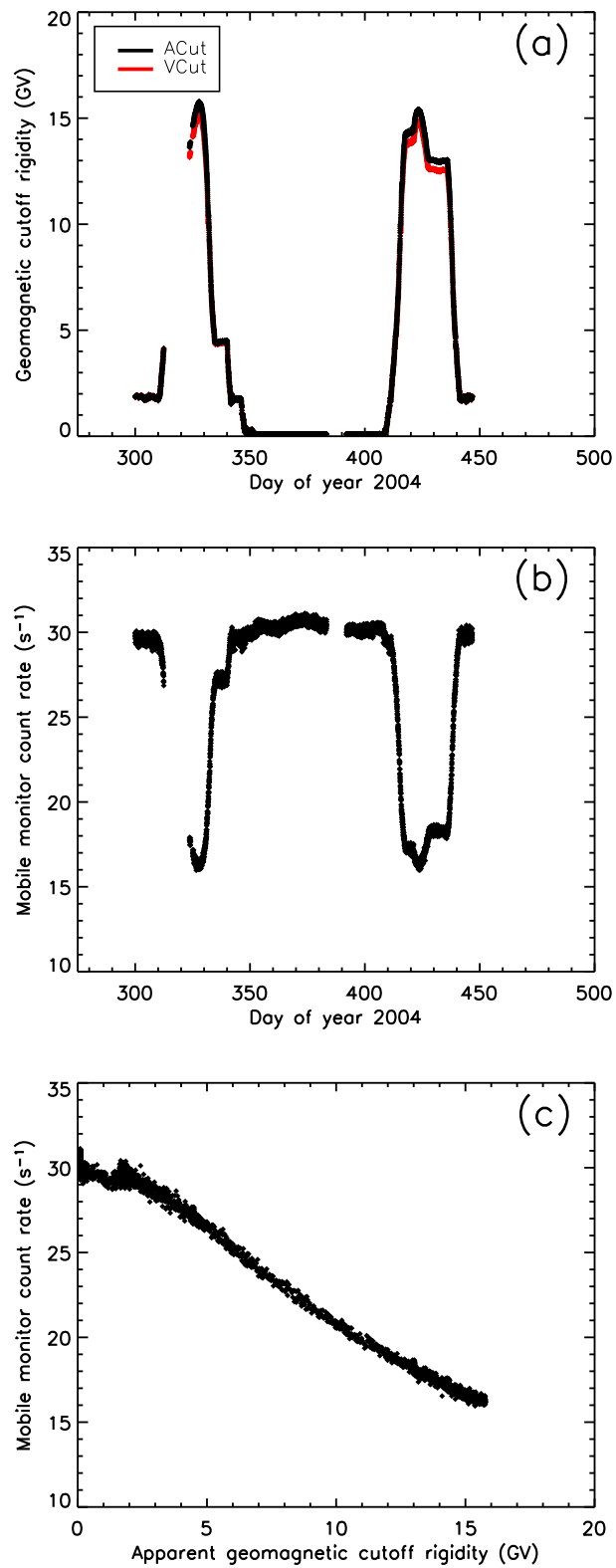


Figure 4.18: Like Figure 4.8, for the 2004 survey year.

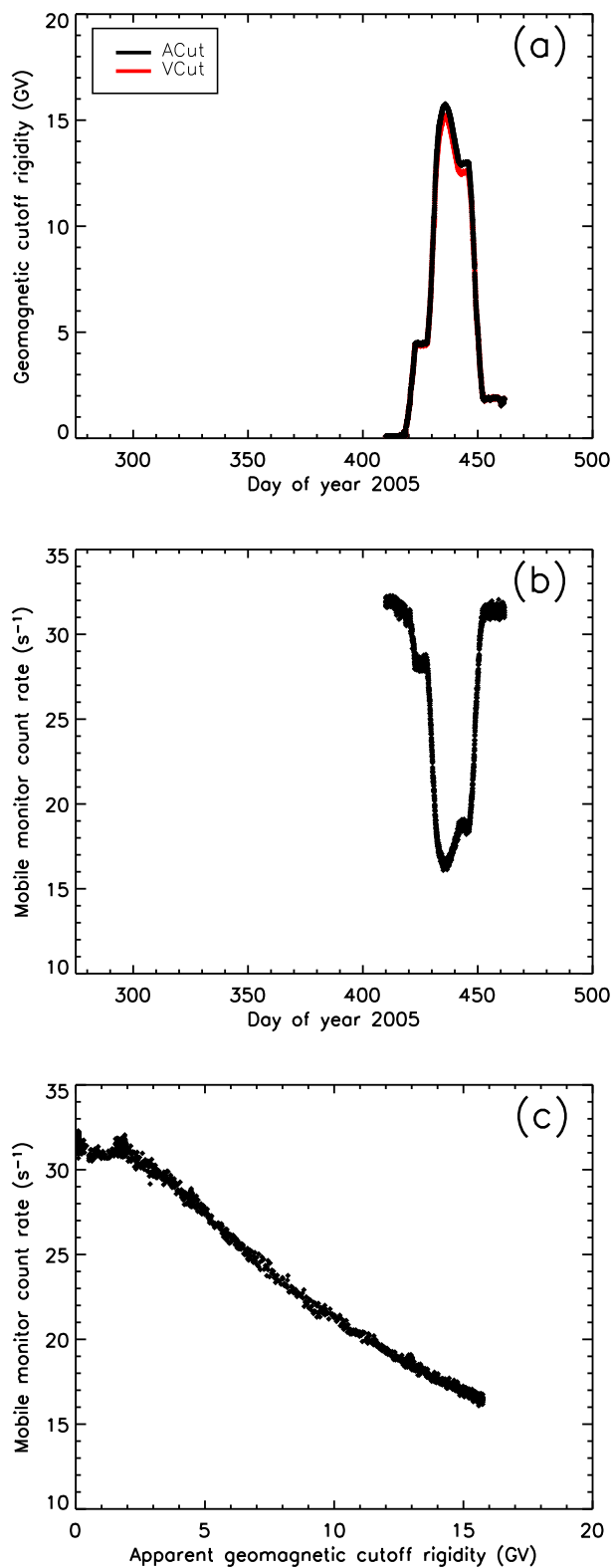


Figure 4.19: Like Figure 4.8, for the 2005 survey year.

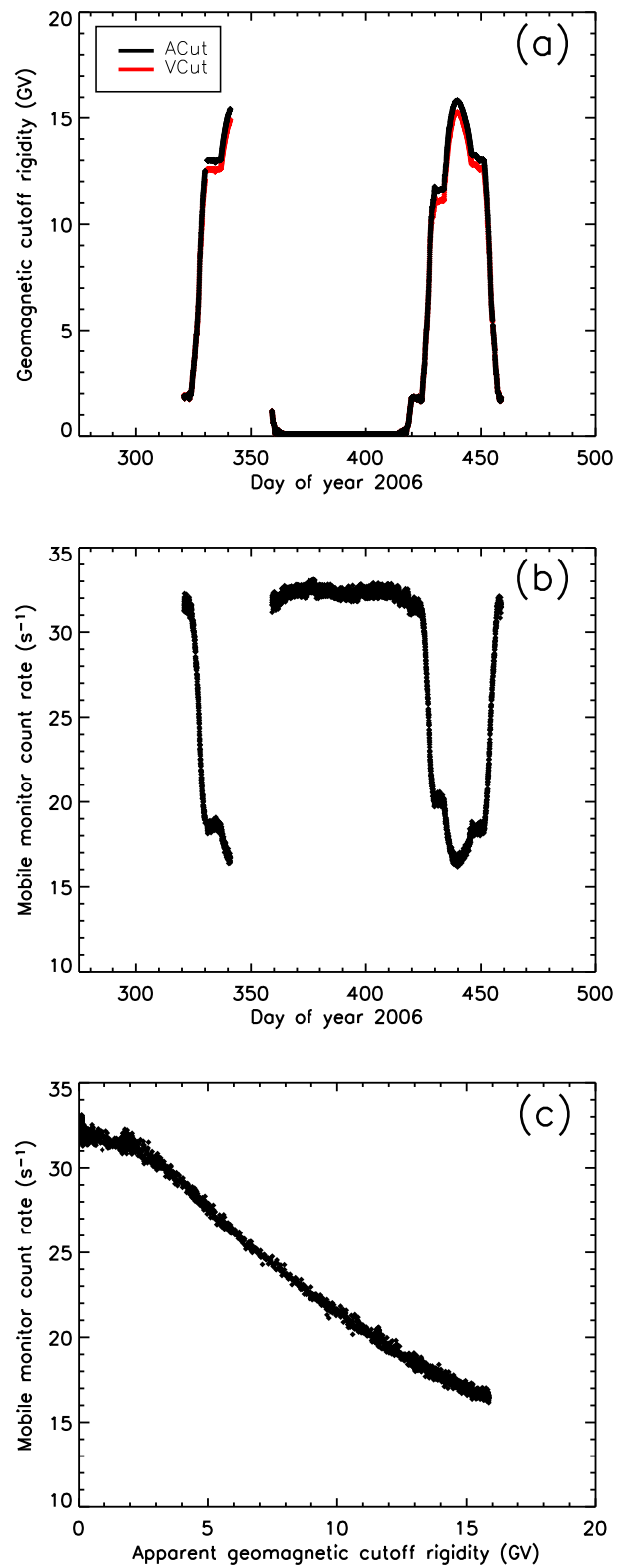


Figure 4.20: Like Figure 4.8, for the 2006 survey year.

Table 4.15: The segment divisions that we used in the Dorman analysis

| Survey Years | Segment A | | Segment B | | Segment C | | Segment D | |
|--------------|-----------|---------|-----------|---------|-----------|---------|-----------|---------|
| | START DOY | END DOY | START DOY | END DOY | START DOY | END DOY | START DOY | END DOY |
| 1994-1995 | - | - | - | - | 427.083 | 453.833 | - | - |
| 1995-1996 | 321.254 | 333.088 | 333.110 | 342.222 | - | - | - | - |
| 1996-1997 | 293.991 | 300.833 | 347.206 | 356.361 | 415.103 | 442.388 | 455.726 | 470.405 |
| | 327.540 | 333.852 | 333.874 | 340.068 | | | | |
| 1997-1998 | 298.348 | 305.699 | 342.334 | 362.302 | 416.641 | 441.995 | 442.016 | 449.132 |
| | 324.446 | 331.837 | 331.858 | 341.518 | | | | |
| | 320.794 | 325.347 | 345.900 | 357.166 | | | | |
| 1998-1999 | 328.900 | 333.451 | 333.535 | 341.050 | 431.328 | 438.463 | 452.303 | 463.113 |
| | 307.622 | 315.413 | 343.929 | 352.293 | | | | |
| 1999-2000 | 320.325 | 325.597 | 325.618 | 334.149 | 421.769 | 433.693 | 463.136 | 471.257 |
| | 310.578 | 324.192 | 338.893 | 349.309 | | | | |
| 2000-2001 | 306.422 | 314.256 | 324.213 | 335.433 | 421.728 | 452.923 | 476.507 | 480.362 |
| | 318.977 | 324.885 | 341.150 | 352.186 | | | | |
| 2001-2002 | 308.386 | 316.896 | 324.906 | 333.396 | 417.488 | 429.386 | 446.259 | 454.188 |
| | 320.579 | 327.883 | 338.436 | 349.246 | | | | |
| 2002-2003 | 323.846 | 329.392 | 327.925 | 350.297 | 432.798 | 446.726 | 459.385 | 473.124 |
| | 333.456 | 339.447 | 339.469 | 360.142 | | | | |
| 2003-2004 | 309.155 | 312.458 | 327.548 | 334.725 | 406.713 | 430.486 | 442.404 | 455.254 |
| | 323.699 | 327.527 | 339.022 | 348.404 | | | | |
| 2004-2005 | - | - | - | - | 435.524 | 442.383 | 442.404 | 455.254 |
| | 323.765 | 330.881 | 327.548 | 334.725 | | | | |
| 2005-2006 | 323.699 | 327.527 | 339.022 | 348.404 | 408.603 | 417.261 | 423.421 | 427.74 |
| | 309.155 | 312.458 | 327.548 | 334.725 | | | | |
| 2006-2007 | 323.699 | 327.527 | 339.022 | 348.404 | 420.860 | 422.355 | 435.374 | 441.703 |
| | 336.046 | 340.979 | 339.022 | 348.404 | | | | |
| 2006-2007 | 323.765 | 330.881 | - | - | 417.813 | 422.355 | 445.810 | 452.436 |
| | 336.046 | 340.979 | 413.997 | 429.070 | | | | |
| | | | 433.897 | 439.126 | | | 451.193 | 456.760 |

4.5 Response Functions

At the beginning of the analysis we intended to use the Nagashima technique as described in Appendix D. Because of some problematic issues, we switched to the method of “direct determination fitted by Dorman technique.”

The corrected mobile monitor count rate as a function of apparent cutoff rigidity represents the integral response function of a 3NM64 neutron monitor. This is plotted for each survey year in Figures 4.21(a)–(d), 4.22(a)–(e), and 4.23(a)–(d) for three modulation periods approximating solar minimum conditions (survey years 1994–1997), the transition from solar minimum to solar maximum (1998–2002), and the return to near solar minimum (2003–2006), respectively (see also Figure 4.1). Averages over 0.5-GV cutoff rigidity bins, averaged over all segments in one survey year, are plotted against apparent geomagnetic cutoff rigidity. If there are multiple segments, the average is indicated by a solid symbol and there is an error bar to represent the standard error among the determinations for different segments, which indicates the systematic (reproducibility) uncertainty. Actual statistical errors are negligible. An open symbol indicates that data were available for only one segment, and the systematic uncertainty has not been determined. The results are also fitted to the Dorman function (Dorman et al. 1970), which can be differentiated to determine the DRF:

$$N = N_0(1 - e^{-\alpha P_c^{-\kappa}}), \quad (4.6)$$

$$N = \int_{P_c}^{\infty} (DRF)dP \quad (4.7)$$

$$DRF = N_0\alpha P^{-\kappa-1}\kappa(e^{-\alpha P^{-\kappa}}), \quad (4.8)$$

where N_0 , α , and κ are free parameters. The values of these three “Dorman parameters” for each survey year from analysis of our fully corrected data for all surveys are shown in Table 4.16. Our fits to determine Dorman parameters excluded data from rigidities below 0.15 GV, and also excluded all hours of data where the cutoff had not changed from the previous time, i.e., when the ship was not moving. The Dorman function has an analytic derivative which immediately gives the differential response functions, denoted as “DRF” in Equations (4.7) and (4.8) and shown in Figures 4.21(e)–(h), 4.22(f)–(j), and 4.23(e)–(h) for different survey years.

Table 4.16: Derived Dorman parameters

| Survey Year | N_0 | α | κ |
|-------------|----------|----------|----------|
| 1994–1995 | 3.08E+01 | 9.05E+00 | 8.99E-01 |
| 1995–1996 | 3.09E+01 | 9.05E+00 | 8.99E-01 |
| 1996–1997 | 3.18E+01 | 7.99E+00 | 8.66E-01 |
| 1997–1998 | 3.14E+01 | 7.95E+00 | 8.62E-01 |
| 1998–1999 | 3.06E+01 | 8.63E+00 | 8.80E-01 |
| 1999–2000 | 2.88E+01 | 1.01E+01 | 9.03E-01 |
| 2000–2001 | 2.80E+01 | 1.10E+01 | 9.26E-01 |
| 2001–2002 | 2.81E+01 | 1.02E+01 | 9.03E-01 |
| 2002–2003 | 2.79E+01 | 1.01E+01 | 8.98E-01 |
| 2003–2004 | 2.83E+01 | 9.74E+00 | 8.89E-01 |
| 2004–2005 | 2.97E+01 | 9.57E+00 | 9.03E-01 |
| 2005–2006 | 3.14E+01 | 8.81E+00 | 8.94E-01 |
| 2006–2007 | 3.17E+01 | 8.74E+00 | 8.94E-01 |

As noted in the introduction, the objective of the present paper is focused on characterizing the evolution of GCR spectra from one solar magnetic polarity to the other. In Figure 4.24 we show the DRF for the two surveys closest to solar minima of opposite magnetic polarity, which clearly manifest the crossover phenomenon. While previous studies have examined the crossover at times near solar minimum, our data for 13 consecutive survey years allow us to examine in detail the transition with solar magnetic polarity. Thus we can address the questions of whether the transition is smooth or abrupt, or a phenomenon that appears as a result of some special conditions that occur only very near solar minimum, and therefore not part of a continuum at all. In summary, we believe that a startlingly simple analysis shows that the crossover is a natural consequence of a major shift in the structure of modulation that occurred rather suddenly at the time of the polarity reversal in the year 2000.

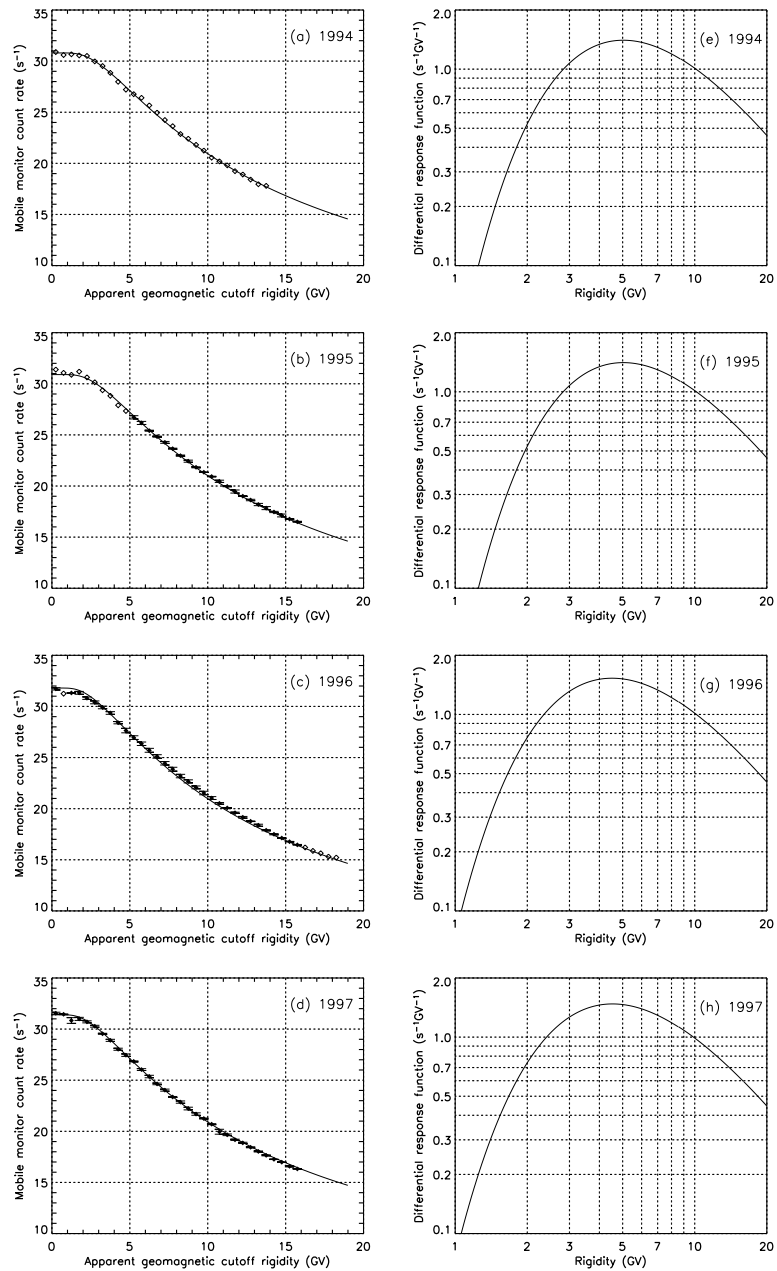


Figure 4.21: (a)–(d) Corrected mobile neutron monitor count rate for survey years 1994 to 1997 (solar minimum conditions) as a function of apparent geomagnetic cutoff (averaged over 0.5 GV rigidity bins). A solid symbol indicates that data were available for multiple voyage segments (as defined in the text). Vertical error bar represents the standard error between multiple segments; in many cases the error bar is smaller than the plot symbol. An open symbol with no error bar indicates that data were available for only one segment. Solid lines indicate Dorman function fits. (e)–(h) Inferred differential response functions, obtained as the derivatives of the Dorman function fits.

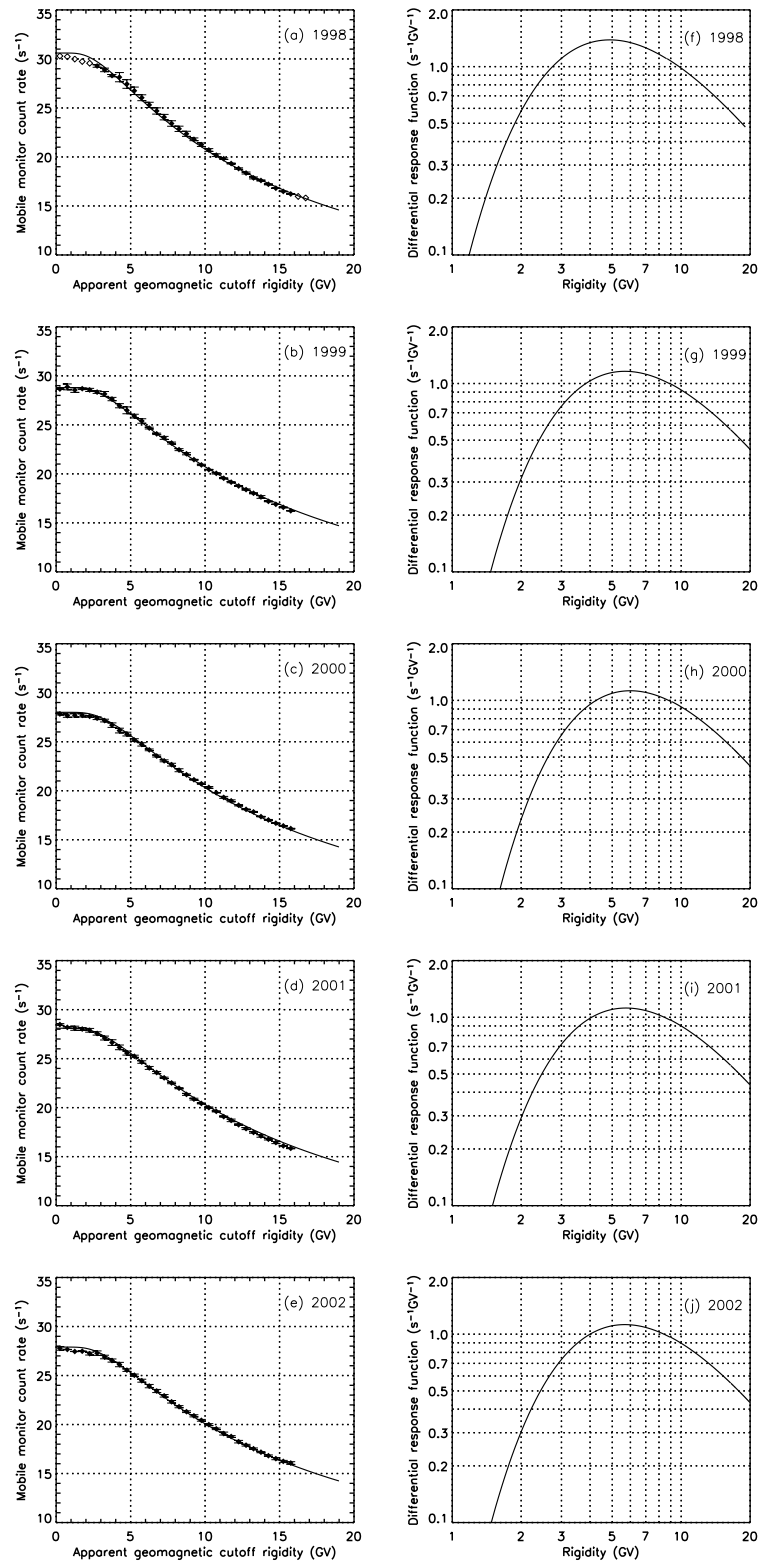


Figure 4.22: Like Figure 4.21, for the 1998-2002 survey years, showing the transition from solar minimum to solar maximum conditions.

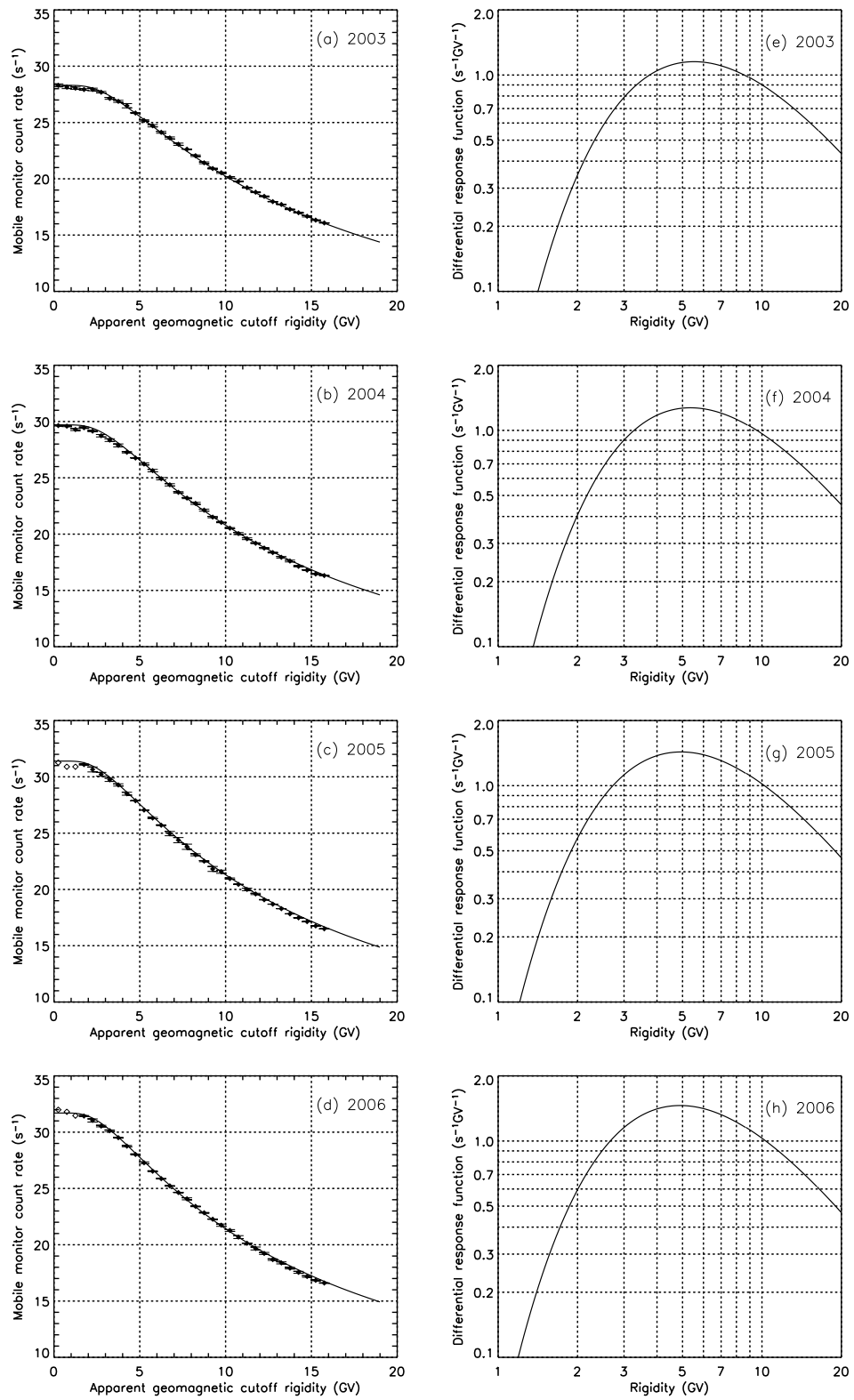


Figure 4.23: Like Figure 4.21, for the 2003-2006 survey years, showing the transition from solar maximum to solar minimum conditions.

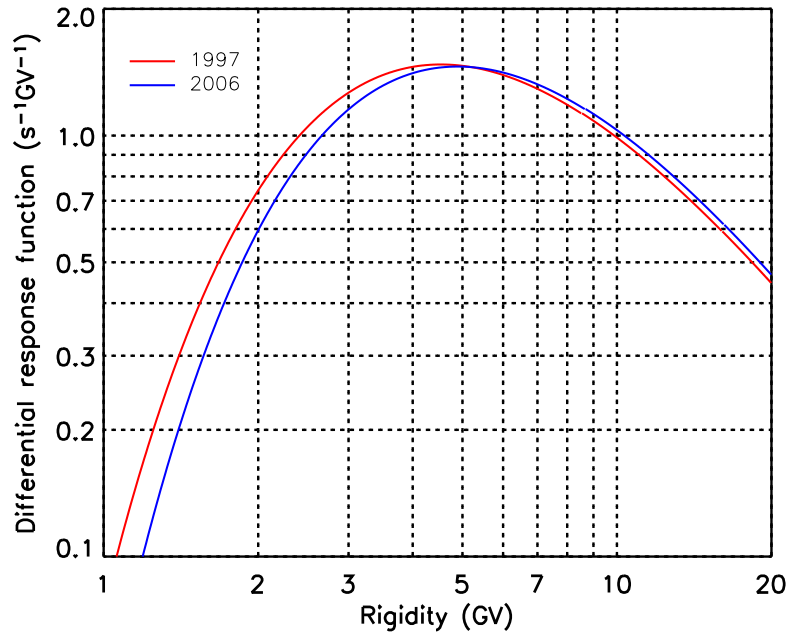


Figure 4.24: Differential response functions for two survey years, near solar minimum, of opposite polarity and similar modulation level. A crossover is apparent near 5 GV.

Our evidence comes not from the details of the evolution of the DRF, which we leave to future work, but rather from a regression analysis of the mobile monitor count rate for various cutoff rigidity ranges against the pressure-corrected McMurdo count rate. For this analysis we use C_{TP} , the count rate uncorrected for short term modulation variations, and we still exclude large Forbush decreases. Figure 4.25 summarizes the analysis, which consists of straight line fits to the data, divided into apparent cutoff rigidity bins of width 1 GV. To cut down on clutter, Figure 4.25 represents each rigidity bin in each survey by a single point at the average value for all data in all segments, whereas the actual fitting was performed for 1-hr or 30-min averages.

There were two surprises in this analysis. The first is how well the regression for each individual rigidity bin against McMurdo for a given magnetic polarity is fitted by a straight line. This will be addressed in the following Section. The second surprise is how cleanly a systematic change in the slopes of these lines is delineated by the solar polarity reversal in the year 2000. This effect can be seen in Figure 4.26, where for clarity the data are shown for every third rigidity bin, including all survey years for both magnetic polarity states.

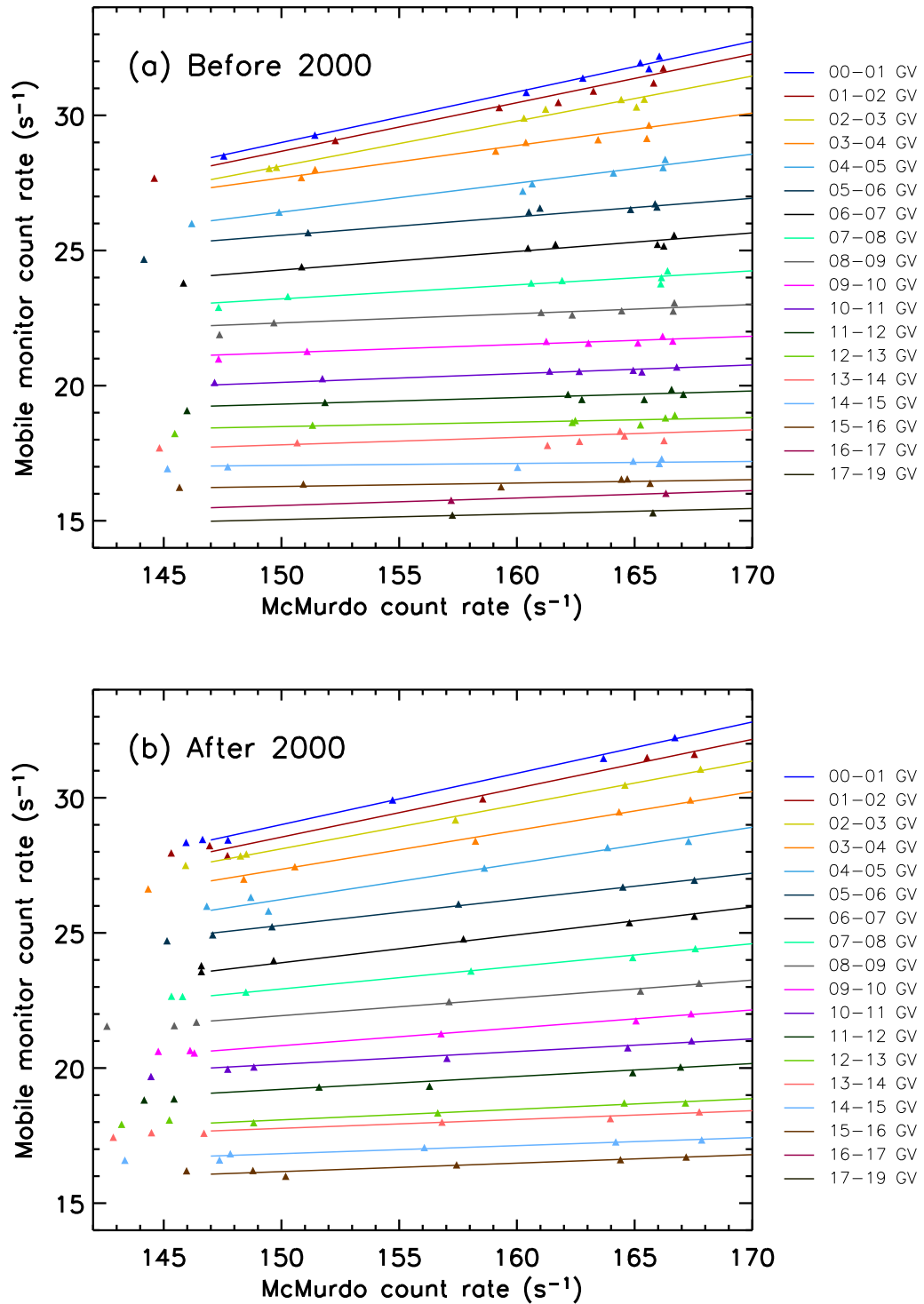


Figure 4.25: Regression of count rates for the mobile monitor in different cutoff rigidity bins against the count rate of the McMurdo neutron monitor during (a) $A > 0$ solar magnetic polarity (before 2000) and (b) $A < 0$ solar magnetic polarity (after 2000). Symbols indicate average values over each survey year.

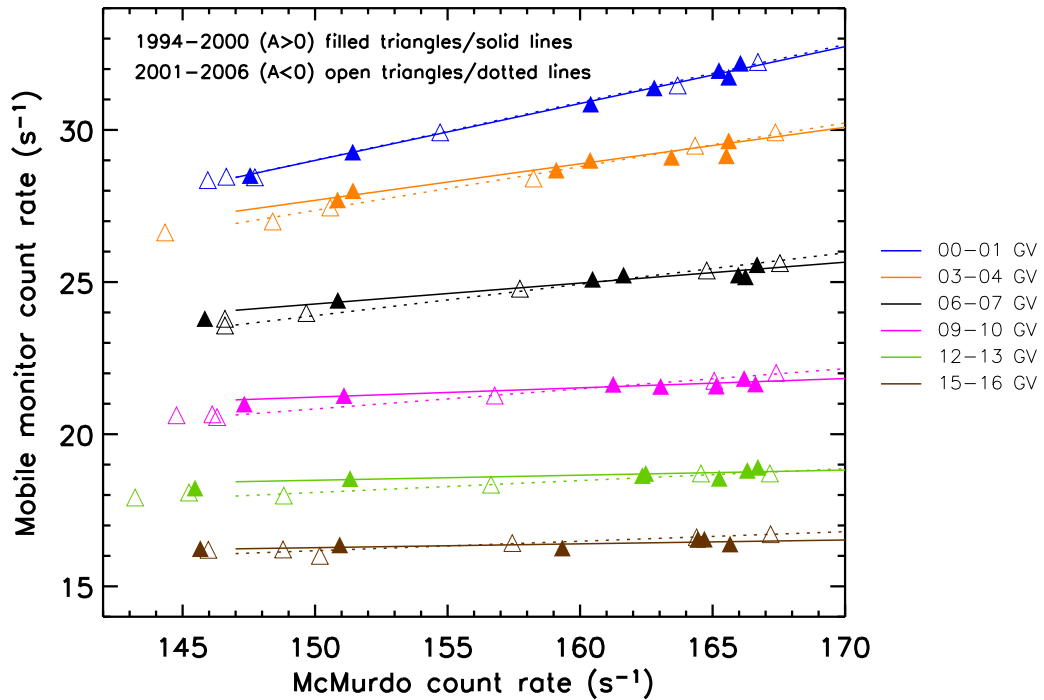


Figure 4.26: Alternative presentation of the data in Figure 4.25 using every third rigidity bin for clarity and superimposing the data for different solar magnetic polarities. Filled triangles are used to indicate positive ($A > 0$) solar magnetic polarity with solid lines showing the linear fits. Open triangles indicate data for negative ($A < 0$) solar magnetic polarity while the dotted lines are linear fits to these data. There are clear differences in cosmic ray modulation before and after the solar magnetic polarity reversal.

Table 4.17 gives the coefficients of the regression analysis for each rigidity bin before and after the polarity reversal. Survey year 2000 itself is excluded from the regression analysis, as were all data with a McMurdo count rate below 147 s^{-1} , so as to exclude the transition period. In the table, C_1 is the mobile monitor count rate at a reference McMurdo count rate of 167 s^{-1} , and the years refer to survey years. Note that in the 0-1 GV bin there is, and should be, no noticeable change in slope with the solar polarity reversal. In this rigidity range, both the mobile neutron monitor and the McMurdo neutron monitor (with apparent geomagnetic cutoff $\approx 0.1 \text{ GV}$) had a yield function dominated by the atmospheric cutoffs, not the geomagnetic cutoff, and the count rates should be directly proportional to one another, regardless of cosmic ray spectral variations. Indeed, the slope in this rigidity range reflects the smaller size of

Table 4.17: Coefficients of a linear regression analysis and force field model between mobile monitor data in multiple cutoff rigidity intervals and McMurdo neutron monitor data. The standard error (SE) refers to the standard error of the coefficient (in this case the slope) deduced from the scatter of the points from the fit line. In the case of the model, this is completely systematic deviation, since the model produces a slightly curved line, not a perfect straight line.

| Apparent Geomagnetic Cutoff Rigidity (GV) | Best fit, 1994–1999 | | | Best fit, 2001–2006 | | | Force Field | |
|--|---------------------|-------|--------|---------------------|-------|--------|-------------|--------|
| | C ₁ | Slope | SE | C ₁ | Slope | SE | Slope | SE |
| 0–1 | 32.2 | 0.187 | 0.0006 | 32.2 | 0.190 | 0.0004 | 0.191 | 0.0001 |
| 1–2 | 31.7 | 0.180 | 0.0008 | 31.6 | 0.181 | 0.0009 | 0.189 | 0.0001 |
| 2–3 | 31.0 | 0.167 | 0.0015 | 30.9 | 0.162 | 0.0018 | 0.172 | 0.0004 |
| 3–4 | 29.7 | 0.120 | 0.0024 | 29.8 | 0.144 | 0.0022 | 0.145 | 0.0008 |
| 4–5 | 28.2 | 0.107 | 0.0013 | 28.5 | 0.134 | 0.0014 | 0.119 | 0.0009 |
| 5–6 | 26.7 | 0.069 | 0.0027 | 26.9 | 0.097 | 0.0023 | 0.098 | 0.0009 |
| 6–7 | 25.4 | 0.069 | 0.0036 | 25.7 | 0.103 | 0.0023 | 0.082 | 0.0008 |
| 7–8 | 24.0 | 0.039 | 0.0040 | 24.3 | 0.084 | 0.0030 | 0.069 | 0.0008 |
| 8–9 | 22.9 | 0.034 | 0.0019 | 23.1 | 0.066 | 0.0028 | 0.058 | 0.0007 |
| 9–10 | 21.7 | 0.030 | 0.0029 | 22.0 | 0.066 | 0.0026 | 0.050 | 0.0006 |
| 10–11 | 20.7 | 0.032 | 0.0026 | 20.9 | 0.047 | 0.0019 | 0.043 | 0.0006 |
| 11–12 | 19.7 | 0.024 | 0.0029 | 20.0 | 0.048 | 0.0014 | 0.038 | 0.0005 |
| 12–13 | 18.8 | 0.017 | 0.0020 | 18.7 | 0.039 | 0.0012 | 0.033 | 0.0005 |
| 13–14 | 18.3 | 0.028 | 0.0012 | 18.3 | 0.033 | 0.0011 | 0.030 | 0.0004 |
| 14–15 | 17.2 | 0.007 | 0.0009 | 17.3 | 0.030 | 0.0014 | 0.027 | 0.0004 |
| 15–16 | 16.5 | 0.013 | 0.0012 | 16.7 | 0.031 | 0.0009 | 0.024 | 0.0003 |
| 16–17 | 16.0 | 0.028 | 0.0016 | – | – | – | – | – |
| 17–19 | 15.4 | 0.020 | 0.0031 | – | – | – | – | – |

the mobile monitor (3 counter tubes) compared with the McMurdo monitor (18 counter tubes), hence the slope close to 1/6. For other low rigidity bins the mobile monitor response was still similar to that at McMurdo, with little change in slope upon polarity reversal. Solar modulation is generally weaker at higher rigidity, hence the decreasing slope when the mobile monitor was at higher rigidity. Because there is little polarity difference for low rigidity and a small slope that was difficult to measure for high rigidity, the difference in slope is clearest at intermediate rigidity (3-13 GV).

4.6 Modeling

To put our observations into the context of conventional modulation analysis, we have examined the predictions of a simple force field model. In particular, we examine whether the linear character of the plots in Figure 4.25 and 4.26 is consistent with such a model. The force field model of solar modulation of GCRs is a well known spherically symmetric model of solar wind convection, adiabatic deceleration, and diffusion. The combined effect of these processes is expressed by a single “modulation parameter” that depends only on position (radius) and time. The force field approximation results from a differential equation for the evolution of the phase space distribution function f of cosmic rays as a function of radius and momentum p , where the rigidity spectrum $j(P)$ is related to $f(p)$ by $j(P) \propto P^2 f(p)$. Our modeling approach is based on that of Caballero-Lopez & Moraal (2004).

The force field model itself (Gleeson & Axford 1968) comes from simplifications of the equation to a form that can be solved by the method of characteristics, so that the solution $f(r, p)$ is constant along contours of the characteristic equation. This relates the spectrum at a position within the heliosphere to the spectrum at a different momentum on the outer boundary; this is the local interstellar spectrum (LIS). With some further assumptions the characteristics reduce to the form $P_b - P = \phi$, where ϕ is the time-dependent “force field parameter” or “modulation parameter” that expresses a decrease in rigidity from the outer boundary to the location of interest, which is a reasonable approximation to the adiabatic deceleration in some circumstances (Caballero-Lopez & Moraal 2004). While the distribution function f is constant along characteristics, the expression for the rigidity spectrum j has the additional factor of P_b^2/P^2 reflecting the difference in the magnitude of the momentum at the two places, so that

$$j(P) = \frac{P_b^2}{P^2} j_b(P_b), \quad P_b(P, t) = P + \varphi(t). \quad (4.9)$$

We use yield functions for protons and alpha particles from Clem & Dorman (2000) that are parameterized, along with several other potentially interesting functions, in Table 4.16 of Caballero-Lopez & Moraal (2012). This paper also has a discussion of the “crossover” and useful formulae for manipulating spectra and yield functions. For the input spectra j_b , we adopted the LIS for protons and alpha particles from the Appendix of Burger et al. (2008); they reported spectra in terms of kinetic energy per nucleon

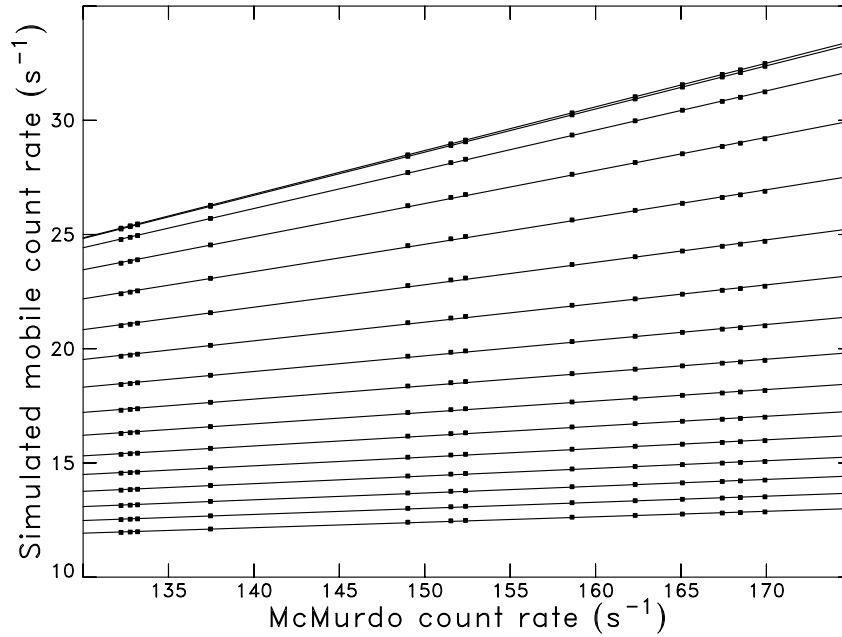


Figure 4.27: Like Figure 4.25, for calculations using a force field model as described in the text. Each line corresponds to a 1-GV bin in apparent cutoff rigidity, ranging from the 0-1 GV bin at the top to the 15-16 GV bin at the bottom.

T as a function of rigidity, which we have multiplied by dT/dP to obtain the rigidity spectrum j_b . For the force field parameter we used the tabulated values of Usoskin et al. (2011), which are based on an analysis of neutron monitors with cutoff of 6 GV or less during the neutron monitor era. Specifically, we used their value for December of the survey year (e.g., we used their December 2006 value for survey year 2006).

With these components, via numerical integration we generated a simulated series of surveys. There is an overall absolute normalization to estimate count rates of the mobile neutron monitor and McMurdo neutron monitor. From these simulations we prepared Figure 4.27, which should be compared to the actual data in Figure 4.25. As before, each point is plotted according to the count rates for each cutoff rigidity bin during each survey year, with a lower mobile monitor count rate at higher cutoff rigidity. Note that in the simulations, each survey takes place “instantly” and therefore at a constant McMurdo count rate. This is why the points for each survey year are vertically aligned. In the real surveys (Figure 4.25), the McMurdo count rate varies with time, so the points for a given survey at varying cutoff rigidity follow a more wandering pattern.

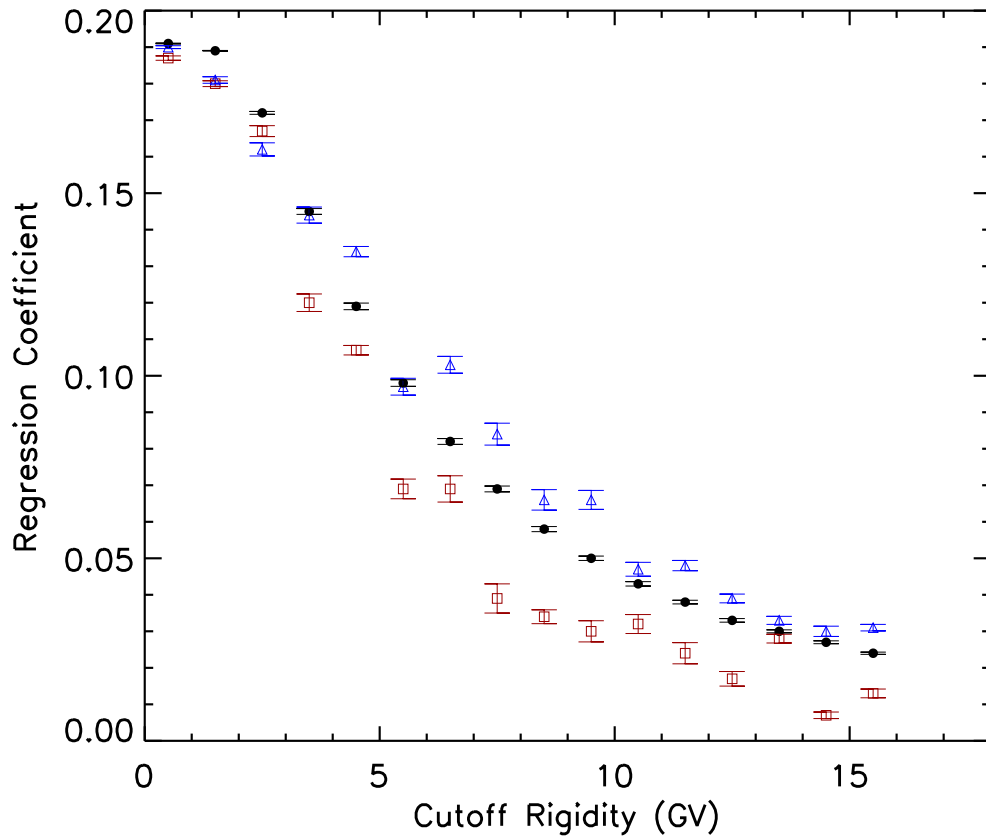


Figure 4.28: Regression coefficients for the lines in Figures 4.25 and 4.27 as a function of apparent cutoff rigidity. Red squares are from fits to data before 2000, blue triangles are from fits to data after 2000, and black circles are from fits to the force field calculation. Vertical error bar represents the standard error of the regression coefficient deduced from the scatter of the points from the fit line. There are clear differences in modulation before and after the solar magnetic polarity reversal.

These simple simulations, and a comparison between Figure 4.25 and 4.27, show that the linear relationship in the plots is a natural consequence of the force field model over the range of modulation appropriate to the series of latitude surveys. For completeness, we note that the linear relationship fails over an extended (and possibly unphysical) range of modulation parameters. The regression line slopes over the cutoff rigidity range of interest are displayed as solid black circles in Figure 4.28, whereas our measured slopes from Table 4.17 are included as open symbols. The measured slopes before 2000 (red squares) and after 2000 (blue triangles) typically bracket the simulated

values. Thus we see that the force field model can qualitatively explain solar modulation for a given solar magnetic polarity. However, there is nothing in the force field model that will produce a crossover or any differences in spectra before and after a magnetic polarity reversal. Thus we confirm that there must be a physical difference in the nature of solar modulation upon a change in solar magnetic polarity.

4.7 Discussion

The crossover as typically defined has to do with spectral comparisons at “similar modulation levels.” This is actually not very specific, and usually something like “solar minimum” or “minimum sunspot number” is used. The simple force field model has only one parameter. “Similar modulation levels” are defined as equal values of this parameter, which by construction produce identical response functions. Our analysis shows that there is a straightforward way of avoiding this ambiguity. The “crossover” is a manifestation of a basic change in modulation that occurs suddenly at the time of the solar polarity reversal. Suddenly, in this context, is of course defined as a year or so – which is also approximately the time it takes for the solar wind to carry the new polarity state to the outer reaches of the solar system. The sudden change of state of the heliosphere is quite like that reported for the relative abundance of protons and antiprotons (Asaoka et al. 2002) and electrons and positrons (Clem & Evenson 2002, 2004). One immediate conclusion from the observation of a rapid change in solar modulation is that we are seeing a phenomenon related to the classic solar wind, not the very distant reaches of the heliosphere at or beyond the termination shock.

Owing to the large detector mass required to detect high-energy cosmic rays, ground-based instruments have remained the state-of-the-art method for studying time variations of these elusive particles (Simpson et al. 1953; McDonald 2000). There have been several direct observations of the full spectrum from balloon-borne and space-based instruments for specific epochs. Typically measurements have not been available for the same instrument and the same level of modulation in opposite polarities, so they have not confirmed a crossover per se. Clem et al. (2003) presented a compilation of proton and alpha particle spectra from several sources. The most direct comparison to the present work is provided by the series of proton spectra from the BESS payload

(Mitchell et al. 2008) that span the year 2000 solar polarity reversal with observations from the same instrument. Mitchell et al. (2008) also fit their data to a force field model which, apart from normalization, has only one adjustable parameter. The fits to the BESS data may be good, but they are not perfect. Close examination reveals that the fits to spectra after the polarity reversal are not as good as those to spectra before the reversal. The fits in fact fail by overpredicting the data at low energy, just as we find in our results. We therefore consider that the BESS data are consistent with our results.

Gradient and curvature drifts are clearly established as an important factor in solar polarity dependence of modulation (Jokipii & Levy 1977) but in many ways the full implication of this remains unclear (e.g., Potgieter 2013). In and of itself the drift picture does not predict a crossover. It is not intuitively obvious why reversal of the drift fields would increase modulation at one rigidity and decrease it at another. Our observation of a rapid switch from one state to another also indicates that the tilt angle of the heliospheric current sheet is not a major factor. As Clem et al. (2000) discuss, for observations at approximately 1 GV, the effect of current sheet tilt angle is clearly observable in precise measurements but it is tiny compared to the abrupt change with the polarity reversal itself.

There are other modulation effects that are sensitive to interplanetary magnetic field polarity. The “twenty-year wave” observed in the phase angle of the cosmic ray diurnal anisotropy (Forbush 1967; Bieber & Chen 1991) has also been attributed to particle drifts by Levy (1976). However Chen & Bieber (1993) showed that it is a consequence of their finding that the cosmic ray scattering mean free path is systematically larger during epochs of negative solar polarity than during epochs of positive polarity.

Here we propose a specific mechanism to explain the different spectral evolution for different magnetic polarities. Diffusion coefficients can change radically with solar polarity because of helicity in the solar wind magnetic field and systematically organized magnetic helicity is actually observed in direct measurements of the interplanetary magnetic field. Bieber et al. (1987a) reported that the net helicity (integrated over wave number) of the magnetic field has a definite dominant sign, negative north of the heliospheric current sheet and positive south of it. The helicity dependence of the mean free path is a function of the product of the sign of the helicity and the polarity of the large-scale field (Bieber et al. 1987b; Bieber & Burger 1990). This means that at any given time the effect upon the mean free path is the same in both hemispheres

(because the helicity and polarity *both* reverse sign across the sheet), but when the solar polarity reverses the magnetic polarity reverses sign, and the helicity does not. This will produce a larger mean free path during negative solar polarity, consistent with the Chen & Bieber (1993) result.

An indication that magnetic helicity may become more important at neutron monitor energies was provided by Smith & Bieber (1993), who measured the magnetic helicity spectrum extended to very low frequency. They found that for frequencies above 5-10 Hz, the helicity fluctuates in sign and is statistically consistent with zero (Matthaeus & Goldstein 1982). At lower frequencies, however, the helicity assumes a definite dominant sign. It is this low-frequency turbulence that corresponds to wave numbers resonant with cosmic rays in the neutron monitor regime.

This produces a natural explanation for the crossover since the enhanced diffusion coefficients would work in the opposite direction of drifts. During the negative polarity state, when drifts operate to limit fluxes, a larger diffusion coefficient, particularly at the higher energies, permits enhanced access. With such competing effects, each having a different energy dependence, a crossover would be just an observational result that one effect dominates at low energy and the other dominates at high energy.

CHAPTER V

DISCUSSION AND CONCLUSIONS

This work has two topics concerning portable neutron monitors. The first topic is the data analysis from a portable calibration neutron monitor (~ 265 kg) which we call the “calmon.” The calmon consists of one ^3He proportional counter tube surrounded by polyethylene moderator, lead producer, and polyethylene reflector. There are two calmons. Both of them were designed and invented by Prof. Moraal’s group of Northwest Univ. (NWU; formerly Potchefstroom Univ.) at Potchefstroom, South Africa in order to calibrate the worldwide neutron monitor network. One of them is taken to various fixed stations among the ~ 40 stations around the world, while another unit is run continuously in Potchefstroom Univ, South Africa. The calmon is largely self-contained, with electronics, CPU and data storage all in a “can” attached to the head of the calmon.

In Thailand, we have the Princess Sirindhorn Neutron Monitor (PSNM) at Doi Inthanon (high altitude greatly improves the count rate). This has 29 tons of lead and 18 $^{10}\text{BF}_3$ counter tubes to provide one of the world’s top count rates, as well as the world’s highest energy threshold due to its location near the geomagnetic equator. The monitor at Doi Inthanon has the highest vertical cutoff rigidity, 16.8 GV, of any fixed monitor in the world. Thus, PSNM is particularly important to the plan to calibrate monitors. The cutoff is reasonably “sharp” in energy, so each monitor measures a sort of integral count rate for energies above its threshold. The calmon came to Bangkok, Thailand in July, 2009. We shipped it to Doi Inthanon in September, 2009. It needs a standard environment, i.e., no obstacles more than 20° above the horizon in all directions and placement above a standard swimming pool with at least 50 cm of water, which moderates the effect of the surface below. This standard setup avoids the configurational effects on the 18-NM64 inside the PSNM station, so the count rate should depend only on cutoff rigidity (latitude, longitude) and altitude. We need to run for several days (in one configuration) to accumulate sufficient statistical accuracy

to calibrate the neutron monitor, which requires several days at PSNM. A calibration has already been performed, with successful runs for 13 configurations of calmon height above the bottom of the swimming pool, water height and electronics at Doi Inthanon, starting in November, 2009 and ending in June, 2010. We also moved the calmon inside the station and put it on the cart placed on the floor to obtain extensive counting statistics. The goal of this was to obtain precise data on the influence of being inside the station on the neutron count rate, compared with a location outside the station.

In analysis of data from the calmon, we found many problems with attaching electronics to calmon, e.g., strong solar heating on the mountain to 50-60°C almost every day, data from S. African electronics needing to be “cleaned” or rejected, a portion of data from Bartol electronics was rejected, and still the calmon/NM count ratio has non-statistical fluctuations. Because of all these reasons, we do not believe that we can control the calibration to within $\pm 0.2\%$, the acceptable level of uncertainty of calibrating neutron monitor count rates (Krüger et al. 2003). However, there were other benefits, i.e., more interaction with the worldwide neutron monitor community, the ability to “fiddle” with neutron monitor equipment, measuring the effect of calmon and water heights on the calmon count rate which makes sense in terms of a “cloud” of neutrons, and comparing with Monte Carlo calculations and directly measuring the effect of the building on the calmon count rate. In future work we will compare the experimental results with Monte Carlo simulation results.

Our physical interpretation of the results for usable configurations as shown in Figure 3.31 is that secondary atmospheric neutrons hitting the concrete and wood under the calmon will cause nuclear fragmentatoin in those materials, generating a “cloud” of neutrons there. As the calmon is raised, it has a slightly lower count rate as it moves out of the cloud. When water is added to the pool, it helps absorb neutrons and lowers the count rate as well.

The effect of the PSNM building is found to be 3%. While a calibration at one epoch may be accurate to within 0.2%, there is some question as to whether the substantial effect of the building varies with the change in the cosmic ray spectrum from solar minimum to solar maximum. Further research is needed to check this.

The latitude survey work is another topic in this work. We did characterize the evolution of the cosmic ray spectrum by using direct determination fitted by a Dorman function of the data from a 3-tube neutron monitor that operated on an icebreaker

ship for 13 years, during its annual runs from Seattle, USA to Antarctica and back, called a latitude survey because the neutron monitor is carried over a wide range of latitudes, including high latitudes (with low vertical cutoff rigidity, i.e., particles can arrive more easily) and low (equatorial) latitudes (with high vertical cutoff rigidity, i.e., particles arrive with more difficulty). We have analyzed the results of the 13 consecutive yearly latitude surveys during 1994-2007 and determined the yearly response function of the neutron monitor as a function of cutoff rigidity as shown in Figures 4.21(a)-(d), 4.22(a)-(e) and 4.23(a)-(d) for three modulation periods. They provide a rather direct measure of the cosmic ray rigidity spectrum. This research topic could extend the knowledge and experience of our research group as a whole, which has never worked on a latitude survey or on measuring the Galactic cosmic ray spectrum. The goals of the project have been defined much more clearly, and required good cleaning of the data. We have shown that the curious “crossover” in spectra measured at solar minima during epochs of opposite magnetic polarity as shown in Figure 4.24 is not the result of continuous evolution, nor is it related to the interplanetary conditions peculiar to solar minimum. Rather it is a result of a discrete shift in the structure of modulation that takes place rather suddenly near the time of the solar magnetic polarity reversal. We suggest that this results from a systematic change in the interplanetary diffusion coefficient for cosmic rays.

In a future project, we plan to use the approach of the straight line fits to find correlations with McMurdo as the basis of a study of fixed neutron monitors. In this case, we can use the regression fit models obtained from Figure 4.25 in different cutoff rigidity bins for positive ($A > 0$) and negative ($A < 0$) solar magnetic polarity. To the accuracy of our annual measurements this change takes place at all rigidities simultaneously as shown in Figure 4.26.

REFERENCES

- Anand, K. C., Daniel, R. R., Stephens, S. A., Bhowmik, B., Krishna, C. S., Aditya, P. K., & Puri, R. K. (1968). Rigidity spectrum of cosmic-ray helium nuclei ≥ 12 GV. *Can. J. Phys.*, 46, 652.
- Asaoka, Y., Shikaze, Y., Abe, K., Anraku, K., Fujikawa, M., Fuke, H., et al. (2002). Measurements of Cosmic-Ray Low-Energy Antiproton and Proton Spectra in a Transient Period of Solar Field Reversal. *Physical Review Letters*, 88(5), 051101.
- Barnden, L. R. (1973). The Large-Scale Magnetic Field Configuration Associated With Forbush Decreases. In International Cosmic Ray Conference. *International Cosmic Ray Conference*, vol. 2, p. 1277.
- Bieber, J. W., & Burger, R. A. (1990). Cosmic-ray streaming in the Born approximation. *Astrophys. J.*, 348, 597–607.
- Bieber, J. W., Burger, R. A., Engel, R., Gaisser, T. K., Roesler, S., & Stanev, T. (1999). Antiprotons at Solar Maximum. *Physical Review Letters*, 83, 674–677.
- Bieber, J. W., & Chen, J. (1991). Solar Magnetic Cycle Variation of Cosmic-ray gradients and Scattering Mean Free Path. In International Cosmic Ray Conference. *International Cosmic Ray Conference*, vol. 3, p. 525.
- Bieber, J. W., Clem, J., Desilets, D., Evenson, P., Lal, D., Lopate, C., & Pyle, R. (2007). Long-term decline of South Pole neutron rates. *Journal of Geophysical Research*, 112, A12102.
- Bieber, J. W., Clem, J., Duldig, M. L., Evenson, P., Humble, J. E., & Pyle, R. (2003). Cosmic Ray Spectra and the Solar Magnetic Polarity: Preliminary Results from 1994-2002. In M. Velli, R. Bruno, F. Malara, & B. Bucci (Eds.), *Solar Wind Ten. American Institute of Physics Conference Series*, vol. 679, pp. 628–631.
- Bieber, J. W., Clem, J., & Evenson, P. (1997). Efficient Computation of Apparent Cutoffs. In International Cosmic Ray Conference. *International Cosmic Ray Conference*, vol. 2, p. 389.

- Bieber, J. W., Clem, J. M., Duldig, M. L., Evenson, P. A., Humble, J. E., & Pyle, R. (2004). Latitude survey observations of neutron monitor multiplicity. *Journal of Geophysical Research (Space Physics)*, 109(A18), A12106.
- Bieber, J. W., & Evenson, P. (1995). Spaceship Earth - An Optimized Network of Neutron Monitors. In International Cosmic Ray Conference. *International Cosmic Ray Conference*, vol. 4, p. 1316.
- Bieber, J. W., Evenson, P., & Matthaeus, W. H. (1987a). Magnetic helicity of the IMF and the solar modulation of cosmic rays. *Geophys. Res. Lett.*, 14, 864–867.
- Bieber, J. W., Evenson, P. A., & Matthaeus, W. H. (1987b). The Nuts and Bolts of Cosmic Ray Modulation. *International Cosmic Ray Conference*, 3, 175.
- Burger, R. A., Krüger, T. P. J., Hitge, M., & Engelbrecht, N. E. (2008). A Fisk-Parker Hybrid Heliospheric Magnetic Field With a Solar-Cycle Dependence. *Astrophys. J.*, 674, 511–519.
- Caballero-Lopez, R. A., & Moraal, H. (2004). Limitations of the force field equation to describe cosmic ray modulation. *Journal of Geophysical Research (Space Physics)*, 109, A01101.
- Caballero-Lopez, R. A., & Moraal, H. (2012). Cosmic-ray yield and response functions in the atmosphere. *Journal of Geophysical Research (Space Physics)*, 117(A16), A12103.
- Cane, H. V. (2000). Coronal Mass Ejections and Forbush Decreases. *Space Sci. Rev.*, 93, 55–77.
- Chen, J., & Bieber, J. W. (1993). Cosmic-ray anisotropies and gradients in three dimensions. *Astrophys. J.*, 405, 375–389.
- Clem, J. (1999). Atmospheric Yield Functions and the Response to Secondary Particles of Neutron Monitors. In International Cosmic Ray Conference. *International Cosmic Ray Conference*, vol. 7, p. 317.
- Clem, J., & Evenson, P. (2004). Observations of cosmic ray electrons and positrons during the early stages of the A- magnetic polarity epoch. *Journal of Geophysical Research (Space Physics)*, 109, A07107.
- Clem, J. M., Bieber, J. W., Evenson, P., Hall, D., Humble, J. E., & Duldig, M. (1997). Contribution of obliquely incident particles to neutron monitor counting rate. *Journal of Geophysical Research*, 102, 26919–26926.
- Clem, J. M., De Angelis, G., Goldhagen, P., & Wilson, J. W. (2003). Preliminary valida-

- tion of computational procedures for a new atmospheric ionizing radiation (air) model. *Advances in Space Research*, 32, 27–33.
- Clem, J. M., De Angelis, G., Goldhagen, W., & Wilson, J. W. (2004). New calculations of the atmospheric cosmic radiation field—results for neutron spectra. *Oxford University Press*, 110, 423–428.
- Clem, J. M., & Dorman, L. I. (2000). Neutron Monitor Response Functions. *Space Science Reviews*, 93, 335–359.
- Clem, J. M., Evenson, P., Huber, D., Pyle, R., Lopate, C., & Simpson, J. A. (2000). Charge sign dependence of cosmic ray modulation near a rigidity of 1 GV. *Journal of Geophysical Research*, 105, 23099–23106.
- Clem, J. M., & Evenson, P. A. (2002). Positron Abundance in Galactic Cosmic Rays. *Astrophys. J.*, 568, 216–219.
- Dorman, L. I., Fedchenko, S. G., Granitsky, L. V., & Rishe, G. A. (1970). Coupling and barometer coefficients for measurements of cosmic ray variations at altitudes of 260-400 mb. *International Cosmic Ray Conference*, 2, 233.
- Dorman, L. I., Villoresi, G., Iucci, N., Parisi, M., Tyasto, M. I., Danilova, O. A., & Ptitsyna, N. G. (2000). Cosmic ray survey to Antarctica and coupling functions for neutron component near solar minimum (1996-1997) 3. Geomagnetic effects and coupling functions. *Journal of Geophysical Research*, 105, 21047–21056.
- Dorman, L. I., & Yanke, V. G. (1981). The Coupling Functions of NM64 Neutron Supermonitor. In *International Cosmic Ray Conference*. *International Cosmic Ray Conference*, vol. 4, p. 326.
- Fan, C. Y., Gloeckler, G., Hsieh, K. C., & Simpson, J. A. (1966). Isotopic Abundances and Energy Spectra of He³ and He⁴ Above 40 MeV per Nucleon from the Galaxy. *Physical Review Letters*, 16, 813–817.
- Forbush, S. E. (1937). On the Effects in Cosmic-Ray Intensity Observed During the Recent Magnetic Storm. *Physical Review*, 51, 1108–1109.
- Forbush, S. E. (1954). World-Wide Cosmic-Ray Variations, 1937-1952. *Journal of Geophysical Research*, 59, 525–542.
- Forbush, S. E. (1967). A variation, with a period of two solar cycles, in the cosmic-ray diurnal anisotropy. *Journal of Geophysical Research*, 72, 4937–4939.
- Fowler, I. L. (1963). Very Large Boron Trifluoride Proportional Counters. *Review of*

- Scientific Instruments*, 34, 731–739.
- Garcia-Munoz, M., Meyer, P., Pyle, K. R., Simpson, J. A., & Evenson, P. (1986). The dependence of solar modulation on the sign of the cosmic ray particle charge. *Journal of Geophysical Research*, 91, 2858–2866.
- Gleeson, L. J., & Axford, W. I. (1968). Solar Modulation of Galactic Cosmic Rays. *Astrophys. J.*, 154, 1011.
- Hatton, C. J. (1971). The Neutron Monitor. In Wilson, J. G., & Wouthuysen, S. A. (Eds.), *Progress in elementary particle and cosmic ray physics*, Amsterdam, Netherlands: North-Holland Publishing Company, vol. 10. p. 1.
- Hatton, C. J., & Carmichael, H. (1964). Experimental Investigation of the NM-64 Neutron Monitor. *Canadian Journal of Physics*, 42, 2443–2472.
- Jokipii, J. R., & Levy, E. H. (1977). Effects of particle drifts on the solar modulation of galactic cosmic rays. *Astrophys. J. Lett.*, 213, L85–L88.
- Jokipii, J. R., Levy, E. H., & Hubbard, W. B. (1977). Effects of particle drift on cosmic-ray transport. I - General properties, application to solar modulation. *Astrophys. J.*, 213, 861–868.
- Jokipii, J. R., & Thomas, B. (1981). Effects of drift on the transport of cosmic rays. IV - Modulation by a wavy interplanetary current sheet. *Astrophys. J.*, 243, 1115–1122.
- Krüger, H. (2006). A calibration neutron monitor for long-term cosmic ray modulation studies. Ph.D. thesis, North-West University.
- Krüger, H., & Moraal, H. (2010). A calibration neutron monitor: Statistical accuracy and environmental sensitivity. *Advances in Space Research*, 46, 1394–1399.
- Krüger, H., Moraal, H., Bieber, J. W., Clem, J. M., Evenson, P. A., Pyle, K. R., Duldig, M. L., & Humble, J. E. (2003). First Results of a Mobile Neutron Monitor to Intercalibrate the Worldwide Network. In *International Cosmic Ray Conference*. *International Cosmic Ray Conference*, vol. 6, p. 3441.
- Krüger, H., Moraal, H., Bieber, J. W., Clem, J. M., Evenson, P. A., Pyle, K. R., Duldig, M. L., & Humble, J. E. (2008a). A calibration neutron monitor: Energy response and instrumental temperature sensitivity. *Journal of Geophysical Research (Space Physics)*, 113, A08101.
- Krüger, H., Moraal, H., Bieber, J. W., & et al. (2008b). Experiments with two calibration neutron monitors. *International Cosmic Ray Conference*, 1, 741–744.

- Krüger, H., Moraal, H., Ruffolo, D., Saiz, A., Nutaro, T., Kamyran, N., et al. (2011). Progress Report on the Intercalibration of the World's Neutron Monitors. In International Cosmic Ray Conference. *International Cosmic Ray Conference*, vol. 11, p. 446.
- Levy, E. H. (1976). Theory of the solar magnetic cycle wave in the diurnal variation of energetic cosmic rays - Physical basis of the anisotropy. *Journal of Geophysical Research*, 81, 2082–2088.
- Lin, Z., Bieber, J. W., & Evenson, P. (1995). Electron trajectories in a model magnetosphere: Simulation and observation under active conditions. *Journal of Geophysical Research (Space Physics)*, 100, 23543–23550.
- Lockwood, J. A., & Webber, W. R. (1996). Comparison of the rigidity dependence of the 11-year cosmic ray variation at the earth in two solar cycles of opposite magnetic polarity. *Journal of Geophysical Research*, 101, 21573–21580.
- Matthaeus, W. H., & Goldstein, M. L. (1982). Measurement of the rugged invariants of magnetohydrodynamic turbulence in the solar wind. *Journal of Geophysical Research*, 87, 6011–6028.
- McDonald, F. B. (2000). Integration of Neutron Monitor Data with Spacecraft Observations: a Historical Perspective. *Space Sci. Rev.*, 93, 263–284.
- Mewaldt, R. A., Davis, A. J., Lave, K. A., Leske, R. A., Stone, E. C., Wiedenbeck, M. E., et al. (2010). Record-setting Cosmic-ray Intensities in 2009 and 2010. *Astrophys. J. Lett.*, 723, L1–L6.
- Mitchell, J. W., Abe, K., Fuke, H., & et al. (2008). Solar Modulation of Low-Energy Antiproton and Proton Spectra Measured by BESS. In International Cosmic Ray Conference. *International Cosmic Ray Conference*, vol. 1, pp. 455–458.
- Moraal, H., Belov, A., & Clem, J. M. (2000). Design and Co-ordination of Multi-Station International Neutron Monitor Networks. *Space Science Reviews*, 93, 285–303.
- Moraal, H., Potgieter, M. S., Stoker, P. H., & van der Walt, A. J. (1989). Neutron monitor latitude survey of cosmic ray intensity during the 1986/1987 solar minimum. *Journal of Geophysical Research*, 94, 1459–1464.
- Nagashima, K., Sakakibara, S., Murakami, K., & Morishita, I. (1989). Response and yield functions of neutron monitor, Galactic cosmic ray spectrum and its solar modulation, derived from all the available world-wide surveys. *Nuovo*

- Cimento C Geophysics Space Physics C*, 12, 173–209.
- Oh, S., Bieber, J. W., Evenson, P., Clem, J., Yi, Y., & Kim, Y. (2013). Record neutron monitor counting rates from galactic cosmic rays. *Journal of Geophysical Research (Space Physics)*, 118, 5431–5436.
- Ormes, J. F., & Webber, W. R. (1965). Measurements of the primary proton and helium nuclei spectra and their modulations using a ballon-borne Cerenkov-scintillation counter. In International Cosmic Ray Conference. *International Cosmic Ray Conference*, vol. 1, p. 349.
- Potgieter, M. S. (2013). Cosmic Rays in the Inner Heliosphere: Insights from Observations, Theory and Models. *Space Sci. Rev.*, 176, 165–176.
- Potgieter, M. S., & Moraal, H. (1985). A drift model for the modulation of galactic cosmic rays. *Astrophys. J.*, 294, 425–440.
- Raubenheimer, B. C., & Stoker, P. H. (1974). Various aspects of the attenuation coefficient of a neutron monitor. *Journal of Geophysical Research*, 79, 5069–5076.
- Reinecke, J. P. L., Moraal, H., Potgieter, M. s., McDonald, F. B., & Webber, W. R. (1997). Different Crossovers? In International Cosmic Ray Conference. *International Cosmic Ray Conference*, vol. 2, p. 49.
- Ryan, M. J., Ormes, J. F., & Balasubrahmanyam, V. K. (1972). Cosmic-Ray Proton and Helium Spectra above 50 GeV. *Physical Review Letters*, 28, 985–988.
- Simpson, J. A. (1957). Solar Origin of Changes in the Primary Cosmic Radiation. *Proceedings of the National Academy of Science*, 43, 42–56.
- Simpson, J. A., Fonger, W., & Treiman, S. B. (1953). Cosmic Radiation Intensity-Time Variations and Their Origin. I. Neutron Intensity Variation Method and Meteorological Factors. *Physical Review*, 90, 934–950.
- Smith, C. W., & Bieber, J. W. (1993). Multiple spacecraft survey of the north-south asymmetry of the interplanetary magnetic field. *Journal of Geophysical Research*, 98, 9401–9415.
- Smith, L. H., Buffington, A., Smoot, D. F., Alvarez, L. W., & Wahlig, M. A. (1973). A Measurement of Cosmic-Ray Rigidity Spectra above 5 GV/c of Elements from Hydrogen to Iron. *Astrophys. J.*, 180, 987–1010.
- Stoker, P. H., Dorman, L. I., & Clem, J. M. (2000). Neutron Monitor Design Improvements. *Space Science Reviews*, 93, 361–380.
- Stoker, P. H., & Moraal, H. (1995). Neutron Monitor Latitude Surveys at Aircraft

Altitudes. *Astrophysics Space Science*, 230, 365–373.

Thambyahpillai, T., & Elliot, H. (1953). World-Wide Changes in the Phase of the Cosmic-Ray Solar Daily Variation. *Nature*, 171, 918–920.

Usoskin, I. G., Bazilevskaya, G. A., & Kovaltsov, G. A. (2011). Solar modulation parameter for cosmic rays since 1936 reconstructed from ground-based neutron monitors and ionization chambers. *Journal of Geophysical Research (Space Physics)*, 116, A02104.

von Rosenvinge, T. T., Webber, W. R., & Ormes, J. F. (1969). A Comparison of the Energy Spectra of Cosmic Ray Helium and Heavy Nuclei. *Astrophys. Space Sci.*, 5, 342–359.

Webber, W. R., & Lezniak, J. A. (1974). The comparative spectra of cosmic-ray protons and helium nuclei. *Astrophys. Space Sci.*, 30, 361–380.

Webber, W. R., & Lockwood, J. A. (1988). Characteristics of the 22-year modulation of cosmic rays as seen by neutron monitors. *Journal of Geophysical Research*, 93, 8735–8740.

APPENDICES

APPENDIX A

LISTS OF PROBLEMATIC TIMES

After we finished the latitude survey data preparation in the format of the Latsur file as explained in Chapter 4, we corrected for several instrumental anomalies by comparing the count rates of three independent neutron detector tubes. We noted everything we did to correct the data for all surveys. Table A.1 shows an example of details of the first correction of three count ratios T1/T2, T2/T3, and T3/T1 for 30-min. data in survey year 1998. We recorded all things we did in the column of “Notes.” Let us explain these definitions:

use (1),(2)and(3) means we preserved the count rates of tubes T1 (left tube), T2 (middle tube) and T3 (right tube) because they had good data.

REMOVE ALL TUBES means we removed T1, T2 and T3 because of bad counts.

DATA GAP means there were no data during that time interval. They may have been deleted in the preparation process because of various equipment problems.

REMOVE(1);use(2)and(3) means we removed the counts of T1 because of a bad count rate but use the data of two remaining tubes which are T2 and T3. The tube number may be changed in this case.

use(1)×frac.num,(2)and(3) means we multiplied T1 by the specified fraction and used the data together with T2 and T3. In the same pattern, if there is a mark “×” and multiplier (fraction number) after any tube number, the count rate of that tube was multiplied by that fraction.

REMOVE(1);use(2)and(3)×frac.num means we removed counts of T1, used T2 and multiplied T3 by the specified fraction. The tube number may be changed in this case.

Table A.2 shows an example of details of the second correction as in Table A.1 but for the daily average tube ratios of the 1998 survey year.

Table A.1: An example of a list of problematic times for the FIRST correction for half-hourly data in the 1998 survey year

| Survey Years | Start DOY | End DOY | Notes | T1/T2 | T2/T3 | T3/T1 |
|--------------|-----------|---------|--|-------|-------|-------|
| 1998 | | | Half-hourly average data | | | |
| | year | year | Before FIRST correction | 0.899 | 0.969 | 1.149 |
| | year | year | After FIRST correction | 0.897 | 1.110 | 1.004 |
| | 307.042 | 307.795 | use (1),(2),and(3) | | | |
| | 307.808 | 307.808 | REMOVE ALL TUBES | | | |
| | 307.839 | 312.119 | use(1),(2),and(3) | | | |
| | 312.135 | 312.727 | DATA GAP | | | |
| | 312.727 | 314.681 | use(1),(2),and(3) | | | |
| | 314.681 | 320.773 | DATA GAP | | | |
| | 320.773 | 325.939 | use(1),(2),and(3) | | | |
| | 325.960 | 325.960 | REMOVE(3);use(1),and(2) | | | |
| | 325.984 | 326.935 | use(1),(2),and(3) \times 0.860 | | | |
| | 327.004 | 329.281 | use(1),(2),and(3) \times 0.725 | | | |
| | 327.090 | 327.090 | REMOVE(3);use(1),and(2) | | | |
| | 327.834 | 327.920 | REMOVE(3);use(1),and(2) | | | |
| | 329.302 | 346.993 | use(1),(2),and(3) \times 0.766 | | | |
| | 347.105 | 348.946 | REMOVE(3);use(1),and(2) | | | |
| | 348.968 | 371.208 | use(1),(2),and(3) \times 0.880 | | | |
| | 350.917 | 351.236 | REMOVE(3);use(1),and(2) | | | |
| | 371.229 | 371.229 | REMOVE(1);use(2),and(3) \times 0.880 | | | |
| | 371.250 | 372.924 | use(1),(2)and(3) \times 0.880 | | | |
| | 371.992 | 371.992 | REMOVE ALL TUBES | | | |
| | 372.055 | 372.055 | REMOVE ALL TUBES | | | |
| | 372.818 | 372.840 | REMOVE ALL TUBES | | | |
| | 372.945 | 373.454 | REMOVE(1);use(2),and(3) \times 0.880 | | | |
| | 373.475 | 376.999 | use(1),(2),and(3) \times 0.880 | | | |
| | 376.818 | 376.882 | REMOVE ALL TUBES | | | |
| | 376.999 | 426.037 | DATA GAP | | | |
| | 426.037 | 442.762 | use(1),(2),and(3) \times 0.867 | | | |
| | 442.783 | 446.404 | REMOVE(1);use(2),and(3) \times 0.867 | | | |
| | 444.604 | 444.604 | REMOVE(1),and(3);use(2) | | | |
| | 446.425 | 453.351 | REMOVE(3);use(1),and(2) | | | |
| | 453.372 | 453.372 | REMOVE(1),and(3);use(2) | | | |
| | 453.393 | 453.520 | REMOVE(3);use(1),and(2) | | | |
| | 453.456 | 453.456 | REMOVE(2),and(3);use(1) | | | |
| | 453.541 | 477.716 | use(1),(2),and(3) \times 0.867 | | | |
| | 453.859 | 453.922 | REMOVE(1);use(2),and(3) | | | |
| | 453.986 | 454.113 | REMOVE(3);use(1),and(2) | | | |
| | 454.642 | 454.642 | REMOVE ALL TUBES | | | |
| | 456.231 | 456.421 | REMOVE ALL TUBES | | | |
| | 473.214 | 473.214 | REMOVE(3);use(1),and(2) | | | |
| | 477.716 | 477.716 | REMOVE ALL TUBES | | | |
| | 477.716 | 478.591 | DATA GAP | | | |
| | 478.591 | 508.264 | use(1),(2),and(3) \times 0.867 | | | |

Table A.2: An example of a list of problematic times for the SECOND correction for daily average data in the 1998 survey year

| Survey Years | Start DOY | End DOY | Notes | T1/T2 | T2/T3 | T3/T1 |
|--------------|-----------|---------|---|-------|-------|-------|
| 1998 | | | Daily average data | | | |
| | year | year | Before SECOND correction | 0.897 | 1.110 | 1.004 |
| | year | year | After SECOND correction | 0.899 | 1.109 | 1.004 |
| | 307.000 | 308.000 | use(1),(2) \times 0.989,and(3) \times 0.970 | | | |
| | 309.000 | 309.000 | use(1),(2) \times 0.990,and(3) \times 0.974 | | | |
| | 310.000 | 310.000 | use(1),(2) \times 0.988,and(3) \times 0.978 | | | |
| | 311.000 | 311.000 | use(1),(2) \times 0.987,and(3) \times 0.976 | | | |
| | 312.000 | 312.000 | use(1),(2) \times 0.990,and(3) \times 0.976 | | | |
| | 313.000 | 314.000 | use(1),(2) \times 0.993,and(3) \times 0.981 | | | |
| | 315.000 | 319.000 | DATA GAP | | | |
| | 320.000 | 320.000 | use(1) \times 0.997,(2),and(3) | | | |
| | 321.000 | 323.000 | use(1) \times 1.002,(2),and(3) | | | |
| | 324.000 | 325.000 | use(1),(2),and(3) | | | |
| | 326.000 | 326.000 | use(1),(2),and(3) \times 0.990 | | | |
| | 327.000 | 328.000 | use(1),(2),and(3) | | | |
| | 329.000 | 329.000 | use(1),(2),and(3) \times 0.985 | | | |
| | 330.000 | 330.000 | use(1),(2),and(3) \times 0.992 | | | |
| | 331.000 | 331.000 | use(1),(2),and(3) | | | |
| | 332.000 | 332.000 | use(1),(2),and(3) \times 0.977 | | | |
| | 333.000 | 333.000 | use(1),(2),and(3) | | | |
| | 334.000 | 334.000 | use(1),(2),and(3) \times 0.978 | | | |
| | 335.000 | 335.000 | use(1),(2),and(3) \times 0.980 | | | |
| | 336.000 | 338.000 | use(1),(2),and(3) \times 0.989 | | | |
| | 339.000 | 348.000 | use(1),(2),and(3) | | | |
| | 349.000 | 349.000 | use(1),(2),and(3) \times 0.995 | | | |
| | 350.000 | 350.000 | use(1),(2),and(3) \times 0.986 | | | |
| | 351.000 | 364.000 | use(1),(2),and(3) \times 0.995 | | | |
| | 365.000 | 365.000 | use(1) \times 1.002,(2),and(3) \times 0.990 | | | |
| | 366.000 | 374.000 | use(1),(2),and(3) \times 0.996 | | | |
| | 375.000 | 376.000 | use(1),(2),and(3) \times 0.998 | | | |
| | 377.000 | 425.000 | DATA GAP | | | |
| | 426.000 | 428.000 | use(1),(2),and(3) | | | |
| | 429.000 | 434.000 | use(1),(2) \times 0.996,and(3) | | | |
| | 435.000 | 444.000 | use(1),(2) \times 0.993,and(3) | | | |
| | 445.000 | 445.000 | use(1),(2) \times 0.991,and(3) | | | |
| | 446.000 | 446.000 | use(1) \times 1.004,(2),and(3) | | | |
| | 447.000 | 452.000 | use(1),(2),and(3) | | | |
| | 453.000 | 455.000 | use(1),(2),and(3) \times 1.004 | | | |
| | 456.000 | 456.000 | use(1) \times 0.992,(2),and(3) \times 1.004 | | | |
| | 457.000 | 462.000 | use(1),(2),and(3) \times 1.004 | | | |
| | 463.000 | 468.000 | use(1),(2),and(3) \times 1.009 | | | |
| | 469.000 | 469.000 | use(1),(2),and(3) \times 1.013 | | | |
| | 470.000 | 471.000 | use(1),(2),and(3) \times 1.009 | | | |
| | 472.000 | 483.000 | use(1),(2),and(3) \times 1.011 | | | |
| | 484.000 | 485.000 | use(1),(2),and(3) \times 1.010 | | | |
| | 486.000 | 489.000 | use(1),(2),and(3) \times 1.009 | | | |
| | 490.000 | 491.000 | use(1),(2),and(3) \times 1.008 | | | |

APPENDIX B

PRESSURE COEFFICIENT DETERMINATION

The secondary cosmic rays could be absorbed in the Earth's atmosphere because of barometric pressure according to

$$C = C_0 e^{-\beta(p-p_0)} \quad (\text{B.1})$$

where C is the neutron monitor count rate, C_0 is the neutron monitor count rate at the reference barometric pressure, p is the barometric pressure, p_0 is the reference barometric pressure and β is the dimensionless barometric pressure coefficient, which is a value indicating the neutron absorption rate when the barometric pressure increases. We assume that β has a specific value that depends only on cutoff rigidity and does not otherwise depend on latitude, longitude, or altitude. This section discusses the pressure coefficient determination, which is applied for each cutoff rigidity, and shows the steps to obtain an empirical pressure coefficient varying with cutoff rigidity. Once we know $\beta(P_c)$, we can derive C_p , the pressure corrected count rate, as an estimate of C_0 .

We consider a linear fitting process for equation B.1, so that

$$\ln C = \ln C_0 - \beta(p - p_0) \quad (\text{B.2})$$

It should be useful if we take 24-hour averages to equation B.2.

$$\langle \ln C \rangle = \langle \ln C_0 \rangle - \beta(\langle p \rangle - p_0), \quad (\text{B.3})$$

If we consider the primary cosmic ray flux at the reference pressure, we could assume that $\ln C_0 \approx \langle \ln C_0 \rangle$ because $\ln C_0$ varies much more slowly than other quantities. From equations B.2 and (B.3), we obtain:

$$\ln C - \langle \ln C \rangle = -\beta(p - \langle p \rangle). \quad (\text{B.4})$$

where p is the barometric pressure recorded for each time and $\langle p \rangle$ is the average barometric pressure during the day.

The data of latitude surveys cover a wide range of apparent cutoff rigidity, from ≈ 0 GV at McMurdo to over 18 GV near Thailand. If we need the count rate corrected for pressure, we should know a best fit relationship between β and the cutoff rigidity for existing latitude survey data. There are many steps to obtain the formula.

In the first step, after obtaining the LatSur files as explained in section 4.3, we sorted the data into cutoff rigidity bins, i.e., 0-1 GV, 1-2 GV, ..., 18-19 GV. In the second step, we analyzed the data for each interval using a C language program to calculate $\ln C - \langle \ln C \rangle$ and $p - \langle p \rangle$. Because the data interval duration was 1 h for survey year 1994 and 30 min for subsequent survey years, the 24-hour-averaged quantities were running averages over 24 data points for survey year 1994 and 48 data points for subsequent survey years. Using equation B.4, we obtain the slope of the linear regression for each rigidity bin as shown in Figures B.1, B.2, and B.3. All slopes from linear regression are noted in the third column of Table B.1. We have no data for cutoff rigidity range 7–8 GV because 24-hour-averaged quantities were not computed if data for part of the day were missing. We discounted the slopes in some rigidity intervals with poor statistics ($R^2 < 0.3$, or there were less than 100 data points), i.e., P_c ranges 6–7 GV, 9–10 GV, 10–11 GV, 13–14 GV, 14–15 GV, 17–18 GV and 18–19 GV. We list the remaining usable data in the fourth column of Table B.1. Then we graph the pressure coefficients against P_c (plotting at the center of rigidity bins). Vertical error bars represent the standard error of the data, about 0.0006. We obtain a formula for an empirical pressure coefficient as a function of cutoff rigidity determined from our survey data, $\beta = (1.006 - 0.0153P_c/\text{GV}) \text{ \%/mm Hg}$ as shown in Figure B.4.

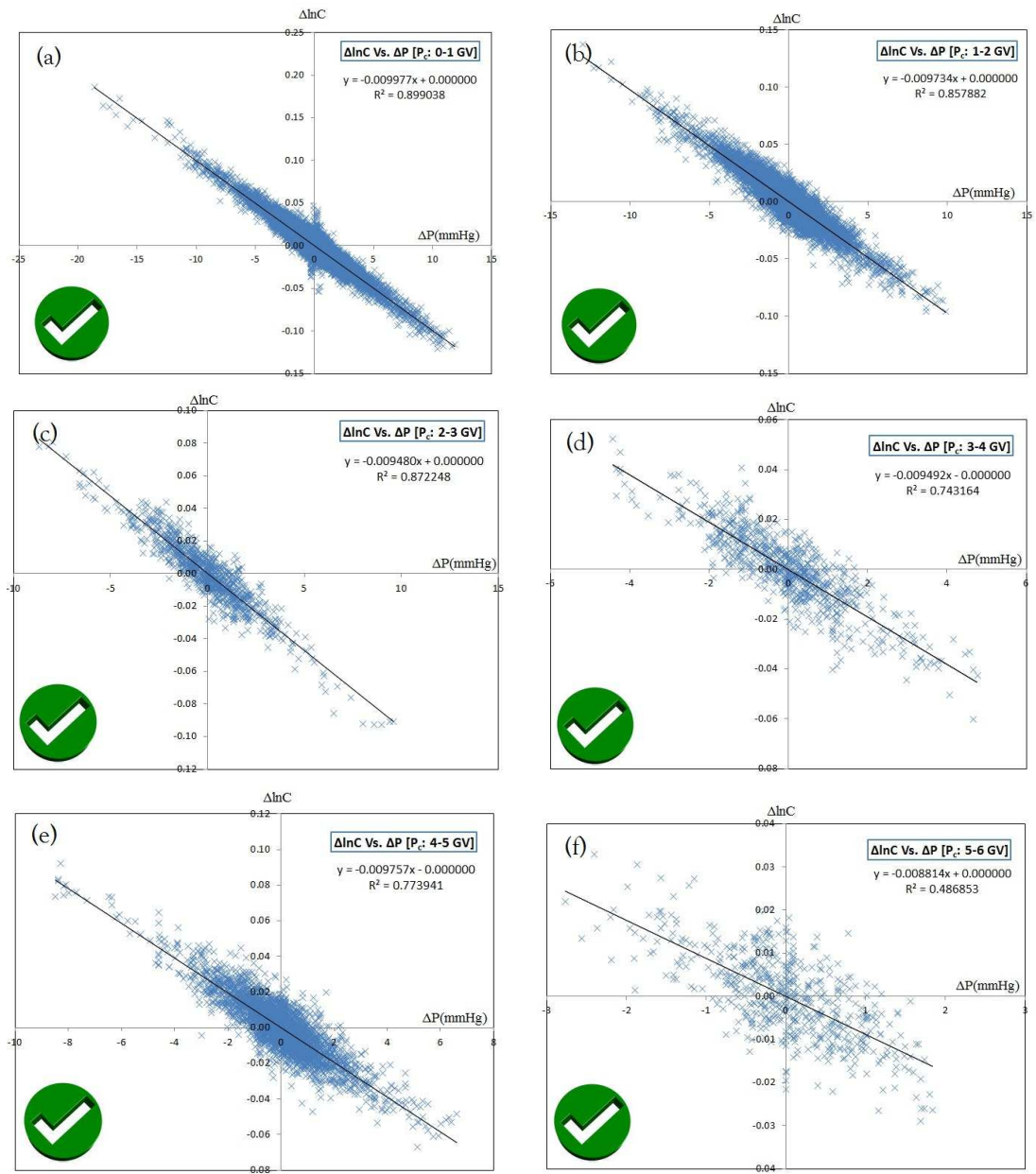


Figure B.1: Linear fitting of residuals from 24-hour averages of the logarithmic count rate and the barometric pressure (mm Hg), using latitude survey data from all survey years to find the slopes for each rigidity bin from $P_c : 0 - 1$ GV to $P_c : 5 - 6$ GV. The symbol \checkmark or \times shows whether we obtained a usable estimate of the slope (pressure coefficient).

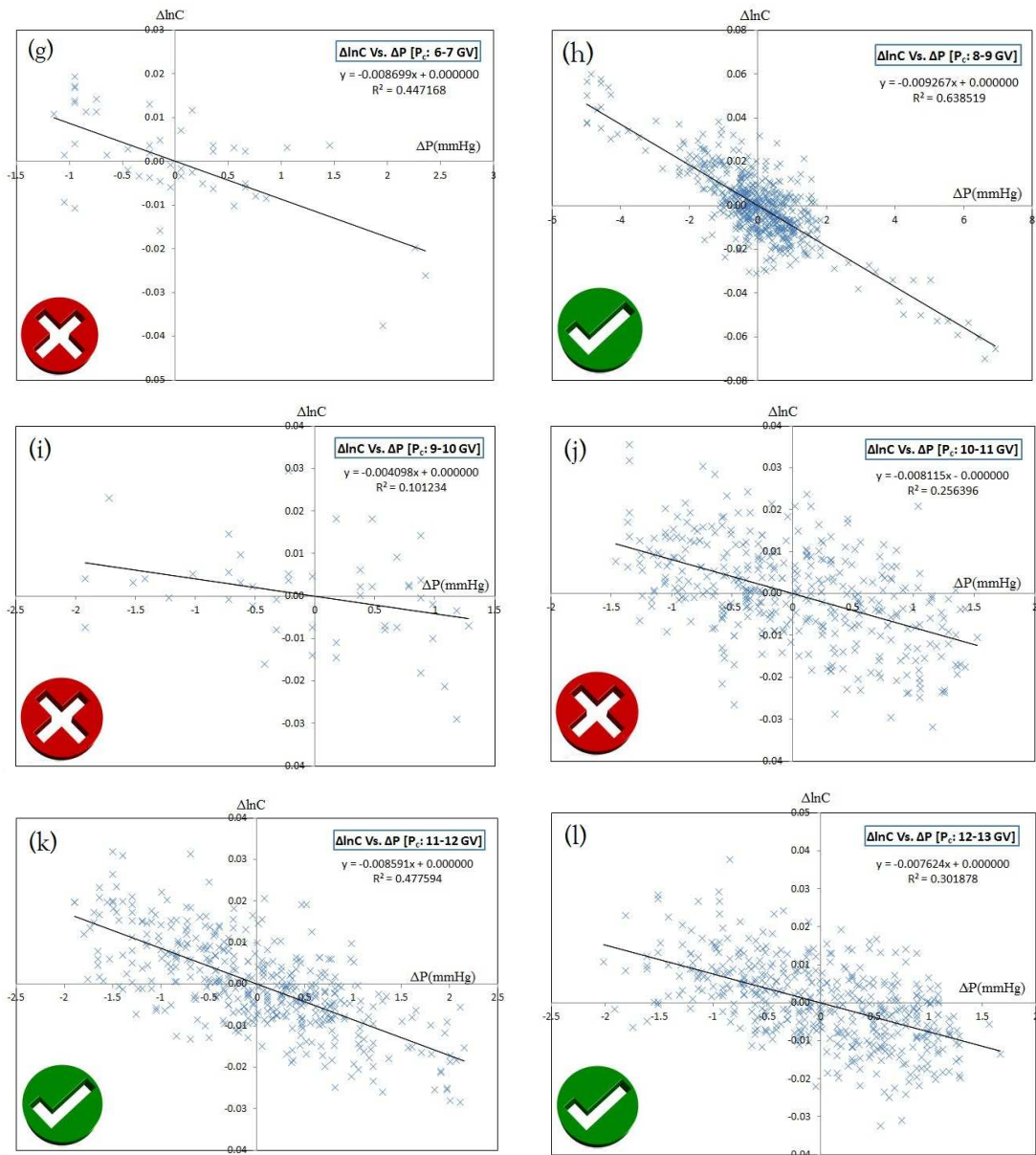


Figure B.2: Like Figure B.1, from P_c : 6 – 7 GV to P_c : 12 – 13 GV.

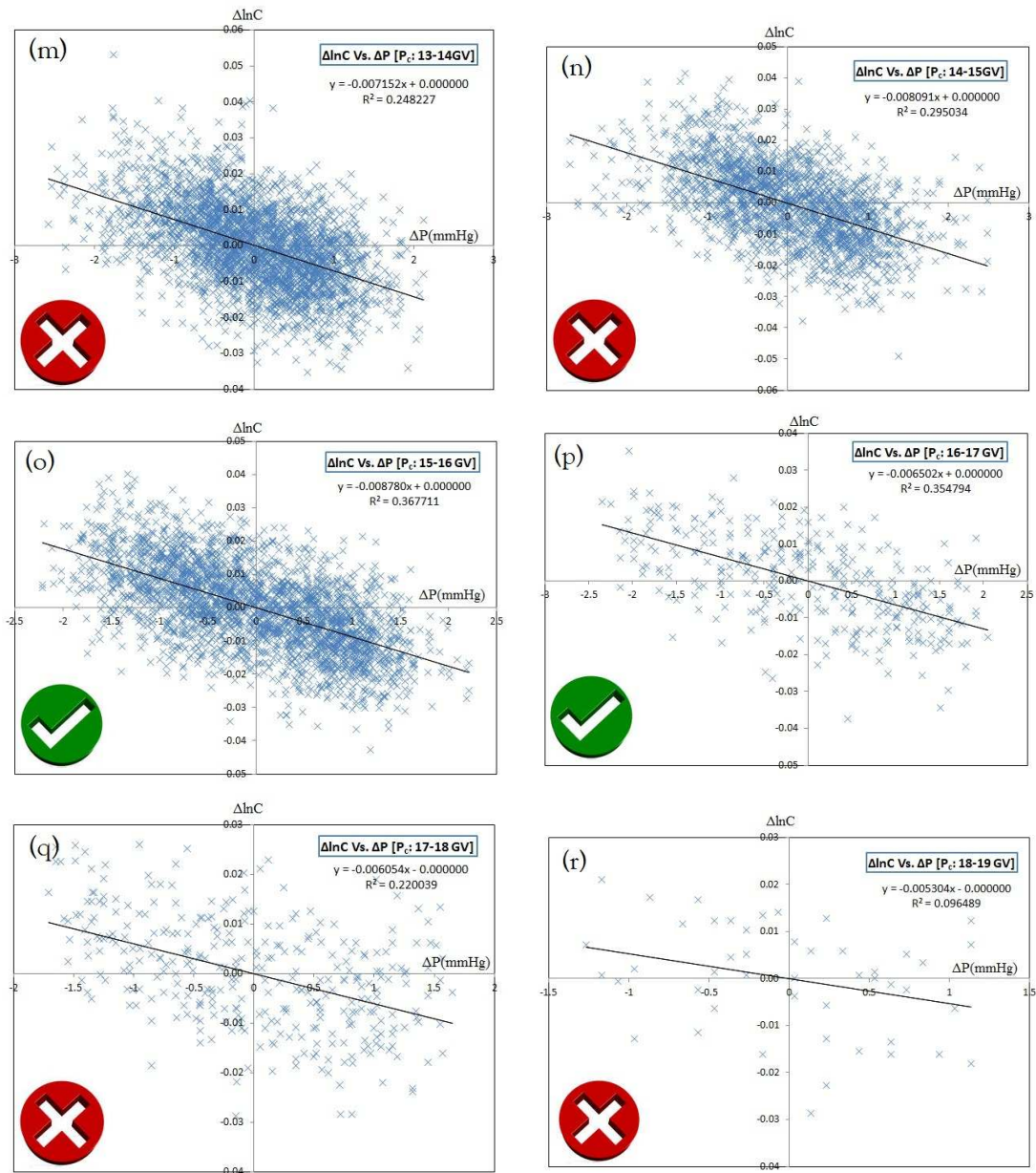


Figure B.3: Like Figure B.1, from P_c : 13 – 14 GV to P_c : 18 – 19 GV.

Table B.1: The data of cutoff rigidity bin (GV), center of rigidity bin (GV), β (all estimates), and β (usable estimates)

| Cutoff Rigidity Bin(GV) | Center of Rigidity Bin (GV) | β^a (all estimates) | β^b (usable estimates) |
|----------------------------|--------------------------------|------------------------------|---------------------------------|
| 0–1 | 0.5 | 0.009977 | 0.009977 |
| 1–2 | 1.5 | 0.009734 | 0.009734 |
| 2–3 | 2.5 | 0.009480 | 0.009480 |
| 3–4 | 3.5 | 0.009492 | 0.009492 |
| 4–5 | 4.5 | 0.009757 | 0.009757 |
| 5–6 | 5.5 | 0.008814 | 0.008814 |
| 6–7 | 6.5 | 0.008699 | – |
| 7–8 | 7.5 | – | – |
| 8–9 | 8.5 | 0.009267 | 0.009267 |
| 9–10 | 9.5 | 0.004098 | – |
| 10–11 | 10.5 | 0.008115 | – |
| 11–12 | 11.5 | 0.008591 | 0.008591 |
| 12–13 | 12.5 | 0.007624 | 0.007624 |
| 13–14 | 13.5 | 0.007152 | – |
| 14–15 | 14.5 | 0.008091 | – |
| 15–16 | 15.5 | 0.008780 | 0.00878 |
| 16–17 | 16.5 | 0.006502 | 0.006502 |
| 17–18 | 17.5 | 0.006054 | – |
| 18–19 | 18.5 | 0.005304 | – |

^aRegression coefficient between $\Delta \ln C$ and ΔP for each cutoff rigidity interval, i.e., 0-1 GV, 1-2 GV, ..., 18-19 GV.

^bThe regression coefficient is considered usable if $R^2 > 0.3$ and there are more than 100 data points.

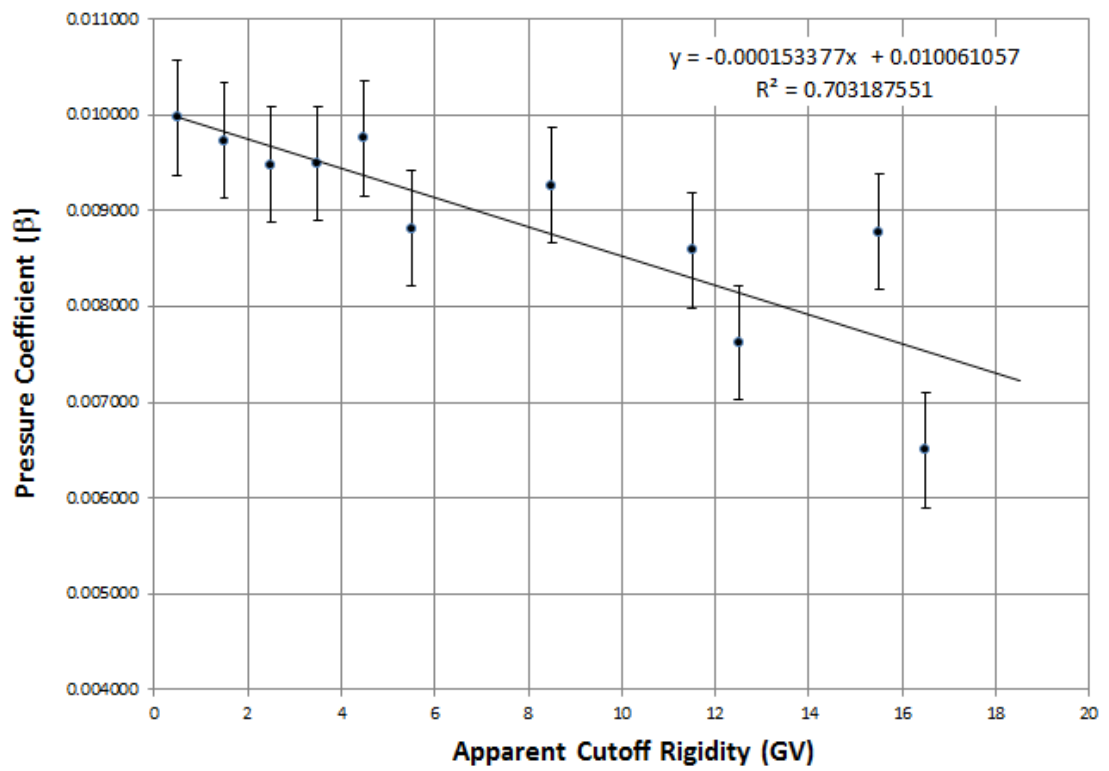


Figure B.4: The pressure coefficient (β) as a function of apparent cutoff P_c

APPENDIX C

REGRESSION COEFFICIENT FOR SHORT-TERM VARIATIONS IN MODULATION LEVEL

After we plotted the mobile monitor count rate from the latitude survey data from 1994 to 2007 as a function of apparent cutoff rigidity, we noticed short-term fluctuations in the data. We plotted the mobile count rate corrected for barometric pressure vs. the McMurdo count rate and apparent cutoff rigidity in three dimensions as shown in Figures C.1, C.2, and C.3 for different survey years. The colored lines explain the code for the segments, i.e., the blue lines indicate “segment A” in which the ship traveled from Seattle (US West Coast) to the Cutoff Equator, CE (similar to the geomagnetic equator), the black lines indicate “segment B” in which the ship traveled from CE to McMurdo (Coast of Antarctica), the green lines indicate “segment C” in which the ship traveled from McMurdo to CE, the orange lines indicate “segment D” in which the ship traveled from CE to Seattle, and the grey lines indicate “all segments.” The grey lines also indicate the projection of data in each plane. We can clearly see variations in modulation level in segment D of survey year 1996 and segment A of survey years 1998 and 1999. The data of segments A and B are separate from segments C and D for survey year 2000. For the survey year 2003, segments C and D were grouped together but segments A and B were separated from them. We identified that whenever the mobile monitor is unusually high for a segment, the McMurdo rate was also high. Especially, the survey year 2003 even has funny ups and downs that mimic changes at McMurdo. Therefore, we should correct the mobile monitor count rate for short-term (sub-year) GCR fluctuations. In other words, we should correct the mobile monitor data for variations at McMurdo to improve the quality of the integral response functions. We proposed that we could determine a slope between mobile monitor and McMurdo data for each rigidity interval, and could correct each year’s mobile monitor data to the average McMurdo value for that year.

There are some steps to obtain an empirical formula for correction of the

variations. The first step is to sort the data into apparent cutoff rigidity bins and plot graphs between the mobile monitor count rate corrected for tube ratios and pressure as a function of the McMurdo count rate corrected for pressure for each rigidity bin, i.e., 0-1 GV, 1-2 GV, ..., 17-19 GV (where 17-18 GV and 18-19 GV were grouped together) to obtain slopes of them as shown in Figures C.4, C.5, and C.6. Then we noted the rigidity bins, center of rigidity bins (mostly with intervals of width 1 GV instead of 0.5 GV) and slopes from the plots in the Table C.1. The final step was to plot a graph of those slopes against the apparent cutoff rigidity. We found that the regression coefficient S as a function of apparent cutoff rigidity P_c was well fit by an exponential function, $S = 0.211e^{-0.141P_c}$, as shown in Figure C.7. We then used this value of S to correct each survey year's mobile monitor data to the average McMurdo value \bar{m} for that survey year according to $C_{TPM} = C_{TP} - S(m - \bar{m})$, where C_{TPM} is the normalized mobile monitor count rate corrected for tube anomalies, pressure, and short-term GCR variations, m is McMurdo count rate, and C_{TP} is the mobile monitor count rate corrected for tube anomalies, normalized to McMurdo, and corrected for pressure, as explained in Section 4.4.

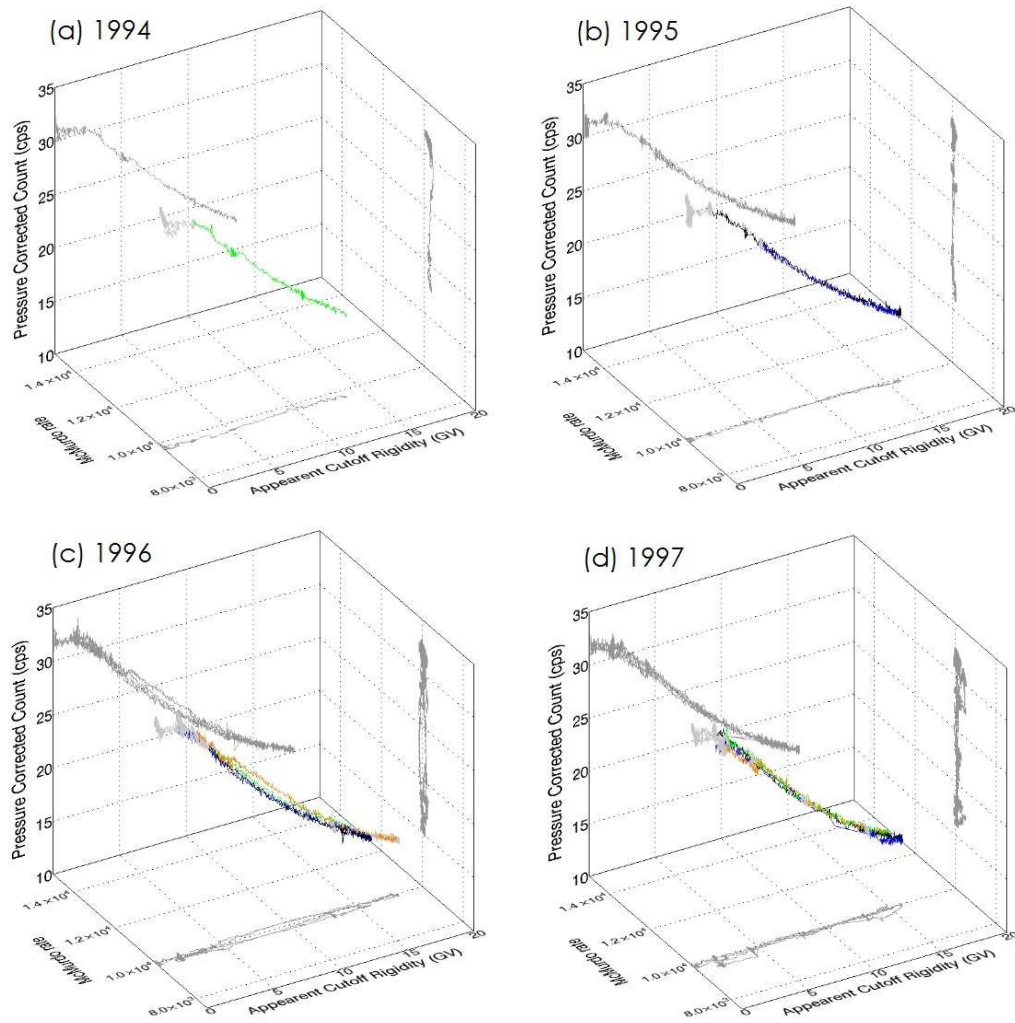


Figure C.1: Three dimensional plot among mobile monitor count rate corrected for tube ratios and pressure (s^{-1}), McMurdo count rate corrected for pressure (s^{-1}), and apparent cutoff rigidity (GV) for survey years 1994-1997.

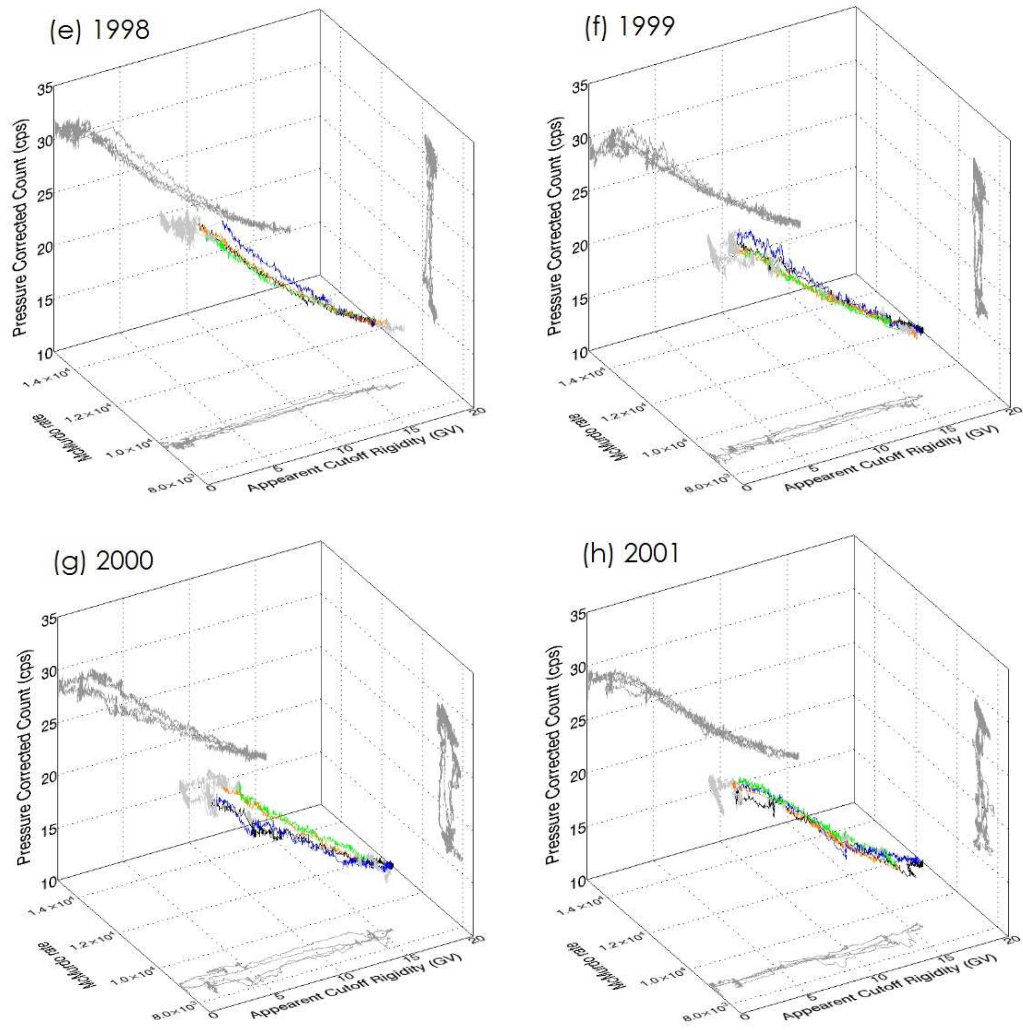


Figure C.2: Like Figure C.1, for survey years 1998-2001.

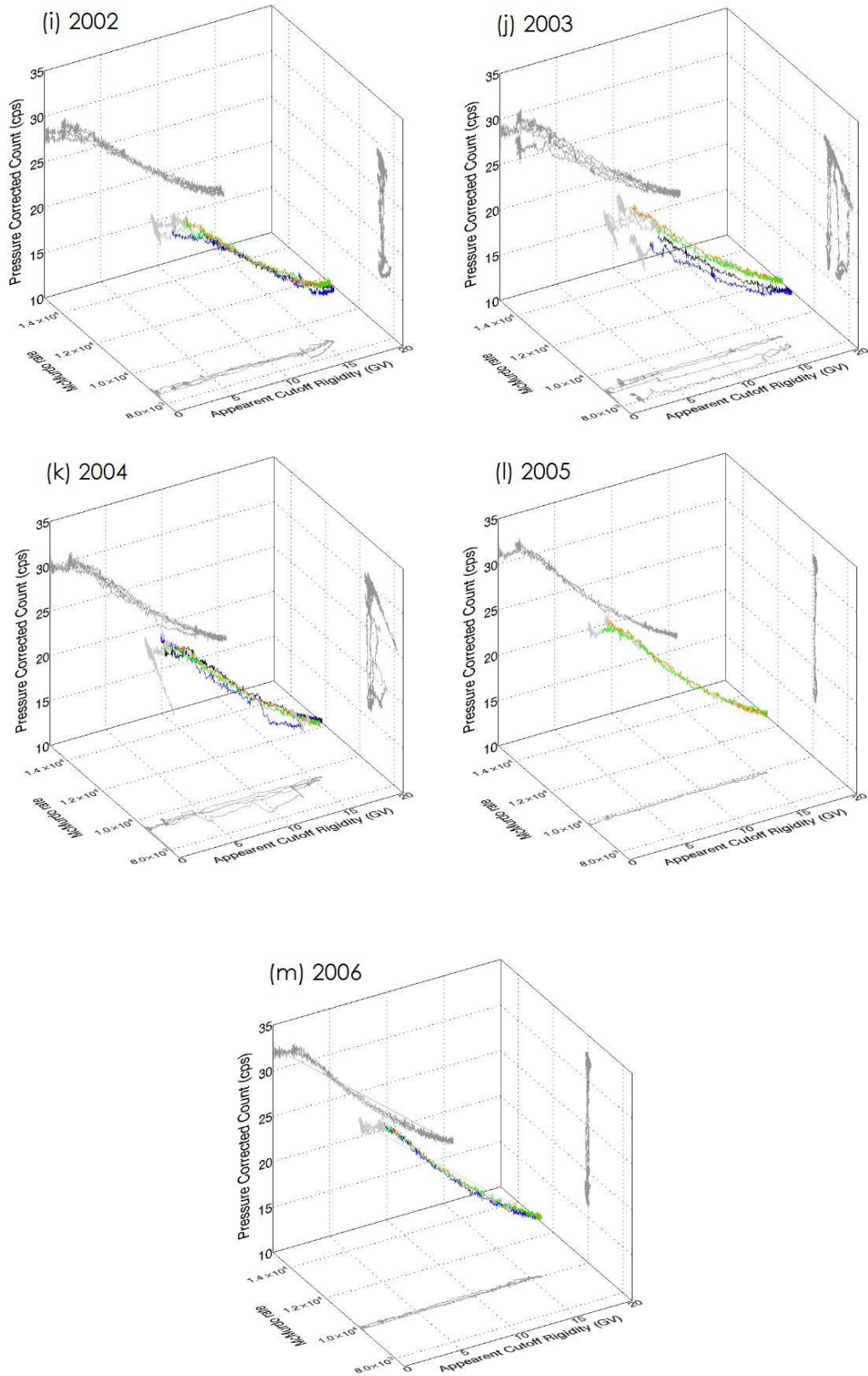


Figure C.3: Like Figure C.1, for survey years 2002-2006.

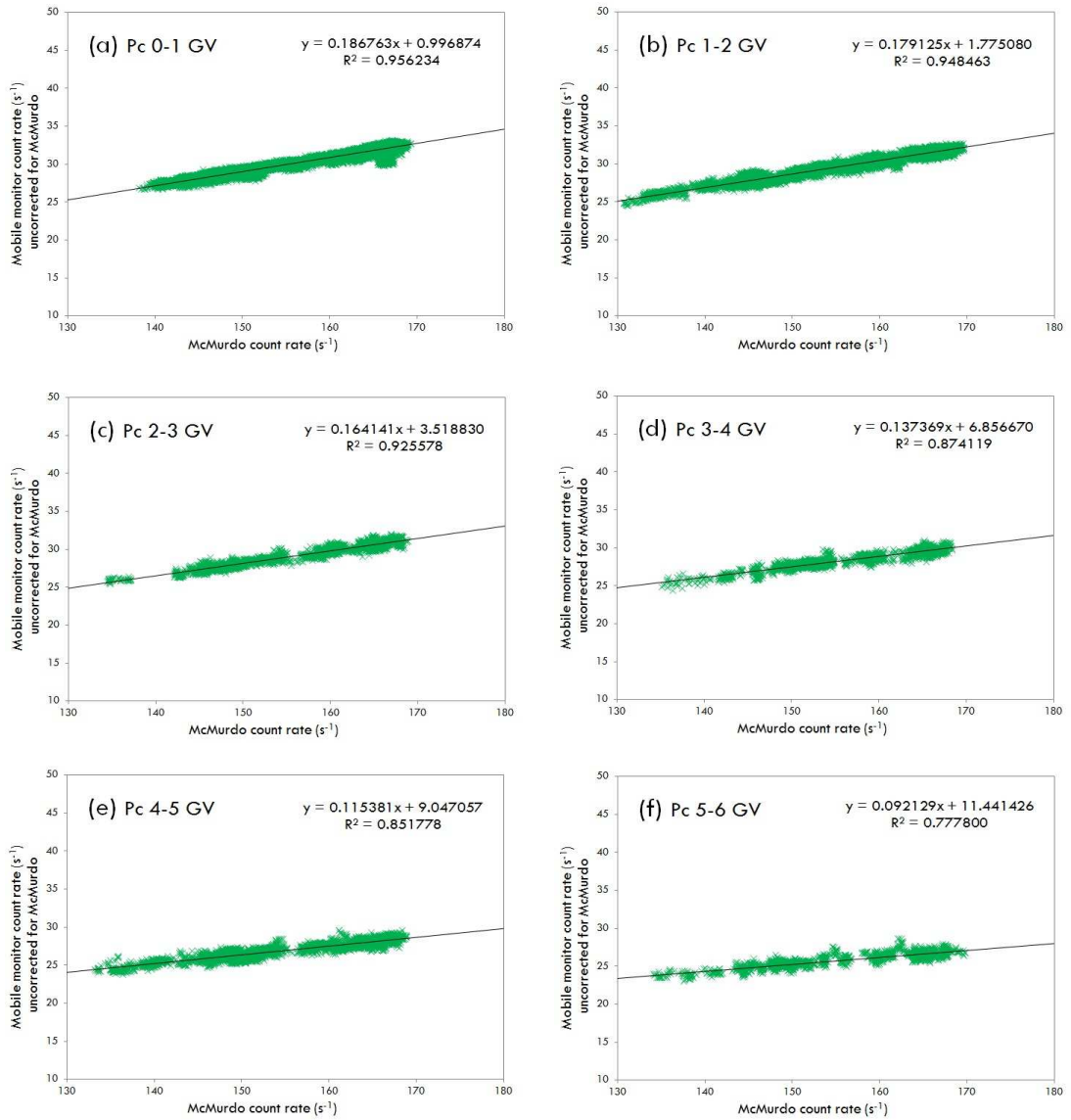


Figure C.4: Linear fitting of mobile monitor count rate (s^{-1}) against McMurdo count rate (s^{-1}) for the 1994-2006 survey years to find the slopes for rigidity bins from 0-1 GV to 5-6 GV.

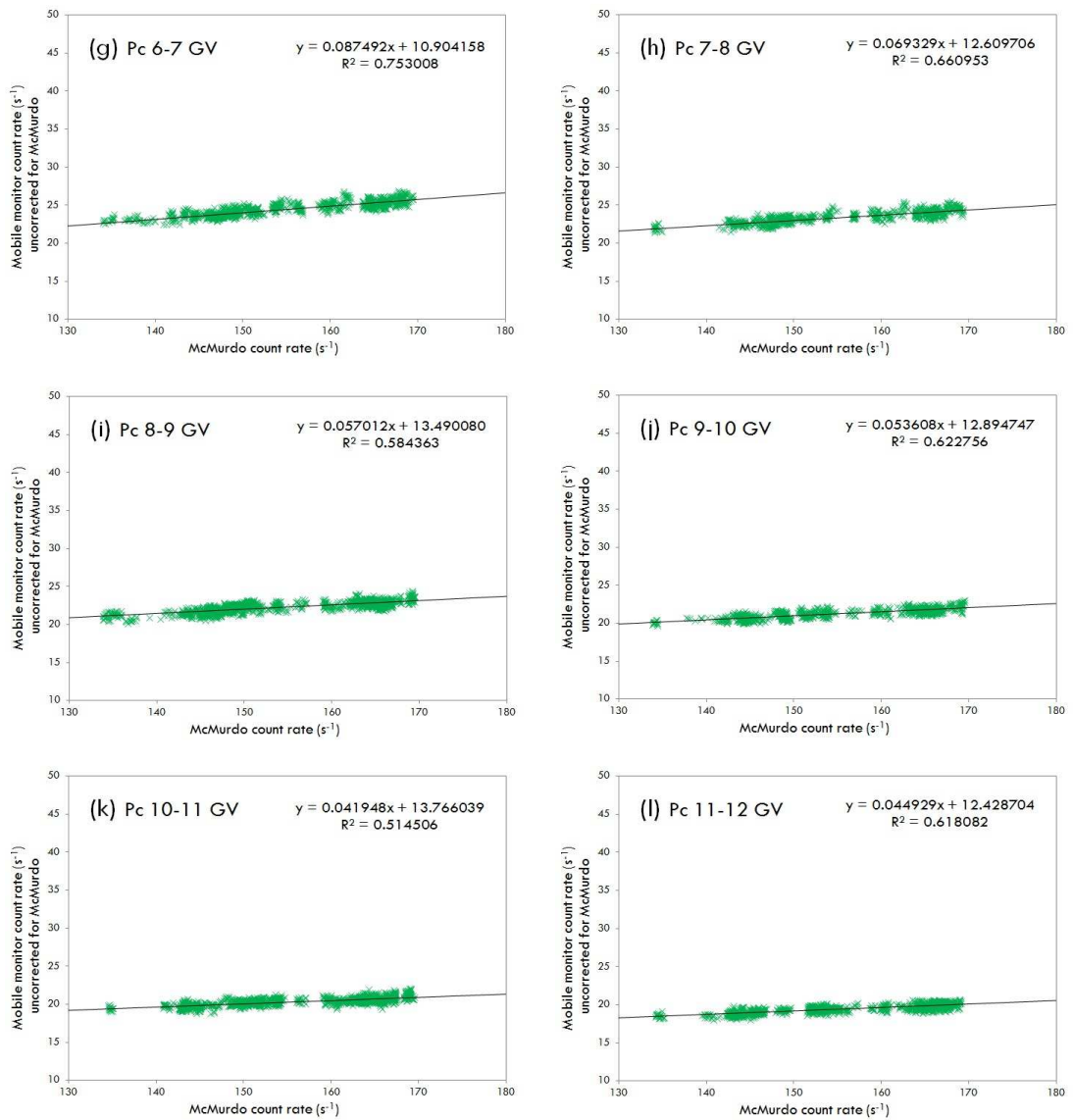


Figure C.5: Like Figure C.4, for rigidity bins from 6-7 GV to 11-12 GV.

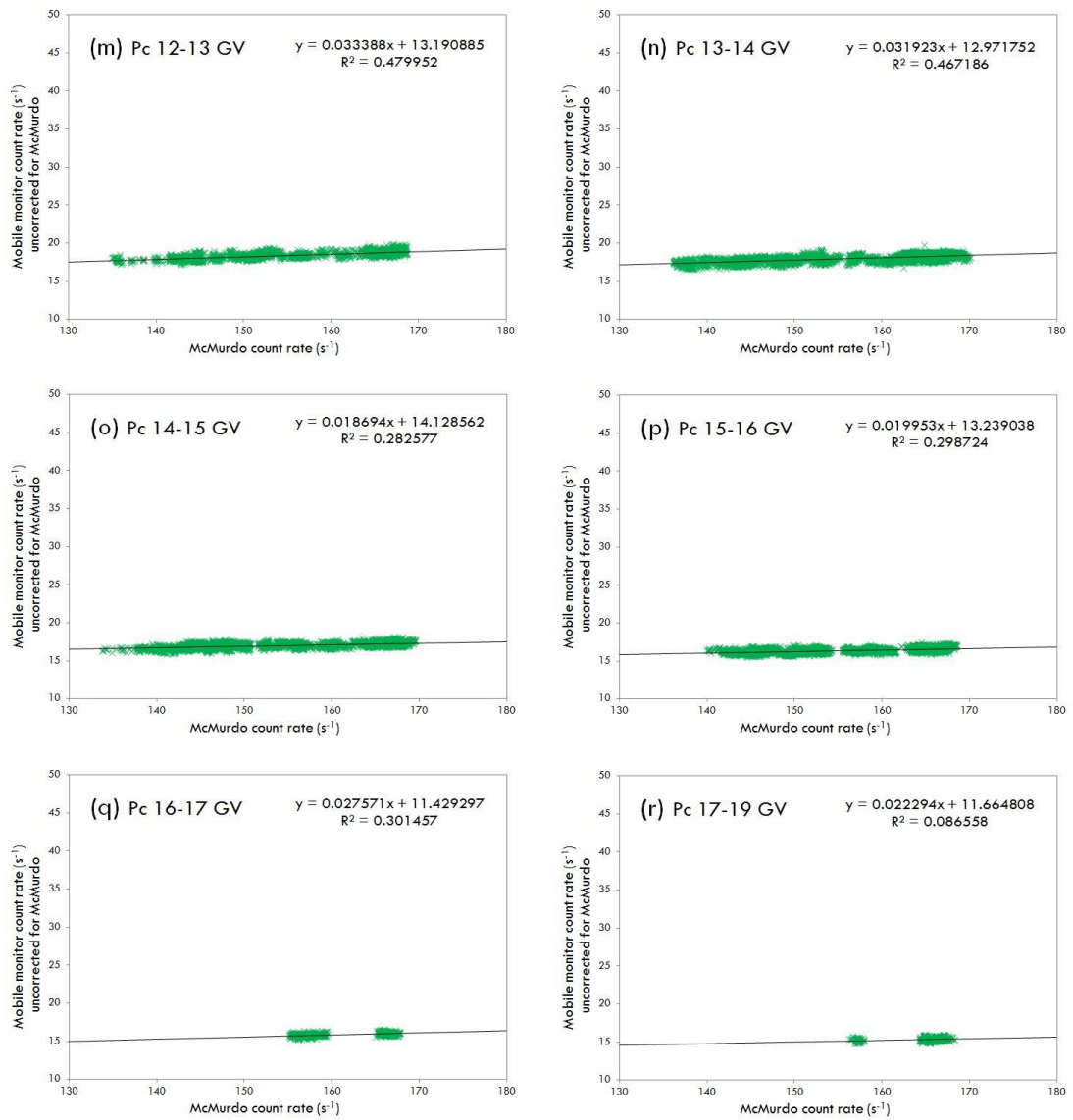


Figure C.6: Like Figure C.4, for rigidity bins from 12-13 to 17-19 GV.

Table C.1: Cutoff rigidity and regression coefficient between the normalized mobile neutron monitor count rate corrected for tube ratios and pressure and the McMurdo count rate corrected for pressure for each apparent cutoff rigidity bin.

| Cutoff Rigidity Bins(GV) | Center of Rigidity Bins (GV) | Regression Coefficient |
|-----------------------------|---------------------------------|---------------------------|
| 0-1 | 1.0 | 0.186763 |
| 1-2 | 1.5 | 0.179125 |
| 2-3 | 2.5 | 0.164141 |
| 3-4 | 3.5 | 0.137369 |
| 4-5 | 4.5 | 0.115381 |
| 5-6 | 5.5 | 0.092129 |
| 6-7 | 6.5 | 0.087492 |
| 7-8 | 7.5 | 0.069329 |
| 8-9 | 8.5 | 0.057012 |
| 9-10 | 9.5 | 0.053608 |
| 10-11 | 10.5 | 0.041948 |
| 11-12 | 11.5 | 0.044929 |
| 12-13 | 12.5 | 0.033388 |
| 13-14 | 13.5 | 0.031923 |
| 14-15 | 14.5 | 0.018694 |
| 15-16 | 15.5 | 0.019953 |
| 16-17 | 16.5 | 0.027571 |
| 17-19 | 18.0 | 0.022294 |

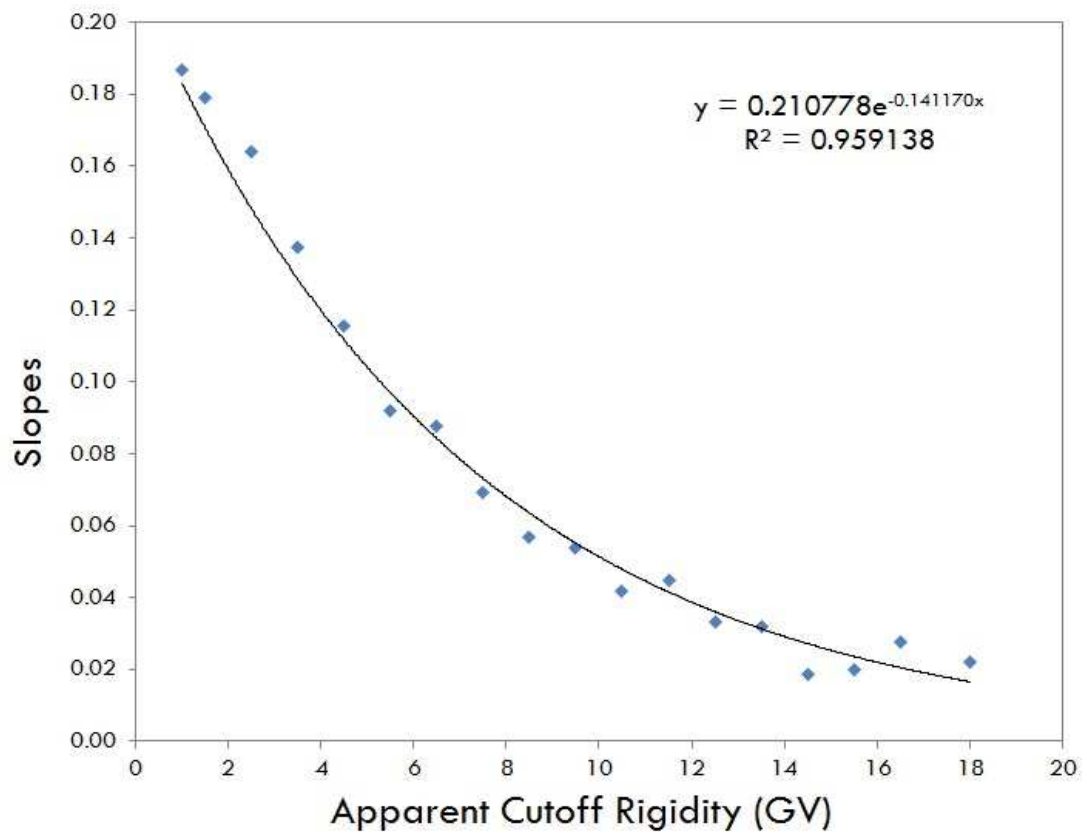


Figure C.7: The regression coefficient S as a function of apparent cutoff rigidity P_c

APPENDIX D

THE NAGASHIMA APPROACH APPLIED TO THE LATITUDE SURVEY DATA

Before we obtained excellent results by using the Dorman technique as described in Chapter 4, we first focused on using the Nagashima technique for determining a response function R of primary cosmic rays. Nagashima et al. (1989) constructed a response function by combining the Galactic cosmic ray spectrum (G), modulation function (M) and yield function (Y) as expressed in equations D.1-D.4:

$$R = - \left[\frac{dN}{dP_c} \right]_P = G(P)M(P, t)Y(P, h). \quad (\text{D.1})$$

$$G(u, \gamma_n) = \frac{\gamma_1}{(\gamma_2 + u)^{\gamma_3}}, \quad (\text{D.2})$$

$$M(P_c, t) = \exp \left[\frac{-\mu_1(t)}{\mu_2 + (P_c/1 \text{ GV})^{\mu_2}} \right], \quad (\text{D.3})$$

$$Y(U, h, \varepsilon, \eta_n) = Y_0 u^\varepsilon \exp \left[-\eta_1 \left(\frac{h}{1033} \right)^{\eta_2} - \eta_3 \left(\frac{h}{1033} \right)^{\eta_4} k_l(u, \eta_5) \right], \quad (\text{D.4})$$

where N is the count rate from a neutron monitor, P is rigidity, P_c is cutoff rigidity, h is depth in the atmosphere and t is time. Nagashima et al. (1989) tried to make their parameterization have some physical content, as opposed to the Dorman function, which has no physical content. From equations D.2-D.4, we can see that there are a total of 14 adjustable parameters. We used the SURVEY program, developed by Prof. Paul Evenson (U. Delaware, USA), to seek optimal parameters to fit latitude survey data. We decided to vary only six parameters, ε , η_1 , η_2 , η_3 , η_4 and η_5 , to describe the yield function, and γ_1 is an overall normalization. The initial values are the values in Nagashima et al. (1989) as explained in chapter 2, i.e., $\varepsilon = 0.0$, $\eta_1 = 2.2$, $\eta_2 = 1.62$,

$\eta_3 = 12.7$, $\eta_4 = 0.50$ and $\eta_5 = 0.42$. We fixed all other parameters to values from Nagashima et al. (1989).

Figures D.1-D.3 below show two kinds of graphs for each survey. The left panels compare the data (black squares) and model fit (red solid lines). The fit error between them vs. cutoff rigidity is shown in Figure D.4. The black bunches may be due to the problem of barometric pressure treatment. The figures also show the “Quality” value, which is square of the accumulated count rate difference. With only one or two exceptions they form a nice pattern. There is little error during solar maximum and a “concave” shape, increasing towards solar minimum, both before and after the polarity reversal.

A key weakness of this technique is a lack of clear information about whether we are getting all of the bugs out of the data and fully correcting for pressure and other effects. Another problem is that the Nagashima spectrum parameterization cannot describe a crossover in the spectrum. Thus addressing the goals of this study would require modifying the Nagashima parameterization. We had hoped that the non-physical parameters like those of the Dorman function, but with more parameters, would help describe changes in the response function better than that the Dorman function. This hope was not realized.

To get the best representation of each annual survey we would generate a sea level response function for the average modulation level of the survey. If we ever decide on what the proper yield function should be we could just divide the response functions by the yield function to get actual spectra. If we get the best parameters of the yield function, we could obtain the cosmic ray spectrum. We thought that this would be easily done in the Nagashima model because the spectrum is separate from the yield function. But finally, we could not obtain good parameters of the yield function from the Nagashima technique. We have used the parameters of the fit for each year, together with the average McMurdo count rate, to generate a differential response function (at sea level) for each year. Figure D.5 shows all the years together. The red upward triangles indicate the data before survey year 2000, the green downward triangles indicate those after survey year 2000, and black squares indicate those of survey year 2000 itself. The yearly plots are also shown in Figures D.1- D.3. There is a nice progression from solar minimum to solar maximum and back, but the issue about the best parameters is still questionable.

One another problem occurred when we ran the barometer coefficient calculation for all of the surveys, with the result shown in Figure D.6. This just confirms that the major apparent difference between the Nagashima analysis and the Dorman analysis is somehow related to getting the barometer correction wrong. The Nagashima analysis builds the systematic variation of the barometer with cutoff into the yield function. The barometer dependence may be taking care of the fluctuations but the extrapolation to sea level is failing. With these problematic issues, we gave up on the Nagashima technique and changed to use the method of direct determination fitted by the Dorman technique instead.

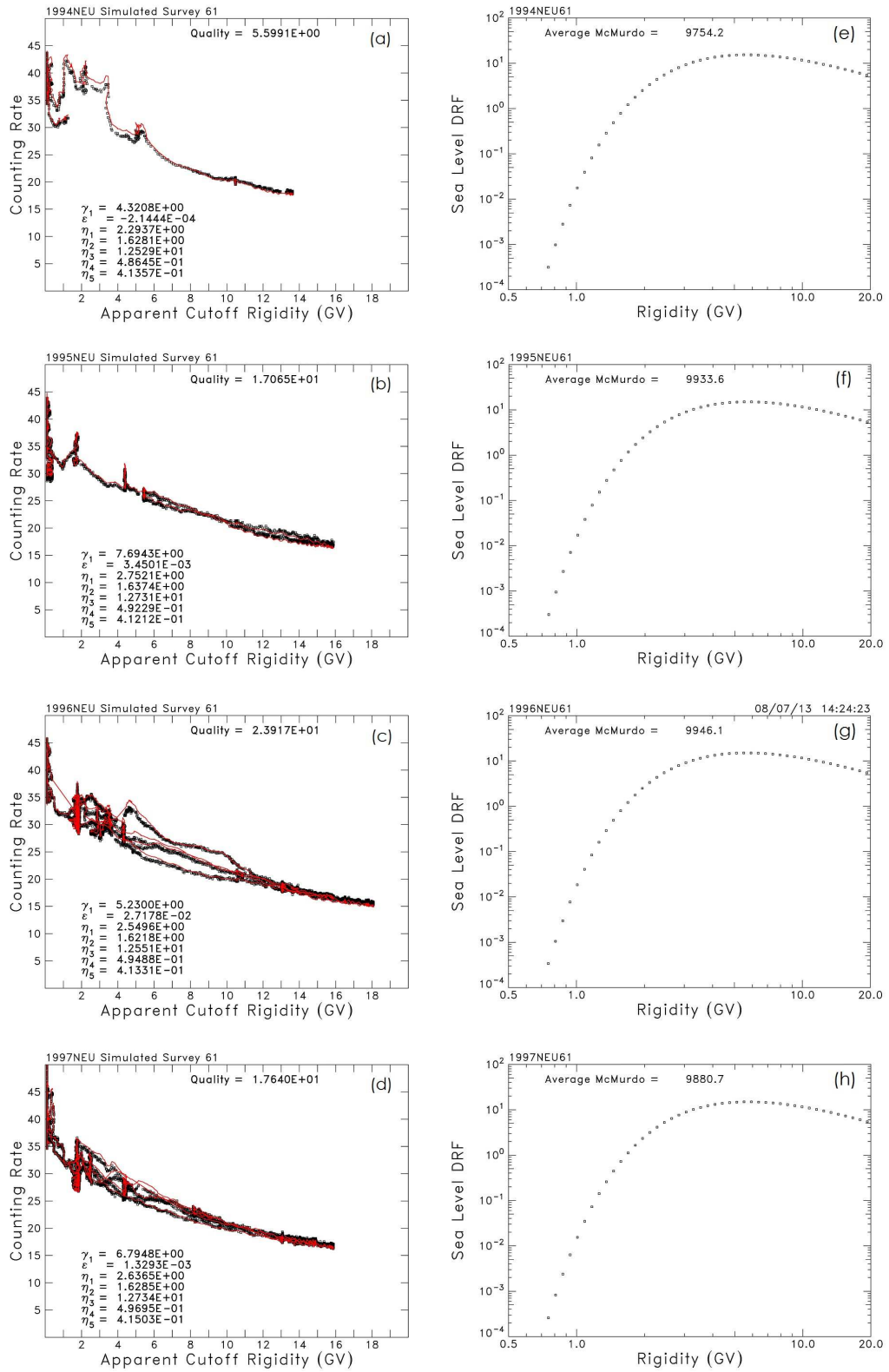


Figure D.1: (a)-(d) Mobile neutron monitor count rate (black squares) and Nagashima model fit (red line) for survey years 1994 to 1997 as a function of apparent geomagnetic cutoff. (e)-(h) Inferred differential response functions (at sea level).

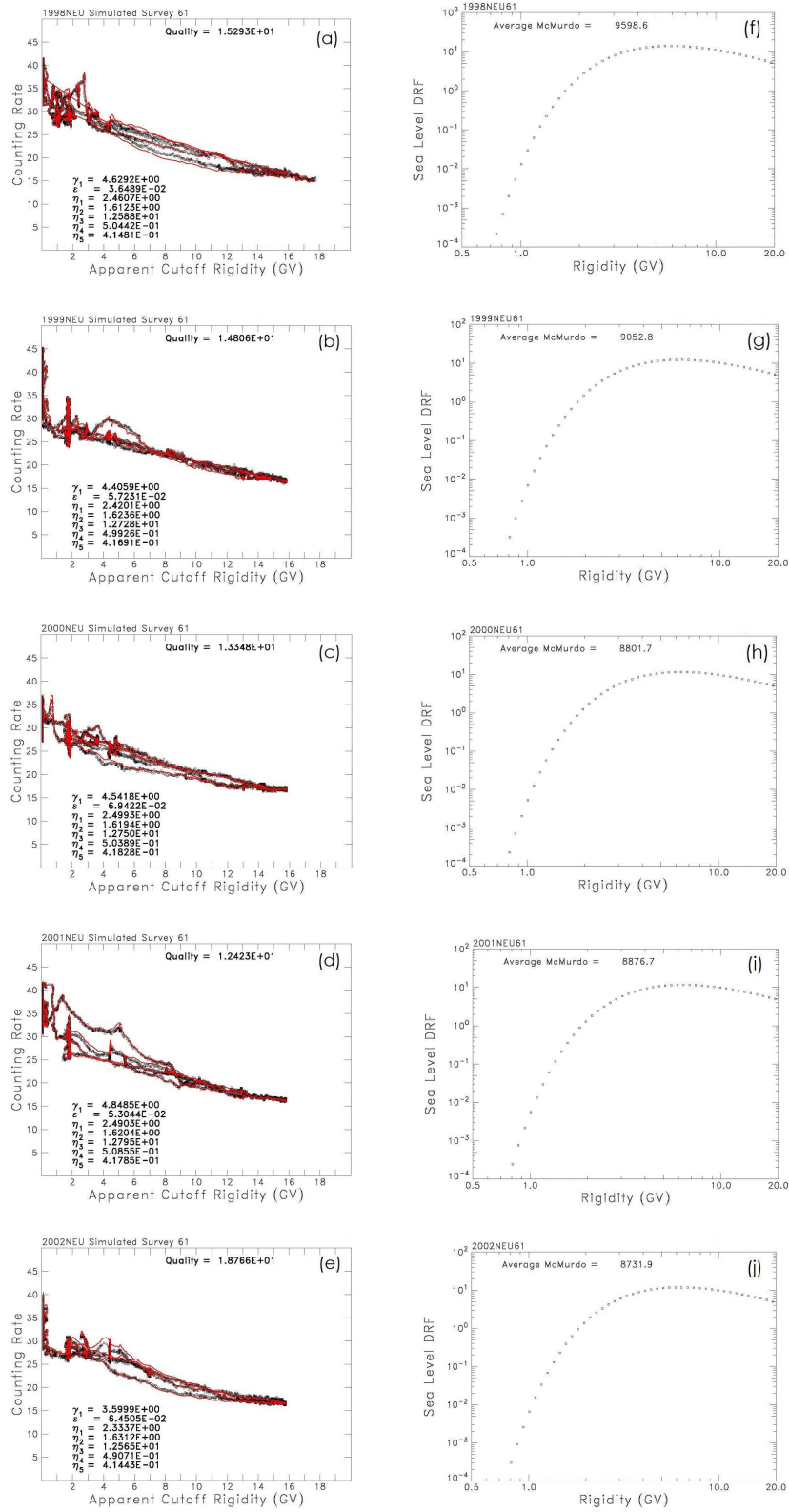


Figure D.2: Like Figure D.1 of Nagashima technique, for 1998-2002 survey years, showing the transition from solar minimum to solar maximum conditions.

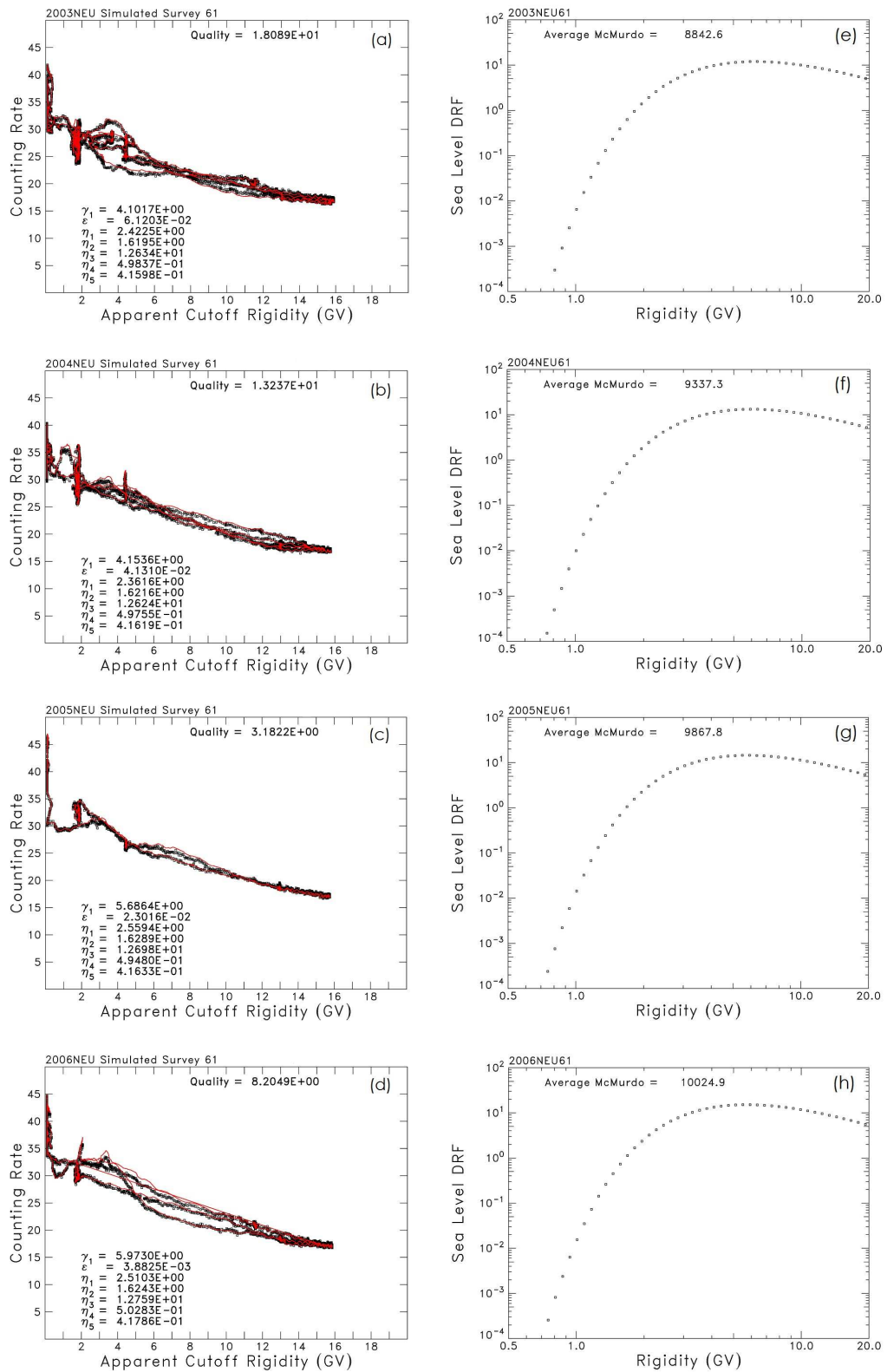


Figure D.3: Like Figure D.1 of Nagashima technique, for 2003-2006 survey years, showing the transition from solar maximum to solar minimum conditions.

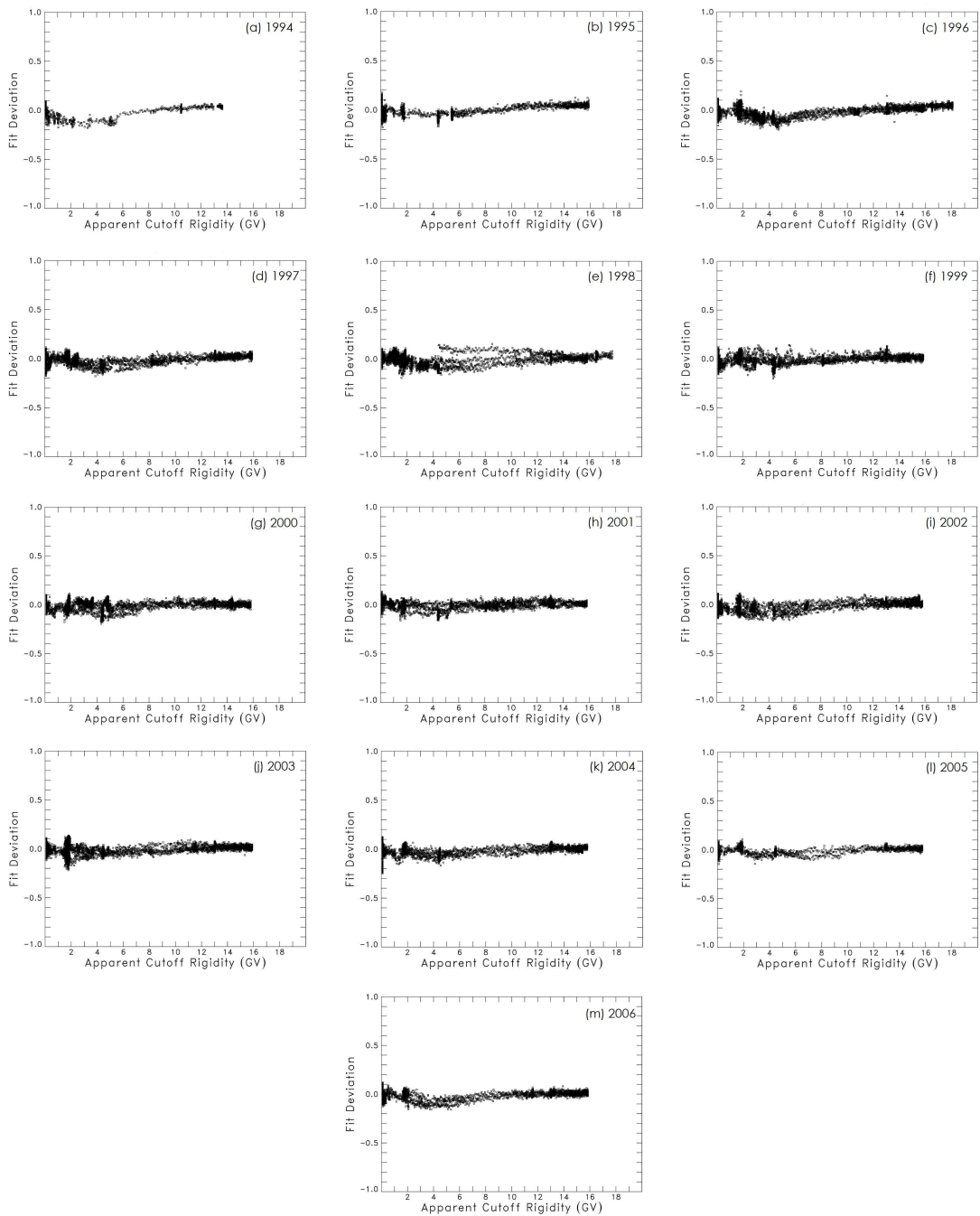


Figure D.4: Residuals (s^{-1}) from the fits between mobile neutron monitor count rate and Nagashima model fit for all survey years as a function of cutoff rigidity.

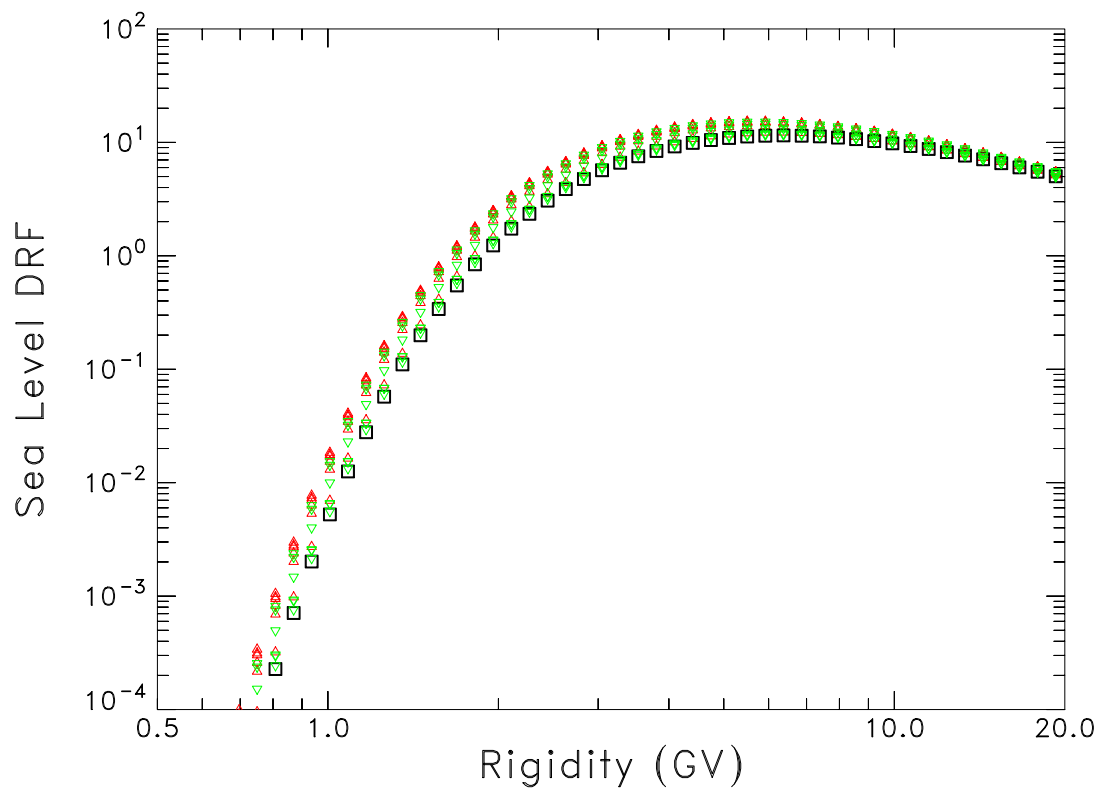


Figure D.5: Differential response functions (at sea level) for all the voyages together as a function of rigidity (GV). Red upward triangles are from data before 2000, green downward triangles are from data after 2000 and black squares are from data of 2000. There is clear no crossover in the spectrum described by the Nagashima technique.

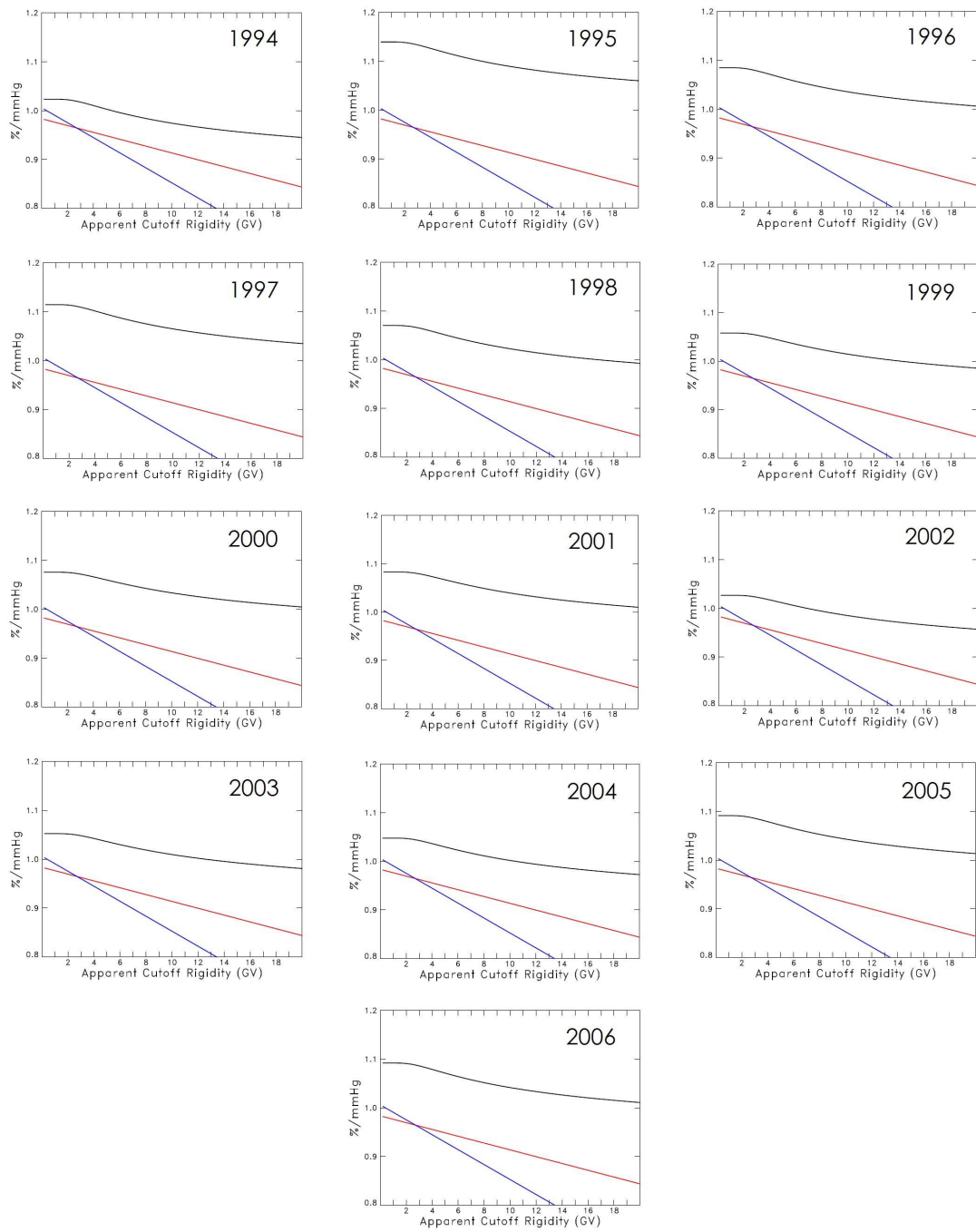


Figure D.6: Comparisons of the barometer correction from equation (2) of Clem et al. (1997) (red lines), from this work following equation 4.2 (blue lines), and from the Nagashima analysis (black lines), which is at a different level for each survey year.

BIOGRAPHY

| | |
|------------------------------|--|
| NAME | Ms. Waraporn Nuntiyakul |
| DATE OF BIRTH | 13 August 1981 |
| PLACE OF BIRTH | Bangkok, Thailand |
| INSTITUTIONS ATTENDED | Silpakorn University, 1999–2002 Bachelor of Science (Physics) Kasetsart University, 2003–2006 Master of Science (Physics) Mahidol University, 2009–Present Doctor of Philosophy (Physics) |
| SCHOLARSHIP RECEIVED | The Royal Golden Jubilee Ph.D. Program |
| RESEARCH GRANTS | Research assistant, Thailand Center of Excellence in Physics |
| POSITION | Lecturer, 2006–Present Physics Program, Faculty of Science, Chandrakasem Rajabhat University |
| HOME ADDRESS | 588/37 Ladprow-Wanghin Rd., Ladprow Bangkok 10230 Thailand E-mail: w.nuntiyakul@gmail.com |
| PUBLICATION | Nuntiyakul, W., Evenson, P., Ruffolo, D., et al. 2014, <i>Astrophys. J.</i> , in press. |
| AWARDS RECEIVED | Outstanding Oral Presentation Award, from RGJ-Ph.D. Congress XV The 2 nd Poster Presentation Award, from the first COSPAR Symposium |